Titre: Title:	Thermal-mechanical fatigue crack growth in aircraft engine materials
Auteur: Author:	Yi Dai
Date:	1993
Type:	Mémoire ou thèse / Dissertation or Thesis
Référence: Citation:	Dai, Y. (1993). Thermal-mechanical fatigue crack growth in aircraft engine materials [Thèse de doctorat, Polytechnique Montréal]. PolyPublie. https://publications.polymtl.ca/57980/

UNIVERSITÉ DE MONTRÉAL

THERMAL-MECHANICAL FATIGUE CRACK GROWTH IN AIRCRAFT ENGINE MATERIALS

par

YI DAI

DÉPARTEMENT DE MÉTALLURGIE ET
DE GÉNIE DES MATÉRIAUX

ÉCOLE POLYTECHNIQUE

THÈSE PRÉSENTÉE EN VUE DE L'OBTENTION
DU GRADE DE PHILOSOPHIAE DOCTOR (Ph. D.)
(GÉNIE MÉTALLURGIQUE)

Mai 1993

ISBN 0-315-86543-1

Canada

yi DAi

tion Abstracts International is arranged by broad, general subject categories. Please select the one subject which most escribes the content of your dissertation. Enter the corresponding four-digit code in the spaces provided.

erials Science

SUBJECT TERM

0794

SUBJECT CODE

U·M·I

Categories

IUMANITIES AND SOCIAL SCIENCES

CATIONS AND THE ARTS

e 0729
..... 0377
..... 0900
..... 0378
..... 0357
Science 0723
..... 0391
ence 0399
nunications 0708
..... 0413
nmunication 0459
..... 0465

..... 0515
ion 0514
Continuing 0516
..... 0517
..... 0273
id Multicultural 0282
..... 0688
College 0275
and Instruction 0727
nood 0518
..... 0524
..... 0277
nd Counseling 0519
..... 0680
..... 0745
..... 0520
omics 0278
..... 0521
nd Literature 0279
s 0280
..... 0522
of 0998
..... 0523

Psychology 0525
Reading 0535
Religious 0527
Sciences 0714
Secondary 0533
Social Sciences 0534
Sociology of 0340
Special 0529
Teacher Training 0530
Technology 0710
Tests and Measurements 0288
Vocational 0747

LANGUAGE, LITERATURE AND LINGUISTICS

Language
- General 0679
- Ancient 0289
- Linguistics 0290
- Modern 0291

Literature
- General 0401
- Classical 0294
- Comparative 0295
- Medieval 0297
- Modern 0298
- African 0316
- American 0591
- Asian 0305
- Canadian (English) 0352
- Canadian (French) 0355
- English 0593
- Germanic 0311
- Latin American 0312
- Middle Eastern 0315
- Romance 0313
- Slavic and East European 0314

PHILOSOPHY, RELIGION AND THEOLOGY

Philosophy 0422
Religion
- General 0318
- Biblical Studies 0321
- Clergy 0319
- History of 0320
- Philosophy of 0322

Theology 0469

SOCIAL SCIENCES

American Studies 0323
Anthropology
- Archaeology 0324
- Cultural 0326
- Physical 0327

Business Administration
- General 0310
- Accounting 0272
- Banking 0770
- Management 0454
- Marketing 0338

Canadian Studies 0385
Economics
- General 0501
- Agricultural 0503
- Commerce-Business 0505
- Finance 0508
- History 0509
- Labor 0510
- Theory 0511

Folklore 0358
Geography 0366
Gerontology 0351
History
- General 0578
- Ancient 0579
- Medieval 0581
- Modern 0582
- Black 0328
- African 0331
- Asia, Australia and Oceania 0332
- Canadian 0334
- European 0335
- Latin American 0336
- Middle Eastern 0333
- United States 0337

History of Science 0585
Law 0398
Political Science
- General 0615
- International Law and Relations 0616
- Public Administration 0617

Recreation 0814
Social Work 0452
Sociology
- General 0626
- Criminology and Penology ... 0627
- Demography 0938
- Ethnic and Racial Studies 0631
- Individual and Family Studies 0628
- Industrial and Labor Relations 0629
- Public and Social Welfare 0630
- Social Structure and Development 0700
- Theory and Methods 0344

Transportation 0709
Urban and Regional Planning 0999
Women's Studies 0453

CIENCES AND ENGINEERING

L SCIENCES

..... 0473
ny 0285
Culture and
on 0475
Pathology 0476
ence and
ology 0359
and Wildlife 0478
lture 0479
hology 0480
rsiology 0817
lanagement 0777
echnology 0746

..... 0306
..... 0287
ics 0308
..... 0309
..... 0379
..... 0329
gy 0353
..... 0369
y 0793
logy 0410
r 0307
ence 0317
raphy 0416
y 0433
..... 0821
y Science 0778
..... 0472

..... 0786
..... 0760

ICES

stry 0425
..... 0996

Geodesy 0370
Geology 0372
Geophysics 0373
Hydrology 0388
Mineralogy 0411
Paleobotany 0345
Paleoecology 0426
Paleontology 0418
Paleozoology 0985
Palynology 0427
Physical Geography 0368
Physical Oceanography 0415

HEALTH AND ENVIRONMENTAL SCIENCES

Environmental Sciences 0768
Health Sciences
- General 0566
- Audiology 0300
- Chemotherapy 0992
- Dentistry 0567
- Education 0350
- Hospital Management 0769
- Human Development 0758
- Immunology 0982
- Medicine and Surgery 0564
- Mental Health 0347
- Nursing 0569
- Nutrition 0570
- Obstetrics and Gynecology .. 0380
- Occupational Health and Therapy 0354
- Ophthalmology 0381
- Pathology 0571
- Pharmacology 0419
- Pharmacy 0572
- Physical Therapy 0382
- Public Health 0573
- Radiology 0574
- Recreation 0575
- Speech Pathology 0460
- Toxicology 0383

Home Economics 0386

PHYSICAL SCIENCES

Pure Sciences

Chemistry
- General 0485
- Agricultural 0749
- Analytical 0486
- Biochemistry 0487
- Inorganic 0488
- Nuclear 0738
- Organic 0490
- Pharmaceutical 0491
- Physical 0494
- Polymer 0495
- Radiation 0754

Mathematics 0405
Physics
- General 0605
- Acoustics 0986
- Astronomy and Astrophysics 0606
- Atmospheric Science 0608
- Atomic 0748
- Electronics and Electricity 0607
- Elementary Particles and High Energy 0798
- Fluid and Plasma 0759
- Molecular 0609
- Nuclear 0610
- Optics 0752
- Radiation 0756
- Solid State 0611

Statistics 0463

Applied Sciences

Applied Mechanics 0346
Computer Science 0984

Engineering
- General 0537
- Aerospace 0538
- Agricultural 0539
- Automotive 0540
- Biomedical 0541
- Chemical 0542
- Civil 0543
- Electronics and Electrical 0544
- Heat and Thermodynamics ... 0348
- Hydraulic 0545
- Industrial 0546
- Marine 0547
- Materials Science 0794
- Mechanical 0548
- Metallurgy 0743
- Mining 0551
- Nuclear 0552
- Packaging 0549
- Petroleum 0765
- Sanitary and Municipal 0554
- System Science 0790

Geotechnology 0428
Operations Research 0796
Plastics Technology 0795
Textile Technology 0994

PSYCHOLOGY

General 0621
Behavioral 0384
Clinical 0622
Developmental 0620
Experimental 0623
Industrial 0624
Personality 0625
Physiological 0989
Psychobiology 0349
Psychometrics 0632
Social 0451

UNIVERSITÉ DE MONTRÉAL

ÉCOLE POLYTECHNIQUE

Cette thèse intitulée:

THERMAL-MECHANICAL FATIGUE CRACK GROWTH IN AIRCRAFT ENGINE MATERIALS

Présenté par: Yi Dai

en vue de l'obtention du grade de : Philosophiae Doctor (Ph.D.)

a été dûment acceptée par le jury d'examen constitué de:

M. DICKSON J. Yvan, Ph.D., président

M. MARCHAND Norman J., Ph. D., membre et directeur de recherche

M. KOUL Ashok, Ph. D., membre

M. HONGOH Masamichi, Ph.D., membre

À mes parents,
à ma femme,
à tous ceux qui
me sont chers

SOMMAIRE

L'augmentation du rapport poussée/poids des moteurs aéronautiques à haute performance requiert maintenant que des températures plus élevées soient utilisées à tous les étages des moteurs. De plus, ces augmentations de températures sont accompagnées d'une augmentation substantielle des contraintes résultant de vitesses de rotation plus élevées (RPM). Par conséquent, les composantes en alliages à base de titane utilisées dans les sections de compression des moteurs doivent maintenant supporter un endommagement par fatigue accélérée en raison d'un environnement et de conditions d'opération plus aggressives. Conjointement, l'application de la conception en fonction de la tolérance au dommage (Damage Tolerance Design, DTD) au design et à l'entretient des moteurs requiert plus de caractérisations de matériaux, d'analyses additionnelles et davantages d'expérimentations. Cette nouvelle situation a incité les fabricants de turbine à gaz à réévaluer la vie en fatigue de leurs matériaux et composantes et en particulier, de toutes les composantes possédant des discontinuités géométriques, sous des conditions de services simulés.

Le test conçu pour étudier en laboratoire, l'endommagement de matériaux soumis à une variation de déformations (ou contraintes) et à une histoire thermique, est appelé test de fatigue thermo-mécanique (TMF). Dans ce type de test, la température ainsi que la déformation (ou contrainte) mécanique imposées à l'éprouvette sont contrôlées indépendamment. Contrairement aux essais de fatigue par contraintes d'origine thermique (TF), en TMF, l'éprouvette est traitée comme

un élément de volume subissant un profil de température uniforme (variant dans le temps) ainsi qu'un champ de déformation connu. Pendant l'essai, la phase entre la déformation et la température peut être modifiée arbitrairement de tel sorte que l'histoire déformation-température d'une composante réelle peut être simulée étroitement.

L'objectif général de ce projet de recherche entre l'École Polytechnique et Pratt & Whitney Canada était (1) de développer la capacité d'effectuer des essais de TMF lesquels permettent de tester des matériaux structuraux sous des conditions de services simulés; (2) quantifier, en situation de fatigue Oligocyclique (LCF), la durée de vie à l'initiation de fissures et le comportement de fissures lors de leurs croissances dans des matériaux utilisés dans les moteurs et sous conditions de services; (3) établir la relation entre l'essai pleine grandeur de composantes et l'essai en laboratoire à l'aide d'éprouvettes possédant des caractéristiques géométriques de la composante et [4]développer une connaissance mécanistique du comportement du matériau sous des conditions isothermiques et de type TMF. Les matériaux sélectionnés dans ce projet ont été deux alliages forges de titane utilisés pour les composantes de moteurs de PWC. Il s'agit du Ti-6Al-4V (Ti64) et du Ti-6Al-2Sn-4Zr-6Mo (Ti6246).

Dans la thèse, une description détaillée du système permettant d'effectuer les essais TMF est présentée. Le système est composé de deux unités de contrôles en boucles fermées indépendantes. Une boucle sert au contrôle de la température, tandis que l'autre effectue le contrôle du chargement mécanique. Les éprouvettes sont chauffées par induction. La puissance livrée est régularisée par un contrôleur

de température digitale. La partie refroidissement du cycle thermique est effectuée par convection forcée dans l'air. Le contrôle précis et stable de la température a été atteint grâce à une bodine d'induction et des distributeurs d'air conçus avec soin, et aussi par un ajustement fin des paramètres de contrôle du système de chauffage par induction et de l'unité de contrôle de température. Le cyclage mécanique est effectué par un système serro-électro-hydrolique. Ce système est équipé d'une unité de contrôle munie d'un interface de communication. Le contôle du test et l'acquisition des données sont faits par une unité HP laquelle est asservie par une station HP.

Un programme (TMF-1) effectuant le contrôle du test et l'acquisition des données, a été développé à partir du système HP9000. Le système est capable d'accomplir plusieurs type de tests utiles pour caractériser les propriétés mécaniques des matériaux structuraux, tel que: (1) test de traction monotone (courbe $\sigma \sim \varepsilon$); (2) test de déformation cyclique; (3) test de fatique oligocyclique isotherme (LCF); et (4) des tests TMF. Les principales caractéristiques du système sont (1) des procédures d'entrée et de vérification des paramètres d'opérations conviviales: (2) mises au point du système et calibration automatique; (3) un suivi et affichage de données en temps réel; (4) récupération et transfert des données ultra-rapides (100,000 lectures/sec) effectués en arrière plan par un système à cannaux multiples; (5) une procédure intéractive du contrôle global du test (i.e. démarrage, cycle d'acquisition, vérification de sécurités, critères d'arrêt, etc.). De plus, le code est structuré en module ce qui accroît sa versatilité à accomoder n' importe quel nouvelle exigence.

Trois types de cycle TMF ont été réalisés à l'aide de cet équipement. La plupart des chercheurs ont considéré originairement deux types de tests TMF, hors-phase (déformation maximum à température minimum) et en phase (déformation maximum à température maximum). Dans cette étude, un type de cycle plus représentatif (en losange) a été ajouté par ce qu'il est perçu comme représentant de façon plus réaliste les conditions de service de disques de turbines.

En effectuant des essais LCF et TMF sur des alliages de titane, ce système a démontré sa capacité à tester des échantillons sous des conditions variées d'histoires thermomécaniques (isotherme et anisotherme) avec un haut degré de précision et de fiabilité.

L' initiation et la croissance de fissures ont été mesurées à l'aide d'une unité de mesure de chute de potentiel de courant alternatif (ACPD). L'optimisation de l'instrumentation et des procédures d'attachements des sondes, ont été effectuées pour plusieurs géométries d'éprouvettes en titane dont la géométrie SEN (en condition isotherme et anisotherme). La réponse des matériaux à différentes fréquences et amplitudes de courants alternatifs, ont été caractérisées.

La sensibilité du système et la linéarité du signal (ACPD) en fonction de la longueur de la fissure sont améliorées par l'effet de peau (skin effect) qui est produit par le passage d'un courant alternatif à haute fréquence (dans cette étude > 30KHz) à travers l'éprouvette. La dépendance linéaire du signal ACPD a été vérifiée par plusieurs résultats expérimentaux. Avec le présent système ACPD, la

croissance de fissures en fonction du nombre de cycles (courbes a-N) peut être facilement obtenue à températures ambiantes comme à températures élevées.

Le présent système ACPD a une probabilité de détection (POD) supérieure à 95% pour une taille de fissure (a_i) d'environ 50 μm. Ce qui est bien inférieur à la taille à l'initiation spécifié par le Engine Structural Integrity Program (ENSIP) utilisé dans la gestion de la vie des composantes pour les moteurs commerciaux de PWC, dans lequel a_i = 1/32" (800μm). Pour cette raison, le système peut être utilisé pour mesurer la vie à l'initiation de fisssures d'éprouvettes ou d'échantillons simulant des composantes. De plus la croissance moyenne de fissures peut être suivie par le système avec une précision d'environ 2μm par 1mv de changement de potentiel à l'ambiante et 18μm par 1mv à haute température. Ceci est également meilleur que les exigences de l'ASTM pour les tests de croîssances de fissures en fatigue. Finalement, le système s'est révélé idéal pour l'étude de mécanimes de fermeture des fissures courtes et longues.

Des tests d'initiation de fissure ont été réalisés pour le Ti64 et le Ti6246 à températures ambiantes et à températures élevées (400°C pour le Ti64, 480°C pour le T6246). Des éprouvettes entaillées d'un seul côté (SEN, B=5.33mm, W=10.67mm) furent utilisées. L'entaille était de forme semi-circulaire et a été dimensionnée pour simuler le facteur de concentration de contrainte (K_t) des trous de boulonnage que l'on retrouve sur les disques de compresseur de PWC. Les éprouvettes ont été cyclées à une fréquence de 10 cpm par contrôle du champ lointain de déformation.

La détection de l'initiation de fissures dans les éprouvettes SEN a été réalisée par la technique de l'ACPD. La relation entre le signal ACPD mesuré et le patron de fissuration a été étudiée. Le nombre de cycle pour l'initiation d'une fissure (N_i) a été défini comme celui à lequel une fissure possédant une profondeur moyenne de 1/64" (0.4 mm) été obtenue au fond de l'entaille. Avec cette définition, N_i peut être aisément obtenu à partir de la courbe $a \sim N$. Une procédure d'analyse de la déformation à l'entaille basée sur le model de Gemma a été développée. Cette analyse établie la fonction qui relie le champ de déplacement lointain aux paramètres déformation/contrainte à l'entaille. Ces paramètres sont la déformation totale, la déformation plastique maximum et l'amplitude de la déformation plastigue au fond de l'entaille. Ces informations ont été utilisées pour corrèler les données sur l'initiation de fissure. Afin d'obtenir les constantes caractérisant le comportement en déformation cyclique des matériaux, des essais en déformation cyclique à hautes températures ont été réalisés. Les résultats des essais LCF obtenus avec les éprouvettes SEN indiquent que:

- il est possible de développer une nouvelle méthodoloqie de prédiction de durée de vie en fatigue de composantes pour les nouvelles conditions d'utilisation en service. Les données sont générées à l'aide d'essais LCF peu coûteux en utilisant des éprouvettes simulant les aspects géométriques des composantes;

- La résistance à l'initiation de fissure (FCI) du Ti64 forgé à l'ambiante et à 400°C est bonne. L'initiation est principalement causée par la déformation plastique cycliques;

- La résistance à l'initiation de fissure du Ti6246 à haute température est faible. Sa FCI est grandement affectée par une fragilisation assistée par l'environnement.

Ces données confirment les résultats observés dans ce domaine et obtenus lors d'essais faits sur des composantes avec des bancs d'essai.

Dès qu'une fissures s'initie, il est important de quantifier leur propagation dévient d'une et prédire sa vitesse de croîssance. Dans ce projet, plusieurs paramètres de la mécanique de la rupture basés sur différentes solutions de facteur d'intensité de contrainte (K) ont été éxaminés afin d'analyser la cinétique de la croissance des fissures. L'effet du champ de contrainte de l'entaille sur la croissance des fissures fût examiné. Le facteur d'intensité de contrainte pour des fissures courtes débouchant en fond de fissure ainsi que celui d'une fissure longue se propageant hors de la zone affectée ont également été calculés.

Avec l'aide de la technique de l'ACPD, les vitesses de croissance de la fissure en fonction du ΔK pour les différents stages de propagation ont été obtenues. Ces études ont produit les résultats suivant:

- Les trois tailles critiques de fissure délimitant les quatres zônes de propagation ont été quantifiées. La zone où la croissance est controlée par la microstructure ($<60\mu m$), par le champ de déformation inélatique de l'entaille ($<130\mu m$), par le champ de déformation élastique de l'entaille ($<420\mu m$) et finalement la zône où la croissance est controlée par le champ lointain;

-Les vitesses de propagation de fissures pour le Ti64 à l'ambiante, 105°C, 260°C et 400°C, lesquelles peuvent être utilisées pour prédire la vie en fatigue propagation de composantes réelles;

-Les vitesses de propagation de fissures pour le Ti6246 à l'ambiante, 150°C, 330°C et 482°C, les quelles peuvent également être utilisées pour prédiction de durée de vie de composantes réelles;

- une quantification de l'effet de la température et de la microstructure sur la vitesse de propagation des fissures dans les alliages de titane.

Ces données ont également servi à la compréhension des mécanismes de propagation des fissures dans les alliages de titane.

Puis qu'il s'agissait du principal objectif du projet, plusieurs essais de TMF ont été réalisés sur les alliages Ti64 et Ti6246. Pour ces essais, des éprouvettes SEN furent utilisées. Les entailles sur les éprouvettes avaient une profondeur de 0.5 mm et une largeur de 0.38 mm et furent usinées par électro-décharge (EDM). Les échantillons furent cyclés dans des conditions de déformation contrôlée à une fréquence de 0.01 Hz (une période de 100 sec). Trois type de conditions TMF ont été étudiés. Les capacités du système à réaliser des essais TMF ainsi que l'applicabilité de la technique de l'ACPD en situation anisotherme ont été démontrées.

Des données concernant la fissuration en condition TMF ont été obtenues pour l'alliage Ti64 pour un cycle thermique entre 150°C (T_{min}) et 400°C (T_{max}), et entre 200°C (T_{min}) et 480°C (T_{max}) pour le Ti6246. Des essais FCG isothermes aux températures T_{min} et T_{max} et à la même fréquence ont également été réalisés pour de fins de comparaison. Les résultats des essais TMF furent correlées avec le facteur d'intensité de contrainte ΔK. À la vue de ces résultats, les conclusions suivantes peuvent être émises:

- Les courbes de propagation en TMFCG pour l'alliage Ti64 et Ti6246 tombent entre celles obtenues en FCG isotherme aux températures extrèmes. De façon plus précise, les résultats des essais TMF en phase sont près de ceux obtenus lors de essais FCG à la température T_{max} tandis que ceux obtenus lors des essais déphasés sont proches des résultats FCG à T_{min};

- un effet de fermeture de fissure prononcé à été observé dans les essais TMFCG avec le Ti64;

- une forte influence de l'environnement (fragilisation par l'oxygène) a été remarquée dans les essais TMFCG à T_{max} pour le Ti6246.

Un modéle simple based sur une analyse phénomènologique additionnant la chrono-dépendance du dommage causé par l'attaque de l'environnement aux conditions isothermes et TMF, a été proposé pour l'alliage Ti6246.

De plus, la croissance accélérée des fissures observée dans les essais TMF en phase explique les résultats en FCG obtenus par d'autres et ceux obtenus avec des bancs d'essais pour les composantes forgées en Ti6246. Ces résultats sont en parfait accord avec d'autres publiés récemment dans une étude indépendante (MTU Allemagne) dans laquelle des composantes forgées similaires en Ti6242 ont été testées à hautes températures.

De nombreuses observations au microscope électronique à balayage (MEB) des surfaces de rupture obtenues sous différentes conditions ont été réalisées. Pour étudier l'influence de la microstructure sur le comportement en fatigue, les différences microstructurales des deux alliages corroyés furent examinées attentiverrent. Des analyses de composition ont également été réalisées à l'aide d'un analyseur spectral. Il a été trouvé que la composition chimique en élément beta-stabilisateur (V dans le Ti64 rt Mo dans le Ti6246) varie significativement dans les phases alpha et béta pour les deux alliages. Ces différences de compositions ont été utilisées comme références pour identifier la morpholoqie de la fracture associée aux différentes phases lors de l'analyse fractographique.

Pour les essais d'initiation de fissures, les analyses au MEB ont principalement portées sur les cites d'initiation des microfissures au fond des entailles. Il a été trouvé que:

- Les sites d'initiation pour les deux alliages sont les particules de phase α et/ou les interfaces α/β, et que la surface de ces sites présente des facettes de quasi-clivage;

- Les grandes zones de facettes de quasi-clivage trouvées dans le Ti6246, pour les essais FCG à hautes températures, sont le résultat de la fragilisation assisée par l'environnement des interfaces α/β ;

-La bonne résistance de l'alliage Ti64 lors des essais d'initiation (FCI) oligocyclique isotherme est associée à une structure équiaxe de la phase α;

-La faible résistance de l'alliage Ti6246 lors des essais FCI est attribuable à la structure acciculaire grossière de la phase α.

Les observations fractographiques concernant la croissance des fissures en conditions isotherme et TMF ont principalement portées sur (1) la relation entre la da/dN microscopique (par comptage des stries) et celle macroscopique mesurée expériment alement; (2) les effets de la microstructure sur la trajectoire de propagation des fissures; et (3) la comparaison de l'allure générale de l'aspect morphologique de la fissuration pour les différentes conditions lors des essais. Cette partie de l'ètude a permis de faire les observations suivantes:

- les vitesses de propagation microscopique correspondent bien avec celles macroscopiques mesurées par ACPD (dans la régions contrôlée par le ΔK, loi de Paris);

- une fissuration secondaire le long des interfaces α/β à ΔK modéré pour l'alliage Ti64 à hautes températures;

- une fissuration préférentielle assistée par fragilisation environnementale (haute température) aux interfaces α/β pour l'alliage Ti6246;

- des différences notables entre les caractéristiques originant de la plasticité en bout de fissure des essais TMF en phase et déphasé pour l'alliage Ti64;

- des différences fractographiques entre les essais TMF en phase et déphasé pour l'alliage Ti6246, résultant d'une fragilisation à l'oxygène.

Ces observations permettent d'avoir une compréhension phénomènologique de la fissuration dans ces deux alliages de titane. Ils ont permis de développer un modèle de fissuration tenant compte de l'intéraction environnement-fatigue pour le Ti6246 ainsi que d'expliquer l'effet important de la fermeture observé lors des essais TMF avec le Ti64.

Les capacités du système développés lors de cette étude ont été utilisées pour tester des alliages de nickel et des géométries d'éprouvettes plus près de celles des composantes réelles. Des essais de LCF ont été réalisés sur des éprouvettes de type " single tooth firtree " (STFT) en PWA1480 monocristalin à 650°C. Ces tests ont servi à vérifier l'efficacité du système. Le but de ce programme était de développer les capacités nécessaires à effectuer des essais de LCF sur des éprouvettes STFT, semblables à celles disponibles au CEB et GESP de PWA. Cette campagne d'essais a permit:

- de confirmer que le banc d'essais TMF peut réaliser les essais de LCF à températures élevées sur des éprouvettes STFT;

- de mettre au point une procédure complètement automatique contrôlée par ordinateur permettant d'obtenir les données sur l'initiation et la propagation de fissures à l'aide de la technique de l'ACPD. Contrairement à la procédure utilisée par PWA, celle développée ici chez PWC, ne nécessite pas d'interruption ni de démantèlement de l'éprouvette pour effectuer des mesures d'avancement de fissure. En conséquence, la procédure développée est beaucoup plus rapide, plus fiable et plus précise que celle de PWA;

- de dupliquer et vérifier les résultats que PWA a obtenu avec des éprouvettes STFT monocristallines en PWA1480 à 650°C.

Dans les chapitres suivants de cet thèse, une revue de littérature sur la fatigue à hautes températures des alliages de titane et de nickel est présentée, dans un premier temps. Par la suite, une description détaillée de tous les résultats importants est faite. Ces résultats sont ensuite analysés et discutés. Finalement, des recommandations pour de futurs travaux sont ennoncées.

ABSTRACT

This thesis summarizes the major technical achievements obtained as a part of a collaborative research and development project between École Polytechnique and Pratt & Whitney Canada. These achievements include: (1) a thermal-mechanical fatigue (TMF) testing rig which is capable of studying the fatigue behaviors of gas turbine materials under simultaneous changes of temperatures and strains or stress; (2) an advanced alternative current potential drop (ACPD) measurement system which is capable of performing on-line monitoring of fatigue crack initiation and growth in specimen testing under isothermal and TMF conditions; (3) fatigue crack initiation and short crack growth data for the titanium specimens designed with notch features associated with bolt holes of compressor discs; (4) thermal-mechanical fatigue crack growth data for two titanium alloys being used in PWC engine components. Those data explained the material fatigue behavior encountered in full-scale component testing; (5) a complete fractographic analysis for the tested specimens which enhanced the understanding of the fatigue crack growth mechanisms and helped to establish an analytical crack growth model; (6) application of the ACPD fatigue crack monitoring technique to Single Tooth Firtree Specimen (STFT) LCF testing of PWA 1480 single crystal alloy. Finally, a comprehensive discussion concerning the results pertaining to this research project is presented.

ACKNOWLEDGEMENTS

I would like to express my gratitude to Prof. Norman Marchand, the supervisor of this Ph.D. program, also a good friend of mine, for his challenging questions and constructive suggestions. I would not have completed the project so successfully without his frequent encouragement and technical support. It was his dynamic and active research style that always inspired me and stimulated my motivation and creativity.

I would like to devote my sincere thanks to Prof. I. Dickson. His enlightening and constructive suggestions greatly helped me in understanding the micro fracture mechanisms of the tests.

I would like also to express my sincere thanks to Dr. M. Hongoh and Dr. A. Koul for many fruitful discussions and for their technical support. The success of the project is very dependent on their outstanding coordination and management skills. I would also like to thank to Dr. J-P. Immagieon, Dr. P. Li and Dr. S. Li for their constructive advises and technical expertise.

I would like to express my gratitude to Mr. R. Pelletier for his great help in preparing the French version of the extended abstract. I will dearly remember the happy moments and time we sheared together in the TMF lab and at the cafeteria in Plant 2 at P&WC. I also would like to thank Mr. J-M. Simard for his help and constructive discussions during STFT tests.

TABLE DES MATIÈRES

PAGE

LISTE DES FIGURES

PAGE

LISTE DES TABLEAUX

PAGE

LISTE DES ANNEXES

INTRODUCTION

The demand for further improvement in thrust-to-weight ratios for high performance aero-engines now requires that higher temperatures be used in all stages of the engines. Furthermore, these increases in temperatures are accompanied by significant increase in stresses which result from the faster rotational speeds (RPM). As a result, titanium-based components used in the fan and compressor sections of the engines are now expected to sustain accelerated fatigue damage due to a more aggressive environment and operating conditions. Concurrently, the application of damage tolerance design (DTD) concept to aircraft engine design and maintenance requires additional material characterization, more analyses and increased testing. This new situation has prompted the gas turbine manufacturers to re-assess the fatigue lives of their materials and components under simulated service conditionsand and, in particular, of all the components with geometrical discontinuities.

The test devised to study material damage under varying strain (or stress) and temperature histories in the laboratory is called the thermal-mechanical fatigue (TMF) test. In this type of test, both the temperature and mechanical strain (or stress) imposed on the specimen are controlled independently. Unlike thermal fatigue (TF) testing, the specimen in the TMF test is treated as an "element" experiencing an uniform temperature profile (which vary with time) and a known strain field. During the testing, the phase relation between strain and temperature

can be varied arbitrarily so that the strain-temperature history of an actual component can be closely simulated.

The general objective of this research project between École Polytechnique and Pratt & Whitney Canada was to (1) develop the TMF testing capabilities which allow structural material testing under simulated gas turbine service conditions; (2) quantify the Low Cycle Fatigue crack initiation lives and fatigue crack growth behavior of engine materials under service conditions; (3) establish the relationship between full scale component testing and testing of a lab specimen with component like features and (4) develop a mechanistic understanding of material behavior under isothermal and TMF conditions. The materials selected in this project were two titanium forgings used by P&WC for engine components. These are Ti-6Al-4V (Ti64) and Ti-6Al-2Sn-4Zr-6Mo (Ti6246).

In Chapter 1, an extensive and updated literature review on the subjects related to LCF and TMF testing and material's behavior of titanium and nickel base superalloys are presented. These include: (1) an introduction to the alloys and their deformation mechanisms at elevated temperatures; (2) the material's LCF/FCG behavior and modeling at high temperature; (3) the TMF testing techniques and modeling; and (4) an introduction to ACPD crack growth measurement technique. This information is the basis for the technical innovations and the analytical modeling described in later chapters.

The TMF testing system is described in Chapter 2. This system is composed of two independent closed loop control units. One loop is for temperature control,

while the other is for mechanical loading control. Three typical TMF cycles were performed in the system. The advanced data acquisition system and software were developed. By carrying out LCF and TMF testing on the titanium alloys, this system was proven capable of cycling specimens under various programmed thermal-mechanical histories (isothermal and anisothermal conditions) with a high degree of accuracy and reliability.

The ACPD crack growth measurement unit used in the fatigue crack initiation and growth testing is also described in Chapter 2. The optimum instrument set-up, probe spot welding procedures and probe configurations were developed for several geometries of titanium specimens including the SEN geometry (for isothermal and TMF conditions). The materials response to different frequencies and amplitudes of AC currents were characterized. The system's sensitivity and linearity with respect to the measurement of crack lengths are discussed.

In Chapter 3, fatigue crack initiation and growth tests for Ti64 and Ti6246 at room and elevated temperatures (400°C for Ti64, 480°C for Ti6246) are described. Single Edge Notched (SEN) specimens were used. The notch was semi-circular in shape and designed to match the notch features (i.e. the stress concentration factor K_t) of bolt holes encountered in P&WC turbine compressor disc. The crack initiation lives in the SEN specimens were detected by the ACPD technique. The relationship between the measured ACPD signal and notch fatigue cracking pattern are studied. A notch strain analysis procedure based on Gemma's model is presented.

The isothermal fatigue crack growth analyses for Ti64 and Ti6246 are reported in this chapter. Several fracture mechanics parameters based on various solutions for the stress intensity factor (K) were investigated for characterizing the crack growth kinetics. The effect of the notch stress fields on the crack growth rates are addressed. The stress intensity factors for small cracks emanating from notches and long cracks growing out of the affected zone are calculated separately.

In Chapter 4, the TMF crack growth testing performed on Ti64 and Ti6246 forgings is reported. SEN specimens were also used for the testing. Three TMF conditions were investigated. The TMF testing capabilities of the rig and the application of the ACPD technique to anisothermal conditions were verified. Thermal mechanical fatigue crack growth data were obtained for Ti64 with temperature cycling between 300°F (T_{min}) and 750°F (T_{max}), and for Ti6246 with temperature cycling between 392°F (T_{min}) and 900°F (T_{max}). Isothermal FCG tests at T_{min} and T_{max} and at the same cyclic frequency were also performed for the sake of comparison. Many new findings are obtained from the data analysis and are presented.

In Chapter 5, extensive microscopic observations made on the fractured surfaces obtained under different testing conditions are presented. To study the effect of microstructure on fatigue, the microstructural differences between the two titanium forgings were addressed. Compositional analyses of the beta stabilizer (V in Ti64 and Mo in Ti6246) were also employed to identify the different phases associated with various fractographic features.

For the fatigue crack initiation tests, the SEM (scanning electronic microscope) fractographic analyses were focused on the microcrack initiation sites at the root of the notches.

The fractographic observations pertaining to crack growth obtained in isothermal and TMF conditions were focused on (1) the relationship between the microscopic da/dN (using striation count techniques) and the experimental macroscopic da/dN measured; (2) the effects of microstructures on the crack paths; (3) the comparison of the overall fracture morphologies associated with different test conditions. These observations resulted in a mechanistic understanding of crack growth for the two titanium alloys, and, in particular, helped in the development of a fatigue-assisted and environment-assisted cracking model for Ti6246 and explained the stronger crack closure effects found in Ti64 TMF tests.

In Chapter 6, the low cycle fatigue testing of Single Tooth Firtree (STFT) specimens of PWA1480 single crystal performed at 650°C is reported. These tests were carried out in an attempt to apply the testing techniques developed with the TMF rig to other nickel based alloys and, in particular, to more realistic "substructure" component tests. These tests were also used as verification tests to develop STFT LCF testing capabilities at P&WC, similar to the ones available at CEB and GESP (P&WA units). The test results are presented.

Finally, the major conclusions are summarized and a discussion of the technical accomplishments and recommendations for future studies are outlined.

CHAPTER 1

LCF AND FCG BEHAVIORS OF TI AND NI BASE ALLOYS AT ELEVATED TEMPERATURES

1. 1 INTRODUCTION

Titanium alloys and nickel base superalloys have been developed for use in elevated temperature applications in which the structural materials must have high strength, excellent corrosion resistance, good creep and fatigue resistance, and outstanding strength-to-weight ratio in certain cases. The primary application of these two types of alloys has been in aircraft jet engines for critical components, Ni-base superalloys for turbine discs, turbine blades, vanes and burner cans, while Ti-base alloys for compressor discs and compressor blades. The working conditions for these components are very severe. For example the turbine disc and airfoils operate under extreme temperature gradients, from around 150° C at the hub to about 550° C at the rim for the disc, and from about 550° C at the root to about 1050°C at the tip for the blade. Some discs may be loaded in excess of 80% of yield strength during certain period of operation. In addition to the high temperature and corrosive environments, extreme temperature and load transients arise as engine operating conditions change, giving rise to thermomechanical fatigue problems. Since an engine operates for considerable periods of time during which the conditions are

relatively stable, the effect of hold time are also of prime concern, and these give rise to possible creep-fatigue interactions[1,2].

As pointed out by Thompson in a NASA Hot Section Technology program report [3], the future development of engine structural elements relies on three key technologies (1) the development of inelastic constitutive models; (2) three-dimensional nonlinear structural methods and code development which includes damage modeling, fracture mechanics analysis and lifing procedures; and (3) reliable experimentation to calibrate and validate the models and codes. These technology areas were selected not only because today's hot section component designs are materially (rapid application of advanced materials) and structurally (e.g. advanced cooling techniques) difficult to analyze with existing analytical tools, but because even greater demands will be placed on the analysis of advanced designs. It can be seen that material properties, micromechanics of material deformation and fracture, constitutive models, structural analysis and material testing are all integrated together to form the basis of designs for the advanced engines of tomorrow. This is one of the greatest challenge for both mechanical engineers and metallurgists.

An extensive literature survey of several topics relating to TMF testing and fatigue crack initiation/propagation in titanium alloys and nickel base superalloys at room temperature and elevated temperatures is presented in this chapter.

A clear understanding of microstructural features is essential for fatigue test data analyses, material deformation modeling and fracture morphology studies.

Hence a review of typical microstructure found in titanium and nickel base alloys is presented at the beginning. It is followed by the materials' deformation mechanisms and their modeling at different temperatures. Recent developments on unified constitutive models based on internal state variables and their relationship to material microstructural kinetics are discussed as well.

In the review on fatigue crack initiation and growth behaviors of titanium and nickel base alloys, the discussion is centered around oxidation assisted surface cracking, interfacial oxygen diffusion, the formation of gamma prime depleted zones near the free surfaces (for Ni base alloys) and the microscopic features of crack initiation and growth in titanium alloys (which are of great interest for these two phase alloys).

An updated review of the recent development of TMF test methods, including loading and heating procedures, specimen shapes, crack measurement, etc., from independent works are compared and summarized. Various TMF data analysis techniques and models for crack initiation and propagation are surveyed and discussed with special emphasis on physically based damage mechanisms. The modeling effort pertaining to material mechanical behavior under combined thermal and mechanical loading which uses advanced unified constitutive laws based on internal state variables theories, is also presented.

In the brief review on the application of the Finite Element Method (FEM) and Boundary Element Method (BEM) to model tested specimens, the discussion is

focused on new techniques of implementing advanced material constitutive models to the FEM codes, which is a very important step for structural applications.

Finally the recent developments with the AC potential drop technique (ACPD) are reviewed. The theory of this crack growth monitoring technique, its application to various alloys in different environments and loading conditions, and its resolutions in terms of detectable crack sizes are summarized.

1.2 DEFORMATION MECHANISMS OF TITANIUM AND NICKEL BASE ALLOYS AT ELEVATED TEMPERATURES

1.2.1 Microstructures of Titanium Alloys

There are various kinds of commercial titanium alloys available and their microstructures depend on their compositions and processing techniques. To get a clearer overview of the major microstructural features of these alloys, the following discussion is centered around forged Ti-6Al-4V (Ti64) and Ti-6Al-2Sn-4Zr-6Mo (Ti6246) alloys.

At room temperature, pure titanium exists in the hexagonal close-packed (hcp) structure (alpha Ti) with c/a = 1.588. Its predominant slip systems are the $\{10\bar{1}0\}\langle\bar{1}2\bar{1}0\rangle$ with some basal $(0002)\langle\bar{1}2\bar{1}0\rangle$ slip. When the temperature is raised to about 882°C, it undergoes an allotropic transformation to body centered-

cubic (bcc) (beta phase). As it is alloyed with alpha stabilizer elements such as Al and Sn, or beta stabilizer elements such as V, Mo Cr and Cu, the transformation temperature will be increased or decreased, and a transformation temperature range will be obtained. Thus titanium alloys are divided into three classes: alpha, alpha-beta and beta alloys[1,4].

Both Ti64 and Ti6246 are alpha-beta alloys with compositions that support a mixture of alpha and beta phases usually at room temperature. In addition, Ti64 is a near α alloy, and Ti6246 is a near-β alloy. A wide range of processing techniques can be applied to the two alloys to produce numerous kinds of mill products exhibiting a wide range of microstructures. Generally, the microstructure of the $\alpha+\beta$ alloys depends on both the thermal and mechanical processing sequences which have been imposed on it. The microstructures frequently appear duplex type as shown in Figure 1.1. The main parameters which are used to describe the microstructures of the alloys are: phase morphology, α-phase volume fraction, distribution of the primary α-phase and its constitution, β-phase volume fraction and distribution of the prior ß-phase regions[5].

The primary α-phase is the results of nucleation and growth in alloys where the final hot working operation is completed below the β-transus temperature, i.e. in the $\alpha+\beta$ phase field. The morphology of the primary α depends on the extent of plastic work performed and can vary from elongated plates in lightly worked material to equiaxed grains in heavy-worked materials (see Figure 1.1a).

The types of nucleation-and-growth occurring during phase transformation strongly relies on atomic diffusion which is thermally activated. In contrast, the martensitic transformations which involve a cooperative movement of atoms, result in a microscopically homogeneous transformation of one crystal lattice (bcc of β-phase) into another (hcp α-phase). Furthermore the processes are athermal. These two competing mechanisms (athermal shear versus diffusion), which occur during thermomechanical processing of titanium alloys, determine the final microstructure of the materials. High quench rates will favor bulk martensitic structures. On the other hand, increasing solute concentration (by adding α or β stabilizers) decreases the occurrence of the athermal transformation[4]. Against this background, there exist a series of quenched structures extending from martensite packets, through acicular martensite, basketweave like Widmanstäten structure, to an acicular α structure. The acicular α-phase is a product of nucleation and growth along one set of preferred crystallographic planes of the prior beta matrix. The α-phase needles lie with their long axes parallel to the {110} planes of the parent retained β-phase. See Figure 1.1b.

The fatigue and fracture toughness properties of Ti64 forgings are found strongly affected by the α-phase morphology of the microstructure. Fined and equiaxed α grains, achieved from $\alpha+\beta$ forging, improve the fatigue and ductility of the alloy, while elongated α grains bring a fall in fatigue strength. An acicular α microstructure (also referred to as lamella structure) with thin α phase along β grain boundary have been reported to have a superior fatigue strength[6]. The effects of the microstructures on the fatigue behavior of the materials are reviewed in Section 1.3.2.

1.2.2 Microstructure of nickel based alloys

Although the nickel-base superalloys are compositionally complex, they are microstructurally simple as compared to titanium alloys. The microstructure consists of (1) a face-centered-cubic (fcc) austenitic matrix or γ -phase (with {111} <110> slip system) which is solid solution strengthened, (2) precipitates (γ', γ'') that are coherent with the matrix and (3) various types of carbides (MC, $M_{23}C_6$ etc.) and other phases which are distributed in the matrix or along grain boundaries.

Ni-base superalloys contain a variety of elements in a large number of combinations to produce desirable effects. Mo, Ta, W, Re are added as solid solution strengtheners. Cr and Al are used to increase oxidation resistance. Al, Ti and Cb are the elements added to form hardening precipitates such as gamma prime (γ') and gamma double prime (γ''). The γ' phase is the key factor responsible for the extraordinarily useful high temperature properties of Ni-base superalloys. In addition, minor elements such as C and B are added to form carbides and borides along grain boundaries of polycrystalline alloys, and these are important features to produce the desired strength, ductility and creep resistance.

The so called γ' phase is an ordered intermetallic compound with face centered cubic (fcc) crystalline structure having the basic composition $Ni_3(Al,Ti)$. As shown in Figure 1.2a, the γ' precipitates have spheroidal and cuboidal morphology in Ni-base alloys (e.g. in Rene 77 and Udimet 700)[2]. The existence of

γ' precipitates act as obstacles to the movement of dislocations, and therefore strengthen the alloy. The mechanisms involved with the interaction of the γ' and the dislocation are well understood[12]. An optimum material strength for a given applications can be achieved by "tuning" the size of the γ' precipitates. However, the strength of the γ'-hardened grains must be balanced with the grain boundary strength which is greatly affected by the $M_{23}C_6$ carbides needed to inhibit grain boundary sliding (see Figure 1.2b).

1.3 DEFORMATION MECHANISMS AND MODELING

Inelastic deformation of titanium and nickel base alloys, like in other crystalline solids, is caused by a number of alternative, often competing mechanisms. The inelastic flow is a kinetic process determined by the kinetics of the processes occurring at the atomic scale: the glide motion of dislocation lines, their coupled glide and climb, the diffusive flow of individual atoms, grain boundary sliding (involving diffusion and defect motion in the boundaries), mechanical twinning and so forth. "Macroscopically speaking", the strength (flow stress) of the solid, in general, depends on both strain and strain-rate, and on temperature[7]. However the internal relationships among those variables are very complicated in cases where more than one deformation mechanisms operate (e.g. at elevated temperatures or under TMF loading), which is the case encountered in most engineering applications.

To describe the interaction effects of deformation mechanisms qualitatively or quantitatively depends strongly on the manner the modeling is carried-out. For example, different treatments of time independent inelastic strain (plastic strain) and time dependent inelastic strain (i.e. creep strain) may result in quite different understanding of the deformation processes[8,9,10,11]. Hence one category of theories assumes a yield condition that separate rate independent recoverable (elastic) deformation from rate dependent nonrecoverable (inelastic) deformation. The other category of theories makes no such separation and viscoplastic deformation along with elastic deformation can occur at any level of stress during loading and unloading[10]. In regard to many viscoplastic theories, it is also wise to keep in mind that they may be either physically based or simply adopted because of numerical convenience. Before reviewing the recent efforts to develop a "unified law" for material deformation, a close-look at fundamental individual deformation mechanisms (which are well described by the deformation map concept developed by Frost and Ashby[7]) is presented.

1.3.1 Deformation mechanisms map

Modeling material deformation behavior is a process of establishing the "constitutive equations" in the current term. Many deformation models have been established for cases where only one mechanism dominates, by means of microscopic kinetic analysis and experimentally based phenomenological methods[11,12].

From a continuum mechanics point of view, plastic flow (or inelastic flow) of fully-dense solids is caused by shearing, or by the deviatoric portion of the stress field $\sigma_s = (1/2 S_{ij} S_{ij})^{1/2}$. The corresponding deformations, caused by dislocations and vacancies etc, are characterized by a shear strain rate. This strain rate $\dot{\gamma} = (2 \dot{\varepsilon}_{ij} \dot{\varepsilon}_{ij})^{1/2}$ is used as an independent variable to describe the individual deformation mechanisms in terms of a rate equation which relates $\dot{\gamma}$ to the stress σ_s, the temperature T, and the material structure:

$$\dot{\gamma} = F(\sigma_s, T, S_i, P_j), \tag{1.1}$$

where S_i is a set of state variables which describes the current microstructural state of the materials, P_j represents a set of material properties such as lattice parameter, atomic volume, bond energies,elastic modulus, diffusion constants, etc.

The state variables S_i are internal variables, which cannot be measured directly. They change as deformation progresses in a manner that is far from being satisfactorily understood and modeled. To simplify the problem, the assumption of constant structure is made, i.e. $S_i = S_i^o$ and $P_i = P_i^o$. Then the general constitutive law can be reduced to:

$$\dot{\gamma} = F(\sigma_s, T) \tag{1.2}$$

which enable us to construct the deformation mechanism map for a given material experiencing steady state deformation. Rate equations for individual mechanisms

have been established in many studies. For example, the low-temperature dislocation glide moving through a field of obstacles was first modeled by Orowan as

$$\dot{\gamma} = \rho_m b \quad \bar{v} \tag{1.3}$$

and later by Argon:

$$\dot{\gamma} = \alpha \, (\sigma_s / \mu b)^2 b \quad \bar{v} \tag{1.4}$$

where b is the Burgers' vector of the dislocation with average velocity $\bar{v}$, ρ_m is a density of mobile dislocations, which is a function of stress and temperature, and μ is the elastic shear modulus. The average dislocation velocity is controlled by the resistance provided by discrete obstacles (precipitates), lattice resistance (Peierls stress) and phonon or electron dragging, etc. For dislocation glide in the presence of lattice resistance, Ashby gives:

$$\dot{\gamma} = \dot{\gamma}_p (\sigma_s / \mu)^2 \exp - \left\{ \frac{\Delta F_p}{kT} [1 - (\frac{\sigma_s}{\tau_p})^{3/4}] \right\}^{4/3} \tag{1.5}$$

where the ΔF_p is total free energy required to overcome the obstacle without aid from external stress. τ_p is the shear strength in the absence of thermal energy. Twinning is also an important plastic deformation mechanism at low temperature in hcp and bcc materials. However, an exact rate equation for twinning is still unavailable.

High temperature inelastic deformation, in most cases, is characterized by power law creep, which is controlled by dislocation glide alone or by dislocation climb and glide. Both mechanisms are thermally-activated, and the modeling must include a description of the balanced hardening-and-recovery processes which permit a steady state. The clamb is controlled by diffusive motion of ions or vacancies. For the lattice diffusion and dislocation core diffusion, the rate equation is given by Robinson and Sherby as:

$$\dot{\gamma} = A_2 D_{\text{eff}} \frac{\mu b}{kT} \left(\frac{\sigma_s}{\mu}\right)^n \tag{1.6}$$

where D_{eff} is the effective diffusion coefficient that is a function of core and lattice diffusion coefficients and stress level. At sufficiently low stress, Harper and Dorn creep (diffusion flow) is given as

$$\dot{\gamma} = \rho_m D_{\text{eff}} \frac{\mu \Omega}{kT} \left(\frac{\sigma_s}{\mu}\right) \tag{1.7}$$

where the Ω is the atomic or ionic volume.

Coming back to the discussion of Ni-base alloys and titanium alloys, it must be emphasise that deformation mechanism maps can be used to clarify the conditions (load level and temperature) in which one particular mechanism is becoming dominant. For example, Figure 1.3 shows the deformation mechanism

maps of pure nickel and Nickel base alloy MAR-M200 with equal grain size (d = 100 μm). These maps schematically illustrate the major operating mechanisms such as ideal crystal rapture, plasticity and creep deformation controlled by different diffusion mechanisms. By comparing the two deformation maps, one can find that the load level to generate significant plastic strain is raised due to γ' precipitation hardening; and that the temperature at which the power law creep becomes dominant is also significantly raised (up to 65% of $T_{melt)}$ as a result of grain boundary carbides and γ' precipitates in MAR-M200 alloy.

As another example, a deformation map of pure titanium, given by Ashby, shows a decline in strength when the temperature passes through the β-phase transus (approximately T/Tm = 0.8). This is a result of the increased number of slip systems as the hcp α-phase transformed to bcc β-phase.

Fracture mechanism maps can also be employed. They are based on the deformation maps relating the fracture modes to the deformation mechanisms. Krishna et al [13] have developed a fracture mechanism map for Ti64.

Although the deformation mechanism maps have found wide applications in identifying the mechanisms by which components or structures deform in service, and estimating the approximate strain rate or the total strain, they provide little information on how these mechanisms interact with each other, and how the deformation proceeds (from transient to steady state), since they assumed constant structures. They can only provide a qualitative understanding of deformation from a modeling point of view. Therefore, more realistic models using internal variables

(material microstructural states) are needed for accurate structural analysis. It is interesting to note that the deformation mechanism maps, on the other hand, can provide a very powerful tool for establishing the evolution law of a microstructural state.

1.3.2 Mechanistic modeling based on internal variables

Unified constitutive models developed by Bodner and Partom, Lee and Zaverl, Walker etc.[14,15,16,17] have shown to be very promising in analyzing high temperature inelastic deformation. As mentioned earlier, these models are based on separating the total strain into the sum of elastic, inelastic and thermal components, and on the introduction of internal variables. No yield condition is required. Recent work of Chan et al[15,16], and Ramaswamy et al[17] have shown good results in modeling B1900+Hf and Rene'80 (both alloys are γ' strengthened nickel base superalloys) deformed at temperature ranging from 760°C to 1093°C and from 538° C to 982° C respectively. Although the models have been verified only in uniaxial conditions, They demonstrated the significance of using internal variables. The basic formulation of their models use two state variables, the back stress and the drag stress, which are interpreted as macroscopic measures of properties of mobile dislocations and their interaction with precipitates, grain boundaries, other point defects, and each other.

The back stress state variable is motivated by the interaction of mobile dislocations with grain boundaries or other barriers. The mobile dislocation gliding

on a slip plane, in a crystallographically preferred slip direction, can be pinned or stopped at a barrier. A second dislocation, following the same path, will encounter the pinned dislocation and be repelled. This effect will be enhanced as more dislocations are piled up. At high temperature, significant reverse anelastic flow can result when the driving shear stress is removed. Physically, this stress is analogous to residual stress embedded in the crystallite. Thus, the net force producing further slip is the difference between the shear stress and back stress due to dislocation interaction. It is worth noting that this stress is anisotropic, and thut produces the Bauschinger effect. Inspired by the work of Prandtl-Reuss and Prager in the classical theory of plasticity, Bodner, Walker, Chaboche, Lee and Zaverl et al. [8,17] suggested that, the inelastic strain rate, $\dot{\varepsilon}_{ij}$ is proportional to the difference between the deviatoric shear stress, S_{ij} and the back stress, Ω_{ij}, i.e.

$$\dot{\varepsilon}^{I}{}_{ij} = \lambda \bullet (S_{ij} - \Omega_{ij}) \tag{1.8}$$

where λ is a scalar parameter which is function of state variables.

Drag stress is included to model the resistance to dislocation glide by the drag of interstitial solute atom atmospheres, particles or precipitates in the microstructure that are generally observed as hardening or softening during cycling. For precipitate hardening material such as nickel base superalloys, the mobile dislocation can shear, climb over, or loop around precipitates in the slip plane. In the shear mechanism, the dislocation pass through the precipitate displacing the precipitate lattice on one side of the dislocation relative the other side of the dislocation. Several dislocations passing through the precipitate will eventually shear

the particle into two or more subparticles reducing the resistance to further slip (softening). As a converse example, dislocation interacting with a precipitate leaves a dislocation ring or loop around the precipitate after it has passed through the region. The dislocation loop increase the effective resistance to the movement of other dislocation (hardening). The drag stress Z (a scalar) is used to represent this isotropic hardening effects, and is generally assumed to monotonically increase or decrease from an initial value to an asymptotic or saturated value. The major difference in back stress and drag stress is that the former represents the build-up of an energy inside the microstructure which can be released subsequently, while the latter relates the energy dissipated (mainly to heat) in the material through deformation.

In the work of Ramaswamy et al[17], for example, the inelastic strain rate $\dot{\varepsilon}_{ij}^{I}$ is written as

$$\dot{\varepsilon}^{I}_{ij} = D\exp[-\frac{A}{2}(\frac{Z^2}{3K_2})^n]\frac{(S_{ij}-\Omega_{ij})}{\sqrt{K_2}} \quad , \tag{1.9}$$

where $K_2 = 1/2\ (S_{ij} - \Omega_{ij})(S_{ij} - \Omega_{ij})$ are the second invariants of the deviatoric overstress (or effective stress) tensor. D, A and n are temperature dependent material parameters. The evolution equation of the back stress Ω_{ij} used in uniaxial case is given to the form:

$$\dot{\Omega} = \tfrac{2}{3} f_1 \dot{\varepsilon}^{I} - \tfrac{3}{2} f_1 \frac{\Omega}{\Omega_s}\left|\dot{\varepsilon}^{I}\right| + f_2 \dot{\sigma} \tag{1.10}$$

where f_1, f_2 are material constants. Ω_s is the back stress at the maximum saturated value (when $\dot{\Omega} = 0$). The first term controls the rate of strain hardening in tension and compression, the second controls the dynamic recovery depending on the accumulated inelastic strain and current state of hardening, and the third term controls the thermal recovery of the initial back stress rate. This model has shown good capabilities predicting the tensile and cyclic tensile response of René 80 at elevated temperatures.

Other developments were made by Chiu, Eftis and Jones in modeling Ti64 using the viscoplastic constitutive theory proposed by Chaboche[10]. They also employed their model to predict the fatigue lives of specimens experiencing creep-fatigue interaction (titanium alloy Ti64 is known to exhibit creep behavior as low as in room temperature). The model is essentially of the same type as mentioned above, except a yield function is used, which is assumed to have the generalized von Mises form:

$$F(S_{ij}, \Omega_{ij}, K) = \sqrt{K_2} - K(|\varepsilon|) \tag{1.11}$$

as such the inelastic strain rate is written as

$$\dot{\varepsilon}^{I}{}_{ij} = \Lambda \frac{\partial F}{\partial (S_{ij} - \Omega_{ij})} \tag{1.12}$$

where

$$\Lambda = \begin{cases} (F/K)^n, & F > 0 \\ 0, & F \le 0 \end{cases}, \tag{1.13}$$

and K and n are material parameters.

Besides the mechanistical-based models, there exist a large number of simplified engineering models for deformation analysis. For example, in a study of stress response behavior of a cast nickel base superalloy (MAR M200) subject to combined creep-fatigue, Plumbridge and Ellison[18] has shown that the Baily-Norton creep law in its general form

$$\dot{\varepsilon} = B \bullet \sigma^{n} \bullet t^{m} \tag{1.14}$$

can be satisfactorily used to correlate the stress relaxation data.

1.4 FATIGUE CRACK GROWTH IN TITANIUM AND NICKEL BASE SUPERALLOYS AT HIGH TEMPERATURE

1.4.1 Oxidation kinetics of alloys

The study on the effect of the gas atmosphere is of special significance because of a characteristic of titanium, namely, its capacity to dissolve gases, especially hydrogen, oxygen, and nitrogen. Gas solubility severely limits the use of titanium alloys at higher temperatures, which results in an increase of hardness and a decrease in ductility.

It has been well established[19,20], when a fresh surface of a metal or an alloy is exposed to an oxidizing gas environment at high temperature, over the range of partial pressures of oxygen and for each temperature (which determine the chemical potential of oxygen), that there exists a specific value (P(d)), corresponding to the pressure of reversible dissociation of the stable oxide that can appear on the surface of the metal. If the partial pressure of oxygen is below this critical value, there exists a strong interaction between the metallic atoms on the surface and the oxygen, which leads to the formation of monoatomic layer of oxygen chemically adsorbed. The adsorption of oxygen on the surface has a gas composition such that no oxidation could occur to form three-dimensional oxide. Moreau and Benard (1956) noted that the selective adsorption of oxygen on the various crystal faces can cause a preferential decrease in the superficial free energy (relative to cleavage energy) of some of the crystal faces.

When the partial pressure value is above this specific value, chemical reaction (e.g. oxidation) may occur with the formation (or nucleation) of the oxide layer. The velocity of oxide formation depends on the difference that exists between the partial pressure of oxygen and the critical pressure corresponding to the reversible dissociation pressure of the oxide. Further oxidation becomes possible when one of the reactants (e.g. oxygen) diffuses through the scaling layer to the other reactant (metallic atoms). Hence the oxidation rate is controlled by diffusion processes and phase-boundary reactions.

At high temperature, the chemical potential provides the driving force for the reaction (in a thermodynamic sense). However, from the oxidation kinetic point of view, the rate of oxide growth is then proportional to the concentration gradient, so that

$$\frac{dx}{dt} = \frac{c}{x} \tag{1.15}$$

where x is oxide thickness, t the time, and C is the concentration of the mobile oxygen atoms. Integration of equation (1.15) leads to the well-known parabolic law for high-temperature oxidation.

The oxygen diffusion process is controlled by Fick's second diffusion equation of the form

$$\frac{\partial c}{\partial t} = D\frac{\partial^2 c}{\partial x^2} \ . \tag{1.16}$$

The coefficient of diffusion D is given by

$$D = D_0 \exp(-\Delta U / RT) , \tag{1.17}$$

where the constant D_0 and the apparent activation energy ΔU are experimentally determined.

Individual titanium oxides - TiO, Ti_2O_3, Ti_3O_5, and TiO_2 (dark blue) can form during the oxidation of titanium. Gulbransen and Andrew (1949) evaluated results of titanium oxidation experiments carried out between 250-600°C assuming that a parabolic rate law presented. From Hauffe[20], the constants for diffusion of oxygen to α-Ti in the temperature range 700 - 800°C were found to be $D_0 = 5 \times 10^{-5}$ m^2/sec, and $\Delta U = 213$ kJ/mol. A more recent data survey by Liu and Welsch[21] showed that in the temperature range ~ 410°C, $D_0 = 5.0\text{-}10 \times 10^{-5}$ m^2/sec, and $\Delta U = 245$ kJ/mol, for diffusion of oxygen in α-Ti; and in the temperature range 900-1050°C, $D_0 = 9.34 \times 10^{-7}$ m^2/sec, and $\Delta U = 151$ kJ/mol, for diffusion of oxygen in β-Ti. However, no data are reported for the diffusion of oxygen along α/β interfaces (or for grain boundary diffusion).

Grain boundary oxidation are observed in numerous cases for the nickel base alloys due to the preferred diffusion along grain boundaries. In the presence of such short-circuit diffusion, the effective diffusion coefficient may be expressed as the weighted sum of the diffusion coefficients for lattice and boundary diffusion,

$$D_{\text{eff}} = D_{\text{L}}(1-f) + D_{\text{B}}f \tag{1.18}$$

where f is the fraction of diffusion sites in the low-resistance paths.

1.4.2 Fatigue crack initiation and growth in titanium alloys

The microstructure of titanium alloys generally does not have significant effect on crack growth behavior[22] at room temperature. However, it is widely accepted that acicular, Widmanstatten microstructure developed as a result of thermal mechanical treatment within the the β-phase region exhibits greater resistance to fatigue crack propagation[23]. This is explained by the crack tip bifurcation and by secondary cracking formed both parallel and perpendicular to the α/β platelet interfaces. A recent study by Matsumoto et.al[6] showed that the finer the acicular α phase is (i.e. thinner the α phase platelet), the better is the improvement in fatigue strength at low temperatures. The acicular α material is superior to the equiaxed α material in fatigue propagation characteristics. However, the equiaxed α structure has greater tensile ductility, fatigue crack initiation resistance and LCF strength at high temperatures[24].

The α/β interfaces have shown considerable effect on materials crack initiation and growth behavior. Williams[5] and Sridhar et. al.[25] found a complex layer of transformation product with a very high density of small α-phase particles at the α/β interfaces. This α/β interface phase is an important microstructural feature, which can grow to widths of up to 500 nm and has been shown to influence the fracture and fatigue properties[5].

In a fatigue study on Ti64 with different volume fractions of primary α-phase and different α/β interface phase widths, Rhodes[26] found cleavage-like fracture through the primary α particles at low ΔK ($<$ 14 Mpa $m^{1/2}$), and a gradually change to striation formation with increasing stress level. The sample having the broadest interface phase had improved the fatigue crack growth resistance and

showed the formation of numerous secondary cracks along interfaces, suggesting that the interface phases could promote crack tip branching .

The hydrogen absorption test on Ti64 alloy conducted by Niinomi et.al.[27] showed that the Widmanstatten α microstructure is sensitive to microcracking during hydrogenation when compared to the equiaxed α microstructures. This is a good indication that enhanced diffusion of hydrogen along interfaces can cause embrittlement of the α/β platelet interfaces.

In their study on the high temperature LCF behavior of Ti-5522S and Ti-6242S as a function of the microstructural conditions, Eylon et. al. [28] found that the cracks initiated from the specimen surface, were mostly along the α-platelets which forms angles of 30° to 45° to the tensile direction. Furthermore the initial crack lengths were much longer for samples having longer $\alpha/$ß interfaces. They concluded that the surface connected interface cracking is a result of environmental effects on fatigue crack initiation. Diffusion of oxygen and other interstitials from the surface into the material is enhanced along the $\alpha/$ß interfaces either by lattice mismatch between the hexagonal α and cubic ß phases or interface stresses developed during the load cycle. It is also possible that interface phase promotes diffusion because of the high surface to volume ratio associated with fine acicular α-particles and high dislocation density. The resulting higher interstitial content will embrittle the interface zone and greatly reduce its plastic deformation capabilities.

The influence of oxygen content on FCG behavior was studied by Welsch and Bunk[29], and by Gray, Luetjering and Williams[30]. With increasing oxygen

content, the fracture facets are seen to become more planar in nature, i.e. cleavage-like fracture. This is are related to higher local plasticity since the effect of oxygen is additive to Al in the solid solution in promoting planar slip in the matrix. Therefore, oxygen intrinsically promotes slip localization. This increases the local stresses at sites, such as the intersection between slipbands and grain boundaries, until the normal stress exceeds the critical value for extension of cleavage-like cracks. This effect is compounded by the fact that there is an oxygen related reduction in the critical macroscopic stress necessary to cause cleavage fracture.

Recent experimental study on Ti64 and IMI834 titanium forgings at 450°C by Specht[22] indicated significantly increased crack growth rates at low stress intensity values (<20 Mpa $m^{1/2}$) as compared with vacuum test results. The fractured surfaces exhibits a crack mode where quasi-cleavage areas dominate. Quasi-cleavage was assumed to be caused by oxidation processes at the crack tip since no cleavage areas were found in the tests carried-out in vacuum ($\sim 10^{-5}$ Pa).

Relatively less attention has been directed on the crack initiation and short crack growth regime for titanium alloys. Four types of crack initiation sites are usually found [31], i.e.

-surface initiation at surface scratches and shot-peenning defects, etc.;

-subsurface initiation;

-surface initiation at Al-rich regions;

-surface initiation at grain egression or "pop-out" sites.

Interesting enough, the fracture surface at the initiation site seem always to be faceted. These facets are thought to have a particular crystallographic orientation with respect to the lattice of the α grains.

There are several mechanisms of fatigue crack initiation operative in $\alpha+\beta$ alloys including α/β interface cracking, primary α cracking at slip bands or slipless cracking, subsurface cracking of cleavage-like types and grain egression. In addition to the effects of microstructure, the operative mechanisms of crack initiation is greatly affected by a variety of mechanical and environmental conditions such as the frequency of loading, the R-ratio, the temperature and the corrosive environment.

Mahajan and Margolin[32] studied crack nucleation and early crack growth of Ti6246 at room temperature. They found that for both the Widmanstatten plus grain boundary α and the equiaxed α microstructures, crack initiation at lower strains occurred at the α/β interfaces and in the transformed β matrix, while at higher strains for both structures, crack initiation took place preferentially within slip bands in the α-phase.

A more recent study on naturally initiated crack in equiaxed α plus transformed β microstructure at room temperature was conducted by Dowson et.al.[33], they also found that crack initiation was associated with the development of intense slip bands either in primary α grains or in closely aligned α colonies at prior beta phase grain boundaries. Cracks were found to form preferentially in the α -phase and on this basis, the intrinsic resistance of the material to crack initiation increases in fully β treated microstructures (acicular). However, at elevated

temperatures, the α/β interface cracking can be expected to cause significant decrease in the FCI resistance. Short crack growth rate data were also reported in this research. It was found that the transition between short and long crack FCG behavior is associated with crack closure.

1.4.3 Fatigue crack initiation and growth in Ni-base alloys in oxidizing environment

In this section, the oxidation assisted fatigue crack initiation and growth mechanisms of nickel base superalloys (coated and uncoated conditions) are reviewed. Considerable evidences have been produced for nickel based alloys to show that oxidation is a major cause of damage during high temperature low cycle fatigue. Many attempts have been made to describe fatigue interactions with creep and environment[34-39].

At high temperature, the Al and Cr in the composition of Ni-base alloy form adherent oxides, typically Al_2O_3 and Cr_2O_3 with particles of $Ni(Cr,Al)_2O_4$[2], on the surfaces of uncoated alloys. These oxides greatly enhance the high temperature oxidation resistance of the material.

Very often the surface compositions of the alloys change during oxidation. For example, a γ' depleted zone or layer will be formed adjacent to the oxides due to the selective oxidation of Al, Cr and Ti. This reduces the fatigue resistance of the material to fatigue cycling. When large compositional differences exist between the different phases in alloys, the oxidation resistance of the respective phases can be

substantially different. Hence severe attacks of the phase having the poorest oxidation resistance will take place, as well as preferential oxygen diffusion along phase boundaries. Both cases will promote crack initiation thus decreasing the fatigue life.

For polycrystalline alloys, preferential oxidation attack of the carbides along the grain boundaries and crack nucleation at oxidized interdendritic carbides have been reported by Rezai-Aria and Remy[38], Malpertu and Rémy[40], Boismier[35] for alloy IN-100 and MAR-M509, and by Sehitoglu[36] for MAR-M247. Particularly in a model of grain boundary oxidation and cracking, Boismier suggested that the creep damages are also enhanced by the oxidation penetration along the grain boundaries.

Oxidation-fatigue interactions have been reported for single crystal superalloys. For example, Wright[37] found that surface crack initiation in René N4 is caused by fatigue-assisted cracking and spalling of oxide products, which produce roughened and pitted surfaces. This process also accelerated the observed oxidation rate since more fresh material was exposed to the environment. With further cycling, these pits developed into oxide spikes and then into sharp fatigue cracks at the surfaces.

The developement of environmentally protective coatings is a rapid growing technology. These coatings isolate the material surface from the environment and significantly improve the fatigue life. However under thermal mechanical loading, severe coating degradation has been observed in the aluminide coated single crystal

PWA1480 specimens[34]. This was attributed to the thermal expansion coefficient and material mechanical properties mismatch between the coating and the substrate. These mismatch can cause coating spalling and cracking followed by the penetration of surface cracking into the substrate. A two-bar model was used in the analysis of coating and substrate stress mismatch in PWA1480 single crystal[34]. Similar methodology was also applied to oxide-substrate analysis for MAR-M509[37]. These simple models were found to qualitatively describe the experimental results. A fractographic observation on fatigue cracking of coated PWA1480 blades during service conditions have been reported by Berstein[41].

Modeling of oxidation assisted fatigue crack initiation and growth has been attempted by Reazi-Aria and Rémy[38] for MAR-M509, a cobalt base cast alloy. A damage model based on intergranular oxygen diffusion and local element fracture criterion concept initially proposed by McClintock[38] was formulated. In their study, the oxygen concentration (C) as a function of distance x along interdendritic area ahead of the oxidized precrack (with interdendritic oxide depth l_{ox}) was assumed to obey

$$C = C_0 \exp(-kx / l_{ox}) \quad . \tag{1.15}$$

Here k is a constant which depends on oxidation kinetics (chemical reaction) and diffusion coefficients. The critical rupture stress of the oxide is given by

$$\sigma_c = \sigma_{c0}(1 - u + u\exp(mx / l_{ox})) \ , \tag{1.16}$$

where the initial value σ_{CO} is given by the Arrhenius law, i.e.

$$\sigma_{c0} = \sigma_0 \exp(-Q/KT) \quad . \tag{1.17}$$

The u, m and σ_O are materials constant at a given temperature T. The K is the universal gas constant and Q is the activation energy. Under oxidizing environment and cyclic loading, the incremental damage dD/dN for the element ahead of the crack during one cycle is

$$\frac{dD}{dN} = \left(\frac{\Delta\sigma}{2S_0}\right)^M / \left\{(1-R)(\sigma_c^* - \sigma)/S_0\right\}^\alpha \tag{1.18}$$

where $\sigma_c^* = \min\{\sigma_f, \sigma_c\}$. α, M, S_0 are constants for a given temperature, σ_f is the fatigue strength, and

$$R = 1 - \Delta\sigma/\sigma \quad \text{when } \Delta\sigma < \sigma$$
$$R = 0 \quad \text{when } \Delta\sigma > \sigma$$

Similar analyses were also performed by Sehitoglu[36] and Wright[37]. They assumed the initiation to occur when a certain depth d_{cr}, of oxidation/fatigue damage (oxide + γ' depletion layer) is reached. The critical depth d_{cr} can be determined by different empirical equations. This oxidation damage parameter is represented by the depth h. In the study of Sehitoglu , h was assumed to follow

$$h = \sqrt{K_p t} \quad , \tag{1.19}$$

where K_p is the parabolic constant which is a function of temperature. The time, t, is the exposure time of fresh metal to the environment.

As far as fatigue crack propagation is concerned, Ni-base superalloys are generally "well behaved", i.e. the crack growth rates can be well correlated by the Paris equation, especially when the da/dN, exceeds approximately $2.5x10^{-5}$ mm/cycle (10^{-6} inch/cycle). Above these rates, oxidation effects are assumed to be less predominant and thus negligible. However the microstructural features have considerable effects on FCG rates. Generally, the material with coarse grains and somewhat overaged γ' exhibits vastly superior FCG resistance.

1.5 THERMAL MECHANICAL FATIGUE TESTING

1.5.1 Introduction to TMF testing

Because of its considerable engineering significance to components operating at elevated temperatures such as nuclear reactors[42], aircraft gas turbine engines[43-53], railroad wheels (during braking)[54-63], etc., thermal mechanical fatigue (TMF) has been extensively studied. Although earlier studies have stressed the comparison of TMF with conventional isothermal fatigue in order to find ways to employ isothermal fatigue data (and lifing methods) to predict the materials fatigue life under anisothermal conditions, recent studies have focused on

understanding and modeling the physical damage mechanisms involved with TMF cycling including cyclic environmental damages. Also advanced constitutive equations are now being developed and tried to model the complex viscoplastic deformation of materials under various strain-temperature histories of TMF.

The test devised to study material damage under varying strain-temperature histories in the laboratory is referred to as the thermomechanical fatigue test. In this type of test, both the temperature and mechanical strain (or stress) imposed on the specimen are controlled independently. During TMF testing, the phase relation between strain and temperature can arbitrarily be varied so that the strain-temperature history of an actual components may be closely simulated. These laboratory studies have primarily considered two baseline TMF tests with proportional phasings: out-of-phase (the maximum strain coincide with the minimum temperature) and in-phase (the maximum strain coincide with maximum temperature).

Compared to isothermal cycling, thermomechanical fatigue cycling is expected to introduce a multitude of cyclic deformation and damage mechanisms. For example, during the higher temperature portion of a TMF cycle, various time-dependent creep mechanisms may be operative along with aggressive environmental attack and metallurgical changes. At the lower temperature portion, the number of possible mechanisms are reduced or excluded because of the lack of necessary thermal activation. The alternate activation of high and low temperature mechanisms can result in a combination of mechanisms not normally encountered in isothermal fatigue. Which ones of the potential mechanisms come into play depends

largely on the particular material tested, the temperature cycling range and rate, overall stress level, environment, and the inelastic deformation occurring at each temperature level.

TMF tests have been performed on several nickel base superalloys, (e.g. Astrolloy-X, B-1900+Hf, DS MAR-M200, Rene 77, IN 100, IN 718, IN 625 etc.), and steels (e.g. 1070 steel, 12Cr-Mo-V-W steel, AISI H13 steel, 1·Cr-1·Mo ferritic cast steel, Type 304 stainless steel, etc.). Quite recently, Sehitoglu and Karayaka[64,65,66] reported their TMF tests on metal matrix composites (MMC), and Pernot[67,68] has carried out TMF tests on intermetallic titanium-aluminide alloys, Ti_3Al, which feature high specific strength, low density and much higher oxidation resistance than titanium. However, few experiments with titanium alloys such as Ti64 and Ti6246 have been reported. One of the reason is that titanium alloys are used in applications where temperatures are below 500°C, and where TMF effect were often thought to be of less significance. However, the test results published by Gysler and Lutjering[69] have shown significant temperature dependence of the tensile properties of titanium alloys tested between room temperature and 500°C (e.g. for the equiaxed Ti64, the change can reach $\Delta\sigma_{0.2}$ = 450 Mpa). This suggests that crack tip plasticity can be greatly affected during temperature cycling and this will influence the overall fatigue crack growth behavior.

The existence of thermal cycling complicates the modeling of crack initiation and growth. Under TMF loadings, the microdamage mechanisms at the crack tip and the environmental attack effects may be quite different from their isothermal

counterpart. New approaches in both fracture mechanics and microdamage mechanics are being developed for TMF problems.

As a result of the increasing capabilities of the available numerical techniques ("crunching power"), the use of more sophisticated models for describing the mechanical behavior of materials under complex loading (including thermal loads) histories is now becoming possible. Besides the theoretical investigations, the experimental verification of the models developed is also very prominent. Actually, most of the models involve a number of material constants to be determined under specific experimental conditions. Thus, it is no surprising that TMF testing has a large potential for checking the prediction of the constitutive equations which model the material behavior under anisothermal loading conditions[43]. On the other hand, these advanced constitutive models will promote the development of new methods for TMF life prediction.

In the following, a brief review of TMF testing is presented. This is followed by summaries of some updated achievements in the modeling efforts surveyed in the literatures of TMF crack initiation and growth, and in the material mechanical behavior under TMF loading.

1.5.2 TMF testing procedures

As mentioned earlier, in TMF testing, the mechanical strain (or stress) and temperature imposed on the specimen are controlled separately. This gives rise to

several technical problem including: (1) mechanical strain measurement and control under varying temperature environment; (2) heating and cooling techniques and (3) material damage (or crack growth) monitoring under anisothermal condition. Although a fair number of TMF tests have been performed for several materials, this type of material testing is still not being standardized by ASTM.

There are two main kinds of TMF testing systems. The first type is an external constraints type tests or a two-bar structure[54] shown in Figure 1.4. In this kind of testing, mechanical strain is obtained by constraining the thermal expansion of the specimen, i.e. the total strain is controlled. This type of testing is not only very helpful for simulating the cases of components subjected to sudden localized heating and cooling, but it is also inexpensive from the experimental facility point of view. However, one of the drawbacks is that the mechanical strain is only controlled (actually calculated) by temperature and the thermal expansion coefficient of the material. This seriously limits the kind of the relationships between mechanical strain and temperature cycling that can be obtained.

The other type of TMF testing system is composed of a data tracking system as shown in Figure 1.5, which imposes the temperature and strain signals to the close loop control elements. In this system, both mechanical strain and temperature can be independently controlled so that they are very suitable to perform faithful simulations of the strain-temperature histories such as those experienced by critical areas of actual components. However, fairly sophisticated testing facilities are required. This testing procedure is becoming increasingly popular as a result of the wide application of powerful microcomputers. Several computerized TMF testing

systems have been developed[49,67,68,70-74]. The base line TMF cycles selected by most of these studies are in-phase and out-of-phase cycles as illustrated by Figure 1.6.

Halford, et. al.[75] have introduced a new type of testing: The bithermal fatigue test, as a link between isothermal and thermomechanical fatigue. As shown in Figure 1.7, the bithermal test aims at capturing the major effects in a TMF test, and appears to have great potential for evaluating damage interaction mechanisms. It could be a simple alternative to TMF testing in a sense of fatigue life prediction. In fact both the isothermal and the bithermal fatigue are special cases of TMF tests. Modern TMF testing system are so versatile that these two types of fatigue tests can easily be performed.

By looking into the details of TMF tests of several independent studies, one can find that a successful TMF test involves the consideration of many factors. The most important ones are summarized as following:

1.5.2.1 Specimen geometry

At least six types of specimen have been used in TMF tests. They are, (1) smooth or notched cylindrical tubular specimens[40,72,73,76-79], (2) solid cylindrical bar specimen[62,63,80], (3) single edge notched (SEN) specimen[48-51], (4) double edge notched (DEN) specimen[67,68], (5) center cracked panel (CCP)[52-53] and (6) compact tension specimen (CT)[67,68]. Tubular specimens

are convenient for fast heating and cooling with small through wall temperature gradient, whereas the plane strain specimens are particularly convenient for damage monitoring and crack growth tests. However, the specimen thickness and temperature cycling rate need to be chosen carefully.

1.5.2.2 Heating and cooling procedures

The most widely used method is the induction heating method coupled with conventional air cooling to achieve relatively high heating and cooling rates in a large temperature range. However, high-frequency heaters may produce high wall thickness temperature gradients (which is normally not easy to calculate for nonaxisymmetric specimens) and severe electrical grounding problems. Furthermore, forced air cooling might induce an undesirable temperature profile. Other workers have used direct resistance heating[52,53] which is believed to produce crack tip overheating. More recently, Pernot and Mall used a quartz lamp heating technique[67] while Malpertu and Rémy used a radiation furnace with four 1500W light bulbs[40] in their TMF testing. These light heating techniques are much easier to control.

Temperature measurement methods are also important for stable and accurate temperature control. Thermocouple and optical pyrometers are the most often used techniques. In most of these cases, the thermocouples were mechanically bonded on the specimen surface instead of being spot welded. This is to avoid crack initiation to occur at spot welds. Although the optical pyrometers are convenient to

use, they can be less accurate, especially in the case of heavy oxide build-up on the specimen surface. Note that the heat emissivity of most metals and alloys varies considerably with relatively small amount of oxidation.

1.5.2.3 Damage monitoring and crack growth measurement

For smooth specimen testing, the load drop criterion (e.g. 20% or 50% drop) of the maximum load of the stabilized cycle is commonly used to estimate the state of damage and failure[62]. Plastic replication techniques were also widely used in TMF testing. Malpertu and Rémy[40] used 300μm and 50μm crack depth criteria observed using a replication technique to define crack initiation lives. A Multiple specimen damage assessment technique has been developed by Neu and Sehitoglu[61-62]. They performed interrupted tests to gain insight into the progression of damage during different phasing conditions. These tests required using a number of specimens for each testing condition and stopping these different specimens at some percentage of the failure life. Specimens from the tests were then sectioned and examined to measure the primary crack length and to detect microscopic damage. Hence the damage as a function of number of cycles can be established. Although extremely time consuming, this technique is particularly helpful when trying to examine the oxide characteristics, the oxide intrusion growth and the progress of internal creep damage along grain boundaries during TMF cycling.

Fatigue crack extension measurement are mostly performed by traveling microscope monitoring methods[52,68,76,81]. DC potential drop method (DCPD) have been used by Marchand[46] and Pernot[67]. However, an advanced AC potential drop techniques (ACPD)[43-49] also started showing promising results in monitoring the crack initiation and propagation. the ACPD technique will be reviewed later in this chapter.

1.5.2.4 Strain controlled and stress controlled TMF tests

The stress controlled TMF testing is technically much easier to achieve than the strain controlled testing. No thermal expansion compensation is needed. However, due to high temperature and stresses (i.e. high inelastic strains), most of the TMF tests are strain controlled, as it is convenient to compare with isothermal LCF tests and is similar to most cases of TMF problems encountered in components. Some testing was performed under stress controlled conditions[47,52,53,67,81] to simulate specific service loading cases such as in small turbine blades[52,82] where the centrifugal forces are more dominant than the thermal loads. There are also tests of combined control mode. For example, in order to evaluate the mean stress effect, Heine et. al[34] performed the strain controlled test with an adjusted load (stress offset).

1.5.3. TMF data analysis

1.5.3.1 Crack initiation data under anisothermal conditions

The definition of fatigue life is always a matter of controversy even for the simplier isothermal LCF tests. The situation becomes more complex with TMF testing on smooth specimens. Most of the time, complete fracture of specimens is avoided to enable metallographic observations. As mentioned earlier, a 50 % or 25 % of load drop of the maximum load found in the stable cycle period is used to define failure of the specimen[61]. To provide a more precise definition of the fatigue life, it is now convention to define crack initiation as the number of cycles to a 0.3-1.0 mm crack depth. This definition also referred as "life to engineering crack initiation". Plastic replication technique has also been used for providing higher resolution for crack initiation life (e.g. life to 50μm crack)[74]. This technique have revealed the early crack propagation included in the engineering crack initiation life, and this is very important for low strain range tests and applications.

For the smooth specimen TMF testing, several models have been proposed to predict the fatigue life. As expected that all the models are extensions of isothermal LCF models. However note that the thermal cycling involved in TMF testing complicates the problem of determining the stress-strain behavior, the environmental attack and, subsequently, the fatigue life. From the engineering point of view, two general attributes[34] are considered highly desirable in guiding selection of a life prediction model. It must have simple physical basis and simple to apply. Therefore it is desirable to avoid integral dependence of the life prediction

model upon complex constitutive models, as well that the life model should be applicable by using parameters estimated from simple constitutive models, albeit with potentially lower accuracy.

Some simple models used in several studies are the classical Manson-Coffin relation[74,83], Ostergren model[34,77,80,84] and Manson and Halford's strain range partitioning (SRP)[78,85-89]. Recently, Heine and coworkers[34] have shown that the tensile hysteresis energy model as proposed by Ostergren (with modification for estimation of the very small inelastic strain range) could yield good results for TMF life prediction for two coated airfoil alloys PWA286, PWA275 and PWA 1480. This model includes the total inelastic strain range and the mean stress, which capture some effects of fundamental life-controlling variables. In their study, a two-bar model was used to consider the effect of coating influence on the substrate hysteresis energy.

The SRP method has been derived to be successfully applied to TMF life predictions for 304 stainless steel[78] and some superalloys (e.g. Rene'80 and Fe-Base Forged Superalloy A286)[88,89], although it is problematic in dealing with TMF testing with small inelastic range. In a recent development of the NASA hot section technology program (HOST)[85], attempts have been made to adapt an improved SRP method to TMF problems. In this method the SRP approach is expressed in terms of total strain range versus cyclic life.

The total strain based SRP approach (TS-SRP) was proposed by Saltsman and Halford[95]. Here the total strain range $\Delta\varepsilon_t$ is expressed by

$$\Delta\varepsilon_t = \Delta\varepsilon_{el} + \Delta\varepsilon_{in} = B(N_f)^b + C'(N_f)^c \quad . \tag{1.20}$$

The time and wave form dependent constant C' is determined using the SRP analysis. Whenever the appropriate elastic and inelastic strain range versus life relations are calculated and added together to obtain the desired total strain range versus cyclic life diagram, the cyclic life is determined directly by entering the known total stain range, without having to calculate the magnitude of the inelastic strain range.

Some other complex models for TMF life prediction have also been developed. For example, the cyclic damage accumulation (CDA) concept is very promising for TMF life prediction. In the NASA/HOST program[85], this concept was used to develop models for describing the fatigue-creep interaction at elevated temperatures. This effort also included the taking into account of the effects of thermomechanical fatigue, multiaxial loading, cumulative damage, environment, mean stress, and coatings on high-temperature crack initiation life prediction of cast nickel-base alloy PWA1455 (B1900+Hf). Most of the TMF tests in this program were performed at temperatures between 538°C to 871°C at 1.0 cpm with total mechanical strain ranges between 0.4 and 0.5 percent. The current form of the model developed for accumulated transgranular damage can be written as

$$1 = \int_0^{N_i} \left(\frac{1}{\varepsilon_p}\right)\left(\frac{1}{G_{NL}}\right)\left(\frac{dD}{dN}\right)_R \left[\left(\frac{\Delta\sigma}{\Delta\sigma_R}\right)\left(\frac{\sigma_T}{\sigma_{TR}}\right) + D_{TD}\left(\frac{f_{OX}}{f_{OXR}}\right)\right] dN \quad , \tag{1.21}$$

where N_i = initiation life, transgranular mode,

$\bar{\varepsilon}_p$ = primary creep ductility,

G_{NL} = nonlinear damage accumulation function,

$(dD/dN)_R$ = reference cyclic damage rate,

σ_T = maximum tensile stress in current cycle,

σ_{TR} = reference maximum tensile stress,

$\Delta\sigma$ = stress range of current cycle,

$\Delta\sigma_R$ = reference stress range,

D_{TD} = time-dependent damage rate modifier,

f_{OX} = oxidation rate for current fatigue cycle,

f_{OXR} = reference fatigue/cyclic oxidation rate.

This model has shown good ability to correlate TMF data for bare and coated materials (MOSTLY, B1900+Hf).

Neu and Sehitoglu[61-62] have developed a damage model for TMF damage in a 1070 steel. The study showed that oxidation and creep damage mechanisms were two primary mechanisms which enhance fatigue damage. Therefore the damage per cycle from these three mechanisms can be summed up to obtain a total damage per cycle,

$$D^{tot} = D^{fat} + D^{ox} + D^{creep}$$

or $$1/N_f = 1/N^{fat} + 1/N^{ox} + 1/N^{creep} \quad (1.22)$$

Here the superscripts "fat," "ox," and "creep" stand for fatigue, oxidation, and creep.In their study, the fatigue damage term, N^{fat} is assumed to be governed by the mechanical strain range. Similar to Eq.(1.20) it can be estimated from

$$\frac{\Delta \varepsilon_m}{2} = \frac{\sigma_f'}{E}(2N_f^{fat})^b + \varepsilon_f'(2N_f^{fat})^c \; . \quad (1.23)$$

Here the material constants (E, σ_f', b, ε_f', and c) are determined from isothermal fatigue tests.

The oxidation damage term depends on the nature of the oxidation-induced crack nucleation and growth mechanisms. For oxidation-induced crack growth caused by the repeated formation of an oxide layer and its rupture at the crack tip (which exposes fresh material to the oxidizing environment) the growth rate can be generally expressed as

$$\frac{dh_0}{dN} = \frac{BK_p^{eff}\beta N^{\beta-1} t_c^{\beta}}{h_f} \; . \quad (2.24)$$

Here K_p^{eff} is the parabolic oxidation constant and the h_f is the average critical oxide thickness at rupture. Note that h_f is a function of the mechanical strain range, the phasing of the temperature and strain, and the strain rate and is expressed as

$$h_f = \frac{\delta_0}{(\Delta \varepsilon_m)^2 \Phi^{ox} \dot{\varepsilon}^a} \quad . \tag{1.25}$$

where ^{ox} is the phasing factor representing different TMF cycling. By combining the above two equations, the oxidation damage term can written as

$$\frac{1}{N_f^{ox}} = \left[\frac{h_{cr}\delta_0}{B\Phi^{ox} K_p^{eff}} \right]^{1/\beta} \frac{2(\Delta \varepsilon_m)^{(2/\beta)+1}}{\varepsilon^{1-(\alpha/\beta)}} \quad . \tag{1.26}$$

One should be cautious when using these oxidation damage models. For some alloys at lower temperature or shorter cycle period, the formation of oxide layer can not be well defined. Also oxidation induced embrittlement at the crack tip can be another mechanism responsible for oxidation assisted cracking.

The creep damage term was written as a function of the effective and hydrostatic stress components, i.e.

$$D^{creep} = \Phi^{creep} \int_0^{t_c} A\, e^{(-\Delta H/RT)} \left(\frac{\alpha_1 \sigma + \alpha_2 \sigma_H}{K} \right)^m dt \quad . \tag{1.27}$$

Here σ is the effective stress (Von Mises), σ_H is the hydrostatic stress, K is the drag stress, α_1 and α_2 are scaling factors which represent the relative amount of damage occurring in tension and compression, Φ^{creep} is the phasing factor; and A and m are material constants.

The results of this TMF life prediction model have been shown good results in providing a quantitative description of oxidation induced crack growth. However, the procedures used to determine those constant such as ^{ox} , ^{creep} , etc. need to be carefully studied. Similar damage analysis were also performed more recently by Sehitoglu and Boismier[35,36] for TMF test of Mar-M247 nickel base alloy. The newly published data on TMF behavior of MMCs by Sehitoglu and Karayaka[64-66] also indicated a successful application of these damage models to more complicated material systems where internal stresses and strains generated by the mismatch of the mechanical and thermal properties of the constituents further contribute to the deformation mechanisms. In their study, the volumetric average stress-strain behaviors rather than localized stress-strain behavior was used to quantify the damage micromechanisms of the metal matrix composites, in spite of the fact that stress concentrations in the matrix due to mechanical property mismatch are the main cause for fatigue crack initiation.

1.5.3.2 Fatigue crack growth under TMF loading

In the last two decades, fracture mechanics has progressed dramatically, and contributed significantly to assess of the integrity of gas turbine engine structural components. Among a variety of fracture theories, linear elastic fracture mechanics (LEFM) and the elasto-plastic fracture mechanics (EPFM) have been used in most occasions. LEFM is a theory concerned with a single fracture mechanics parameter such as the stress intensity factor (K), or the energy release rate (G). It is based on

the assumption of small-scale yielding (SSY) and have found enormous applications in brittle fracture and fatigue life predictions[90].

The majority of the analyses on TMF fatigue crack growth (or TMFCG) assumed that the crack is described by a fracture mechanics parameter, such as the stress intensity factor (K_σ), the strain intensity factor (K_ε), the J-integral, the crack opening displacement COD, and the C^*-integrals or combination of them.

In the pseudo linear elastic conditions (i.e. LEFM), the stress intensity factor range (ΔK_σ) was used to correlate the fatigue crack rate (da/dN) data. The ΔK_σ are computed using

$$\Delta K_\sigma = \Delta\sigma\sqrt{\pi a}\, f(geometry) \quad , \tag{1.28}$$

where a is the crack length, $\Delta\sigma$ is the stress range (applied or measured), and f is a function which characterizing the geomety and loading conditions of the specimens. The ΔK_σ was shown to provide good correlations of TMFCG data under stress controlled condition for IN X-750 (with consideration of crack closure)[47], IN100 and Astroloy[52-53]. Studies by Marchand[48,50] on Hastelloy-X, Jordan and Meyers[72,73,76], and Gemma[91] indicated that by using the measured nominal stress range in the strain controlled TMF tests and with consideration of crack closure effects, K_σ can give reasonable correlation for the da/dN data.

Because TMF tests are often performed in strain controlled mode, the strain intensity factor, although lacking real physical meaning in regard to the crack tip

stress fields, has also been a popular parameter for TMFCG data correlation. It is defined as

$$\Delta K_\varepsilon = \Delta \varepsilon \sqrt{\pi a}\, f(geometry) \ . \qquad (1.29)$$

Several successful correlations have been reported by applying this parameter to TMF tests[82,83,92,93] although some bad correlations have also been reported[46,48,72,73,76].

The application of the cyclic J-integral (ΔJ) to fatigue crack growth[94-96] is always very controversial from a theoretical point of view. However the studies of Okazaki and Koizumi[97,98] indicated considerable success in correlating TMF testing data of Type 304 steel, 1Cr-1Mo and 12Cr-Mo-V-W steels. On the other hand, the results for nickel base superalloys indicated that the correlations using the J-integral are similar to that of the strain intensity factor[45,72]. A comparison of the strain intensity and cyclic J approaches to crack growth can be found in the study by Starkey and Skelton[95]. In most studies, the ΔJ is defined as

$$\Delta J = \frac{\Delta K^2}{E} + F(a/b, L, N)\left(\frac{1}{N}+1\right) a\, \Delta W_p \ . \qquad (1.30)$$

Here ΔW_p is the hysteresis strain energy (work). E is the elastic modules, N is the hardening coefficient, and F(a/b, L, N) a geometrical factor for the specimen considered.

The crack opening displacement (COD) has appeared as a very attractive parameter for TMF data reduction. This is because it explicitly contains the temperature-dependent material properties (elastic modulus E, yield stress σ_y and strain hardening exponent n). It is possible that the temperature dependence of TMFCG, as revealed by ΔK_σ, ΔK_ε or ΔJ reduction, may be less significant (or disappear) when the correctly evaluated COD is used to correlate the da/dN data. Generally, there are two methods used to calculate COD. One is based on the Dugdale model [58] and is computed using

$$\Delta\delta_t = \frac{8\sigma_0}{\pi E} a \ln(\sec\frac{\pi\Delta\sigma}{2\sigma_0}) \quad . \tag{1.31}$$

The other is based on the relationships between the COD and the J-integral as derived from the finite element solutions of McMeeking[73], i.e.

$$\Delta\delta_t = 0.55\frac{\Delta J}{2\sigma_y}(\frac{2}{\sqrt{3}}(1+\frac{1}{N})\frac{N\sigma_y}{E})^{1/N} \quad . \tag{1.32}$$

Reasonable correlation results have been reported for a 1070 steel and for Hastelloy X [58,72,73,76].

In high strain range TMF test, these fracture mechanics parameters have difficulties in characterizing the local crack tip fields. Marchand et. al [45] described in length the problems involved in using ΔJ to correlate fully plastic crack growth data. It is worth noting that all these parameters do not include the effects of time

dependent deformation during temperature cycling, and the environmental attack on the crack growth.

In order to consider rate dependent visco-plasticity, Ohtani et al [81] have proposed the use of two equations to describe the cycle-dependent and time-dependent fatigue damage. Hence, the fatigue J-integral range ΔJ_f and the creep J-integral ΔJ_c were calculated from the analysis of the hysteresis loop area. An equation was proposed to separate the cyclic-dependent fatigue dominated cases from the time-dependent fatigue cases, which can be written as:

$$\Delta J_c = \frac{C_f}{C_c} (\Delta J_f)^{m_f} \quad . \tag{1.33}$$

Here C_f, C_c, and m_f are material constants. This method was verified on 0.16% carbon steel cycled in a temperature range of 200°C to 500°C.

The study conducted by General Electric (GE) for the NASA/HOST program investigated several new path-independent (PI) Integrals proposed in the past few years[85,99]. Specifically, some PI integrals proposed by Tada, Ainsworth, Blackburn, Kishimoto and Atluri[99-103] have been found suitable for analysis of crack tip stress fields involving nonlinear and time-dependent thermomechanical response. The traditional Rice J-integral, however, becomes path dependent and loses its physical significance for thermomechanical loading. However few actual applications of these PI integrals for correlating the TMF crack growth have been reported so far.

Besides the study of oxidation crack extension by Neu[62], some new achievements on this topic have also been made by Liu and Oshida in the NASA/HOST program[85,104] for IN 718, IN X-750, ASTROLOY, etc. In their study, oxygen arriving at a grain boundary crack was assumed to diffuse into the region ahead of the crack in order to form oxide along the grain boundary. When the crack tip grain boundary oxide, at a given stress level, reaches a critical size δa, the oxide was then assumed to rupture and the crack to grow by an amount δa. This critical size δa was shown to be dependent on the stress intensity level during the holding period. The model can be expressed in a simple form as

$$(\frac{da}{dN})^{ox} = \beta' (\frac{D_{gb}}{f})(\frac{B}{\delta a})^{1-n/n} . \qquad (1.34)$$

where ß' is a proportionality constant, B is the magnitude of the diffusion jumping vector or interatomic spacing, D_{gb} is the grain boundary diffusion coefficient, n is a positive exponent (less than unity) and f is the frequency of the load cycling.

Although the applicability of this model was only illustrated in isothermal high-temperature environments, it is theoretically feasible to apply this model to TMF conditions. The major problem is how to determine the grain boundary diffusion coefficient D_{gb} as a function of temperature. Note that the environmental effects on TMF were also studied by Wright[37], Jones[102], Skelton and Wong[105]. From the fractographic observations of failed specimens under TMF loadings[46,47,73], it was found that the fracture mode in TMF tests were either

transgranular dominated mode or intergranular dominated mode. The occurrence of a mode depends on the main type of damage (that reveals cycle-dependent or time dependent damage). Heil[68,106] used a linear cumulative damage model which sums cycle-dependent, mixed-mode, and time-dependent damage terms to predict thermal-mechanical fatigue crack growth rates for Alloy IN 718. This model can be expressed as

$$\left[\frac{da}{dN}\right]_{total} = \left[\frac{da}{dN}\right]_{time} + \left[\frac{da}{dN}\right]_{mixed} + \left[\frac{da}{dN}\right]_{cycle} . \qquad (1.35)$$

The model gave very good prediction for TMF crack growth while it being based soley on the isothermal fatigue and sustained load cracking data. The mixed-mode damage term was assumed insignificant and its contribution was neglected.

1.5.4 Effect of TMF cycling on material microstructure.

The effect of TMF cycling on material microstructural features of Cast B-1900+Hf nickel base alloy was studied by Marchand[44]. The changes in γ' precipitate morphology and introduction of a dislocation network around the γ' precipitates were noticed for in-phase and out-of-phase conditions. Increased flow stress due to higher density of dislocation networks surrounding the γ' in the in-phase condition while lower flow stress and less dense dislocation network under out-of-phase cycling were found in this study.

Recent study by Christ and Mughrabi[107] on AISI 304L steel (a material with strong dynamic strain ageing effect) reported that in the TMF test a more wavy slip occurs as consequence of cyclic deformation at temperature above and below the regime of dynamic strain ageing during each TMF cycle. The dislocation substructure in the isothermal fatigue test at the mean temperature is determined by dynamic strain ageing and largely by planar slip. The same study on the γ'-hardened monocrystalline Ni-base superalloy CMSX-6 found that the directed γ' structure and soft γ-matrix channels along {111}-planes were formed preferentially under out-of-phase TMF conditions. Another new study on MA760, an oxide-dispersion strengthened superalloy, by Vasseur and Remy[108] suggested that TMF cycling gives rise to dissolution and precipitation processes of γ' phase for the material with lower solvus temperature.

No data on the effect of TMF cycling on titanium alloy microstructure have been reported.

1.5.5 Material behavior modeling under TMF loading

Earlier efforts to model the stress and strain histories of materials under cyclic TMF loading have been made by McGowan and Liu[109], Levy[110] etc. using thermal elastic plastic finite element (FEM) Code supported by conventional theory of elastic plastic deformation. Recently there has been a renewed interest in unified theories for predicting the high-temperature material behavior. However, study by Cook et al[80], Assaker and Hogge[111], and Marchand[112] showed that

the classical constitutive models are still very promising for certain materials under certain types of thermomechanical loading where the time-dependent deformation is not a dominating factor. Accounting for the time-dependent deformation, Slavik and Sehitoglu[55] used the time-dependent theories based on classical plasticity concepts by adding time-dependent strains to plastic strains separately in their prediction of the general features of material (1070 steel) deformation under TMF loading. A simple but purely empirical formulation of a temperature dependent strain hardening law was proposed by Kim[113] for aluminum. This model was reported quite successful in correlating the stress strain curves obtained from tensile experiments under different temperature and strain rate conditions.

The importance and attractive features of the modern unified constitutive laws, as discussed earlier, with regard to TMF analysis is that, the internal variables used in these equations can be related to the physical damage mechanisms observed in TMF tests[8,60], and effects of varying temperature can be well represented in the constitutive models.

The unified creep-plasticity model are generally expressed in terms of a set of coupled differential equations for the inelastic strain rate, the drag stress and back stresses (i.e. the internal state variables). In their model, developed from TMF tests of a 1070 steel, Slavik and Sehitoglu[55] used an inelastic strain rate taken from Bodner's model which does not employ a back stress variable (isotropic model). More recently, Sehitoglu[60] proposed a new form of this model that uses a back stress variable directly based on the experimental observations. He also studied the

changes of the internal variables at elevated temperatures and its connection with metallurgical effects.

Ohno et al[42] have successfully simulated the anisothermal cyclic plasticity of a 304 steel by using a quite complicated constitutive model based on a plastic strain region, called the cyclic nonhardening region, as well as on two stress surfaces, i.e. the yield surface and the bounding surface. Efforts were made to determine the material constants under isothermal conditions and to extend the evaluative equations of isotropic and kinematic hardening to thermomechanical cycling.

A practical three dimensional turbine blade analysis in cyclic thermo-viscoplasticity using a unified elasto-viscoplastic constitutive model was successfully performed by Géradin et al[114]. Their analysis was based on the unified constitutive model proposed by Chaboche, and was implemented in the 3D-FEM code SAMCEF (used for aircraft engine stress analysis). The material assumed in the calculation was IN100. The 3D-FEM model had 877 degrees of freedom (the CPU time used for each load cycle was up to 4.5 hours on average). Their results indicated that the complex thermomechanical history of a blade can be modeled and thus allow more accurate predictions of the cyclic lives, albeit the calculation was expensive in terms of CPU time required.

In the NASA/HOST program[3,85,115], unified constitutive models have also received extensive attention. Some models have been implemented into a FEM code (MARC) for structural analysis of isotropic materials. This includes the models of Walker and Bodner-Partom. The results of calculation show that for the cast

nickel-base alloys studied, B1900+Hf and MAR-M247, both isothermal and anisothermal complex loading histories can be well predicted using the unified constitutive model approach with all the necessary material constants derived solely from isothermal test data. This research program has demonstrated rather conclusively that the unified constitutive model concept is a very powerful tool for predicting material response of hot section components under complex, time-varying, thermomechanical loading. Besides, the computation efficiency with these unified models are as good or even better than the ones using classical models, as has been shown in the analysis of an airfoil of a typical cooled turbine blade[3]. Constitutive modeling for anisotropic materials and thermal barrier coatings are also being developed in the HOST program. Hence, for the single-crystal material PWA 1480, two separate unified viscoplastic models have been formulated and are under extensive verification.

Modeling for crack growth under TMF loading, especially under high strain fatigue conditions (general yielding condition) or in the case of significant time-dependent crack growth phenomena, has not been addressed. At the present time, there is no unique parameter that correlates the crack growth data under isothermal and TMF conditions. Hence, the crack tip cyclic visco-plastic stress-strain fields have not really been identified and are far from being described. It is worth noting that the identification of a sound and physically based parameter is still a challenging issue.

As for crack initiation prediction, it appears that much effort has been devoted on material modeling using advanced constitutive models in comparison

with the experimental determination of the material mechanical responses under complex loading histories, and its relation with damage mechanism. Few efforts have been focused on the calculation of the crack tip stress/strain fields and the investigation of the fracture mechanics features associated with TMF loading. This is important for more accurate estimation of the effects, such as crack closure, crack tip opening, etc., which are known to have significant influence on TMF crack growth. Actually, concerning TMF loading, some modifications of fracture mechanics parameters, for example J integral, only included the thermal stress terms. The effects of varying the temperature and the material mechanical properties at the crack tip are not well understood. For example, imagine a cracked plate loaded with a constant uniform tensile load while the temperature is cycled in a certain range. In this case, besides the creep effect, the crack tip plastic zone size should change with the temperature. How this extra plastic flow will contribute to crack growth and how it be represented in fracture mechanics parameters are of great interest[116].

Oxidation-induced crack extension can be modeled fairly well now. This is a significant progress in the study of TMF in terms of accounting for the environmental effects. The study of Neu and Sehitoglu[61] indicated that in 1070 steel, the mismatch of the thermal expansion coefficient between the metal and the oxide has little influence on cracking behavior in TMF cases. This was supported by running thermal cycling under zero applied mechanical load. This conclusion simplified the modeling effort. However, this conclusions needs to be proven applicable for other alloy systems. For examining the interaction between different phase (particles) of various alloys due to thermal expansion coefficient mismatch,

which is specially interesting for carbides and gamma phase grains in Ni-based alloys, thermal cycling under zero applied stress test is also needed. The modeling of environmental attack involves many material properties such as oxidation kinetics, material surface condition, oxygen diffusion efficiency, oxide mechanical properties, and so forth, which are not always easy to obtain. It may be easier to separate the environmental damage term by running thermal cycling with constant mechanical load (strain or stress) at different levels.

Besides, the studies associated with TMF analysis have revealed that there are a lot of promising concepts and methods pertaining to crack initiation, creep crack growth, etc., developed for isothermal fatigue problems that can be extended to anisothermal conditions. For example, the "crack tip local strain concept" proposed by Shimada and Furuya[117] is an attractive approach for unifying the two processes of fatigue crack initiation and propagation. The works of Kujawski and Ellyin[118,119], and Rie[120] are helpful for connecting crack growth law with the crack tip fields which are strongly influenced by TMF loading. No doubt that these two methods, just to name a few, will be the subject of further research.

1.5.6 Application of numerical methods in LCF and TMF analysis

Numerical methods are essential in engineering structure analysis, where there are geometrical discontinuities, complex loading conditions (including thermal loading) or nonlinear material behavior. In this section, the application of finite element method (FEM) and boundary element Method (BEM) to LCF and TMF

analysis with focus on implementing new material models mentioned earlier in FEM and BEM are reviewed.

Regarding to the analysis and interpretation of test data, these two methods are used when the specimens have notched edge (e.g. SEN and DEN), nonsymmetrical geometry (e.g. CT) and through thickness holes or cracks (e.g. CCT). These techniques have also been used when there was the presence of non-uniform temperature distribution, such as in Thermal Fatigue (TF) tests. In many situations, test data reduction or correlation relies on parameters that are calculated by the numerical analysis[121] simply because they can not be measured directly during the test.

The FEM is the most popular and commercialized tool for both linear and nonlinear structural material analysis. The basic concept of FEM is to discretize the domain of the problem into a number of elements. The governing equations of the problem are then approximated over the element by functions which fully or partially satisfy the boundary conditions[122].

As an alternative to the 'domain' methods such as the FEM, the BEM is attractive because of its lower cost of computation, better approximation of boundary conditions, very general geometry definition, and good ability to represent regions of stress concentration. It uses approximating functions that satisfy the governing equations in the domain but not the boundary conditions. The boundary conditions are applied by boundary integration techniques[123]. The shortcoming of this method is its strong dependence on the approximating functions, which are

based on theoretical derivation and difficult to establish for nonlinear problems. This has limited the application of BEM mostly to linear elastic problems[124].

Many achievements have been made recently in the implementation of new constitutive models into the existing FEM and BEM codes, although few information are available on the detailed processes. It is an important step for applying those advanced material models such as those discussed in the earlier sections on structural analysis, material processing simulation and fatigue life prediction. In the HOST program, the models of Walker[70,71] and Bodner-Partom[10,128] have been implemented into a large commercial nonlinear finite element computer code MARC[15,16]; The BEM code BEST3D developed under P&WA contract is now incorporates a variable stiffness plasticity algorithm which is capable of handling a variety of constitutive models[3]. A unified model has been implemented to FEM code SAMCEF by Géradin et al[114].

In the nonlinear problems, the system equations used by FEM becomes a nonlinear and iterative solutions such as the Newton-Raphson methods must be used. In most cases, the general form of the equation cannot be directly derived and as a result its incremental forms are used. The earlier solution algorithm for inelastic analysis are based on initial strain method. Levy[110] implemented an anisothermal inelastic material model into a FEM procedures initially based on the classical theory of plasticity. He separated the total strain increment into elastic, plastic, creep and thermal expansion components. The plastic strain was determined by the Prandtl-Reuss flow rule, and the hardening law was based on the Prager-Ziegler kinematics hardening theory. The creep strain rate for multiaxial state of

stress was calculated from the equivalent strain rate and stress concepts. By applying the principle of minimum potential energy, the initial strain method was formulated in an incremental form which consists of the nodal displacement incremental vector, the elastic stiffness matrix, the incremental applied load vector, the 'pseudo-load' vectors associated with plastic and creep strain, which were determined at the current temperature. The equations can be solved by an iterative method. To treat the rate formulated component such as creep strain, Levy used a time integral procedure to calculated the predicted value of the creep strain, which can be written as:

$$\left\{\Delta\varepsilon^{c}\right\}_{i}^{pr} = \Delta t_{i}\left\{\Delta\dot{\varepsilon}^{c}\right\}_{i-1} + \frac{(\Delta t)^{2}}{2\Delta t_{i-1}}\left[\left\{\Delta\dot{\varepsilon}^{c}\right\}_{i-1} - \left\{\Delta\dot{\varepsilon}^{c}\right\}_{i-2}\right]. \qquad (1.36)$$

Here, the time integral procedure is a very important step for implementing the state variable rates based theories.

In the work of Géradin et al[114], the unified elasto-viscoplastic model is written as

$$\dot{\varepsilon}^{in} = \frac{2}{3}\dot{p}\frac{(S-\alpha)}{J(S-\alpha)} \quad . \qquad (1.37)$$

Here p is the accumulated inelastic strain, S and α are matrice of deviatoric stress and back stress respectively, and J is the second invariant of the overstress. The constitutive equations are integrated with time using the Adam's formulas.

Lifetime prediction procedure is also carried out in their work. The damage evolution formula used were the creep damage law by Kachanov. Calculations were carried out for IN100 alloy blade 3D model.

An anisotropic model of continuum damage mechanics model was successfully implemented to the FEM code by Chow and Sze[126]. The generalized concept of effective stress proposed by Lemaitre[127] for triaxial state of stresses and a damage evolution rule was used.

Chan and Lindholm[15,16] formulated an anisothermal unified constitutive models as

$$\begin{aligned}
\varepsilon^{in} &= f(\sigma, x, T) \\
\dot{x} &= g(\sigma, x, T) \\
\dot{\sigma} &= D(\dot{\varepsilon} - \dot{\varepsilon}^{in}) + \theta(\alpha, D)\dot{T} \\
\theta(\alpha, D) &= [\varepsilon - \varepsilon^{in} + \alpha(T - T_0)\frac{\partial D}{\partial T} - D[(T - T_0)\frac{\partial \alpha}{\partial T} + \alpha] \; . \qquad (1.38)
\end{aligned}$$

In their work, an implicit time operator η ($0 < \eta < 1$) was used for integrating the rate equations in the unified models, which can be written as

$$V = \Delta t\{(1-\eta)^a V + \eta^b V) \quad . \qquad (1.39)$$

where V stands for the variables ε^{in}, ε, x, or σ. Note here the the integration techniques play a key role in implementing rate equation based unified models into FEM codes.

A Runge-Kutta (fourth order) algorithm was employed for the numerical time integration of the Bodner-Partom equations by Kolkailah and McPhate[125]. Again, the pseudo-plastic force method was used to obtain the inelastic component of strain in triangular constant strain elements.

Recently, Chulya and Walker[128] summarized various algorithms for integrating the inelastic constitutive models, and proposed a new implicit and iterative formulation which is convenient for implementing into the FEM codes.

1.6 ACPD FATIGUE CRACK GROWTH MEASUREMENT

The potential drop technique makes use of an increase in electrical resistance of conducting material due to crack initiation and growth. The well established DC potential drop method uses constant DC current passing through the specimen and measures the potential drop between the probes on either side of the crack or notch. However, the DCPD require large currents to produce an adequately measurable potential drop, which is problematic for measuring small cracks when high resolution is required.

The ACPD potential drop methods use high frequency AC current of constant amplitude passing through the specimen and measure the potential drop between the probes. As compared with DCPD, the sensitivity and linearity of ACPD system are enhanced by the skin effect resulting from the high frequency current passing through the specimen[129,130]. With the development of new generation lock-in amplifiers, the AC potential measurement techniques have been greatly advanced in the recent years.

When an AC current is passed through a conductive material, the distribution of the electric field strength $\tilde{\mathbf{E}}$ in the specimen obeys the Maxwell's wave equations and Ohm's law. In a simplified form this can be written as

$$\nabla^2\tilde{\mathbf{E}} = \mu\sigma_c \frac{\partial \tilde{\mathbf{E}}}{\partial t} \quad . \tag{1.40}$$

where the μ is the magnetic permeability and σ_c is the conductivity of the material. Thus the potential drop ΔV between any two points on the surface of the specimen can be computed provided that the $\tilde{E}$ field is known. Unfortunately, the analytical solution for Eq. (1.40) is only available for simple 2D geometrie for axially symmetric cases (i.e. long cylindrical conductor). For cases such as SEN specimens with bolt hole notches a general analytical solution is not available and numerical solutions are being developed[130].

As illustrated in Figure 1.8, a simplified procedure can be used to estimate the distribution of the inductive electrical field . This is the "skin depth" δ approach which is defined as

$$\delta = \frac{1}{\sqrt{\pi f \sigma_c \mu}} \quad . \tag{1.41}$$

Here f is the frequency of the AC current while δ is the "thickness" in which most of the conductive and inductive currents are passing through. For titanium alloy Ti64, the skin depth δ is estimated to be 3.7 mm for a 30kHz current and 2.4 mm for a 100kHz current. Although this value is much larger than that of magnetic materials such as nickel-based alloys, the current density at the surface of a specimen will be still much higher than that of the average values in the cross section. This effect, which increases the potential drop for a given total current, results in an increased sensitivity for detecting material damage. The sensitivity increases with increasing AC frequency.

Verpoest et al.[131] performed theoretical and experimental analysis of ACPD response of cylindrical specimen with smooth surface. He showed the

beneficial effect of using high frequencies, the "coil" effect of the probe configuration to the ACPD output, and the magnetomechanical effect. In their study, the minimum detectable crack was claimed to be 65μm (area of 0.0066 mm^2 0.05% of cross section) for the steel specimen tested. Due to the limitation of signal processing technique at the time, the PD signal output was in μV scale (15 μV ACPD change corresponding to 600μm crack). This caused higher data scatter in high frequency (f > 40KHz) applications. Lugg [132] studied the sparse data in ACPD crack growth monitoring. He also showed good linear relationship between ACPD and crack length for thin-skin and thick-skin materials.

A 3D numerical d.c potential field analysis was performed by Ikeda[133]. The theoretical calibration curve for the penny-shaped crack was found to be in very good agreement with the experimental data. However, the analytical formulas failed to implement the skin effect and cannot be applied to the AC potential method.

Hwang and Ballinger[134] recently developed a multifrequency ACPD system (17 - 203KHz). The measurements were performed during smooth round bar specimen fatigue testing of a nickel-base alloy in aqueous environment at room temperature and 350°C. Single crack initiation size of 50 μm resolution was reported. In their study, the pronounced sensitivity of ACPD and signal phase shift, at high frequencies, to probe spacing and configuration was observed. This set very high requirement for probe set-up for each test to ensure reproducible calibration data. Good linear relationships between the measured ACPD and crack depth at high frequencies were again confirmed. The study suggested that the ACPD technique was more suitable for constant load than for dynamic loading.

The application of high frequency (>10KHz) ACPD technique to fatigue testing is still in its early stages. Although some application of alternating DCPD methods (sometimes also referring to ACPD), which are not "skin effect" based but signal differential techniques, were reported in the gas turbine industry[135] for long crack growth measurement, no data on the application of ACPD technique in TMF testing and for titanium alloys were found in the published literature.

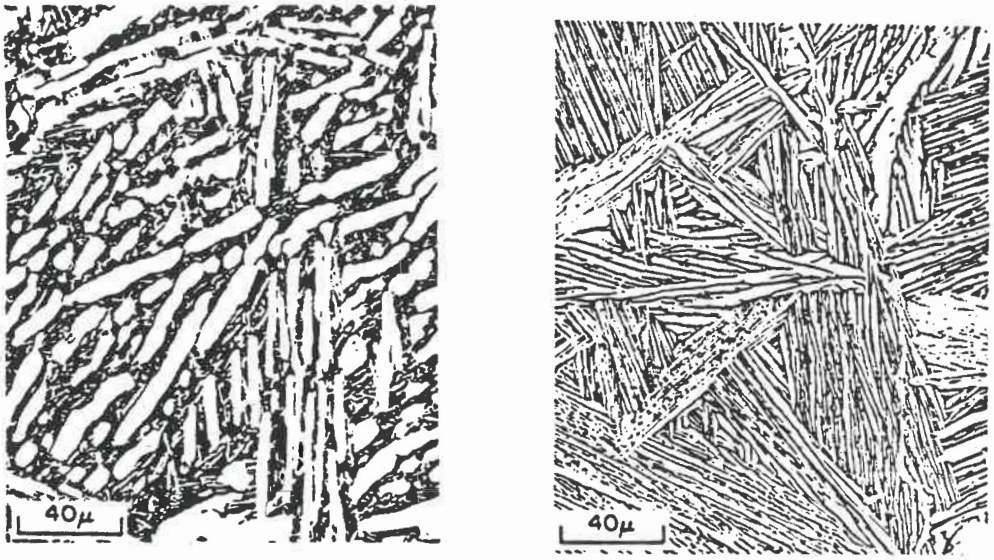

Figure 1.1 Typical duplexed microstructures of $\alpha+\beta$ titanium alloys; (a) lightly worked nucleation-and-growth type; (b) basketweave like Widmanstatten structure.

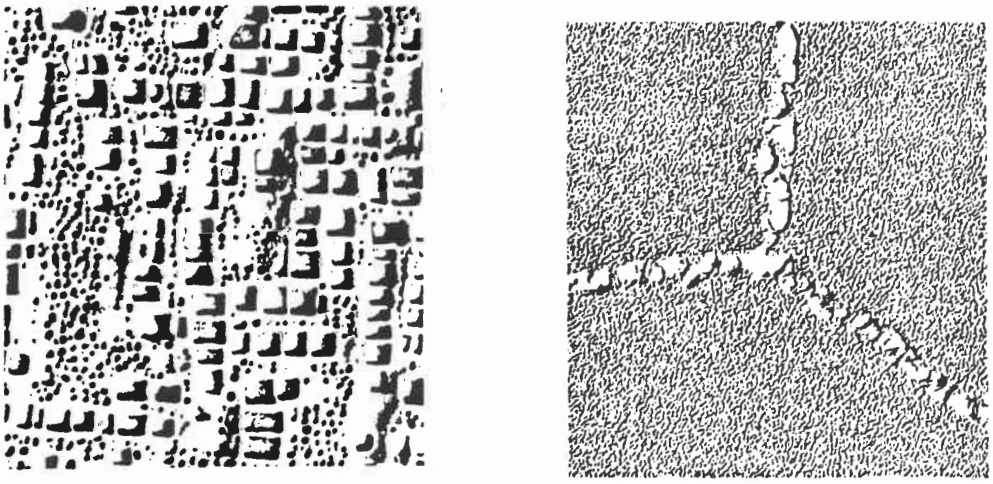

igure 1.2 Basic constituents in nickel base superalloys; (a) cuboidal γ' particles; (b) ıe MC carbides formed along grain boundaries.

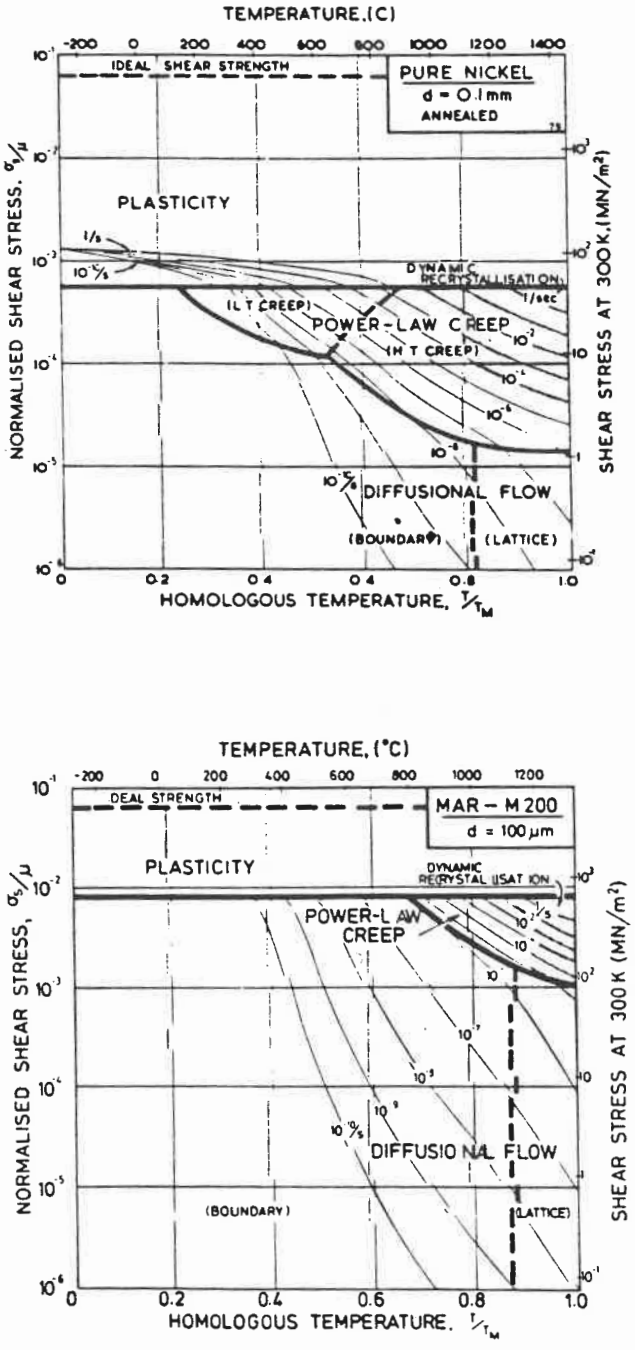

Figure 1.3 Deformation maps for pure nickel and MAR-M200 alloy of the same grain size (d= 100μm).

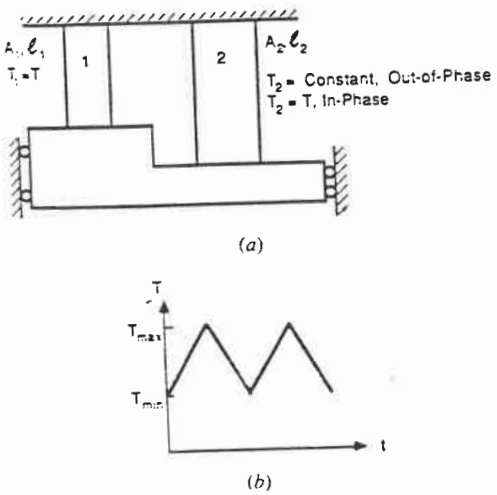

Figure 1.4 The scheme of the total strain controlled two-bar TMF system.

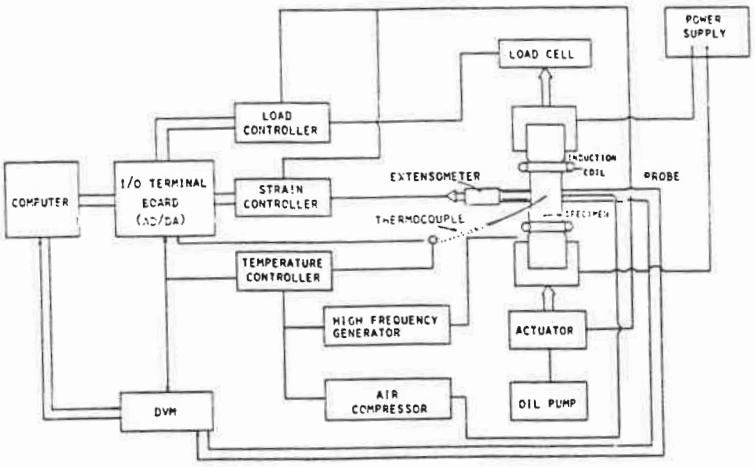

Figure 1.5 The scheme of computerized data-tracking TMF system.

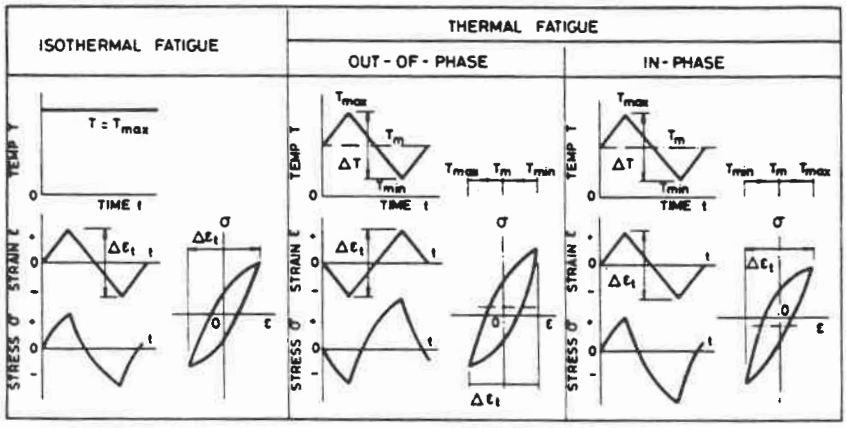

Figure 1.6 The base-line TMF cycles (T_m - the mechanical strain).

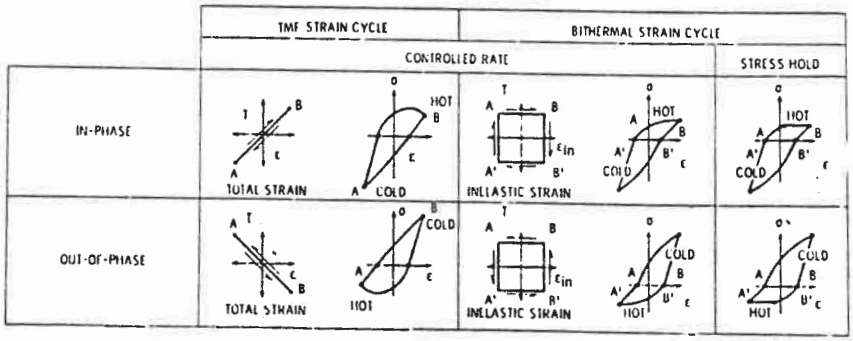

Figure 1.7 The relationship between bithermal strain cycle and TMF cycling.

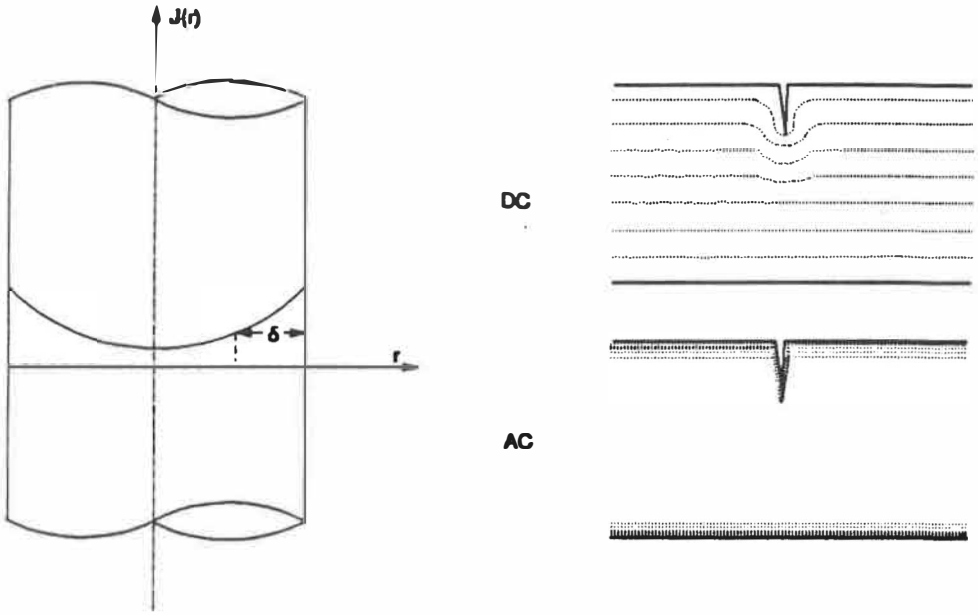

gure 1.8 A schematic illustration of the principle of high frequency ACPD crack easurement technique.

CHAPTER 2

EXPERIMENTAL PROCEDURES

2.1 INTRODUCTION

The testing materials and specimen used in the LCF and TMF tests are described in this chapter. The materials' microstructural features and the specimen machining procedures are addressed. This information are of great importance for the analyses presented in the later chapters.

To develop a fully computerized thermal mechanical fatigue testing rig is one of the important tasks of the research project. In the following sections, an overview of the TMF testing rig is also presented, which includes the system logic interface design, field wiring and calibration, induction heating and convection cooling control, specimen temperature measurement, and test control and data acquisition software design ideology.

Another important feature of the project is the successful application of ACPD technique in crack growth monitoring. Detailed procedures of this technique are described in this chapter. Special attention is placed on the probe set-up for the SEN specimen under the induction heating environment. The sensitivity and reliability of this technique are demonstrated by presenting some typical ACPD measurement results from LCF and TMF tests.

Finally, the test data reduction procedures are summarized. These include final crack length measurement, da/dN data calculation, post-testing data processing software and test data retrieval techniques.

2.2 TESTING MATERIALS AND SPECIMENS

2.2.1 The SEN specimen

As mentioned in the earlier report[136], two titanium alloys were chosen for the LCF and TMF testing. They include Ti-6Al-4V (CPW41) and Ti-6Al-2Sn-4Zr-6Mo (CPW459) forgings. The specimens were fabricated directly from P&WC engine compressor disc forgings. Figure 2.1 shows the locations of specimen blanks (16.5x16.5x82 mm) that were extracted by the EDM machining along the circumferential directions of the disc forging.

Single edge notched (SEN) specimens were used to study the LCF crack initiation at the root of a notch. As shown in Figure 2.2, the square-sectioned specimen (W=10.67 mm and B=5.33 mm) is provided with a simi-circular notch. The radius of the notch is ρ= 0.042" (1.06 mm), which gives ρ/W = 0.1.

For the TMFCG tests, similar SEN specimens were used. However the specimens were pre-cracked using EDM. The diameter of the EDM wire used was

0.015" (0.38 mm) and the notch depth is around 0.020" (0.5 mm). Before each test, the specimen was cycled to produced a sharp factigue crack tip.

All the specimens were machined with surface finishing 32AA (by conventional milling), which is the standard surface finish (spec. CPW32) being used in production lines for compressor discs. No subsequent heat treatment was carried out to erase residual stresses generated during machining. The mechanical properties and microstructural conditions of the specimens matched well those of real discs (of the same material). The surface finish of the circular notch was kept between 15-32 AA.

Before testing, all the specimens were cleaned using the following procedures:

1. Soak in hot PS101[1] solution for 2 minutes, rinse;
2. Immerse in PS222[1] solution for 30 seconds; and
3. Allow to air dry. but with no air blast.

During preparation and testing, direct finger touching to the specimen surface was strictly avoided. This was to prevent the possible surface contamination (by oxygen, nitrogen and chlorides) which may lead to multiple surface cracking, hence reduction in fatigue-crack initiation life.

---

[1] P&WC internal number for material processing solutions

2.2.2 Ti64 forging

Several specimens were sectioned to check the microstructures. Figure 2.3 shows the microstructure of the Ti64 forging. This is $\alpha+\beta$ forged and solution treated alloy. Here the primary equiaxed α grains (light) with average size about 32 μm are in transformed beta matrix containing fine acicular α-phase (dark). The volume fraction of the primary equiaxed α-phase is about 50 %. This type of microstructure in Ti64 forgings has long been equated with maximum tensile ductility and strength. The cyclic behavior of the alloy at 400°C has been tested and modeled as described in Appendix 2.

Compositional analyses were performed using a JEOL 840 SEM with LINK spectrum analyzer. The chemical compositions of the β-stabilizer V was found relatively higher in the $\alpha+\beta$ matrix than that in the equiaxed α-phase particles.

2.2.3 Ti6246 forging

The microstructure of Ti6246 specimens is shown in Figure 2.4. The alloy was β forged and solution treated in the β region (i.e. above the β transus). A predominant coarse microstructure of acicular α-phase of basketweave like platelets (light) in the transformed-beta matrix (dark), and relative coarse grains can be observed. This near-β $\alpha+\beta$ titanium alloy has a typical β-forged solution treated microstructure, which is known to give higher fracture toughness and good elevated-temperature creep resistance. The average α lath length shown in this figure is

about 60 μm and width 2 μm. The volume fraction of the acicular α-phase is about 60-70 %. The cyclic behavior of the alloy at 480°C has been tested and modeled as described in Appendix 2.

The X-ray energy dispersive chemical micro analyses on the microstructure by a scanning electronic microscope have shown that the chemical composition of the β-stabilizer Mo was relatively higher in the transformed β-matrix than that in the acicular α-phase needles. These relative compositions were used as references to identify the fracture morphology associated with each phase during the fractographic analysis.

2.3 THERMAL-MECHANICAL FATIGUE TESTING RIG

2.3.1 An overview of the TMF system

The photographs in Figure 2.5 provide a general view of the computerized TMF system. As indicated in the schematic diagram in Figure 2.6, this TMF testing facility consists of two independent closed-loop control units. One is desiged to control the testing temperature. In this unit, the heating power is generated by a 15KW RF induction heating power supply (TOCCO), and applied to the specimen through a specially designed induction coil. An universal digital temperature controller UDC3000 is used to read the programmed temperature functions and regulate the RF power output. A thermalcouple (TC) was attached to the specimen to feed back the actual temperature reading to the temperature controller.

The other data tracking control loop is designed for mechanical loading [135]. It is a part of the INSTRON 8500 servohydraulic material testing system which consists of hydraulic power station, a machine main frame, an hydraulic actuator, an electro-hydraulic servo valve system, a load cell, an extensometer and the 8500 INSTRON digital control console. This control system has analog and GPIB (HP-IB) digital interfaces built in. It can provide analog strain and load signals to the user data aquisition instruments and read mechanical load command signals from an external function gernerator. At the same time the system can easily be controlled and programmed by the user computer system through HP-IB.

The HP3852A data acquisition/control unit consists of a main frame and several plug-in accessories including an HP44702B DVM, an HP44713A high speed multiplexer, HP44726A DAC programable function generator, an HP44713A digital switching card and an HP44715A event counter. This data acquisition and control unit is used to (1) collect/transfer multi-channel data from INSTRON 8500 tower and UDC3000 temperature controller to the HP9000 Series 300 workstation, (2) generate two synchronous temperature and mechanical load/strain signals in the two closed loop control units, and (3) control the testing procedures. The central controller (HP9000 series 300 system) is equiped with two 1.4 MB floppy disc driver and one 150MB (28 ms) hard disc and a graphic monitor (16" with 6 plane) used to plot and display the testing data. This computer system is used to program the testing software and control the whole testing processes.

Figure 2.7 shows an on-going high temperature (480°C) LCF test using the Ti6246 SEN specimen. In order to assure good alignment of the loading train, the lower part of the specimen grip is connected to an in-house designed Wood's metal pot. After the specimen is installed, the pot is heated by a resistance heating jacket until the Wood's metal is melted. Then the possible bending moment on specimen during gripping can be eliminated.

During the fatigue test, all the major variables can be monitored in real time on the HP workstations terminal. As shown in Figure 2.8, the data display screen was designed with two panels. The first one displays testing variables such as stress, strain, and stroke as functions of time, and strain vs. stress curves. The "stroke" here refers to load actuator position. it is normally it is used to check back-lash as load pass zero. The second panel is used to plot crack growth data derived from the ACPD measurement as function of the number of cycles, the change of peak stress during the strain controlled cycling, the ACPD signal vs. time, and the test temperatures vs. the mechanical strain. Using "On-Key" event branching programming techniques, the testing operator can easily switching between the panels, changing test limits or stopping test during the test.

Figure 2.9 provides a close view of a TMF testing set-up for Ti64 SEN specimen. The heating coil, cooling air jets and the extensometer can be seen and understood easily. The ACPD probes on the specimen were used to measure the ACPD signals. They will be explained in the later section. As shown in Figure 2.10, the TMF testing paramters were also monitored at the terminal. Here the lively plotted mechnanical strain is calculated from the measured total strain substracting

the thermal strain recorded during thermal cycling at zero stress. The in-phase relationship between mechanical strain with the temperature is clearly displayed.

2.3.2 Temperature cycling for TMF tesing

Accurate temperature control with respect to temperature stability and reproducibility (which depends on feedback temperature and command input) and uniform temperature profile within the gauge section of the specimen are critical factors for both TMF and isothermal testing.

Temperature measurements by thermocouples in inductive heating magnetic fields can be seriously affected by RF, radio frequency, noise and SCR, saturated core reactor, pulses (which are used to regulate the RF power output). In the present study has shown that ungrounded shielded Type-K thermocouples should be used. The shield material was Incoloy-600, and the thermocouple has an outer diameter of 0.02 in. Using fine wire thermocouples is believed to give faster response to dynamic temperature field. Combined with a low-pass filter located at DVM input connection (HP44713A wiring terminal), the RF noise can be reduced to minimum and smooth temperature control (stability, reproducibility and minimal temperature gradients) can thus be achieved.

As explained in an earlier report[137], the temperature control TC is tightly bonded to the specimen surface using a thin piece of titanium sheet spot welded onto the surface. Efforts were made to compare the readings of the thermocouple so

attached to the ones measured by a thermocouple directly spot welded on the specimen. It was found that the difference is less than 5°C. Furthermore, it was verified that the TC point-attached to the specimen (by hand) gave readings that were much lower (up to 50°C lower) than the ones measured by using thermocouple bonded to the surface with a spot-welded sheet. This indicates that a good contact between the thermocouple and the specimen is very important. On in the other hand, this also demonstrated that the TC itself will not be significantly heated by the induction heating.

Figure 2.11 illustrates the temperature cycling set-up for TMF testing with the SEN specimen. Since the total specimen length (76 mm) is controlled by the diameter of the compressor disc studied (Figure 2.1, the testing section is only 1.5" (38 mm). As a result, the cooling air system must be designed rather compact. Two circular air distributors were used and were located at both ends of the specimen. They were designed to provide similar air pressure at the four evenly spaced air jets. Each air jet has a side hole facing the specimen to increase the cooling rates at the specimen ends where the mass is larger. The cooling air manifold was controlled by the alarm switches of the temperature controller. The compressed air can be turned on or off by digitally adjustable temperature set points corresponding to the input temperature wave function. Hence thermal cycling at different rates can be closely simulated.

The typical dynamic temperature control results for Ti64 are schematically shown in Figure 2.12. With 100 sec. period temperature cycles used in the TMF program, the maximum deviation (between command and feed back) were 18°C

near the low temperature peak. Still better results can be achieved when higher T_{min} cycling is used. However this would decrease the desired temperature cycling range. The lower curve of this plot is the thermal strain of the specimen. It was being recorded during thermal cycling at zero load. This data was used to form the total strain waveform corresponding to applied testing mechanical strain. The thermal strain data were updated during selected intervals to take into account the possible shifting due to creep.

During the tuning period of thermal cycling, the specimen was under zero stress control mode. The temperature was plotted as a function of thermal strain, as shown in Figure 2.13. This plot indicates the uniformity of the temperature profile within the gauge section. In the ideal case (which normally can only be achieved with very slow heating and cooling rates), the curve will repeat itself and no hysterisis loop can be observed. Using this information, the testing operator can finetune the control parameters (P.I.D. and cooling set points) and determine if it is time to start applying the mechanical cycling.

Three types of TMF cycling were used in the TMF test plan. As shown in Figure 2.14, the relationship between temperature and strain cycling were controlled to be in-phase (IP), out-of-phase (OP) and counter clockwise diamond (CCD). Figure 2.15 shows the total strain and its components as function of time in the CCD TMF condition. The mechanical strains are directly plotted with temperature change in Figure 2.15b.

2.4 ACPD FATIGUE CRACK GROWTH MONITORING SYSTEM

The fatigue crack initiation and growth processes are monitored by CGM5[2], a newly developed ACPD measurement system[129,134]. Inside the system, there is a current source that generates AC current of constant amplitude passing through the specimen. The frequency of the current is selectable from 0.3 to 100 KHz. Potential signals from the two sets of probes welded on the specimen are amplified by the CGM pre-amplifier and then phase shifted through the PSD (phase shift detection) circuits. Final filtered and amplified ACPD signals (in mv scale) can then be sent to DVM from the analog output of the system.

2.4.1 ACPD probe set-up

For the titanium alloys, working currents of 500 mA to 1200 mA, and a frequency of 30 KHz, were used. The system amplification gain was normally chosen to be 60 db or 70 db. Pure titanium wires of 0.01" (0.25mm) in diameter were used for the probes to measure the ACPD signals, and the same kind of wires (0.02" (0.5mm) in diameter) were used to lead the AC current. Figure 2.16 shows how those wires were spot welded on the specimen. To take into account possible current and temperature drift, and the mechanical strain contribution, one of the ACPD channels is used as a reference while the other channel measures the ACPD

---

[2]The modified CGM5 crack growth monitor is a trade mark of MATELECT Ltd, 33 Bedford Gardens, London, W8-7EF, UK.

signal produced by the working probes (where the cracking has the greatest chance to occur, e.g. at the root of the notch). The reference signal is therefore used to compensate the signal measured by the working probes. The probes and current lead in the high temperature test zone are protected and spaced using ceramic tubes. These spacers are also helpful in keeping the configurations of the wires.

It was found that the positions of the spot welds, the weld quality as well as the shielding and insulation procedures to protect the probe wires from the inductive heating magnetic field, are critical to the sensitivity of the system. To maintain the reproducibility of the spot welding for each specimen, as shown in Figure 2.17, a new type of UNITEK weld head was used. It can keep constant welding pressure for selected power levels. A specially designed specimen holder was also used, which can facilitate the welding procedure and the positioning and handling of specimens with delicate probes.

2.4.2 ACPD signal analysis

As a step to check the probe connections and CGM5 system linearity, several ACPD readings are taken for step increases of AC current (of selected frequency) after the specimen has been mounted. Typical results are shown in Figure 2.18. Since the initial ACPD readings are functions of current, frequency and detailed probe configurations etc., the output offsets (as indicated in the plot) are normally used so that the initial PD reading is close to zero at the working current (1000 mA

in this example). This offset can also help in fully using the resolution of the DVM to detect the possible small change of ACPD during the cycling.

As explained in chapter 1, the system's sensitivity and linearity regarding to crack growth are enhanced by the skin effect due to the high frequency current. For the SEN specimens tested under cyclic strain controlled condition at room and elevated temperatures, typical ACPD response (working probe) as a function of time are displayed in Figure 2.20. It can be seen that the ACPD signals continuously changed during each load cycle, as a result of straining, crack opening/closure and complex mechanical-magnetic interactions. By plotting the ACPD change as a function of the far field stress, see Figure 2.19, an hysteresis loop behavior can be observed, which is associated with the stress-strain relationship at the notch and crack closure effects. Furthermore, if the ACPD response of two consecutive cycles are plotted, then a small shift of ACPD signal near the maximum load can be found. This is the result of crack growth within one cycle.

As the cracks grow with increasing number of cycles, the potential gradually shifts upward as shown in Figure 2.21. Figure 2.22 shows the ACPD measurement result for Ti64 tested at 750°F. Here, the peak values of the ACPD loops were plotted as a function of the number of cycles. From this plot, a clear picture of the crack initiation and growth processes can be obtained. As can be seen, the reference ACPD signal is constant which indicates that the testing temperature and far field strain were stable throughout the test. The gradual change of the working ACPD signal is due to crack initiation and growth at the root of the notch. At the end of this particular test, the crack length was measured to be 1.07mm (0.042"). Thus the

ACPD crack growth monitoring resolution is about 18 μm per mv ACPD change (at 60dB). The peak stresses remain almost unchanged during the test. This shows that any load drop criterion for crack initiation is very inaccurate and could produce highly nonconservative estimation of the initiation life for these alloys. Furthermore, much higher crack detection resolution was achieved for tests carried-out at room temperature since there was no RF noise interference coming from the induction heating system. At room temperature, the crack growth measurement could be performed with a resolution of 2μm per mv ACPD change (at 60dB).

Figure 2.23 gives a direct example of the ACPD system in terms of the sensitivity to detect short cracks (naturally initiated) at the root of the notch. With almost 40mv change of the ACPD, multiple crack initiation (maximum depth about 0.4 mm or 1/64") can be confidently detected using a conventional digital volt meter (DVM) to digitize the output of the CGM5. By analyzing the various ACPD curves, the system was confirmed to have the capability of detecting cracks as small as 50μm (average crack depth).

For isothermal LCF testing, a linear relationship was found between the ACPD response and the physicaly measured crack length, as shown in Figure 2.24. The slope of the curve is affected by the testing temperature and by the probe positioning. For example, this figure shows that higher temperatures reduce the sensitivity (the slope) due to increased skin depth. Nevertheless, this feature of linearity is another advantage of ACPD technique over other crack detection technique (e.g. DCPD).

Since the initial readings of the ACPD signal were sensitive to factors such as probe length, probe position and spacing and connections etc., which are difficult to control. In contrast to the signal processing procedures used by Hwang and Ballinger[133], normalization of the ACPD signals was not used in the present study. The initial ACPD readings were simply set close to zero at the beginning of a test to fully utilize the resolution of the DVM. After testing, the crack growth a-N curves were linearly interpreted from the ACPD curves by measuring the final crack depth on the fracture surface.

A linear relationship between the ACPD response and the measured crack depth was also found for TMF crack growth testing, as shown in Figure 2.25. Here the sets of data were taken from two tests of Ti6246 under IP and OP TMF conditions. The distance between the two curves was due to the difference during the initial reading offsetting. It can be seen the linearity and the slope of the calibration curves are not affected by the TMF cycling. This conclusion was further supported by comparing the ACPD peak values vs. cycle curves obtained from TMF cycling and pure thermal cycling at zero load (when the thermal strain data were recorded) using a 50db gain. As shown in Figure 2.26, this comparison indicates that the ACPD peak value change is only sensitive to crack growth, although the detailed ACPD change during each cycle can be dependent on the TMF loading history. Thus using the measured ACPD peak values as a function of number of cycles shown in Figure 2.27, the a ~ N crack growth curve can be obtained.

2.5 PRELIMINARY TEST DATA REDUCTION

2.5.1 Feature crack length measurement

In order to linearly transform the ACPD curves into a vs.N curves, the total crack growth for each test must be physically measured. The crack fronts were marked using heat tint technique at the end of a test. The fracture surfaces of failed specimens were photographed in low power optical microscope (x 80). The average crack lengths were calculated from the color prints by measuring the total cracked areas devided by the thickness of the specimen. All the tested specimens were documented in a data base. The specimen crack growth profiles were recorded as shown in Figure 2.28a

2.5.2 Crack growth rate calculation

The recommended data reduction techniques by ASTM E647[138] were used to derived the da/dN data from the measured an a vs.N curve which was obtained from a ACPD vs. N curve . In this procedure, a second-order polynomial (parabola) to sets of 7 successive data points were determined by the least squares method (i.e., minimization of the square of the deviations between observed and fitted values of crack length). The rate of crack growth was obtained from the derivative of the parabola.

2.5.3 TMFCG post-testing data processing software

TMFCG is a home developed post-testing data reduction software. It is based on IBM PC and employs the working environment of LAB WINDOWS[3]. As shown in Figure 2.28b, the output panel of the program displays the crack growth a vs. N curve, the far field stress change during the strain controlled cycling, the rate of crack growth as a function of crack length (measured from specimen edge), and the final da/dN ~ ΔK curve for the test. All test results were documented in the form of Figure 2.29. This figure also shows the accuracy of the FCG testing system.

Another PC-based TMF testing loop data playback software was also developed in order to retrieve time sets of recorded cycles. This program can read and plot directly the binary data transformed from the HP system. For example, as shown in Figure 2.30 for an in-phase TMF testing, the sample stress, mechanical strain, temperature and ACPD signal during two cycles are replayed. The in-phase temperature vs. strain relationship and preliminary ACPD analysis are also displayed.

---

[3]A window based commerial lab data processing software package developed by Texas Instrument Inc.

2.6 DISCUSSION AND CONCLUSIONS

By carrying out LCF and TMF tests on the two titanium alloys, this TMF system has been shown capable of cycling the specimen with various programmed thermal-mechanical histories (isothermal and anisothermal conditions) with satisfactory temperature control accuracy. The TMF test control and data acquisition software have been confirmed to be very efficient and easy to use. A more detailed description of the system wiring and the complete source code are presented in Appendix 1 and 4.

The materials' response to different frequencies and amplitudes of AC current have been characterized for titanium specimens. The sensitivity of the ACPD system and its linearity with respect to the measurement of crack length are enhanced by the skin effect resulting from the high frequency AC current. This has been verified by the tests performed. With the present ACPD system, the crack growth as a function of the number of cycles (a-N curve) can be easily obtained for room and elevated temperatures.

The current ACPD system has achieved average crack initiation detection limit of about 50μm with a probability of detection (POD) of better than 95%. This is well below the crack initiation size specified by Engine Structural Integrity Program (ENSIP) used in component life management planning for P&WC engines[139], where a_i = 1/32" (0.8 mm). Hence the system can be used to measure the crack initiation life of specimens. In turn, the average long crack growth can be monitored by the system with an accuracy about 2 μm per mv ACPD change at RT

and 18 μm per 1 mv at high temperature. This also meets the requirements for ASTM E647 for long crack fatigue propagation testing.

Furthermore, the system was shown to be promising for studying the closure mechanisms for short and long cracks. However, further studing on the ACPD response during each load cycle need to be carried-out to allow quantification of the different effects occurring during the fatigue loading.

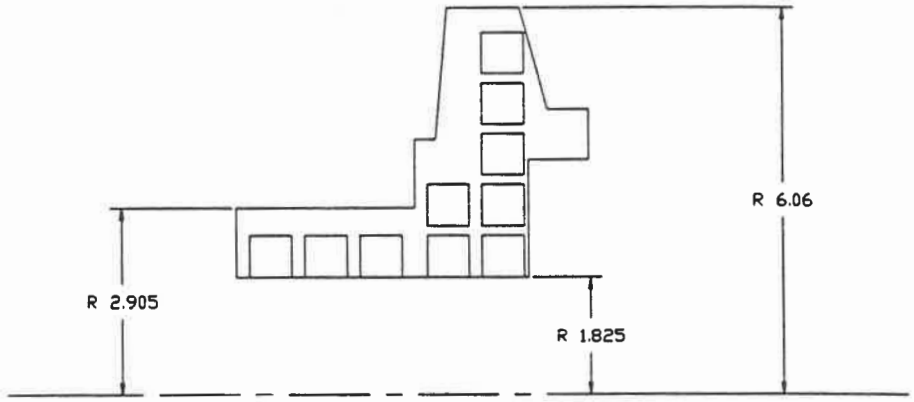

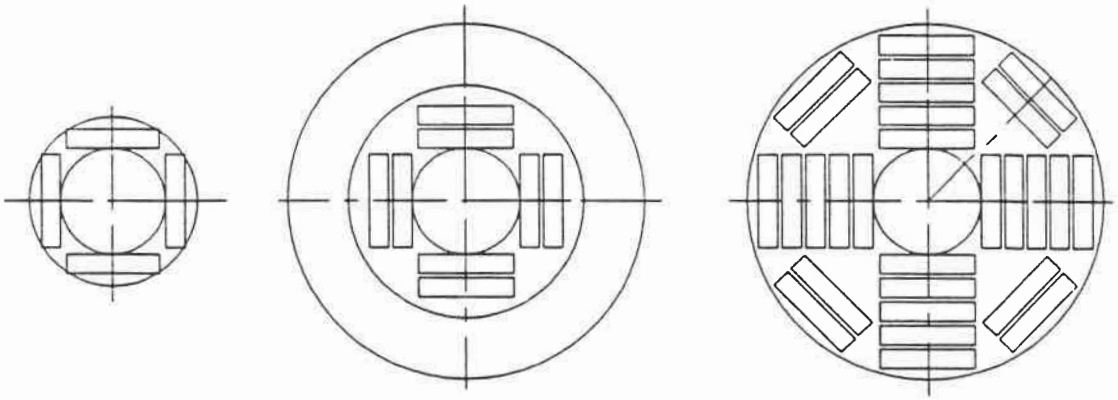

Figure 2.1 The locations of specimen blanks in the PWC engine compressor disc forgings.

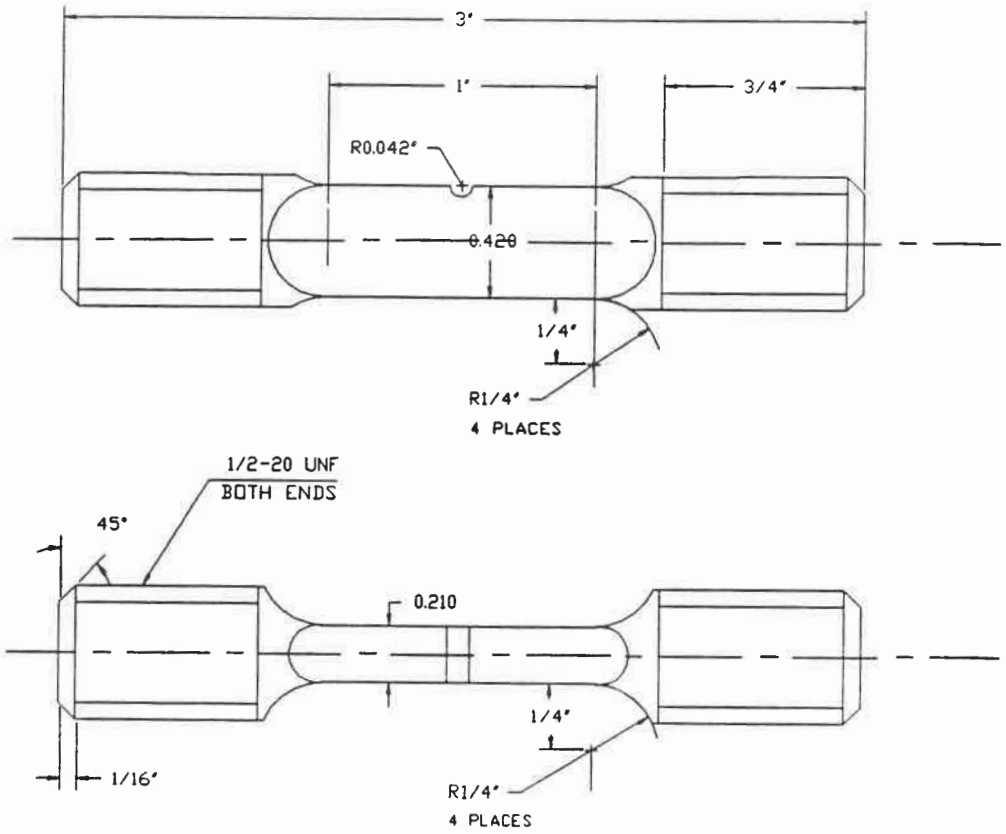

Figure 2.2 The detailed geometry of the SEN specimen used in the testing program.

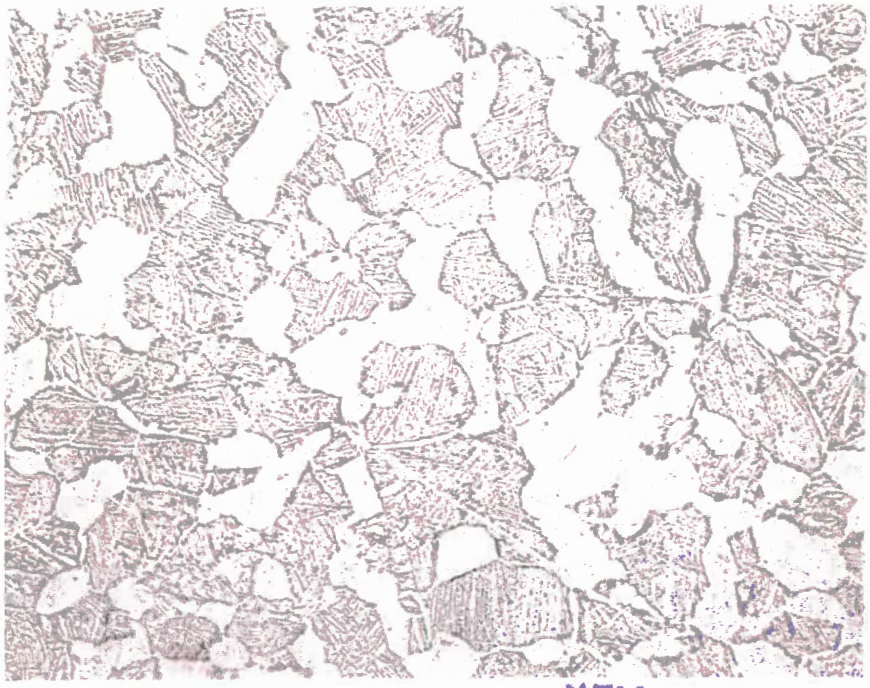

Ti-6Al-4V

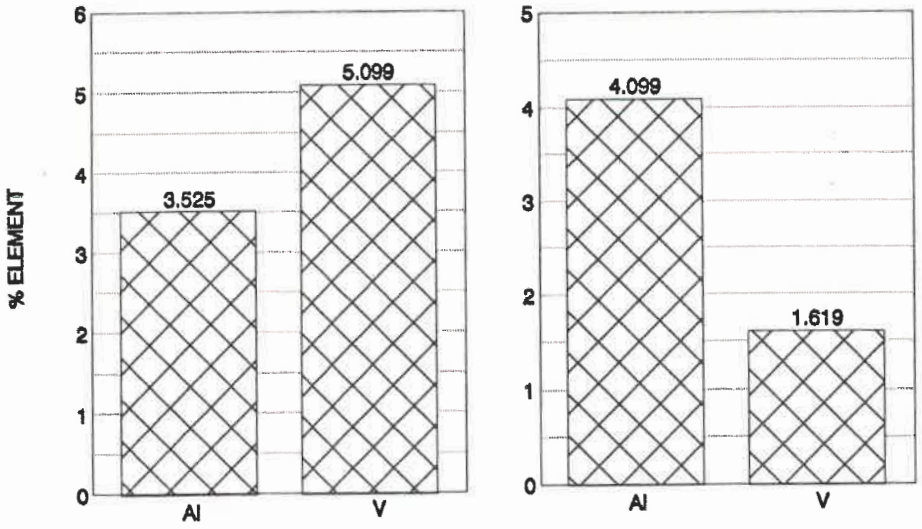

α+β matrix equiaxed α particles

Figure 2.3 The microstructure of the Ti64 forging, and the typical result of β stabilizer composition analysis.

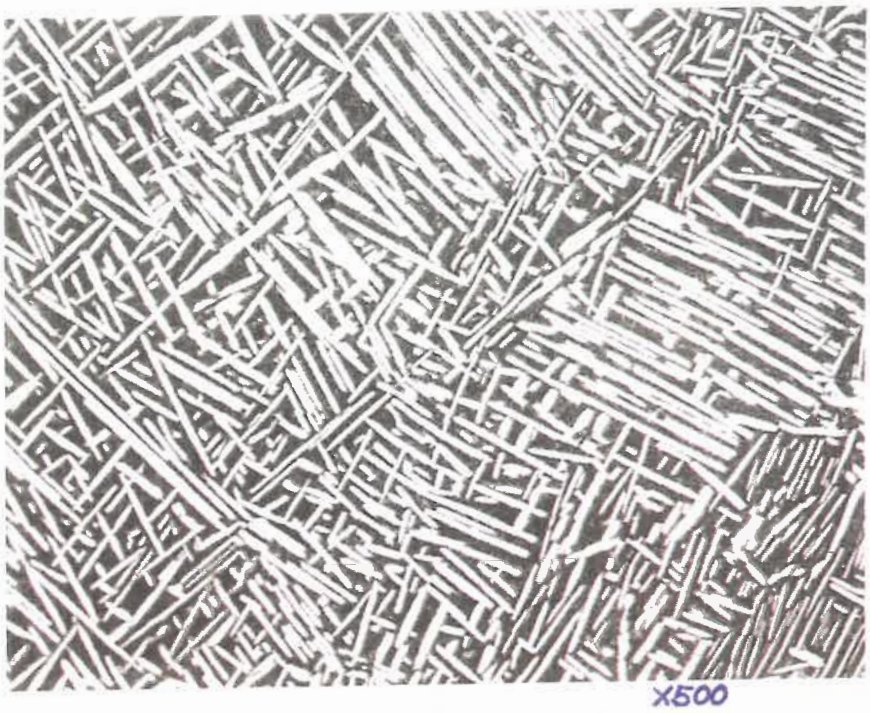

Ti-6Al-2Sn-4Zr-6Mo

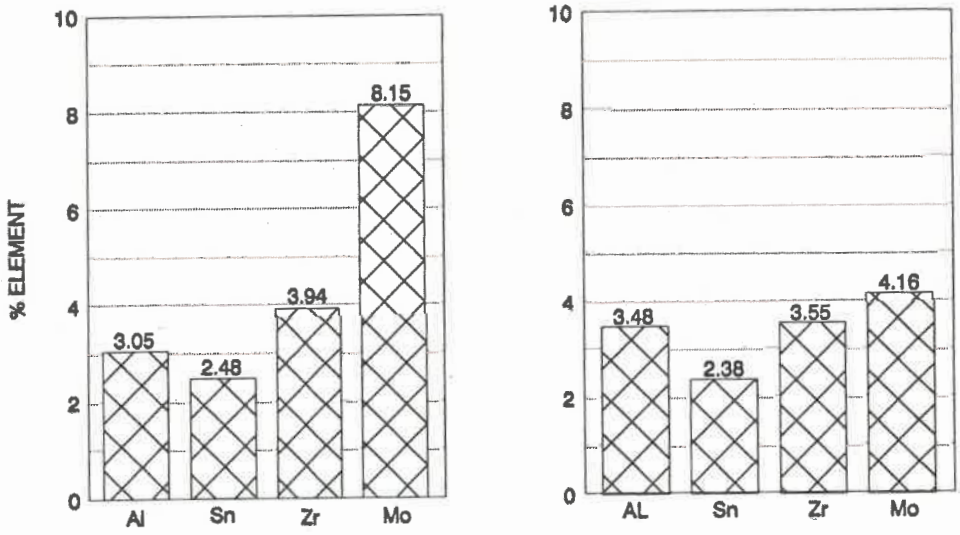

igure 2.4 The microstructure of the Ti6246 forging, and the typical result of β abilizer composition analysis.

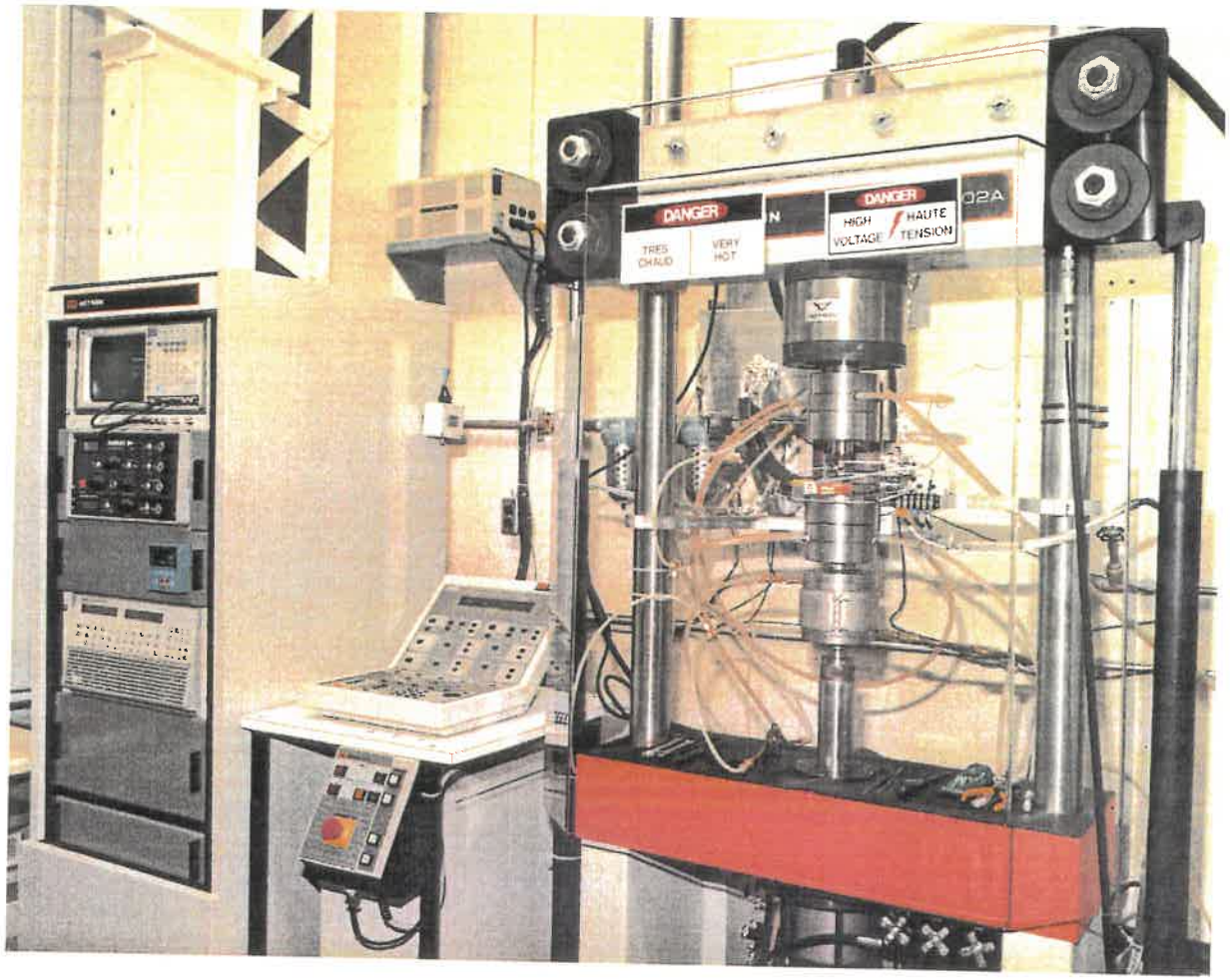

Figure 2.5 An overview of the TMF testing rig.

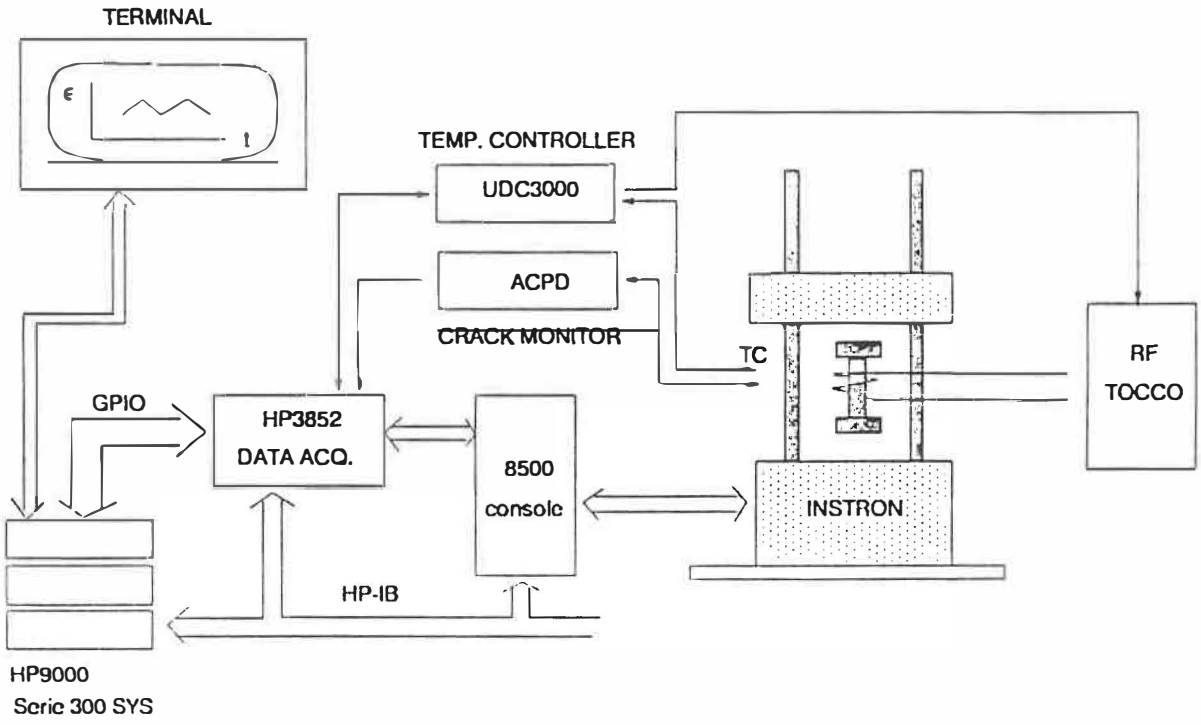

Figure 2.6 A schematic illustration of the TMF test system.

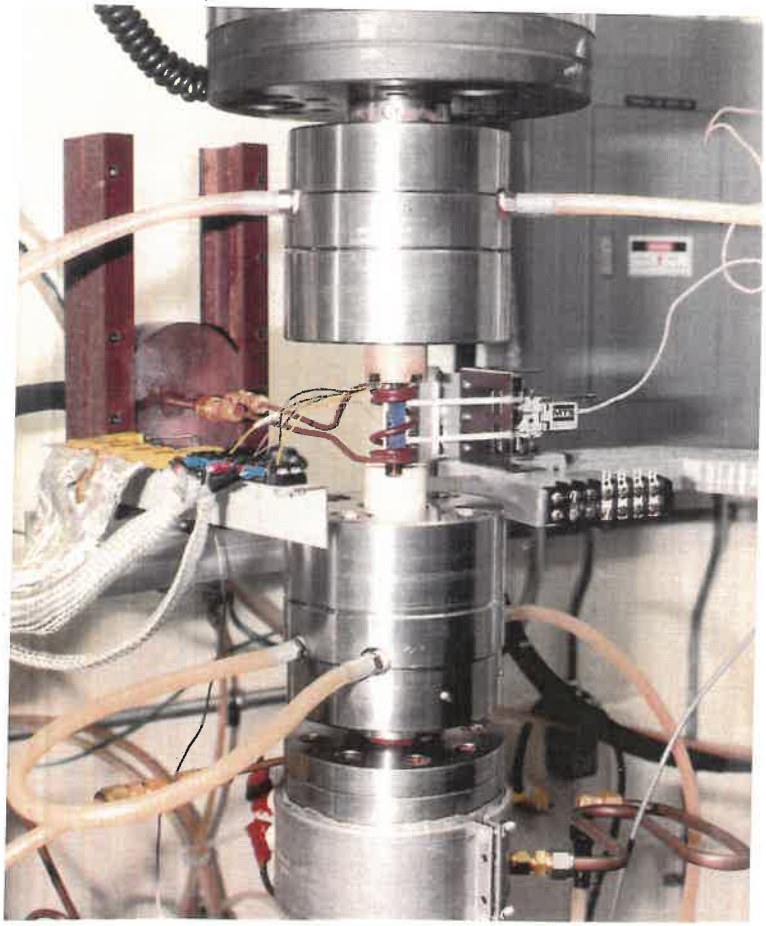

Figure 2.7 A closer view of an on-going LCF test using a SEN specimen and the ACPD technique.

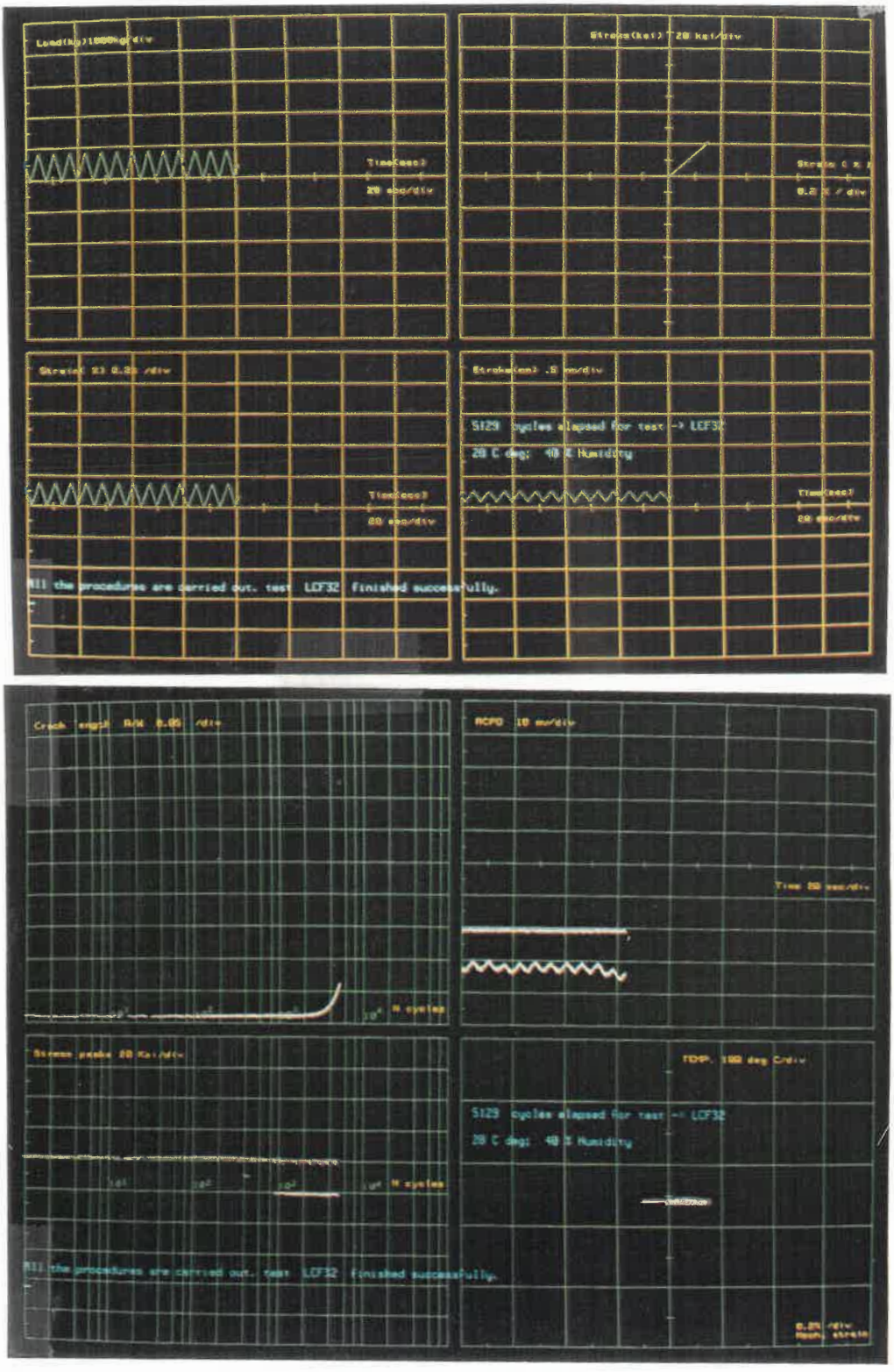

Figure 2.8 Photographs of the two-plane test parameter monitor. An isothermal LCF test of Ti64 at 400°C is illustrated.

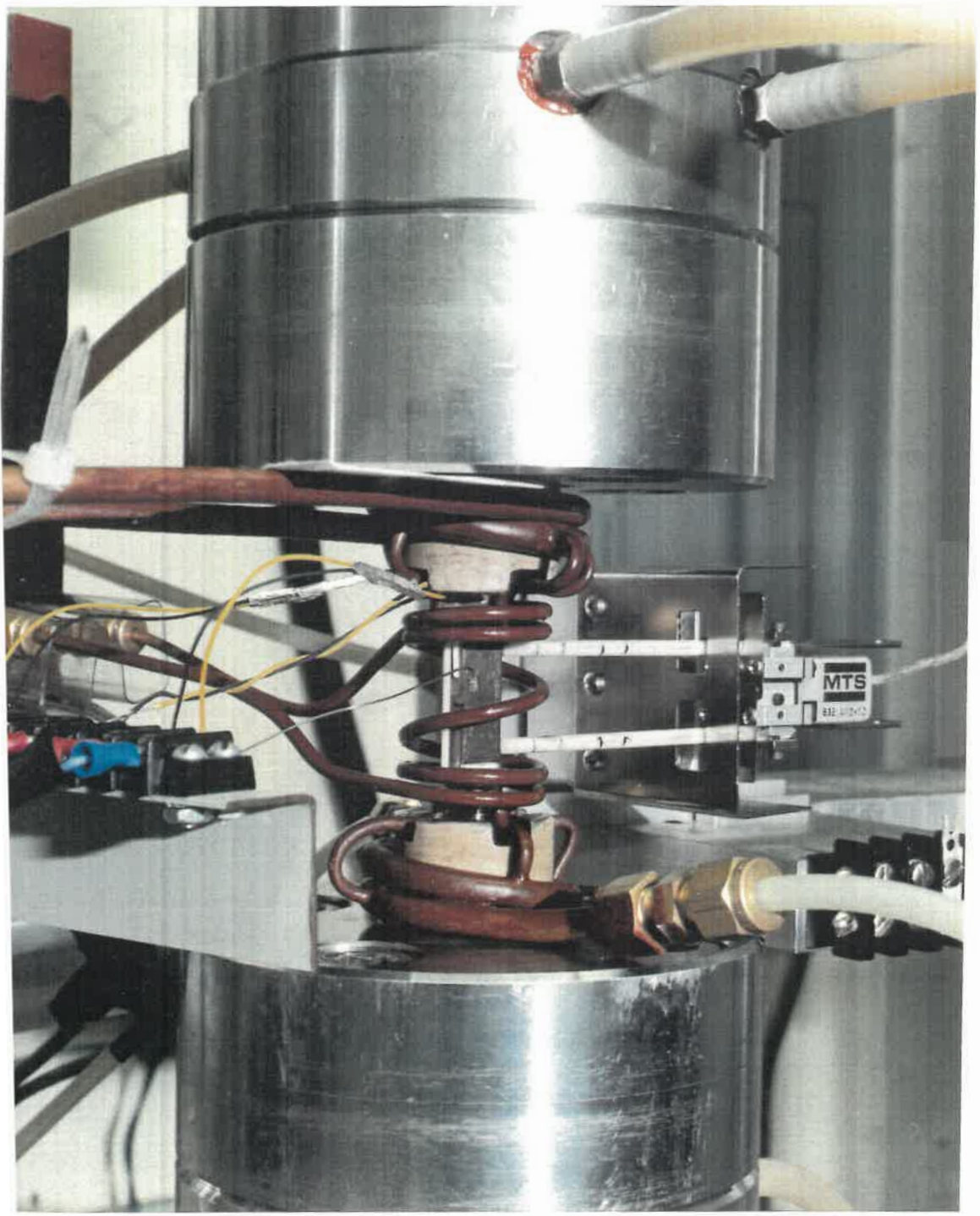

ure 2.9 A closer view of the TMF testing set-up. The SEN specimen is heated by inductive heating coil and cooled by two sets of air jets. The ACPD probes are lded on the specimen for monitoring the crack growth.

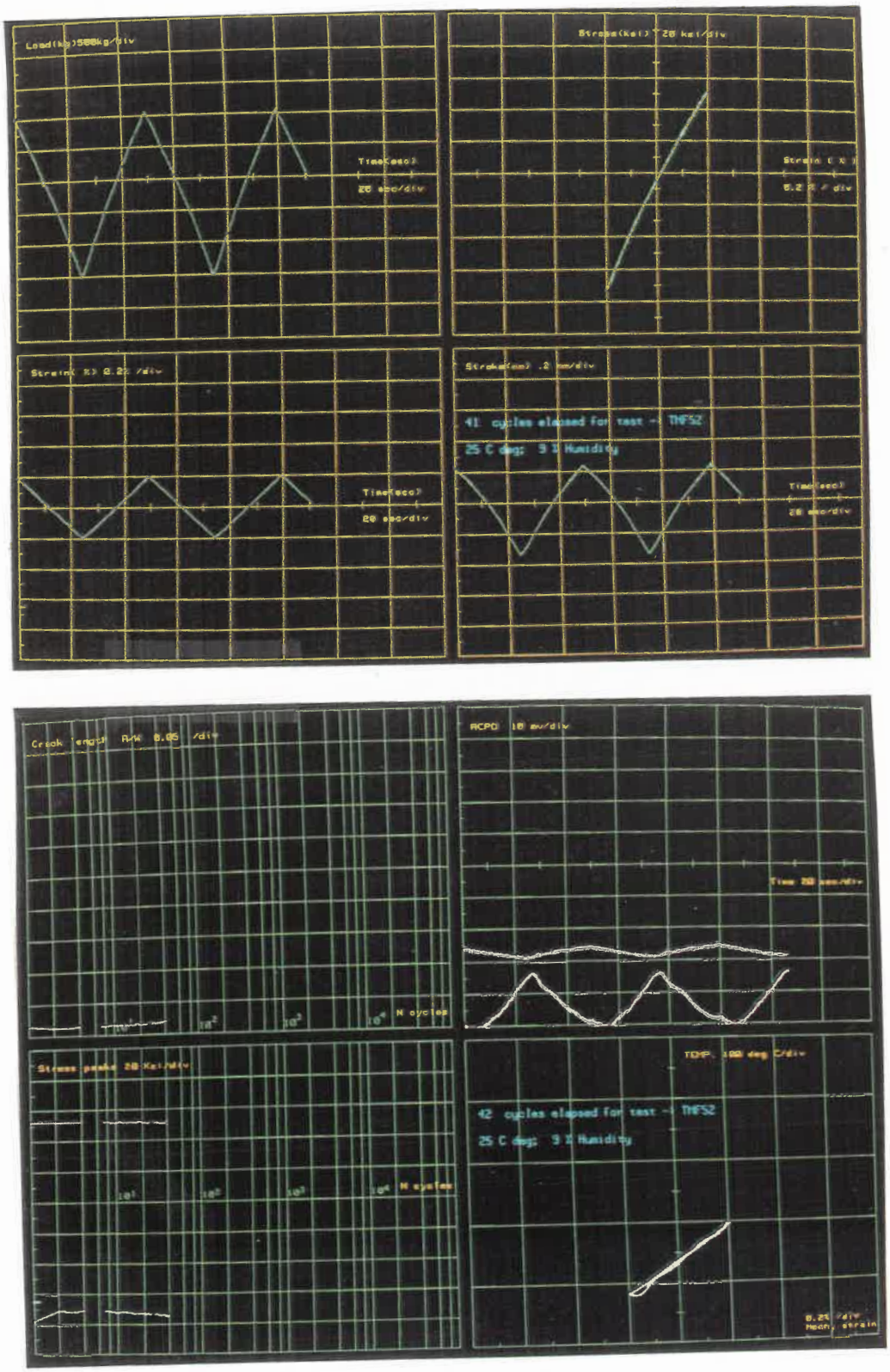

Figure 2.10 Photographs of the two-plane test parameter monitor. An on-going in-phase TMF time series are displayed.

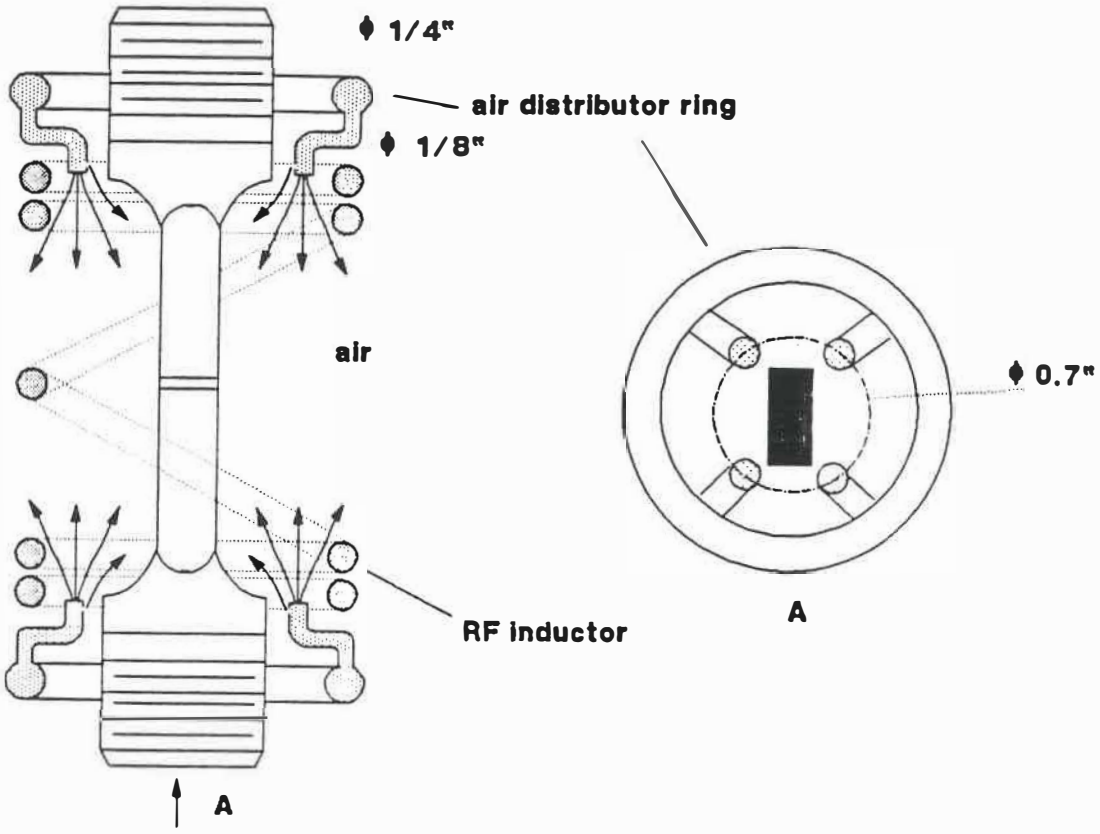

Figure 2.11 A schematic illustration of the TMF test convection cooling and inductive heating set-up.

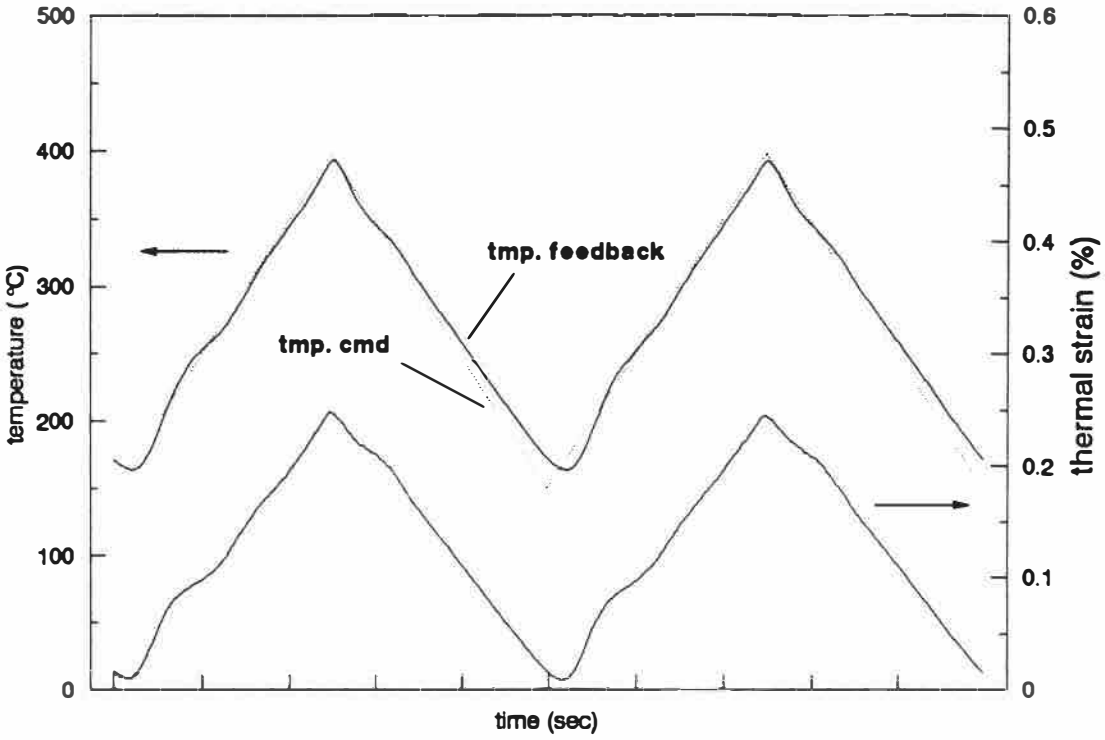

igure 2.12 Dynamic temperature control and specimen thermal expansion curves pecimen was under zero stress control).

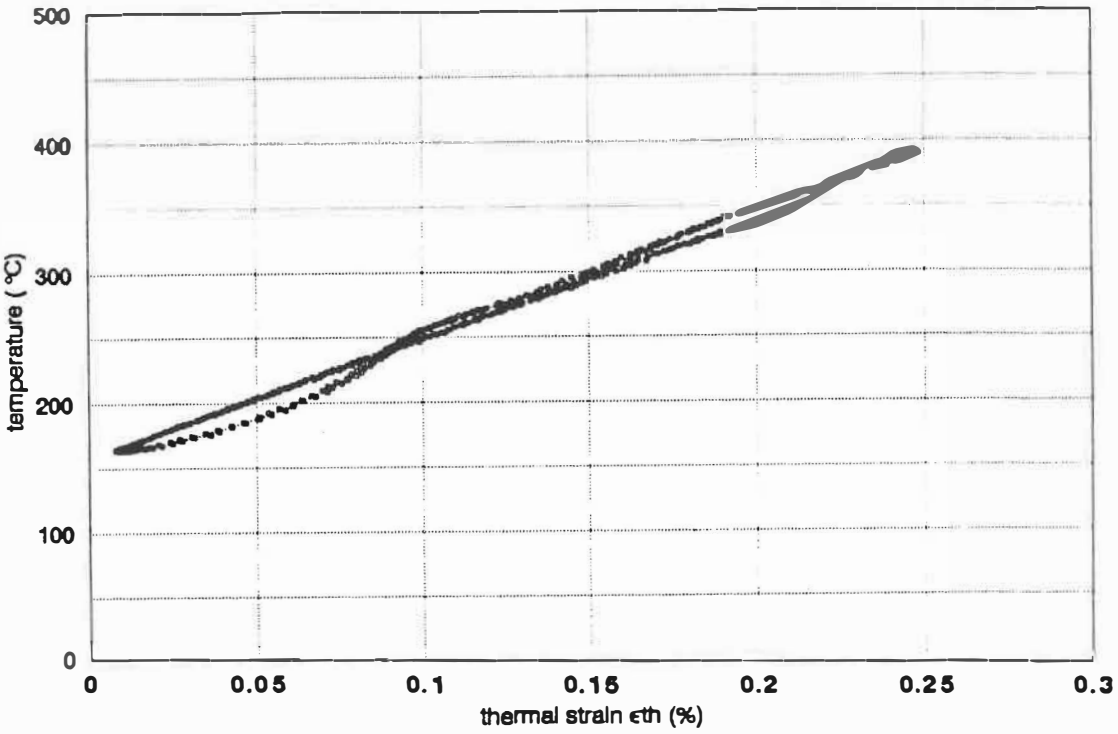

Figure 2.13 A plot of temperature as a function of thermal strain during the temperature cycling in TMF test.

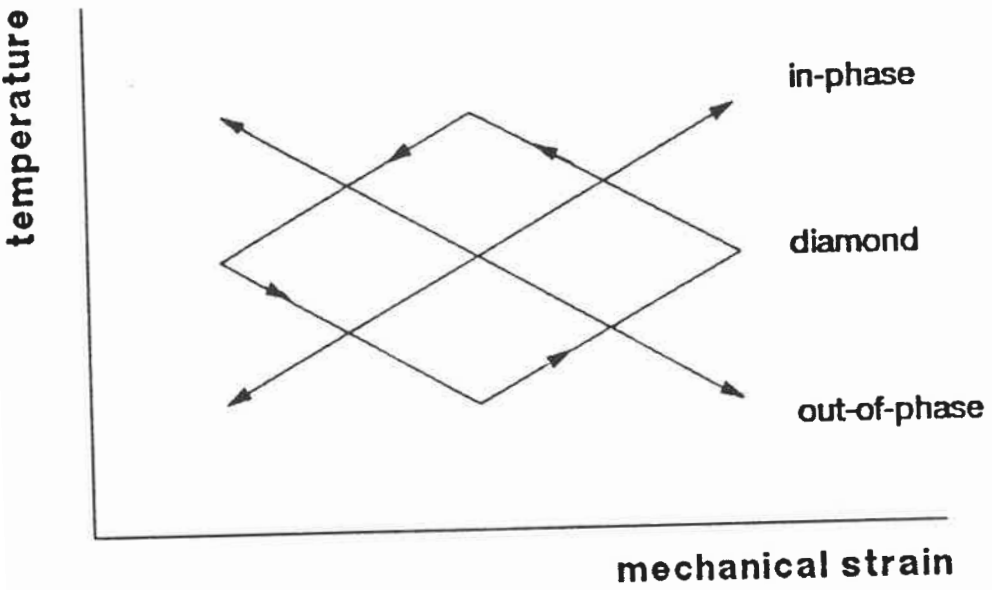

re 2.14 Three typical TMF cycles selected in the TMF test plan. The ionships between temperature and strain cycling are in-phase, out-of-phase and ıter clockwise diamond.

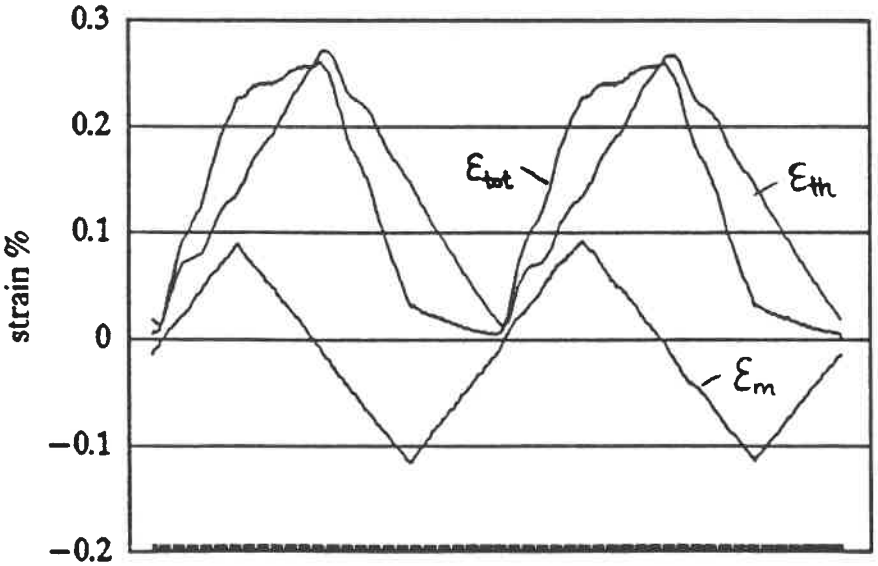

(a)

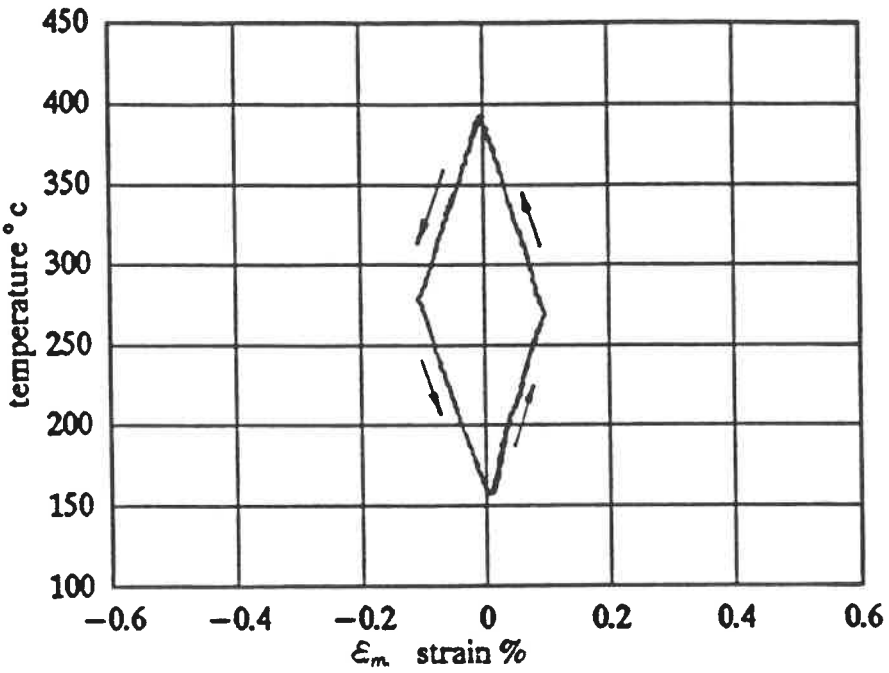

(b)

Figure 2.15 (a). The time series of strain components of a counter clockwise diamond TMF test. (b). The actually measured temperature vs. mechanical strain response.

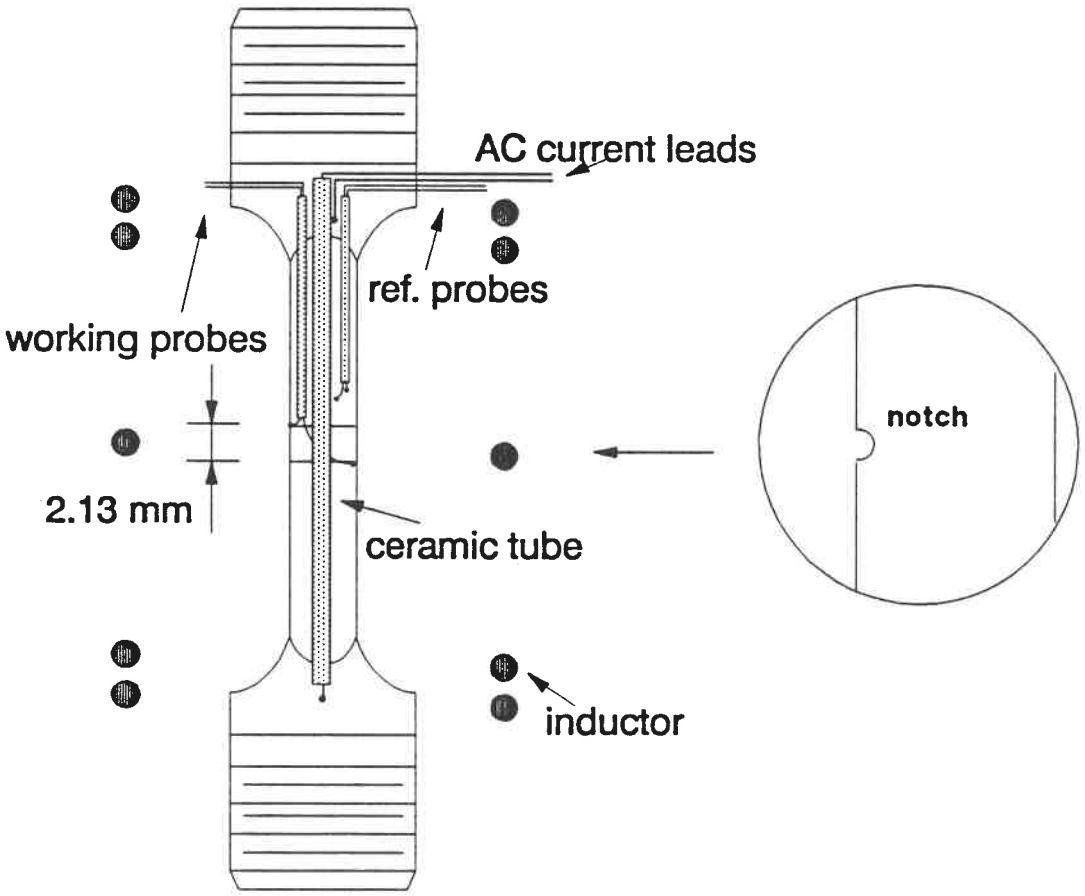

Figure 2.16 Scheme for ACPD probe set-up for notch crack initiation and propagation monitoring.

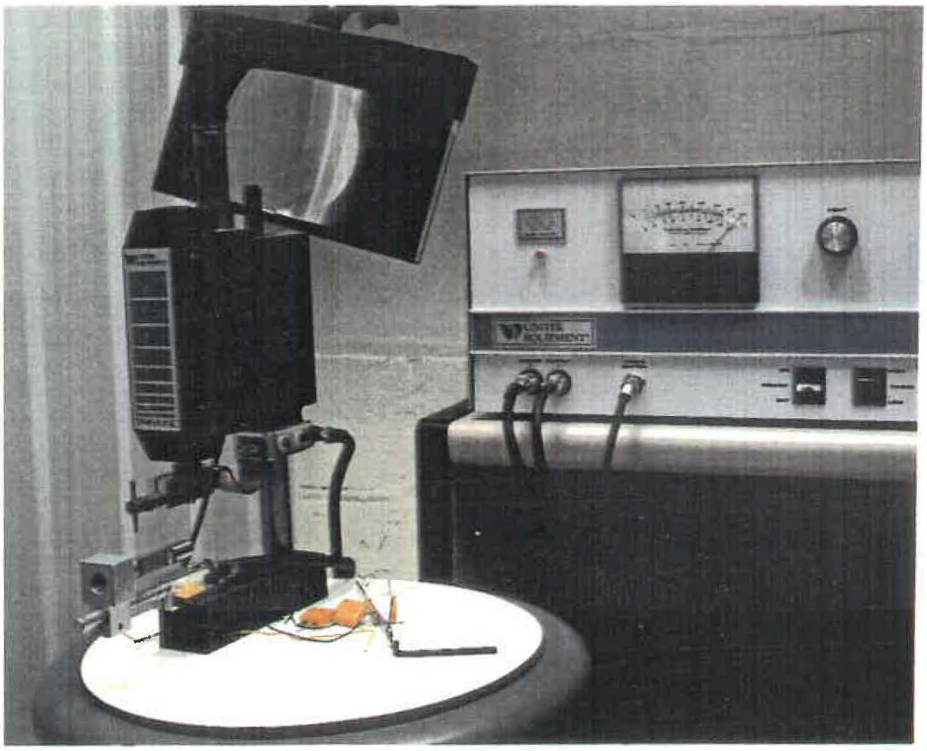

Figure 2.17 An overview of ACPD probe spot weld instruments.

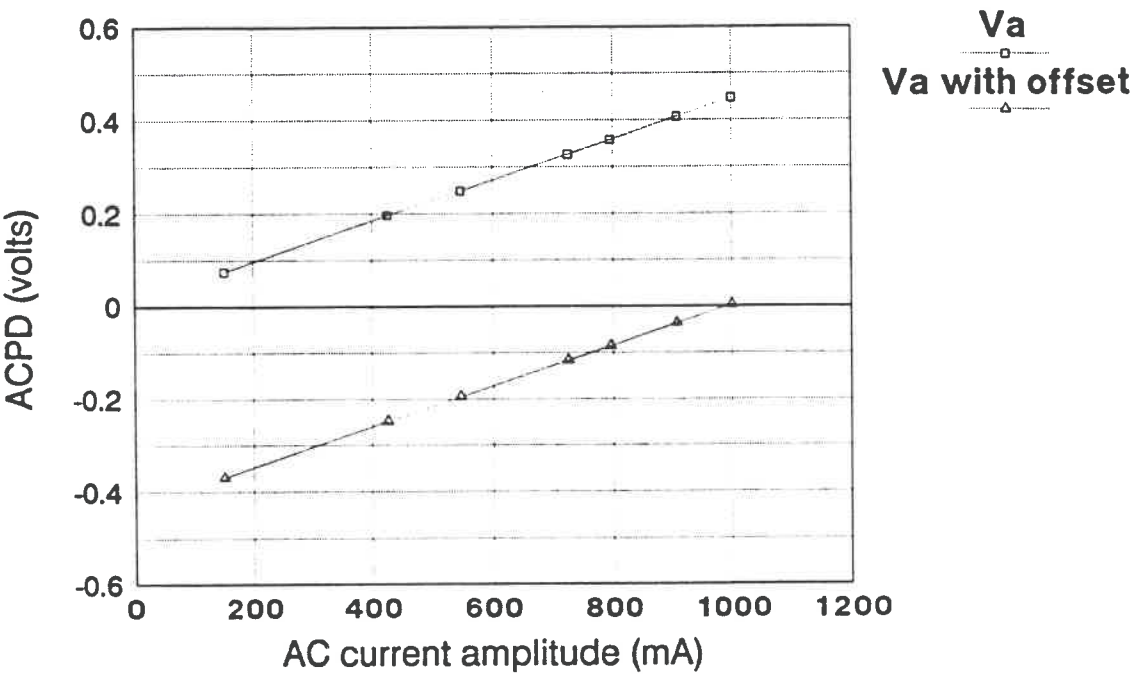

igure 2.18 A typical result of ACPD readings as a function of working current
:tting (Ti64, 30KHz AC current). Signal offset is used to obtain a desired ACPD
ıitial value at a selected working current.

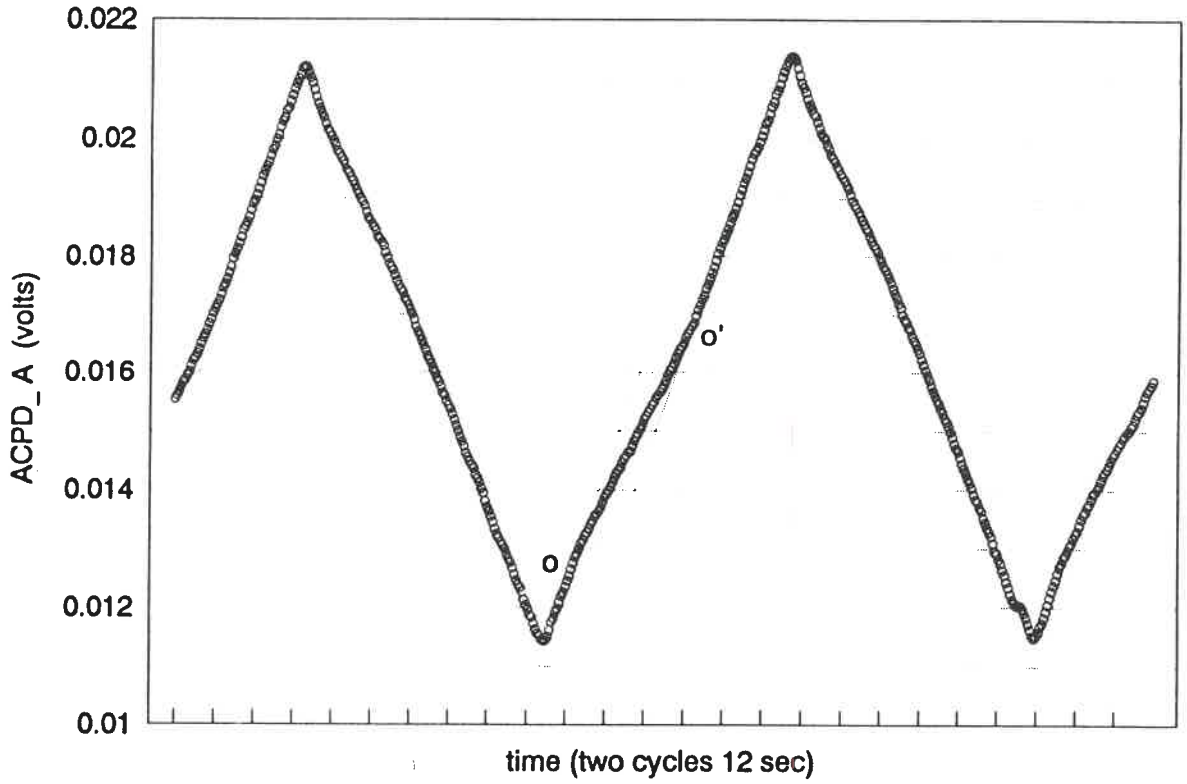

Figure 2.19 A closer view of the ACPD signal changes in two load cycles. Here points o and o' could be attributed to the crack opening processes. (Ti6246, RT).

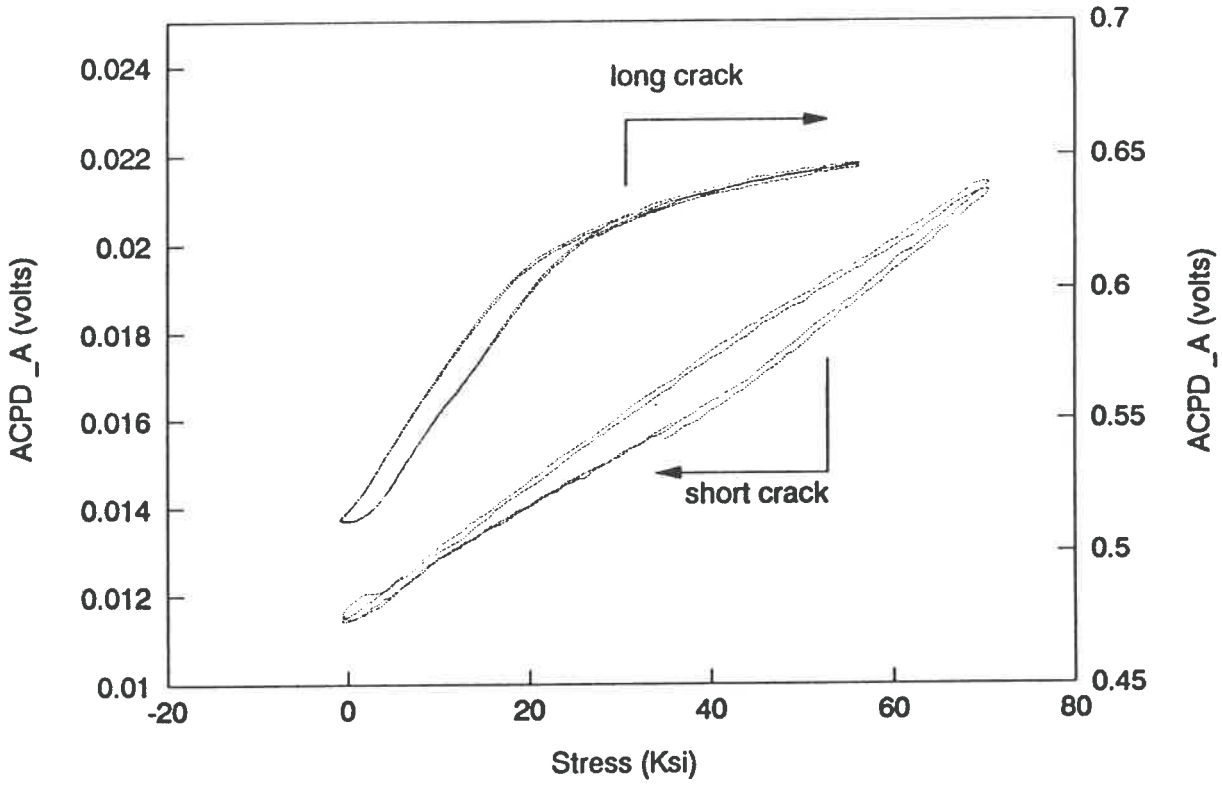

Figure 2.20 Typical ACPD signal change as plotted against the applied stress for short and long crack cases (Ti6246, RT). A small increase of the ACPD reading can been seen at the maximum stress level during each cycle as a result of crack propagation.

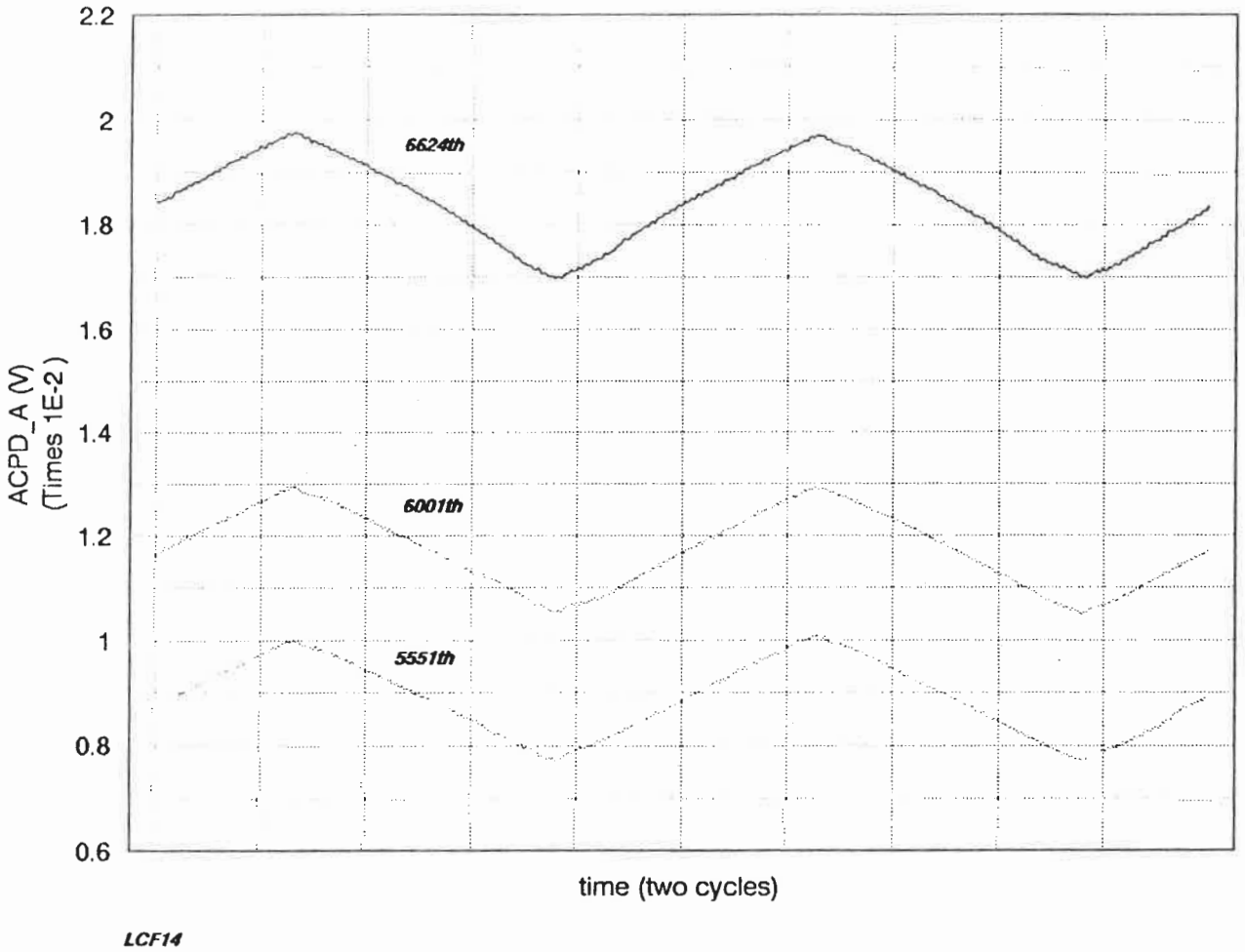

Figure 2.21 ACPD cycle loop data at three cycling stages. The ACPD curve shifted up with increasing number of cycles due to crack propagation (Ti6246, RT).

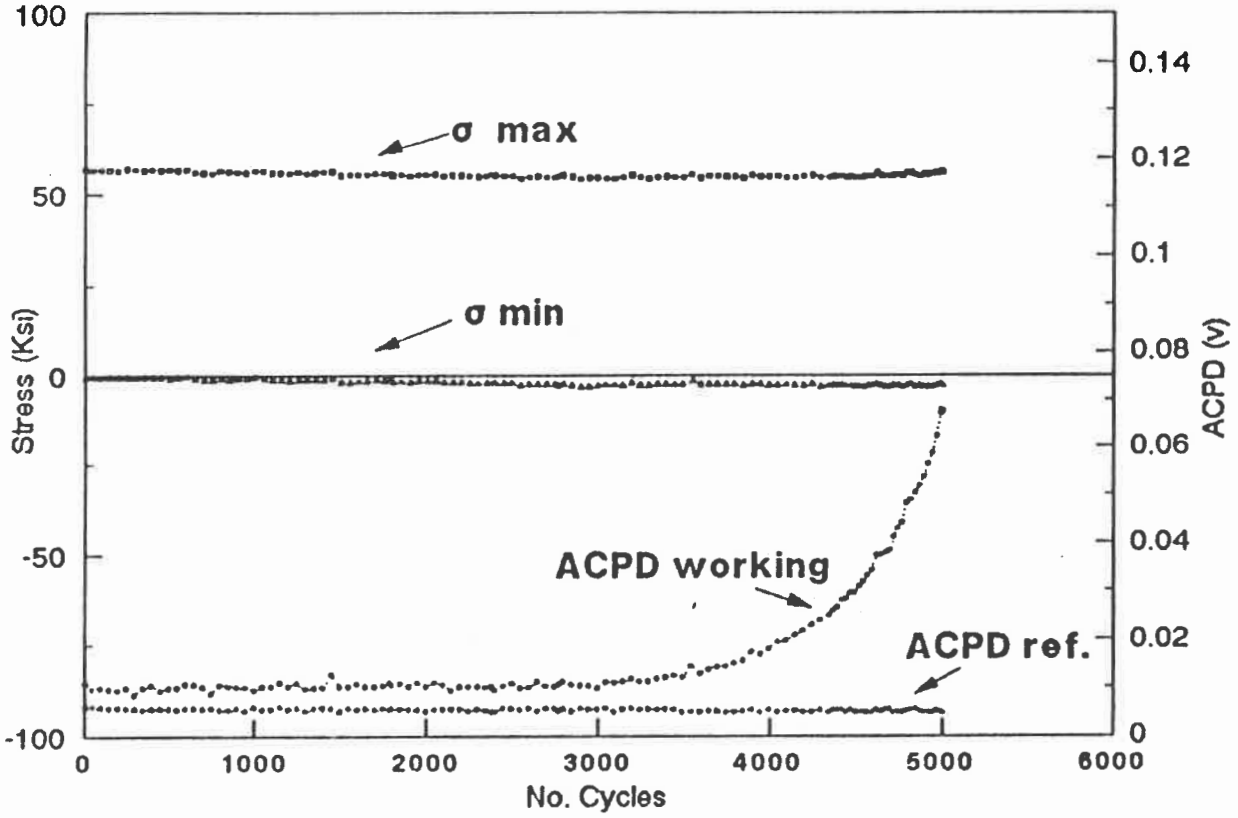

Figure 2.22 While far field stresses remain stable, the ACPD signal from working probes increases with increasing number of cycles as a result of crack initiation and growth. The relative stable ACPD signal curve was from the reference probes, which indicated stable temperature and far field strain (Ti64, 400°C).

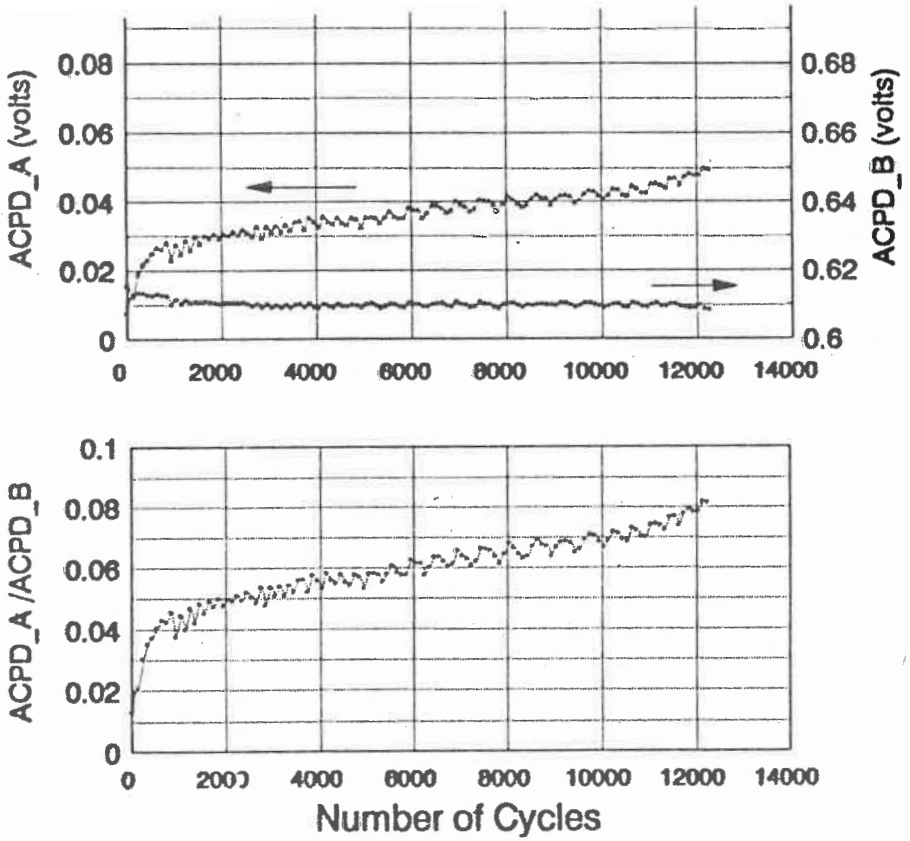

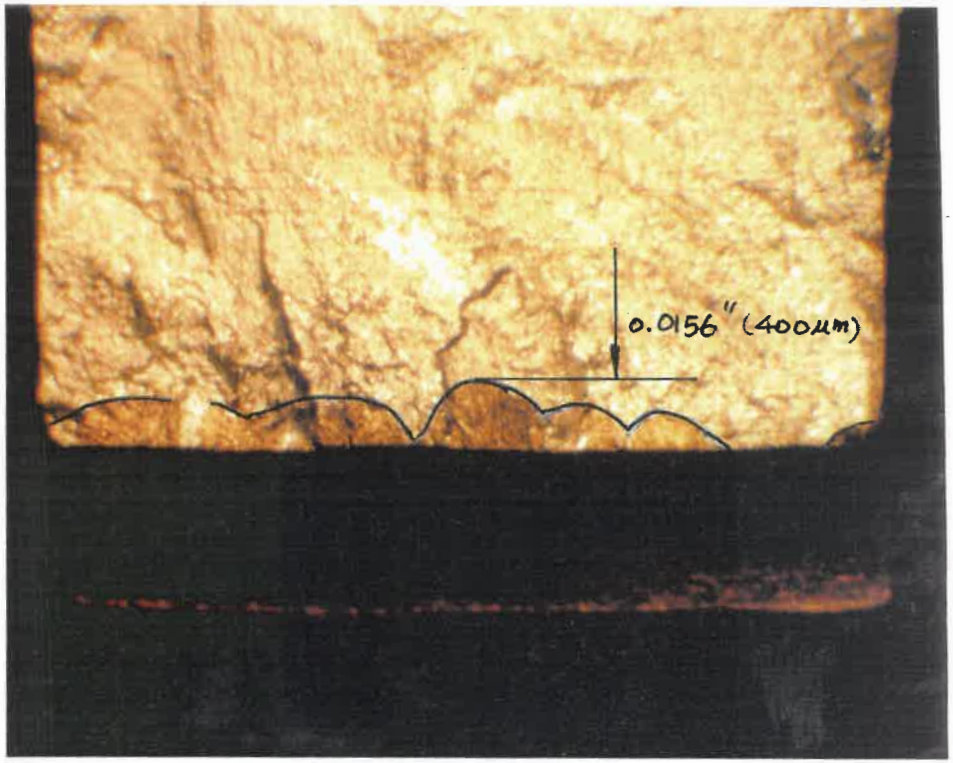

Figure 2.23 A direct comparison of ACPD response to multiple fatigue crack initiations at the root of the notch (Ti64,RT).

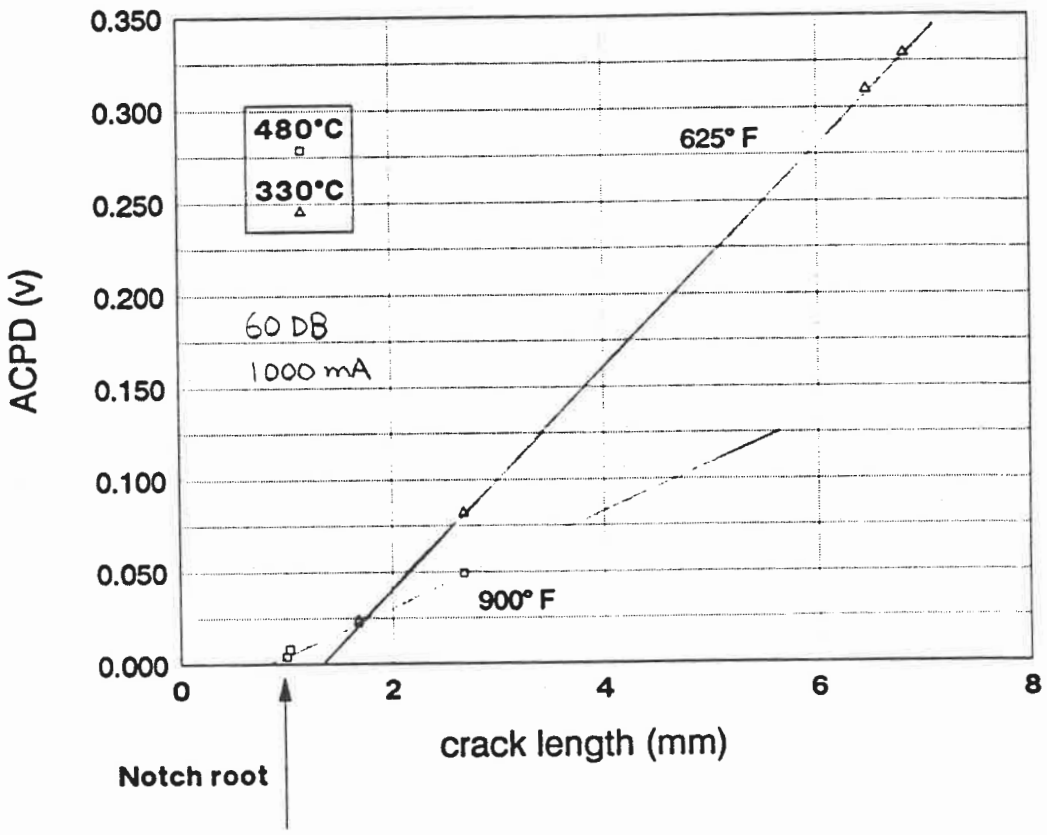

gure 2.24 Calibration curves for ACPD signal vs. crack length at two temperatures r Ti6246 LCF tests. A higher temperature yields a lower sensitivity of the system lope of the curves) due to the decrease in the magnetic permeability.

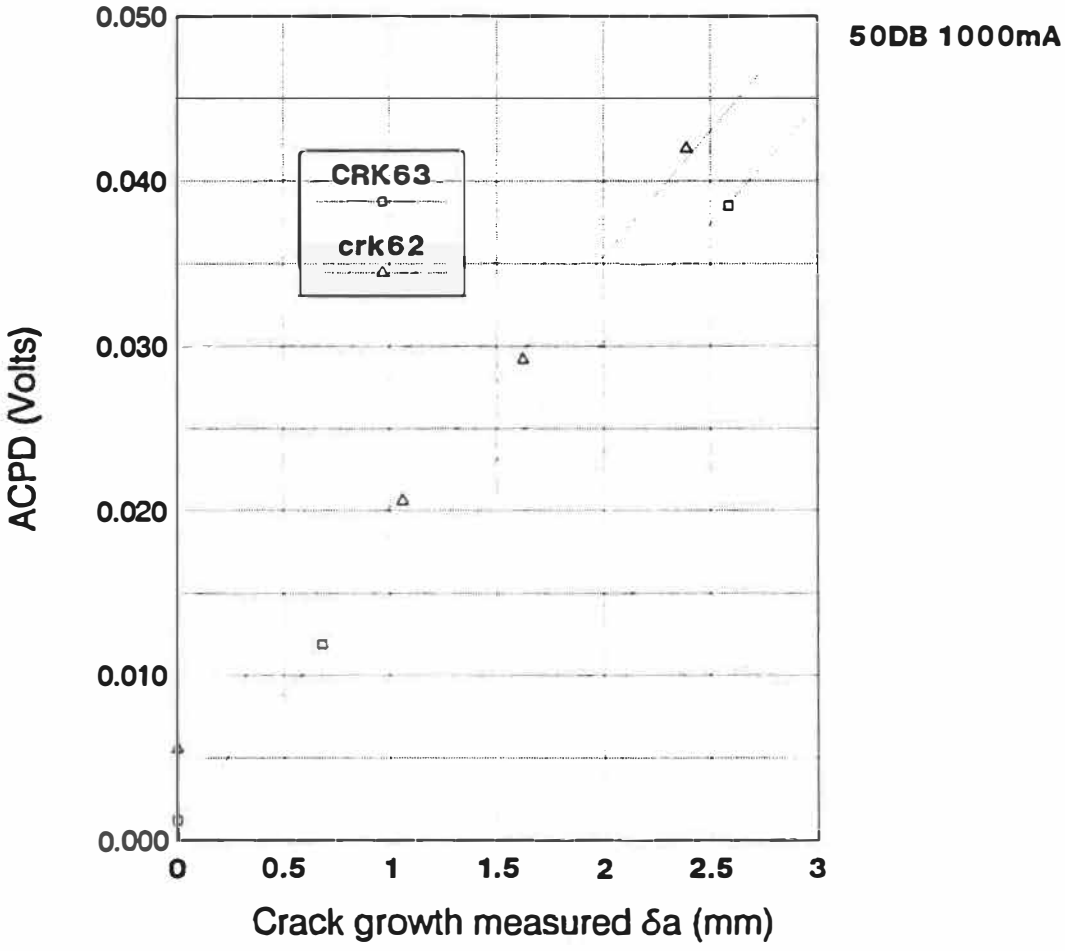

Figure 2.25 The calibration curves for ACPD signal vs. crack depth for TMF tests (TI6246). Here CRK63 and CRK62 correspond to two specimens used in calibration measurement.

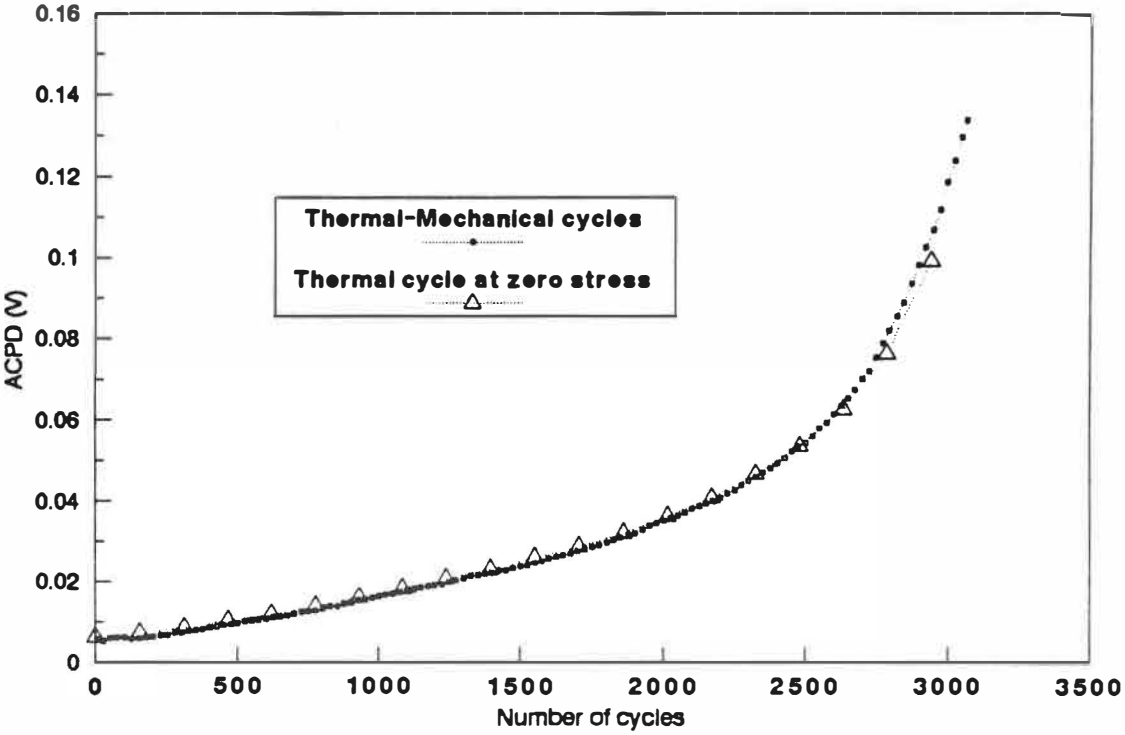

igure 2.26 A Comparison showing that the effects of pure thermal cycling on the CPD curves are small.

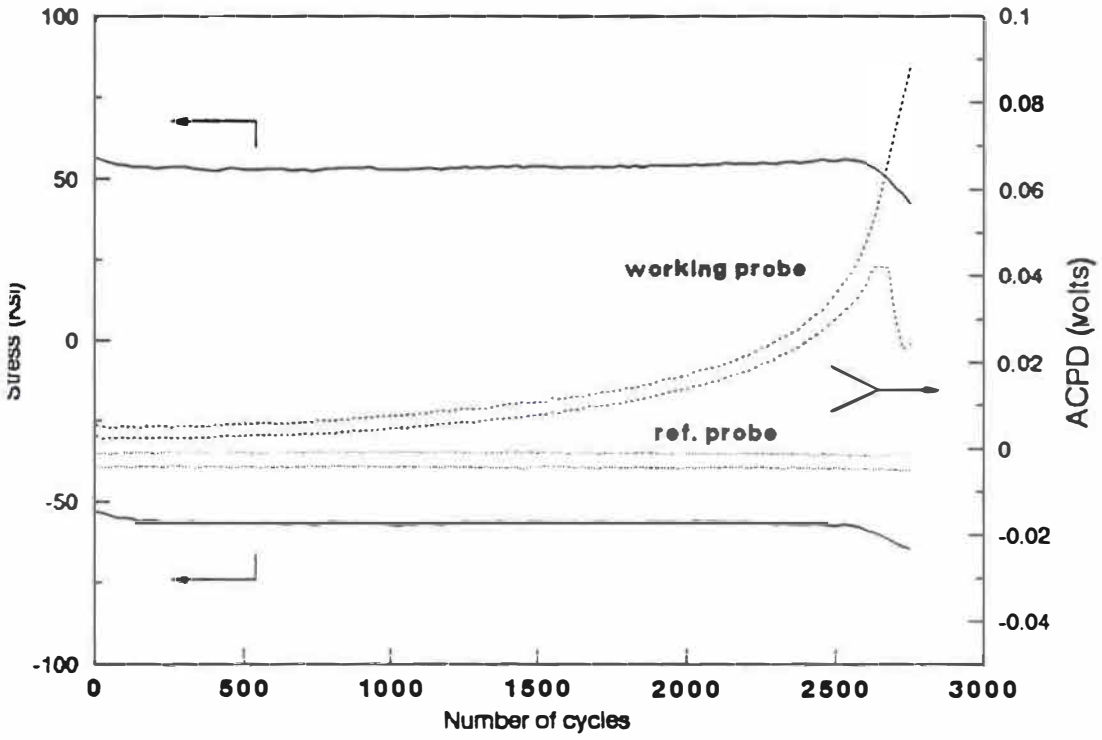

gure 2.27 The far field stress and ACPD signal change are plotted as a function of
e number of cycles for an in-phase TMF test (Ti64).

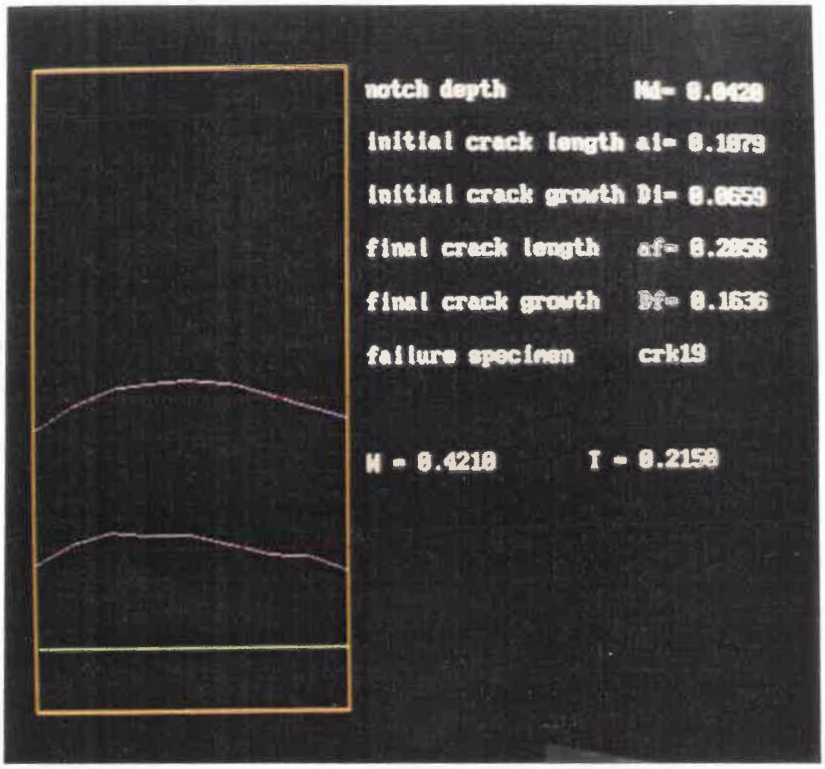

ure 2.28a A typical output of final crack length measurement and documentation gram.

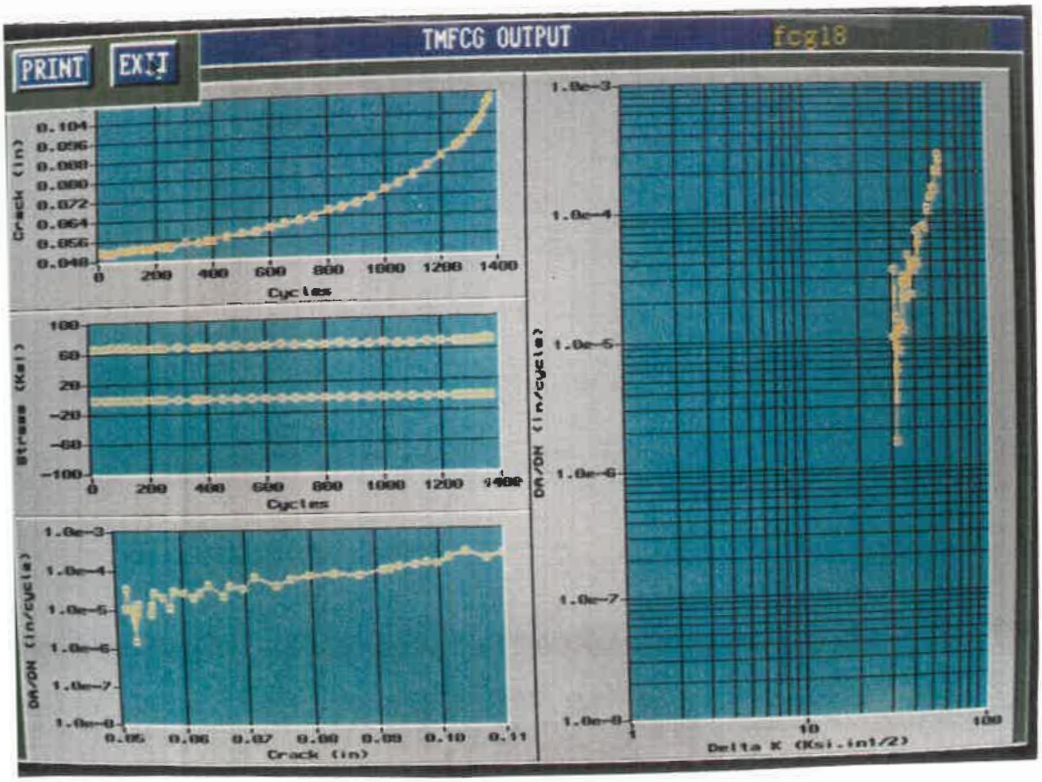

re 2.28b A typical output of post-test data reduction software "TMFCG".

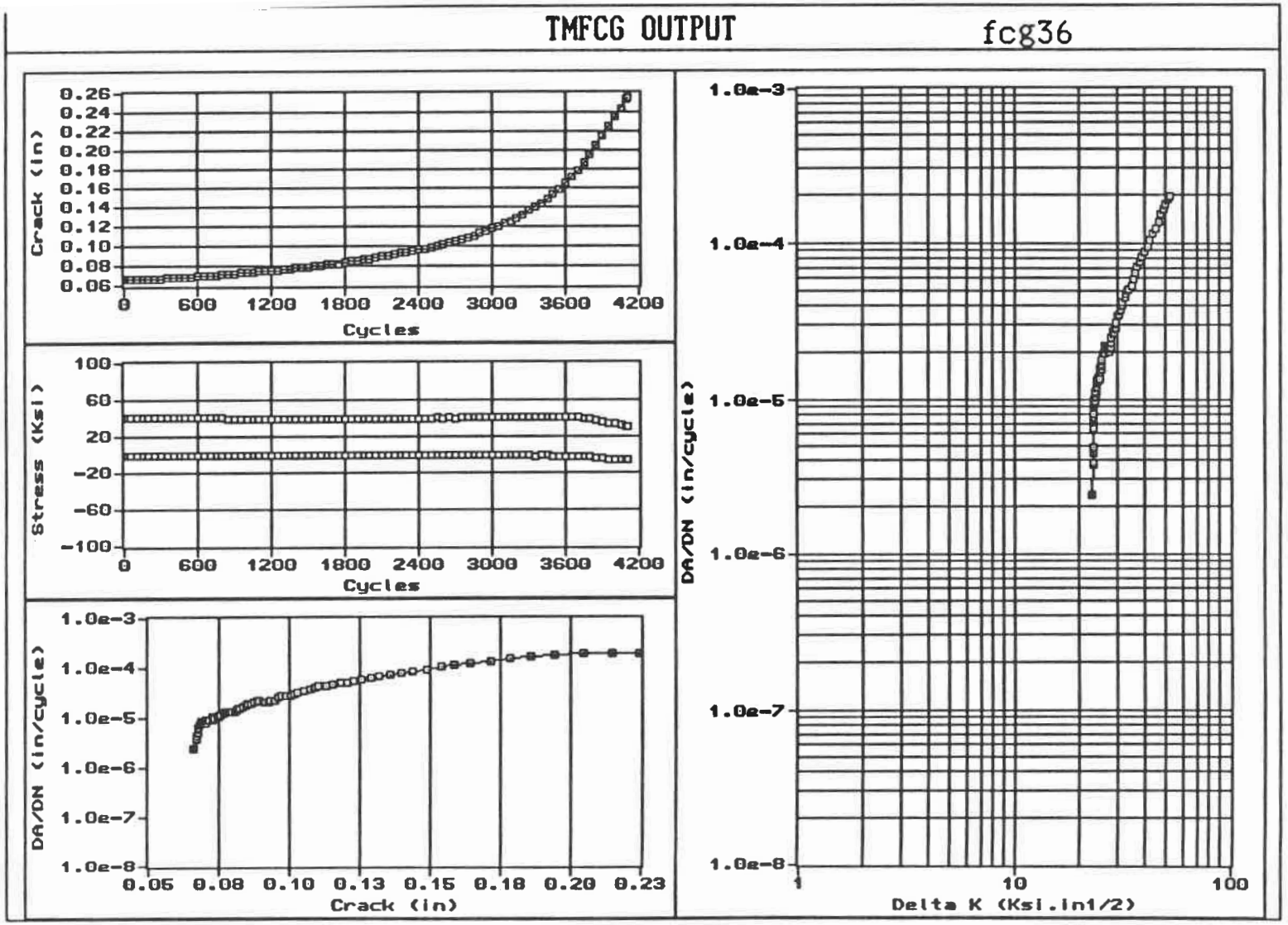

Figure 2.29 A complete test result documentation plot for a crack propagation test.

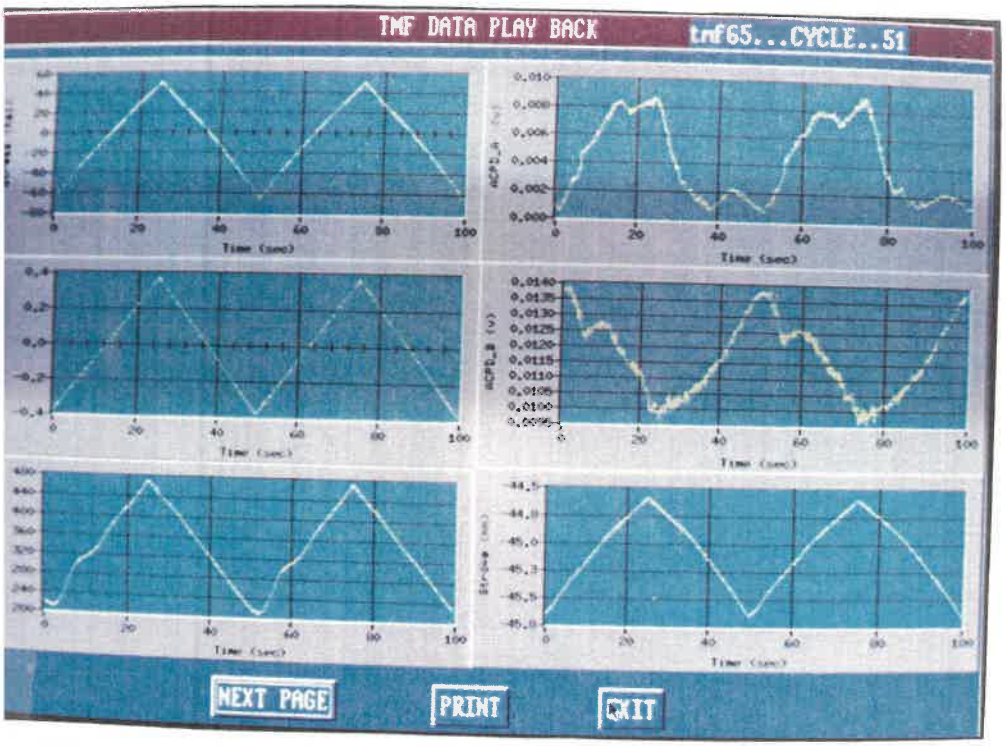

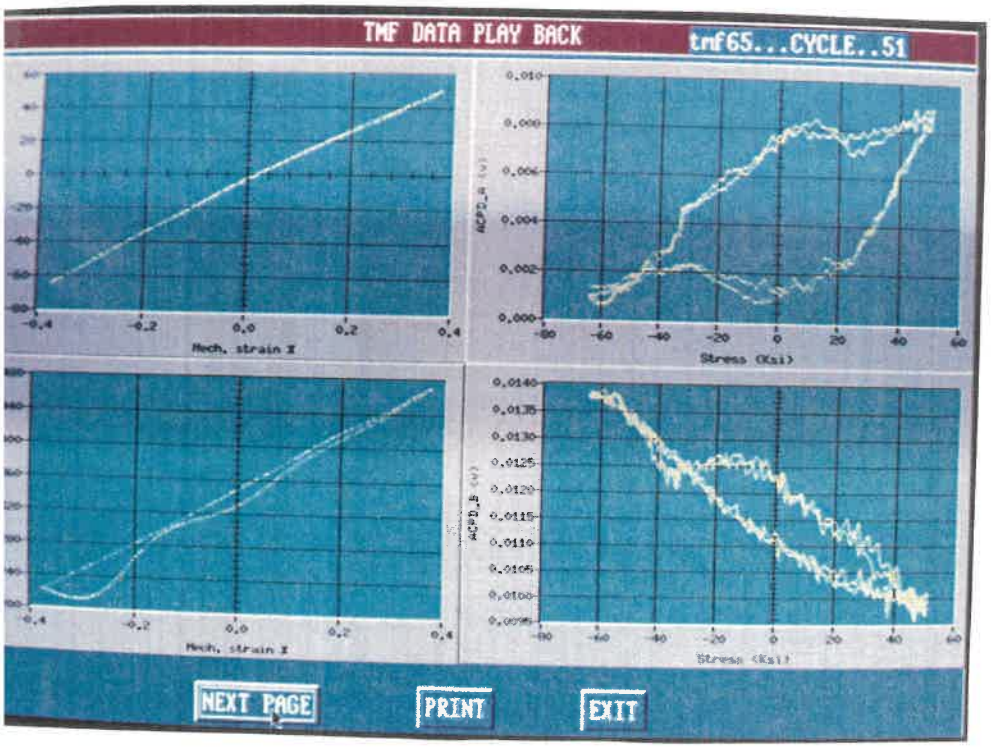

gure 2.30 Typical output of TMF test cycle loop data retrieve program.

CHAPTER 3

FATIGUE CRACK INITIATION AND GROWTH IN TITANIUM ALLOYS AT HIGH TEMPERATURES

3.1 INTRODUCTION

The material's resistance to fatigue loading is considered a basic property of the material. Correspondingly the fatigue strength has been mostly quantified in terms of the number of cycles to failure under a given alternative stress level (i.e. the so called S-N curves) using smooth cylindrical specimens. However, with the rapid development of fracture mechanics and material damage mechanics analysis, it is now accepted that short crack growth takes a large portion of the fatigue life (or LCF life) of a component. Some new procedures consider that there are always crack-like defects in components, and/or the short cracks can form at a relatively early stage, grow for a short period and then be arrested by different microscopic barriers. Hence the material's fatigue life depends mainly on the growth rate of these defects[140-141] under the applied load.

Fatigue crack initiation and short crack growth involves many complex processes which depend on factors such as component geometry, surface finish conditions, loading conditions, microstructural deformation history, localized stress/strain fields and environmental conditions etc.. Although much effort has

been expended to identify a controlling parameter for short crack growth similar to the stress intensity factor for long crack propagation[141], so far there is no generally accepted and practical engineering parameters available. Furthermore, from the design point of view, it is impractical to perform cyclic elasto-plastic finite element analysis with a super fine mesh (at least < 1/64" (0.4 mm) provided crack initiation depth = 1/64") for engine components due to the lack of accurate material constitutive models. Therefore, the concept of "substructural" component testing must be used to bridge the basic material property testing and the costly full scale component testing, such as spin pit tests for turbine discs. Hence single tooth fir tree (STFT) specimen testing as well as the single edge notched (SEN) specimen tests such as those described in this study are examples of this kind of low-cost substructural testing. In the later case, for example, the notch geometry can be designed to match engine components with notch features similar to typical bolt holes.

Quantitative measurement of fatigue damage during the substructural tests has been difficult and time consuming. Methods such as visual observation using a traveling microscope and various replica techniques are widely employed. These techniques may introduce undesired human intervention as well as interruptions of a test. Fortunately, as mentioned earlier, the recent development in ACPD technique has permitted continuous monitoring of short crack initiation and short crack growth at the root of a notch. As compared with the conventional DCPD technique (also called EPD), the sensitivity and linearity of the ACPD crack measurement system are greatly enhanced by the skin effect which results from the high frequency AC current. From the measured ACPD signal as a function of the

number of cycles, the LCF lives to a particular crack initiation size (e.g. 1/32") can be determined for the specimens.

In the following sections, the results of high temperature isothermal LCF tests on the two titanium alloys using SEN specimens are presented. Fatigue crack initiation and propagation behavior at the root of the notch are studied.

3.2 DEFINITION OF CRACK INITIATION LIFE

Conventional procedures for generating the LCF S-N (or ε-N) curves for various alloys are mostly based on testing smooth cylindrical specimens. In those tests, the LCF lives are usually defined by a load drop criteria and/or surface replica techniques. With the newly developed ACPD crack growth monitoring system, it is possible to use a more accurate definition of fatigue crack initiation life for the SEN specimen testing.

As suggested in the Engine Structural Integrity Program (ENSIP)[139] and in the component life management planning for P&WC engines[142], the fatigue crack initiation life N_i of gas turbine engine components is defined as number of cycles to initiate a crack with a surface length of 0.8mm (1/32"). For surface cracks emanating at the root of a notch, the aspect ratio (length/depth) is often taken as 2.0 (or a/c=1.0). Figure 3.1 describes the crack initiation cases at the root of the SEN specimen. In an ideal case, as shown in Figure 3.1a, a single crack initiates at the center of the notch with a depth at the deepest penetration of 0.4 mm (1/64 ").

As has been discussed in Chapter 2 on the test programs, the ACPD signal is in fact proportional to the area of cracked surface. Therefore the present ACPD system measures the effective crack length that is defined as the total cracked surface area divided by the thickness of the specimen. Since it is not known prior to a test if one or several cracks will initiate at the root of the notch, the determination of an effective crack initiation length a_i is difficult. As shown in Figure 3.1a and Figure 3.1b, the ideal penny-shaped crack with surface length of 0.8 mm (1/32") initiated at the midpoint of the notch will give an average depth of 0.05 mm (0.002"). This size is impractical to be used in defining a_i, and it is also dependent on the specimen thickness. To circumvent this problem it was decided to define the crack initiation as the occurrence of a through-thickness crack (2D) with a depth of 0.4 mm (1/64"), see Figure 3.1c. Since multiple crack initiation sites were observed in all the tests studied by SEM (scanning electronic microscope), this definition of crack initiation life was shown to be appropriate and convenient to apply. For a more conservative definition, one can also use the ratio of the cracked surface area of the ideal penny shaped crack to its surface length (1/32") as the effective crack initiation length. This will give $a_i = 0.31$mm (0.0122"). See Figure 3.4d. After all, with the ACPD measurement, a continuous a-N curve can be obtained. Thus the initiation lives N_i can be easily determined for various definitions of a_i. In the LCF data reduction, the effective crack initiation length is chosen as 0.4 mm (1/64").

To avoid difficulties in measuring the average crack length for multiple crack initiation cases such as those shown in Figure 3.1e, most of the tests were stopped when a well defined through thickness crack had been developed as indicated in

Figure 3.1f. At this stage, the crack coalescence processes have been completed[143]. The effective crack length can be obtained from the equally spaced measuring points (n) by

$$a = \sum_{i=1}^{n} \frac{a_i}{n} + \frac{a_1 + a_n}{2(n-1)} .$$

Figure 3.2 shows the procedure to obtain the crack initiation lives N_i from the measured a ~ N curves for one loading (strain level) case. The scatter of N_i data is represented by the intersections of the crack initiation definition line with the a ~ N curves. The a ~ N curves, depending on the ACPD signal quality (RF noise pick-up can be high in high temperature test with 60db gain), are smoothed using polynomial functions.

3.3 NOTCH STRAIN ANALYSIS

The correlation of the LCF data (N_i) for the SEN specimen is based on a notch strain field analysis. A relationship between the notch strain/stress field and the far field strain (controlled) is needed to effectively estimate the notch strain parameters. Both an analytical approach and numerical calculations are carried out for this purpose.

3.3.1 BE and FE analyses for the SEN specimen

Linear elastic boundary element (BE) analyses were carried out to determine the strain concentration factors (K_ε) at the root of the notch. The single edge notch specimen shown in Figure 2.2 was modeled by "BEST2D", which is a 2D boundary element method stress analysis program developed by P&WC. The notch was modeled by 12 evenly divided quadratic boundary elements. The model has a total of 80 quadratic elements, and is loaded at both ends by specifying *uniform vertical displacement* of Δy (refer to Figure 3.3a). Using plane stress option (regarding the similar calculation on impeller bolt holes with approximately same thickness as a guide), stresses were obtained for nodes on the boundaries. Stress and strain for any points lying inside the boundary can be obtained by simply specifying their coordinates in the code. Two internal lines (L1, L2) were used for this purpose, with the line L2 being at the location of the extensometer. Figure 3.4 shows the principal strain distribution along the ligament of two applied strain levels. For the geometry and loading conditions considered, the strain concentration factor was found to be $K\varepsilon = 3.36$. Here the strain concentration factor is referred to as the ratio of notch root strain to the strain imposed between the gauge section which is experimentally known.

According to Neuber[144], the stress concentration factor (K_t) for a notch is the ratio of notch root peak stress to the nominal stress σ_n. From the same boundary element analysis with far field *stress boundary* conditions, and taking into account the bending effect associated with the single edge notch, the K_t value was calculated as K_t=2.12. However, considering the actual grip and loading (displacement

controlled) conditions in the test specimen, the strain concentration factor K_ε was used. Here $K_t = K_\varepsilon = K_\sigma$ for the elastic analysis.

2D and 3D elasto-plastic FEM analyses were also carried out for the SEN specimen. The 2D model used triangular constant strain elements and was based on P0831 in-house FE code of P&WC. The typical results are in good agreement with those obtained from the analytical model in Figure 3.3b. The 3D FE model shown in Figure 3.3b is based on the "ABAQUS" FEM code. The 3D results which are quite similar to the 2D model are summarized in a separate report[145].

3.3.2 Analytical notch strain calculation based on Neuber's relations

Gemma[144] proposed an approximate elasto-plastic analysis procedure to take into account of the effect of plane strain at the root of a notch. Here a constraint parameter λ is used to represent the plane strain effect and the state of stress at the midpoint of the notch root surface. As shown in Figure 3.5, the true stresses at the origin can be written as

$$\sigma_{ij}(0,0,0) = \sigma \begin{pmatrix} \lambda & 0 & 0 \\ 0 & 0 & 0 \\ 0 & 0 & 1 \end{pmatrix} \quad . \tag{3.1}$$

Assuming that the materials obey the Ramberg-Osgood equation, i.e. $\varepsilon = \sigma/E + (\sigma/\sigma_0)^n$, the plastic strain is derived as

$$\varepsilon_{ij}{}^{p} = \frac{1}{2}(\lambda^2 - \lambda + 1)^{\frac{(n-1)}{2}} \left(\frac{\sigma}{\sigma_0}\right)^n \begin{pmatrix} 2\lambda - 1 & 0 & 0 \\ 0 & -(\lambda+1) & 0 \\ 0 & 0 & -(\lambda-2) \end{pmatrix} . \qquad (3.2)$$

The usual form of the Neuber relationships is

$$K_t{}^2 = K_\sigma K_\varepsilon \quad , \qquad (3.3)$$

or

$$K_t^2 = \sigma_{33}\varepsilon_{33} / (N_{33}e_{33}) \quad , \qquad (3.4)$$

where $K_\sigma = K_\varepsilon$ in elastic conditions, and the N, and the e are the far-field stress and strain tensor which can be represented as

$$e_{ij} = \frac{1+\upsilon}{E}\left(N_{ij} - \frac{\upsilon}{\upsilon+1} N_{kk}\delta_{ij}\right), \qquad (3.5)$$

and

$$N_{ij} = N \begin{pmatrix} \lambda & 0 & 0 \\ 0 & 0 & 0 \\ 0 & 0 & 1 \end{pmatrix} \quad . \qquad (3.6)$$

From which, $N_{33} = N$, and $e_{33} = N/E(1-\upsilon^2)$, with E the Young's modules and υ the Poisson ratio.

In the-back face strain controlled SEN specimen tests, the far field stress/strain can be easily measured so that the ratio $E' = \frac{N_{33}}{e_{33}}$ is experimentally known. The measured ratio E/E' was used as a correction factor for each test. As a result, for the same controlled far field strain, the notch plastic strain ε_p can vary from test to test due to the slight differences in stiffness of the specimens, which all caused by small variations in notch depth and radius.

Combining the above equations and considering plane strain condition (i.e. $\varepsilon_{11}(0,0,0)=0$), the constraint factor λ can be obtained from

$$\left(\frac{\lambda-\upsilon}{2\lambda-1}\right)^{1/(n-1)}\left(\frac{1-\lambda\upsilon}{\lambda^2-\lambda+1}\right)\left\{1+\left(\frac{2-\lambda}{1-\lambda\upsilon}\right)\left(\frac{\upsilon-\lambda}{2\lambda-1}\right)\right\}-\frac{E/E'(K_t N)^2}{(2\sigma_0^n/E)^{2/(n-1)}}=0\,, \qquad (3.7)$$

using an iteration method. Then the notch stress and strain can be easily calculated from Eq.(3.2) and Eq.(3.3). For the plane stress condition, i.e. $\lambda=0$, the same procedure can be used. The Neuber's equation based notch strain analysis procedures have been shown to be in very good agreement with the elasto-plastic FE analysis in monotonic loading cases by Gemma and in cyclic loading cases by Ohnami[146].

As shown in Figure 3.6a, the notch strains as functions of far-field strains can be obtained from this model. The total notch strain ($\Delta\varepsilon$) as well as its elastic and plastic components are plotted. The elastic notch strain procedure, $\varepsilon_n = K_\varepsilon \Delta\varepsilon$, is

shown not to be valid when the notch root strain range $\Delta\varepsilon > 0.2\%$, or the plastic strain at the notch becomes significant.

The elasto-plastic finite element results agree very well with the analytical model for monotonic loading cases as shown in Figure 3.6b. Furthermore, the calculated notch stress as a function of notch strain is indicated in Figure 3.7 for Ti64 at 400°C. As noted, a small change in stress results in a large change in strain in the plastic region. This explains the fact that the strain-based life prediction procedures have advantages over the stress based ones for notch configurations.

Since the fatigue lives are correlated by the plastic strain range in most of the LCF tests on smooth specimens, the effective plastic strain range $\Delta\varepsilon_{pl}$ at the root of a notch is calculated in a model schematically illustrated in Figure 3.5. Here the material is assumed to be isotropic. As the far-field strain goes back to zero, the total notch strain is assumed to go back to zero as well. The stress at point B is equal to the stress at point C. Hence the notch effective plastic strain range $\Delta\varepsilon_{npl}$ can be obtained from the total strain.

3.4 FATIGUE CRACK INITIATION LIFE FOR SEN SPECIMENS

Fatigue crack initiation (FCI) tests, here also called LCF test, were performed on Ti64 and Ti6246 at 400°C and 480°C respectively. During each test, the SEN specimen was cycled under far-field strain-controlled conditions. The crack initiation at the root of the notch was monitored by the ACPD measurement system

described in the last chapter. The test was stopped when a well defined through thickness crack had formed. The crack shape was marked by a heat tinting technique. Then the crack initiation life could be determined later by the procedures in Section 3.2.

Table 3.1 is the test matrix for Ti64, and Table 3.2 lists the main results of the LCF tests. Here, the far field strains controlled vary from 0.3% to 0.4%, and the strain rates are such that the cycling rate is kept at 10 cpm for all the tests. The strain R-ratio based on the far-field strain was set to 0.0.

Different notch field parameters were used to correlate the LCF results. Figure 3.8 shows the S~N results using the (notch) principal peak stress. A Manson-Coffin type relation can be observed. However, with stress change less than 50 Mpa (7.25Ksi), the fatigue life can vary by a factor of 10. This is inconvenient for the design. As the result, the notch-strain based parameters were used. As shown in Figure 3.9, the LCF data for the SEN specimen is correlated by the notch total strain at the maximum load. Figure 3.10 shows the results correlated with the notch plastic strain at the peak load, and Figure 3.11 shows the results correlated using the notch effective plastic strain range. An improved correlation can be obtained. The latter provides a procedure to compare the SEN LCF data with the data obtained from smooth specimens. However from the design point of view, the notch plastic strain is more appropriate for the engine structural FEA life procedures. In addition, both Figure 3.9 and Figure 3.11 show no significant decrease in FCI life as the test temperature changes from RT to 400°C for the Ti64 alloy.

The LCF test matrix and main results for Ti6246 are shown in the Table 3.3 and Table 3.4. Figure 3.12 and Figure 3.13 illustrate the FCI results correlated to the total notch strain and the notch plastic strain respectively. As compared with Figure 3.9, Figure 3.12 indicates a remarkable decrease in FCI life as the test temperature changes from RT to 480°C for the Ti6246 alloy. This phenomenon will be explained in Chapter 5 to be the result of oxidation-assisted cracking at 480°C.

The notch effective plastic strain range was also tried in the FCI data correlation for Ti6246. It is found that the FCI is not controlled by the notch plastic strain range. As shown in Figure 3.14, the dramatic changes in the strain range results in little change in the FCI lives, and the calculated notch plastic strain ranges are much smaller as compared with those obtained for the Ti64 specimen at similar far field strain. This is due to a difference in the cyclic behavior of Ti6246 which has notably higher Young's moduli and strain hardening moduli than those of Ti64 alloy (see Appendix 2).

Figure 3.15 shows an attempt to compare the two titanium alloys in terms of their FCI resistance. When correlated by the total notch principle strain, it can be seen that for the same notch strain level, the Ti64 at 400°C has higher FCI resistance than Ti6246 at 480°C. This difference becomes more prominent when the FCI data is correlated using peak notch plastic strain as shown in Figure 3.16.

However, an interesting result can be observed if the FCI data are correlated with the notch root peak stresses, as illustrated in Figure 3.17. It indicates an

opposite result that for the same notch stress level, the Ti6246 at 480°C has higher FCI resistance than Ti64 at 400°C.

3.5 STRESS INTENSITY FACTOR FOR THE CRACK GROWTH DATA

After a crack has initiated at the root of the notch, an accurate solution for the stress intensity factor (K_I) is required to describe the crack growth behavior. The stress intensity factors for small cracks emanating from the notch were calculated using the model proposed by Schijve[147]. In this model, Schijve assumes that similar K_I values will apply to small cracks at notches if the notch peak stress σ_{pk} and notch radius ρ are similar. Thus the K_I can be written as

$$K_I = C(\frac{\ell}{\rho})\sigma_{pk}\sqrt{\pi\,\ell} \quad . \tag{3.8}$$

Here the peak stress is taken as $\sigma_{pk} = K_t\,\sigma_n$, with K_t the stress concentration factor (here $K_t = K_\varepsilon$ in the linear elastic analysis) and σ_n the far field nominal stress. the C $(\frac{\ell}{\rho})$ term is the notch geometry function which depends on ℓ the crack depth measured from the surface of the notch root and on ρ the radius of the notch. The function C $(\frac{\ell}{\rho})$ derived by Schijve has the form

$$C(\frac{\ell}{\rho}) = 1.1215 - 3(\frac{\ell}{\rho}) + 4(\frac{\ell}{\rho})^{1.5} - 1.7(\frac{\ell}{\rho})^2 \quad . \tag{3.9}$$

This model is in excellent agreement with Newman's FEA results[147] on small cracks at various elliptical holes up to $\ell/\rho \sim 0.5$ for the SEN specimen. Since the average crack depth is measured by the ACPD technique, this 2D crack model is appropriate for calculating the average K_I across the SEN specimen thickness, avoiding the difficulties with the detailed notch crack configurations such as encountered in the Newman's models[148-150].

When the crack depth was long compared with ρ, the K_I's were computed using the equation derived by Marchand et al[51] for a SEN specimen under far field fixed-ends displacement conditions. This solution can be briefly written as

$$K_I = (N/BW)\sqrt{\pi a}\, H(\zeta, \eta, \eta_b) \quad . \tag{3.10}$$

Here N is the normal load *measured* during the test, B and W are the thickness and the width of the specimen, a is the crack length including the notch depth and $H(\zeta, \eta, \eta_b)$ is a geometrical correction factor which takes into account the actual loading conditions in the test. An improved procedure was proposed to determine the $H(\zeta, \eta, \eta_b)$ more accurately. It is presented in Appendix 3.

Kujawaski[151] recently proposed a model to estimate the stress intensity factors for small cracks at notches. For the semi-infinite plate with an edge notch (with depth a) and a through-thickness crack measured from the bottom of the notch (with length ℓ), the model can be written as:

$$K_I = \frac{f}{1-1/K_t}\left[(1+2\frac{\ell}{\rho})^{-1/2}+(1+2\frac{\ell}{\rho})^{-3/2}\right]\sqrt{\frac{\ell}{\rho}}\cdot 1.122\sigma_n\sqrt{\pi a}\,, \qquad (3.11)$$

where $f = 1$ for $\ell/\rho < 0.2$

and $f = 1 + \frac{\tan(\pi/2K_t)}{2.8}(\ell/\rho - 0.2)$ for $\ell/\rho > 0.2$

Figure 3.18 shows the comparison of K_I factors calculated by the three models as functions of normalized crack length a/w. It can be seen that Schijve' model Eq.(3.8) agrees very well with Kujawaski's model Eq.(3.11) for the small cracks, and there is a transition crack length a/w~0.14 which separates the short and long crack solutions. Since Kujawaski's model does not take into account the specimen's finite boundary conditions that are considered in Marchand's model Eq.(3.10), the last model was used to calculate the K_I factors for the long cracks when a/w>0.14. Fett[152] recently also showed a similar transition in stress intensity factor for the notch crack.

3.6 SHORT AND LONG CRACK GROWTH DATA

The short and long fatigue crack growth (FCG) testing conditions are included in Table 3.1 and Table 3.3. The FCG tests performed for Ti64 at 400°C and Ti6246 at 480°C are the same tests used to study materials' FCI behavior, which are

indicated as LCF tests. The FCG tests for the two alloys at lower temperatures (<400°C) were performed after high temperature LCF crack initiation tests on the same specimens. These enabled us to clearly obtain heat-marked cracks which had naturally initiated at the root of the notch during FCI testing, as well as the information on the materials' long crack FCG behavior at other temperatures.

A typical crack growth rate vs. crack length curve (Ti64 tested at 400°C) is shown in Figure 3.19. When the cracks are short with their average depth from the root of the notch less than 60μm, which is of the order of the microstructural characteristic features in Figure 2.4, the da/dN varies erratically with increasing crack length. In this region most of da/dN data spans two orders of magnitude, which is a similar to the phenomenon reported by Miller[140] and Newman[148] for aluminum alloys. This implies that these growth rates (for a<60μm) are mostly controlled by local microstructural events and thus cannot be taken into account by a fracture mechanics parameter alone. On the other hand, when the crack grew longer than 60μm, their growth rates start increasing monotonically with increasing crack length. This suggests that the da/dN's are controlled by fracture mechanics parameters soon after the average crack depth has reached 60μm for Ti64. This further indicated that da/dN can be correlated to the appropriate fracture mechanics parameters. A similar notch crack behavior was also found in the Ti6246 forgings tested.

The da/dN~ΔK curve pertaining to results shown in Figure 3.19 is presented in Figure 3.20. In this plot, the short crack K-solution (i.e Eq.(3.8)) was used for crack lengths ranging from 60μm to 420μm while the long crack solution

(i.e. Eq.(3.10)) was used for a > 420μm (a/W > 0.14). For comparison, a set of long crack growth data are also plotted. The da/dN for short cracks (60μm< a<130μm) are higher than the long crack propagation rates at the same level of ΔK. This accelerated crack growth is believed to be caused by the plastic deformation zone at the notch during cyclic straining, since the elasto-plastic finite element calculations indicated the occurrence of small zones of inelastic deformation at the root of the notch. As soon as the cracks grew outside the pre-damaged zone and into the elastic notch field (i.e 130μm<a< 420μm), the da/dN of the short crack became similar to that of the long cracks at the same ΔK. This also indicates that Schijive's K-solution takes properly into account the *elastic notch field*. The notch plastic zone size r_p can also be easily estimated from a model proposed by Creager[153], which gives

$$r_p = \rho\left[\left(\frac{K_t\sigma_n}{\sigma_y}\right)^{2/3} - 1\right] \quad . \tag{3.12}$$

Here σ_y is material's yield stress. For Ti64 at 400°C, σ_y= 462.5 Mpa (ref. to Appendix 2). Using the notch peak stress ($K_t\sigma_n$) obtained from the notch strain analysis procedure as shown in Figure 3.7, the r_p can be calculated as 258 μm. It can be seen that the notch plasticity controlled zone for the da/dN data terminates close to $r_p/2$.

The present study has clearly shown that the short cracks emanating from notches can be considered as experiencing the following stages: (a) microstructural controlled growth, (b) inelastic damage controlled growth, (c) notch elastic field

controlled growth, and (d) far-field stress controlled growth. As a result, for the notched specimen tested, there exist three transitional (critical) crack lengths which are 60μm, $r_p/2$ and 420μm for Ti64. Similar results were also found for the Ti6246.

The long crack growth data are fitted by an interpolative hyperbolic sine model (SINH), which followed the procedures developed by P&WA under an USAF contract[53]. In this model, the da/dN is based on:

$$\log\left(\frac{da}{dN}\right) = C_1 Sinh\left(C_2(\log\Delta K + C_3)\right) + C_4 \quad , \tag{3.13}$$

where the coefficients have been shown to be functions of test frequency (υ), stress ratio (R) and temperature (T). Using the least square methods, the coefficients can be determined for each set of test conditions.

Figure 3.21 shows the da/dN values as a function of ΔK for Ti64 at the three temperatures. The data is then fitted by the SINH functions. A considerable decrease in FCG resistance can be observed as the temperature increases. The data is compared with the historical FCG data from P&WA data base in Figure 3.22. It is found that the P&WA da/dN curve at RT is much higher than that at all the three test temperatures. Since insufficient information is available regarding to the conditions of the test materials used by P&WA, an explanation is not attempeted.

Figure 3.23 presents typical da/dN data scatter of Ti6246 at 625°F (330°C), which can be very well fitted by a SINH curve. Figure 3.24 summarizes all the FCG

data for Ti6246 at three temperatures. A more significant decrease in FCG resistance can be observed as the temperature increases up to 900°F (480°C). This is explained on the basis of environment assisted crack growth discussed in Chapters 4 and 5. The FCG data at 900°F (480°C) is found to be in very good agreement with the P&WA historical data for Ti6246 at the same conditions. The FCG data at RT is also reasonably close to the P&WA data at RT.

3.7 DISCUSSION

The three models used to calculate the stress intensity factors, as shown in Figure 3.18, are based on effective through thickness crack length values that can be obtained from the ACPD measurement. Some concern arises, however, since in reality the short cracks remain penny-shaped for a considerable length prior to turning into through thickness cracks. As a result, the K_I value for short cracks using Schijve and Kujawaski's models may not represent true K_I values operative ahead of the crack tip. In this respect, a surface crack model proposed by Newman[148-150], as illustrated in Figure 3.25, was used to calculate the K_I for a penny-shaped crack initiated at the center of the notch root. An aspect ratio $a/c=1$ was chosen for the calculation. The geometry function F_{sn} were calculated based on the procedure suggested by Newman[148]. As shown in Figure 3.26, K_I values were obtained for several crack sizes for the SEN specimen used in the test program. Here the points indicated by star symbols represent the results with $\frac{a}{w}$ being the crack length at the deepest penetration. In order to compare with the other three through thickness

crack models, the results from Newman's model are also plotted using the effective crack length as illustrated by the filled squares. The effective crack lengths, again, are calculated by the cracked areas divided by the specimen thickness. As can be seen, the results from Newman's model are quite close to those from the Schijve and Kujawaski's models for the short crack region and from Marchand's model after the transition to longer crack lengths. This implies that the K_I calculation procedures used in the previous sections can very well represent the crack tip situation for a penny-shaped surface crack at notch center when the effective through thickness crack length is used.

In reality, multiple crack initiation at the root of the notch was observed in most of the tests. The interactions between neighboring cracks and the crack coalescence processes are very complicated to model. However, it is believed that the current K_I calculation procedure can be used to evaluate the average K_I values operative ahead of the crack tips at the notch.

It is worthwhile to point out that the results illustrated in Figure 3.26 may not be valid for the general SEN specimen geometry, since the function is not normalized due to the fact that short crack length and long crack length are defined differently.

3.8 CONCLUSIONS

From the above sections, the major conclusions of this chapter can be summarized as follows:

- Fatigue crack initiation and growth in fracture mechanics specimens as well as in component-like specimens can be accurately monitored by the ACPD techniques at room and elevated temperatures.

- LCF lives (a_i = 0.4 mm , 0.8mm (1/64", 1/32") etc.) of notched specimens can be quantitatively determined. The resulting S-N and ε-N curves are directly applicable to components having such notch features.

- The fatigue crack growth processes (for both short and long cracks) in Ti64 and Ti6246 are controlled by their proper ΔK soon after crack initiation (i.e. for $a_o > 60\mu m$).

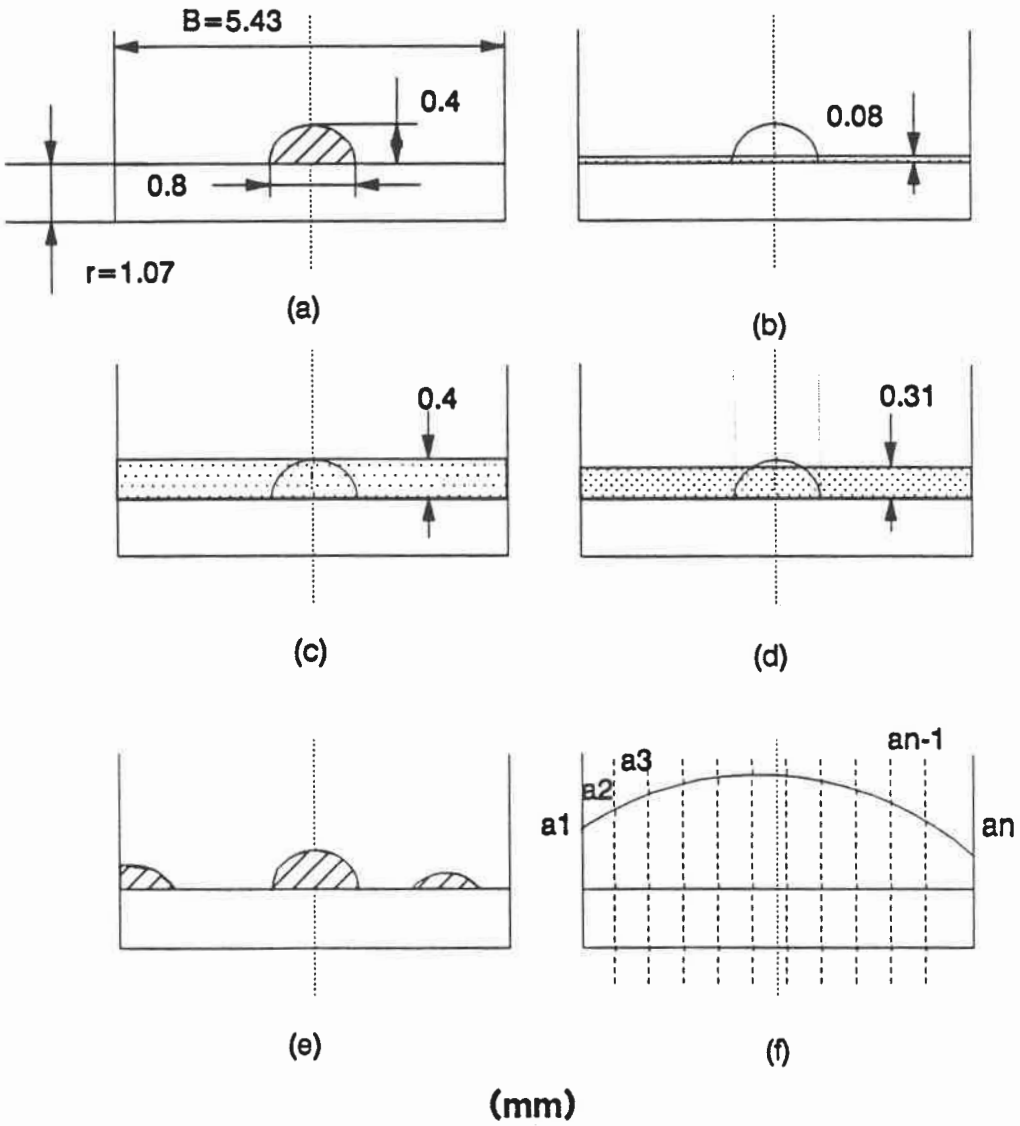

gure 3.1 A scheme for defining fatigue crack initiation in a SEN specimen. A cross ction view at the root of the notch is illustrated. (r: the radius of the notch; B: the dth of the specimen)

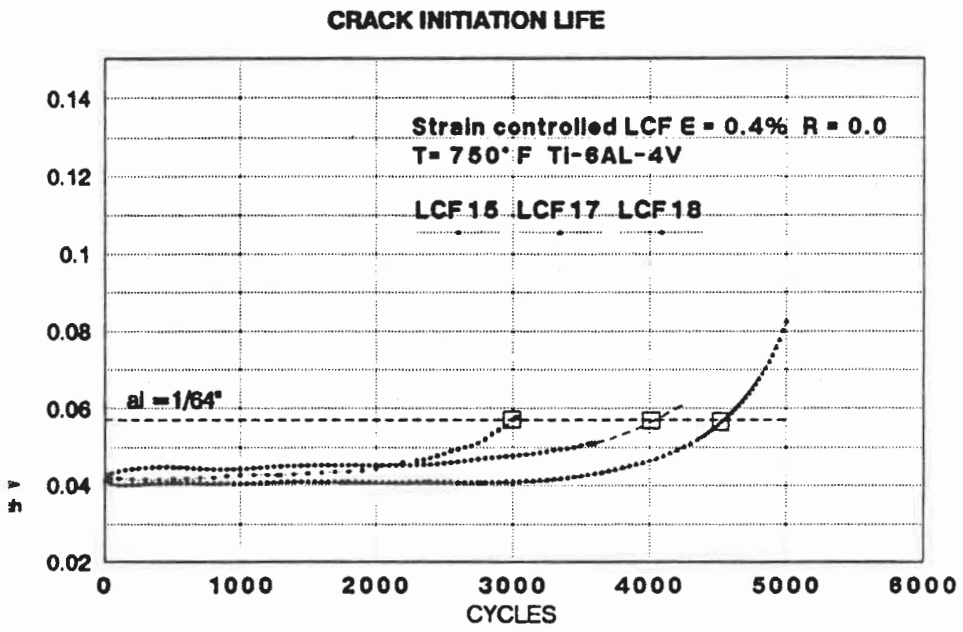

ure 3.2 A procedure to calculate the LCF lives corresponding to a specified crack iation depth for the SEN specimens. (Ti64, 400°C).

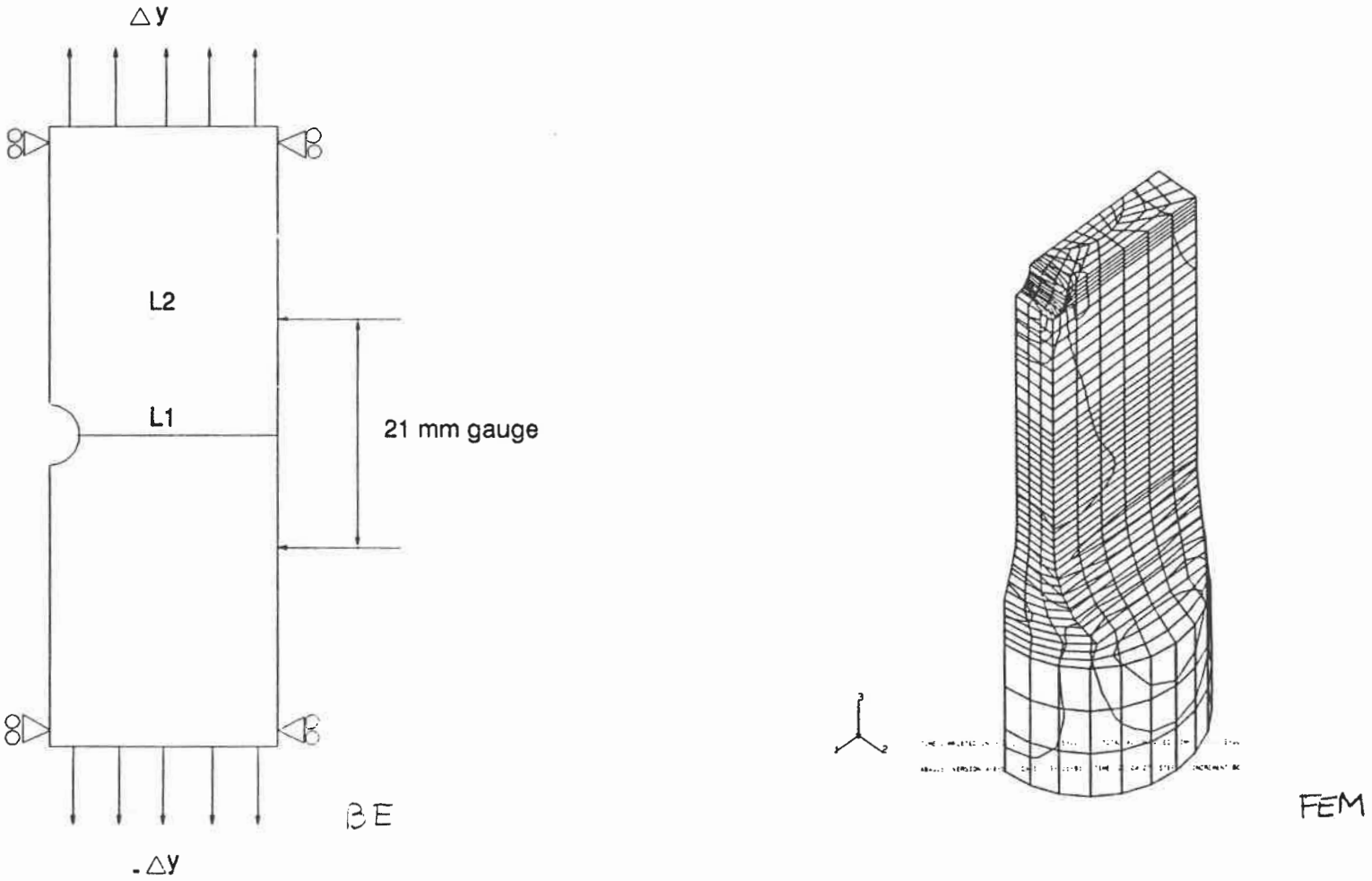

Figure 3.3 The boundary element and 3D finite element models for the SEN specimen.

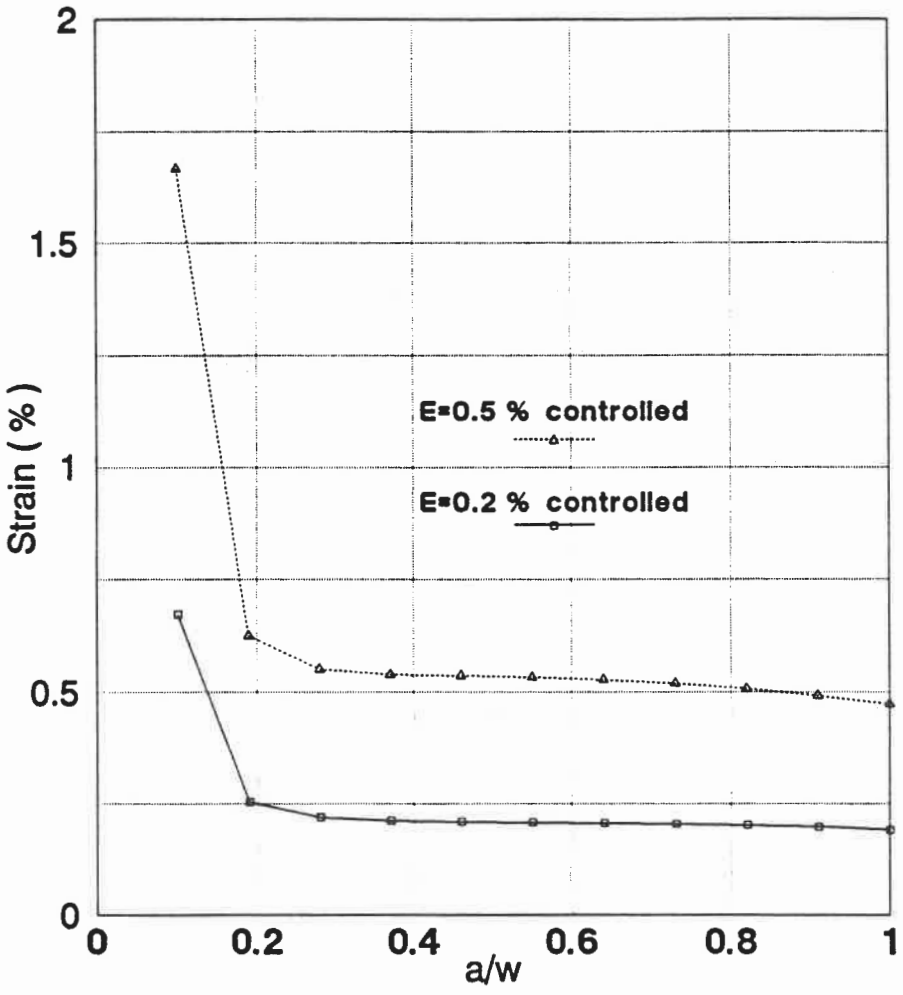

3.4 The strain field at the root of the notch calculated by the BEST2D
n.

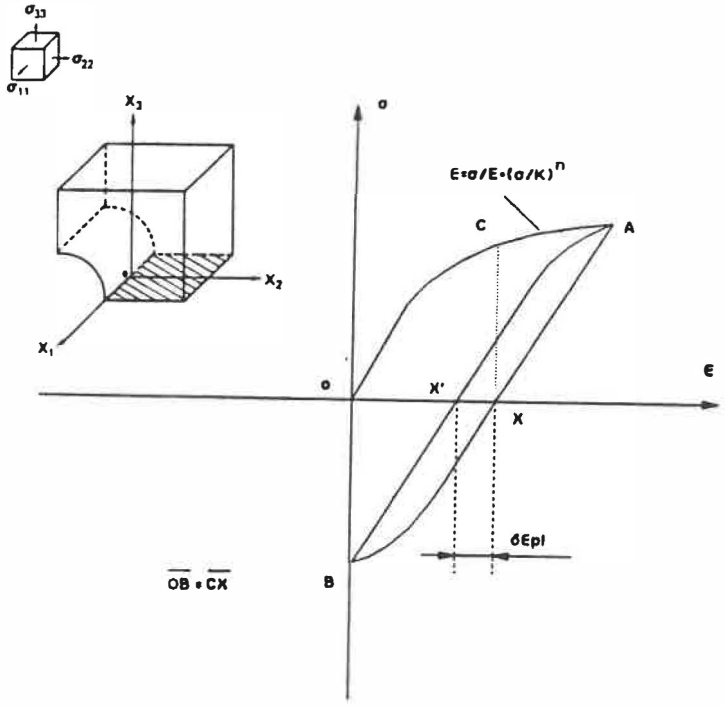

igure 3.5 An illustration of a method used in notch strain analysis and the notch lastic strain range definition.

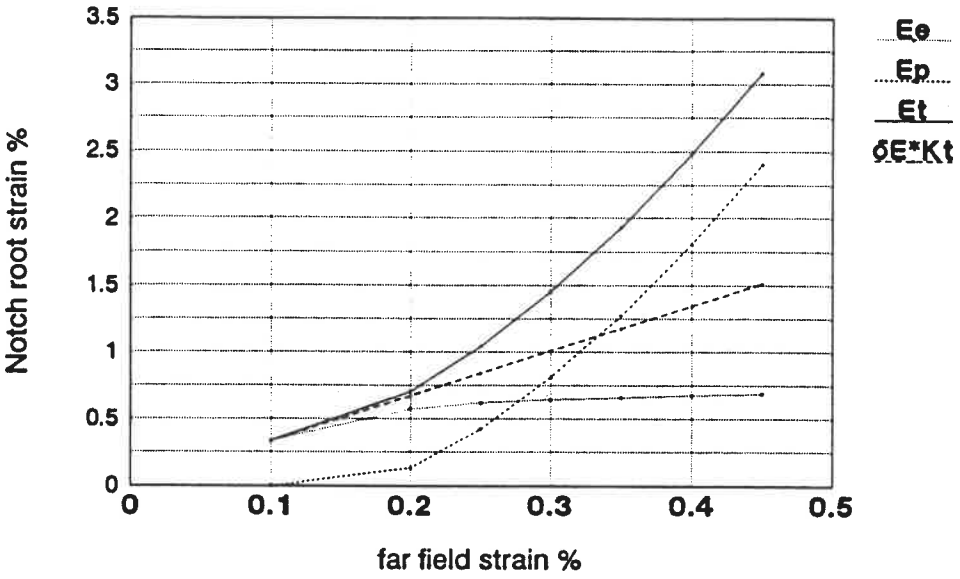

(a)

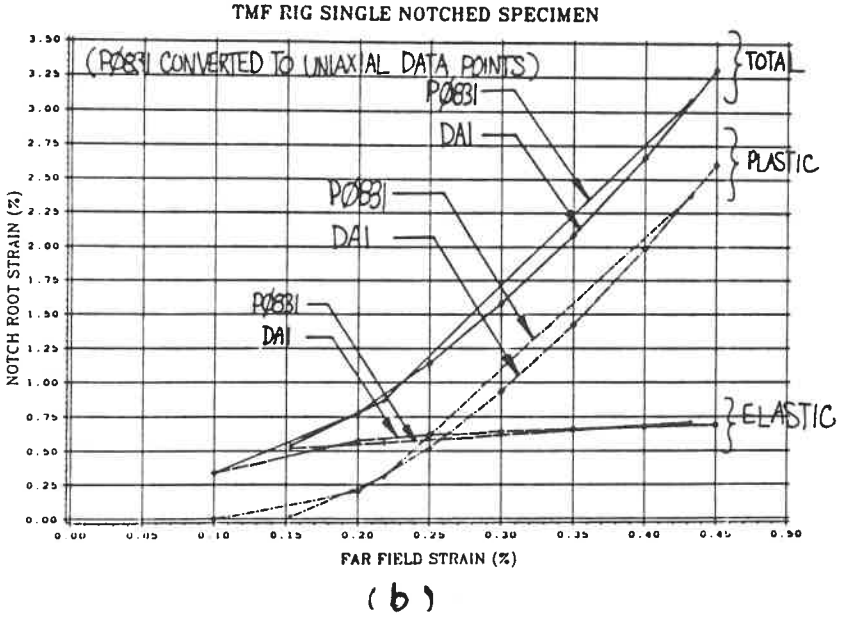

(b)

gure 3.6 (a). A plot of the calculated notch strains as functions of far-field applied ain. (b). A comparison of the analytical notch strain model with the FEM lculation results (here P0831 is the code name of the FEM program in P&WC).

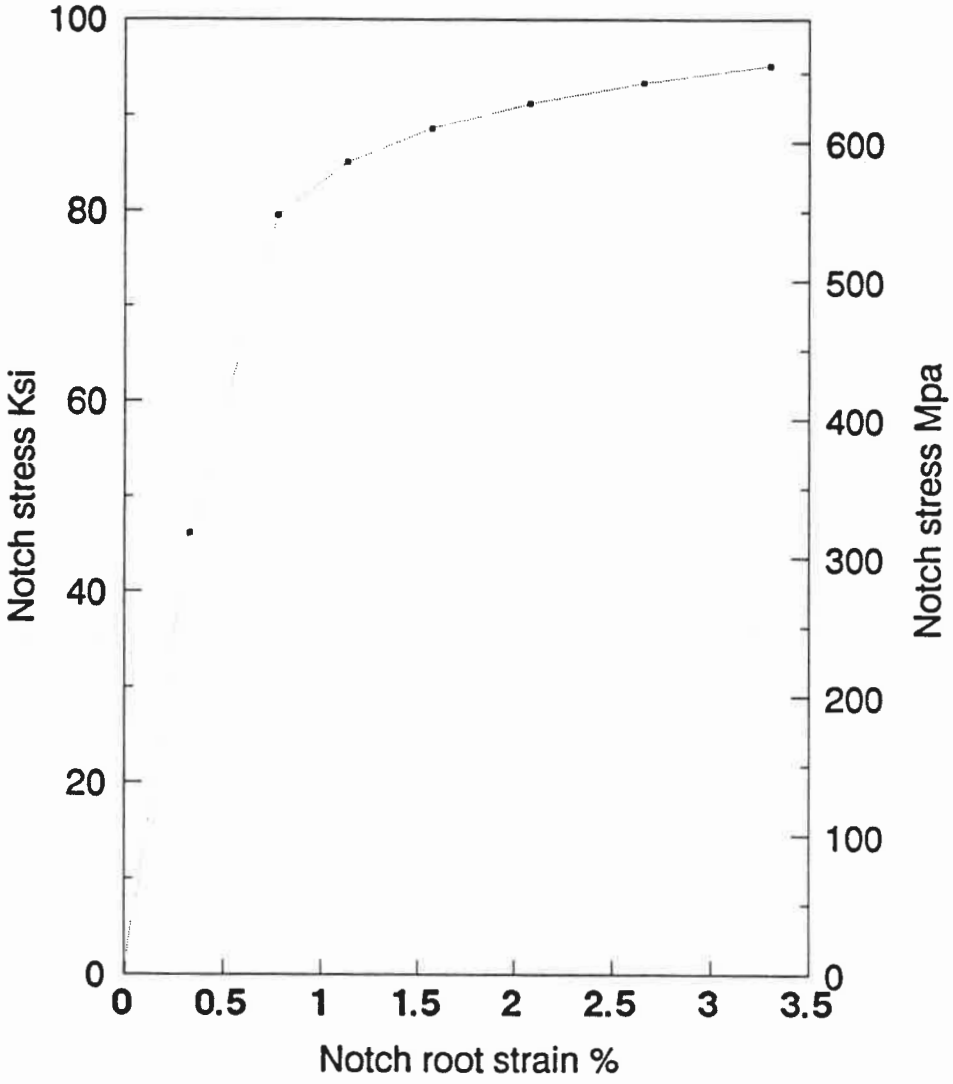

ure 3.7 The analytical result of the notch root stress as a function of the strain.

TS_NAME	Sp. No.	δε %	R_ratio	ε sec-1	waveform	Temp. (°F)	Remarks
LCF15	TIA15	0.40	0	1.3333E-3	triangular	750	LCF STNC
FCG15	TIA15	0.40	0	1.3333E-3	triangular	220	FCG STNC
LCF17	TIA17	0.40	0	1.3333E-3	triangular	750	LCF STNC
FCG17	TIA17	0.40	0	1.3333E-3	triangular	RT	FCG STNC
LCF18	TIA18	0.40	0	1.3333E-3	triangular	750	LCF STNC
FCG18	TIA18	0.40	0	1.3333E-3	triangular	220	FCG STNC
LCF19	TIA19	0.35	0	1.1667E-3	triangular	750	LCF STNC
FCG19	TIA19	0.35	0	1.1667E-3	triangular	600	FCG STNC
LCF20	TIA20	0.35	0	1.1667E-3	triangular	750	LCF STNC
FCG20	TIA20	0.35	0	1.1667E-3	triangular	600	LCF STNC
LCF21	TIA21	0.35	0	1.1667E-3	triangular	750	LCF STNC
FCG21	TIA21	0.35	0	1.1667E-3	triangular	750	FCG STNC
LCF22	TIA22	0.35	0	1.1667E-3	triangular	750	LCF/FCG STNC
LCF23	TIA23	0.30	0	1.0000E-3	triangular	750	LCF STNC
FCG23	TIA23	0.30	0	1.0000E-3	triangular	750	FCG STNC
LCF24	TIA24	0.30	0	1.0000E-3	triangular	750	LCF STNC
FCG24	TIA24	0.30	0	1.0000E-3	triangular	750	FCG STNC
LCF25	TIA25	0.30	0	1.0000E-3	triangular	750	LCF/FCG STNC
LCF26	TIA26	0.30	0	1.0000E-3	triangular	750	LCF STNC
LCF27	TIA27	0.30	0	1.0000E-3	triangular	750	LCF STNC
FCG27	TIA27	0.30	0	1.0000E-3	triangular	RT	FCG STNC
CYC28	TIA28	0.3-1.2	-1	1.0000E-3	triangular	750	cyclic curves
LCF29	TIA29	0.35	0	1.0000E-3	triangular	750	LCF/FCG STNC
LCF30	TIA30	0.40	0	1.0000E-3	triangular	750	LCF STNC
FCG30	TIA30	0.40	0	1.0000E-3	triangular	RT	FCG STNC

STNC: strain controlled test

LCF: crack initiation test

FCG: crack propagation test

SPECIMEN	δEf %	δEnpl %	TEMP. °C	R_ratio	Ef s-1	Nf (af=0.4 mm)
LCF15	0.40	1.2290	400	0	0.00133	3,029
LCF17	0.40	1.2350	400	0	0.00133	4,564
LCF18	0.40	1.2410	400	0	0.00133	4,400
LCF30	0.40	1.1830	400	0	0.00100	6,376
LCF19	0.35	0.7153	400	0	0.00117	7,777
LCF20	0.35	0.8247	400	0	0.00117	5,400
LCF21	0.35	0.6911	400	0	0.00117	12,205
LCF22	0.35	0.8127	400	0	0.00117	7,923
LCF29	0.35	0.6709	400	0	0.00100	10,451
TCG23	0.30	0.3146	400	0	0.00100	20,325
TCG24	0.30	0.2082	400	0	0.00100	38,350
LCF27B	0.30	0.2591	400	0	0.00100	58,088
LCF25	0.30	0.2367	400	0	0.00100	32,219

δEf : far field strain range;
δEnpl : notch effective plastic strain range
Ef : far field strain rate

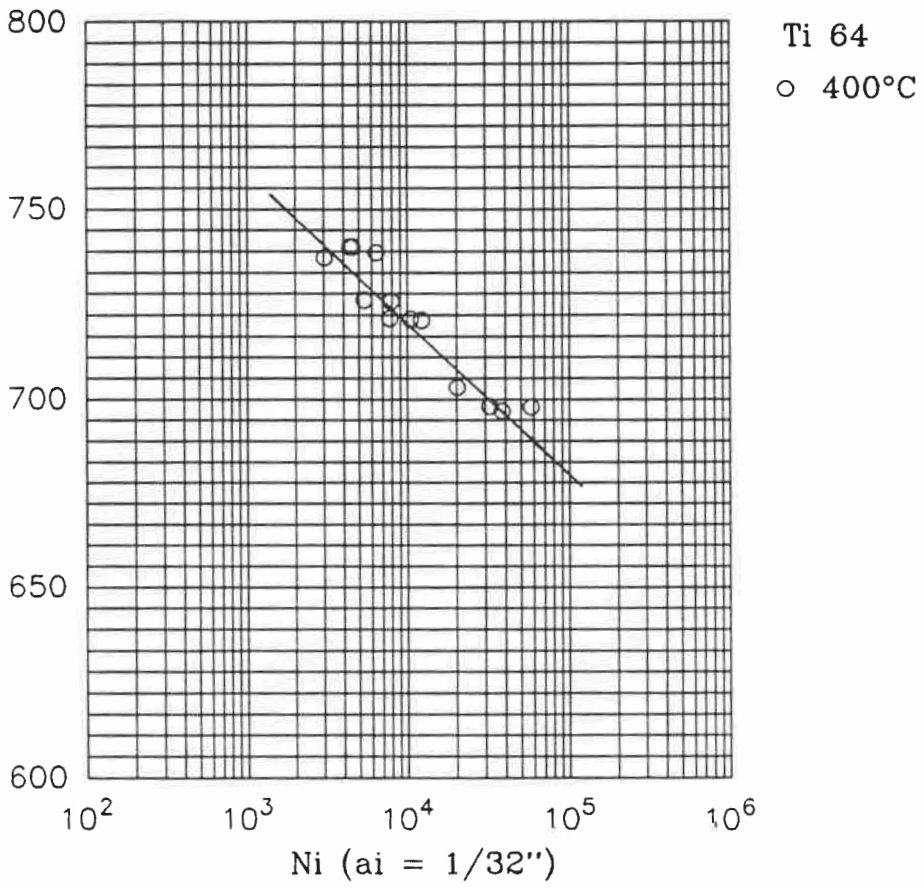

e 3.8 LCF life data of the SEN specimens correlated to the notch root peak (Ti64, at 400°C).

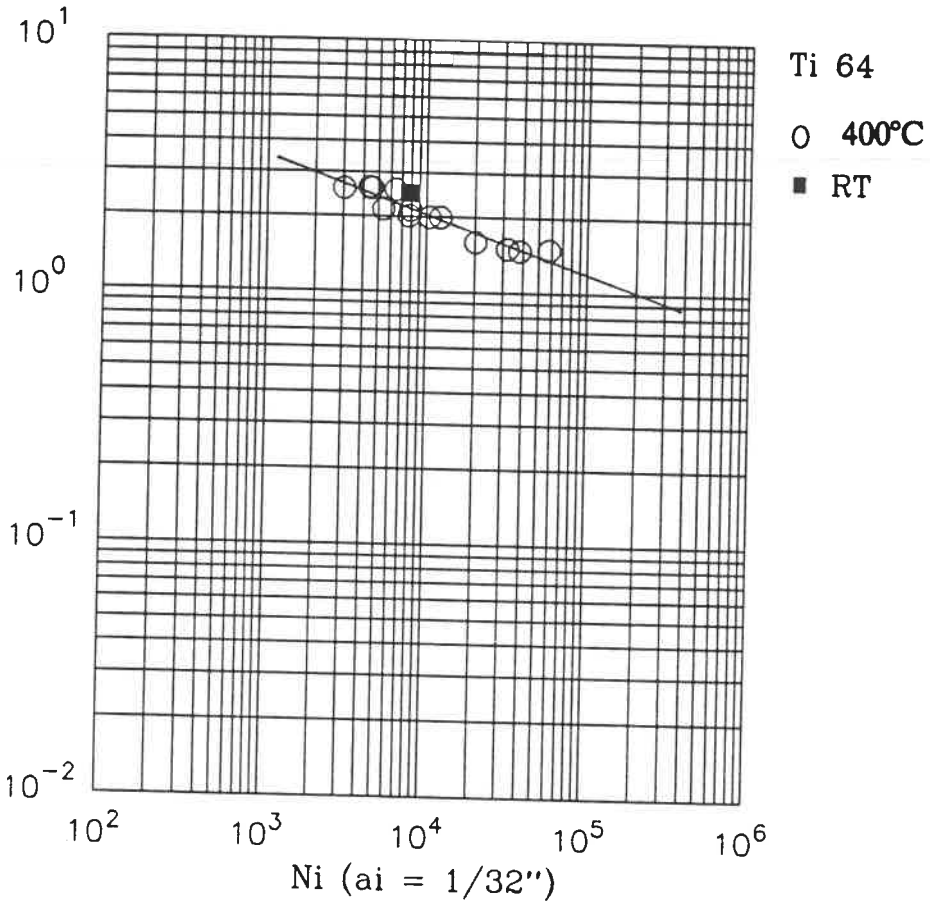

3.9 LCF life data of the SEN specimens correlated to the notch total strain. at 400°C and RT).

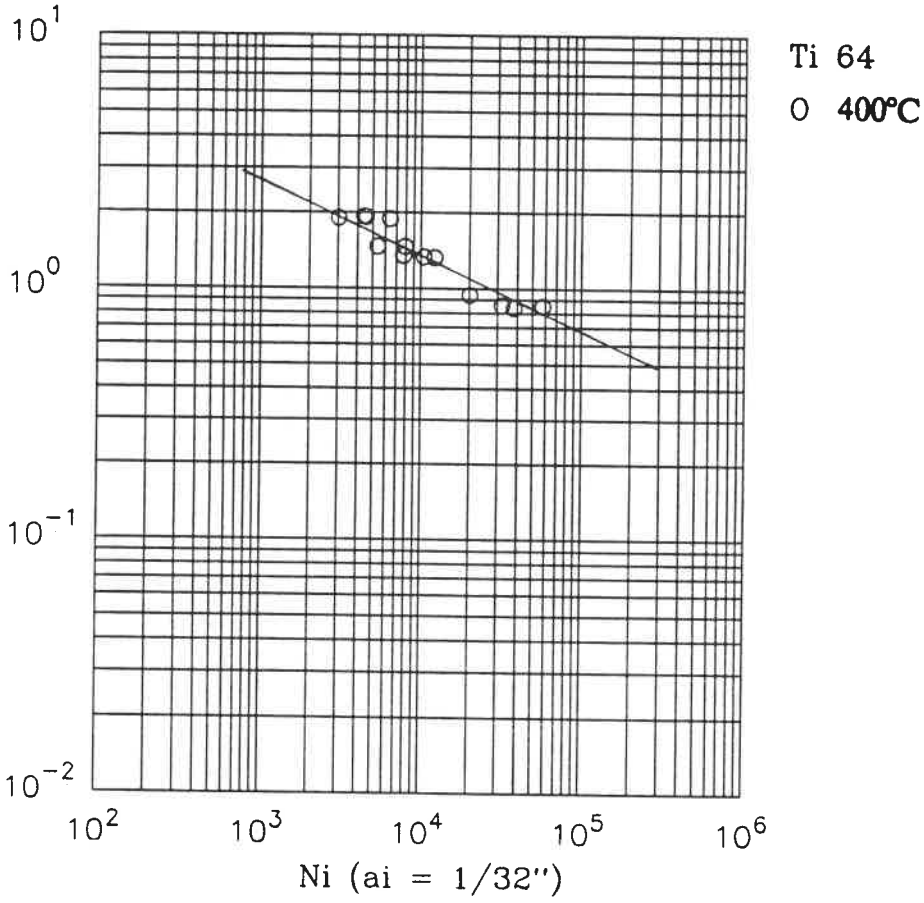

ıre 3.10 LCF life data of the SEN specimens correlated to the notch plastic in. (Ti64, at 400°C).

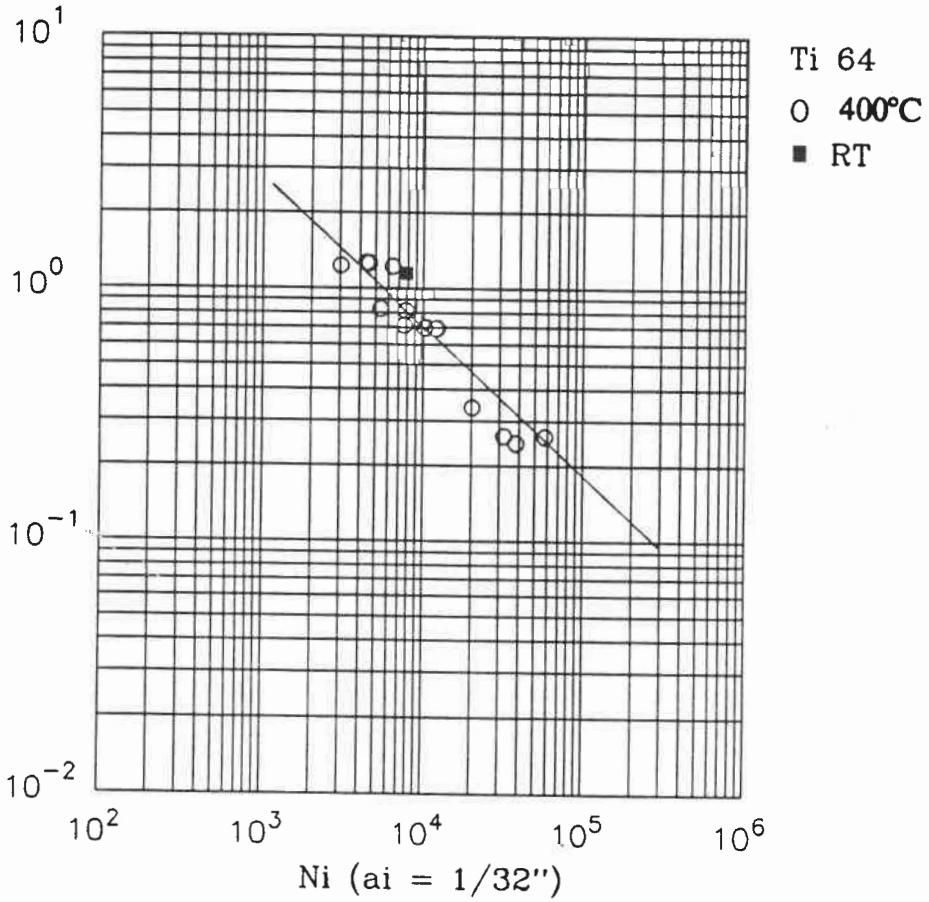

gure 3.11 LCF life data of the SEN specimens correlated to the notch plastic ain range. (Ti64, at 400° C and RT).

TS_NAME	Sp. No.	δE %	R_ratio	E sec-1	waveform	Temp. (°F)	Remarks
LCF31	TIB31	0.350	0	1.1667E-3	triangular	900	LCF+FCG STNC
LCF32	TIB32	0.300	0	1.0000E-3	triangular	900	LCF STNC
FCG32	TIB32	0.300	0	1.0000E-3	triangular	220	FCG STNC
LCF33	TIB33	0.300	0	1.0000E-3	triangular	900	LCF STNC
FCG33	TIB33	0.200	0	0.6666E-3	triangular	RT	FCG STNC
CYC34	TIB34	0.3-1.2	-1	1.0000E-3	triangular	900	cyclic curves
LCF35	TIB35	0.250	0	0.8333E-3	triangular	900	LCF STNC
FCG35	TIB35	0.200	0	0.6666E-3	triangular	625	FCG STNC
LCF36	TIB36	0.250	0	0.8333E-3	triangular	900	LCF STNC
FCG36	TIB36	0.250	0	0.8333E-3	triangular	625	FCG STNC
LCF37	TIB37	0.300	0	1.0000E-3	triangular	900	LCF STNC
FCG37	TIB37	0.250	0	0.8333E-3	triangular	RT	FCG STNC
LCF38	TIB38	0.250	0	0.8333E-3	triangular	750	LCF/FCG STNC
LCF39	TIB39	0.300	0	1.0000E-3	triangular	750	LCF/FCG STNC
LCF40	TIB40	0.275	0	0.9166E-3	triangular	750	LCF/FCG STNC
LCF41	TIB41	0.250	0	0.8333E-3	triangular	750	LCF/FCG STNC

STNC : straincontrolled test
LCF: crack initiation test
FCG: crack propagation test

Table 3.4 The main result of LCF testsσn Ti6246 at 480°C.

SPECIMEN	δEf %	δEpl %	Temp. °C	R_ratio	Ef s-1	Nl (al=0.4mm)
LCF31	0.350	0.5389	480	0	0.00167	3,758
LCC36	0.350	0.7208	480	0	0.00167	2,410
LCF38C	0.350	0.8007	480	0	0.00167	2,621
LCF32	0.300	0.3943	480	0	0.0010	3,919
LCF33	0.300	0.3939	480	0	0.0010	4,802
LCF37d	0.300	0.2446	480	0	0.0010	9,181
LCF39	0.300	0.4213	480	0	0.0010	5,719
LCF40	0.275	0.3602	480	0	0.00092	4,905
LCF35	0.250	0.1734	480	0	0.000833	6,193
LCF38	0.250	0.1848	480	0	0.000833	47,880
LCF41	0.250	0.1751	480	0	0.000833	7,691

δEf : far field strain range;
δEpl : notch effective plastic strain
Ef : far field strain rate

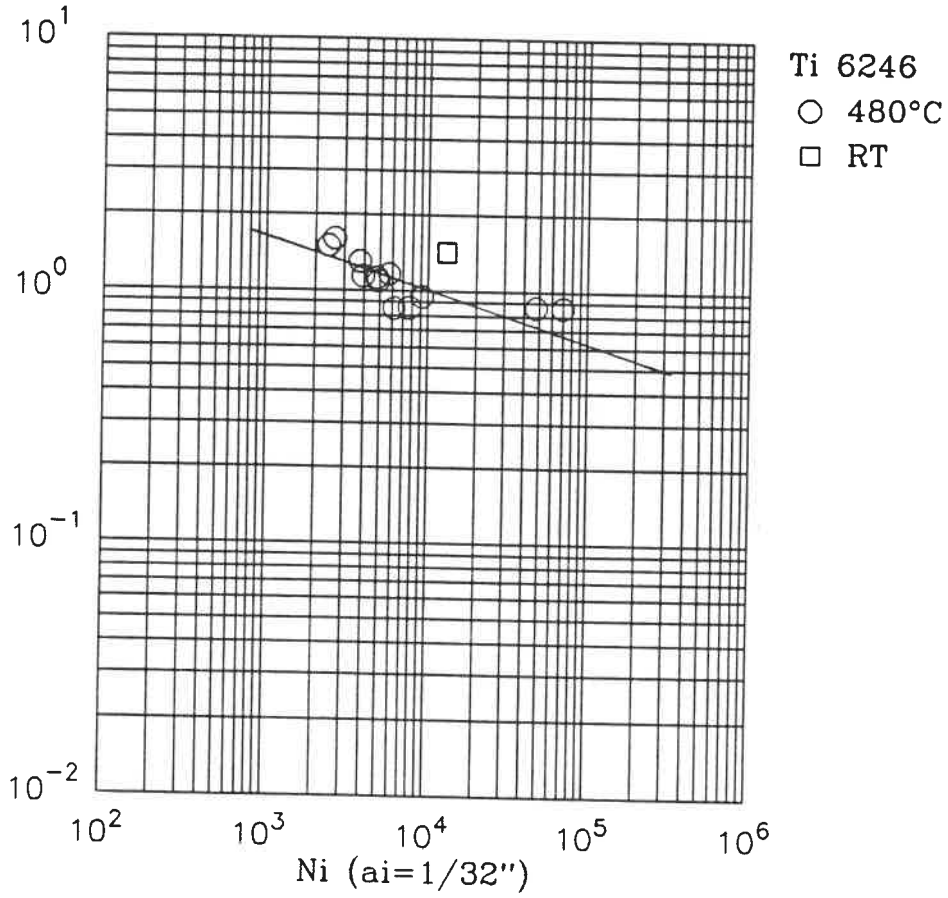

ıre 3.12 LCF life data of the SEN specimens correlated to the notch total strain.
246, at 480° C and RT).

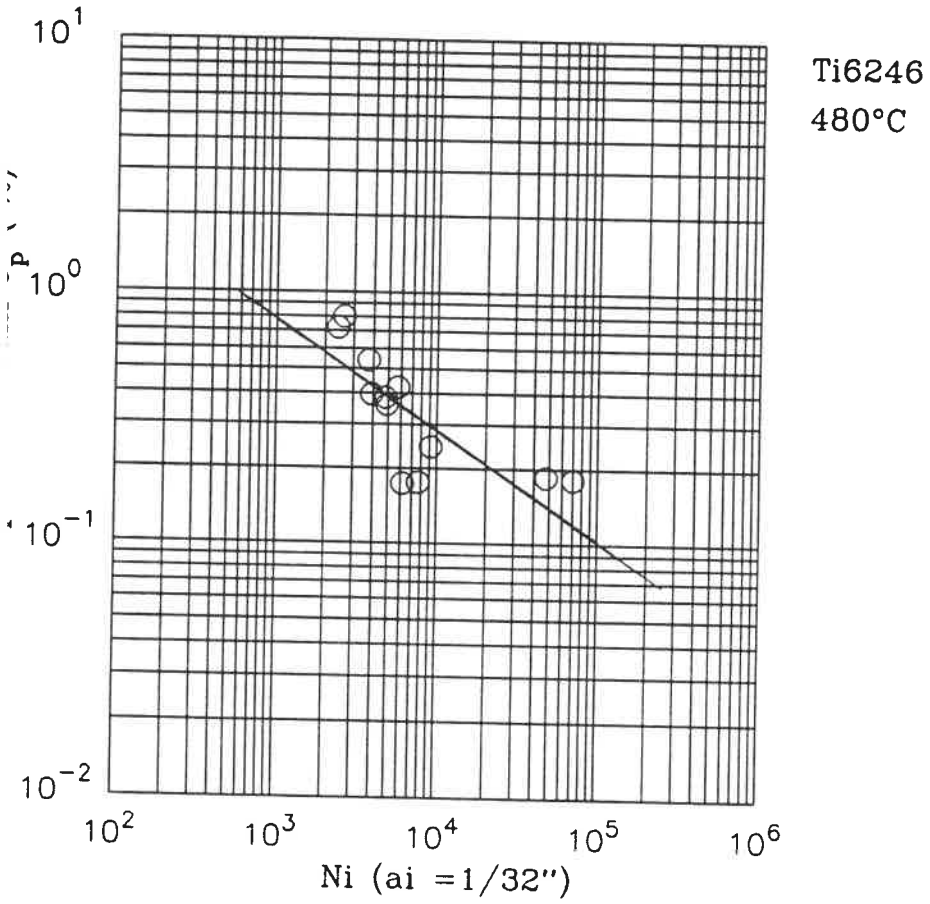

ure 3.13 LCF life data of the SEN specimens correlated to the notch plastic in. (Ti6246, at 480°C).

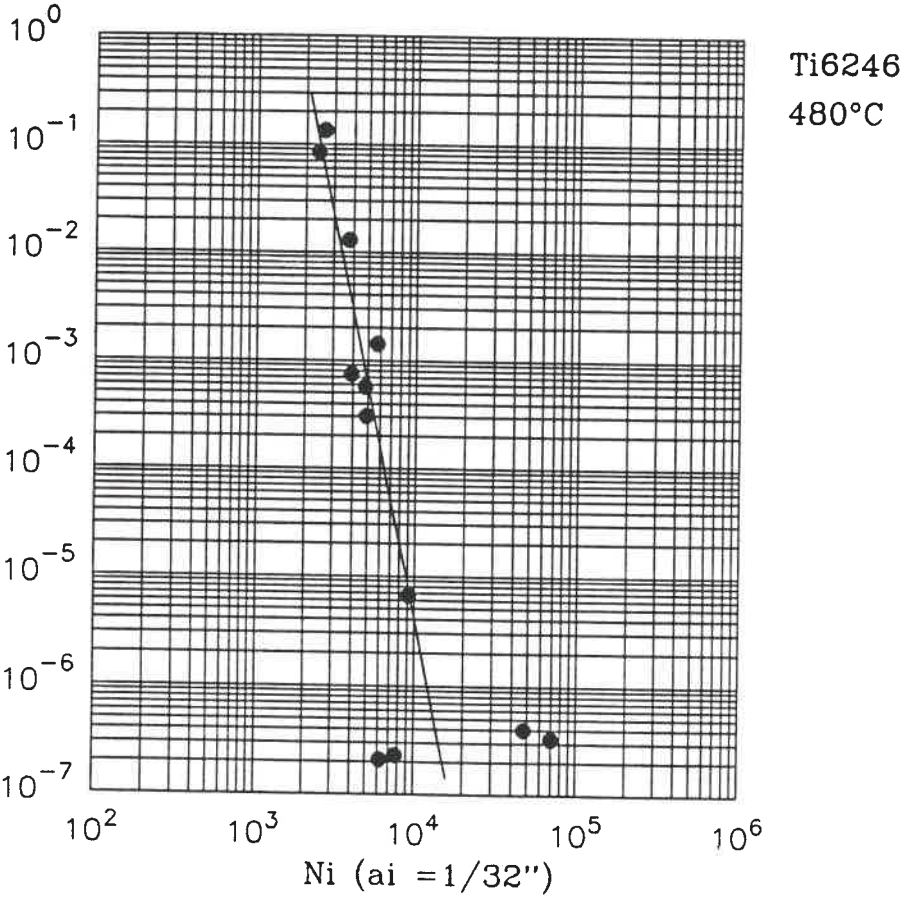

ıre 3.14 LCF life data of the SEN specimens correlated to the notch plastic in range. (Ti6246, at 480°C).

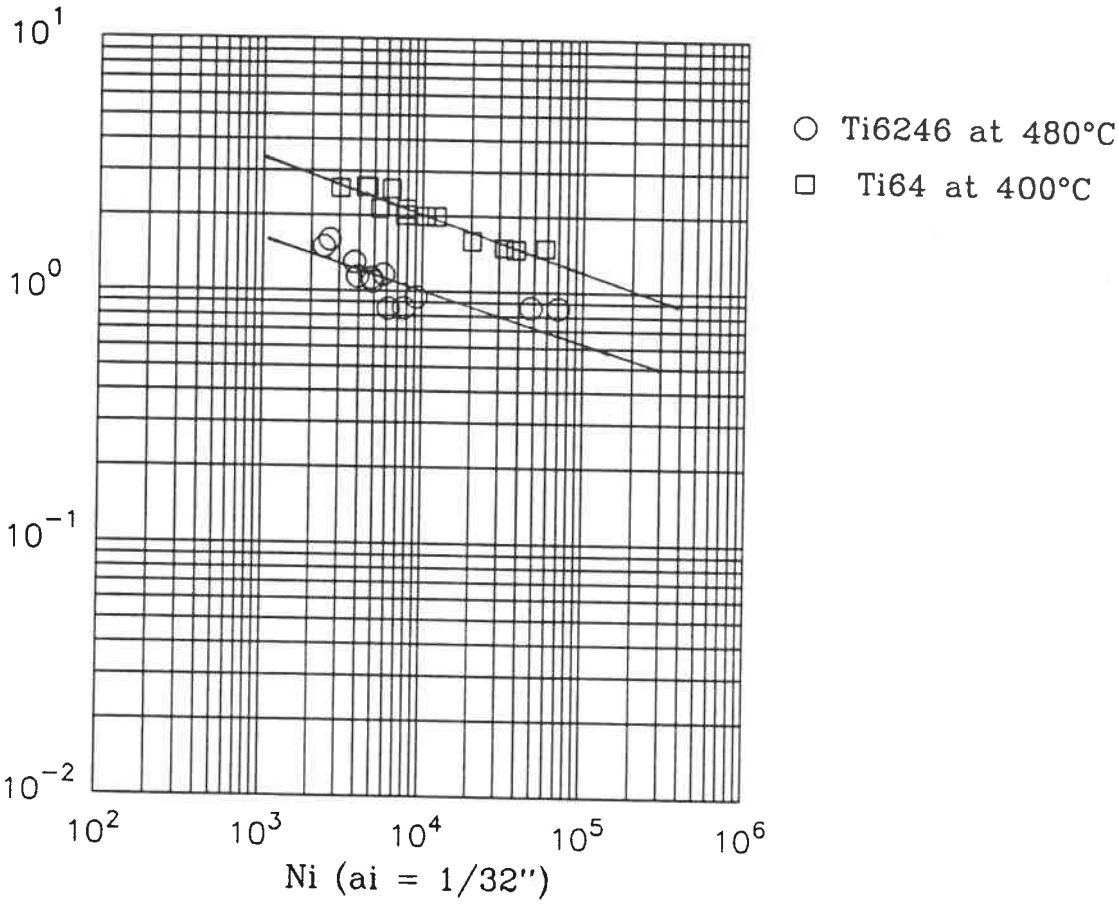

re 3.15 A comparison between the LCF life data of Ti6246 at 480°C and that of at 400°C when correlated to the notch total strain.

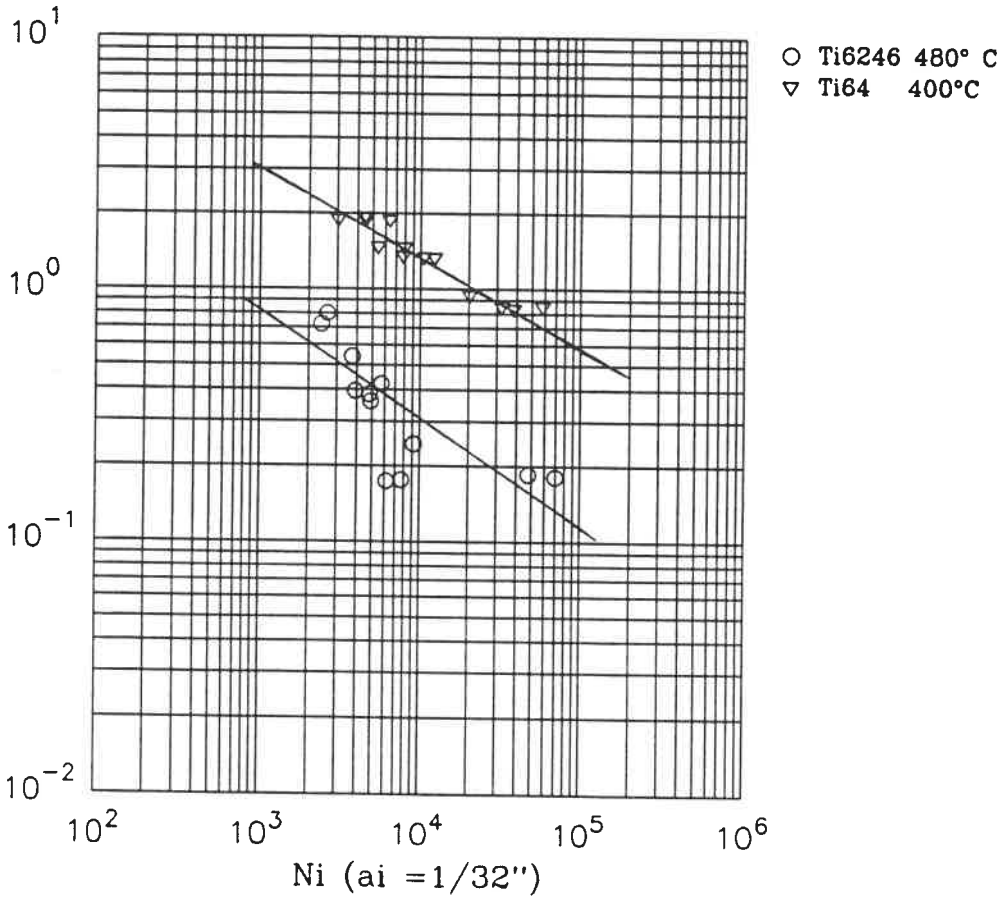

re 3.16 A comparison between LCF life data of Ti6246 at 480°C and that of at 400°C as they are correlated to the notch plastic strain.

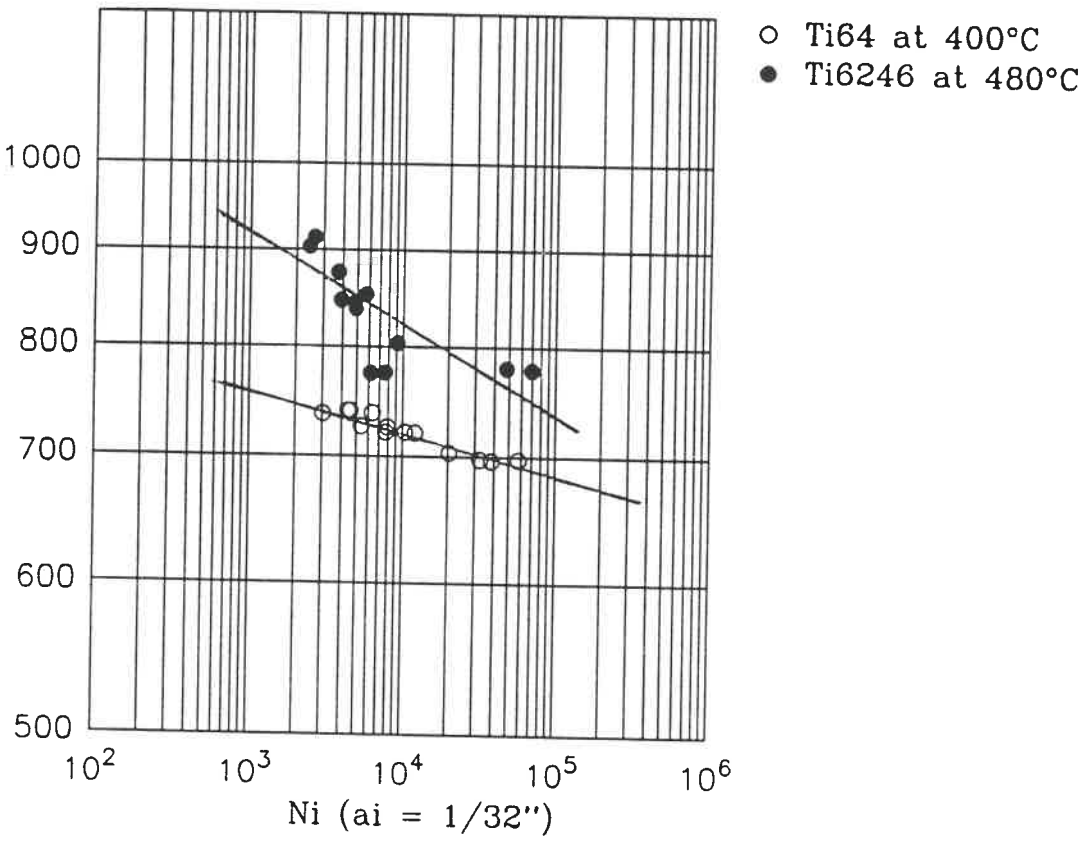

3.17 A comparison between LCF life data of Ti6246 at 480°C and that of t 400°C when they are correlated to the notch root peak stress.

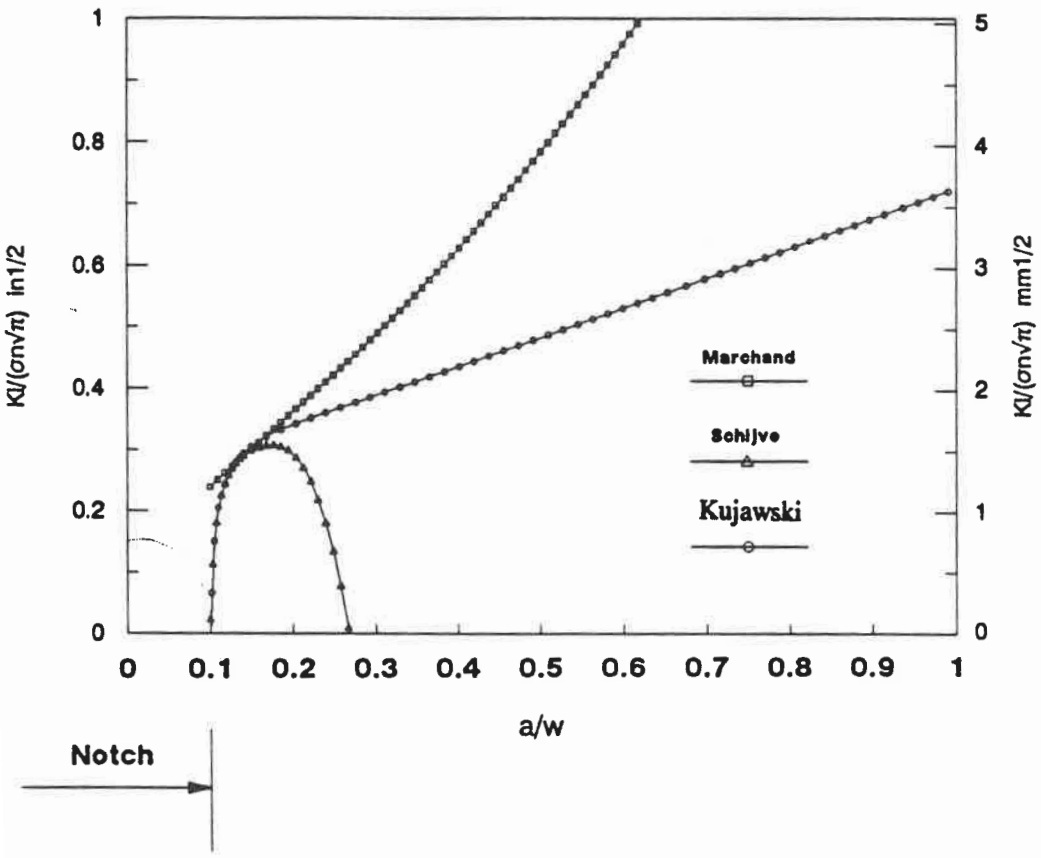

gure 3.18 The three stress intensity factor solutions for the cracks emanating from e root of the notch. They are either based on the notch elastic stress or the far ld stress for long cracks.

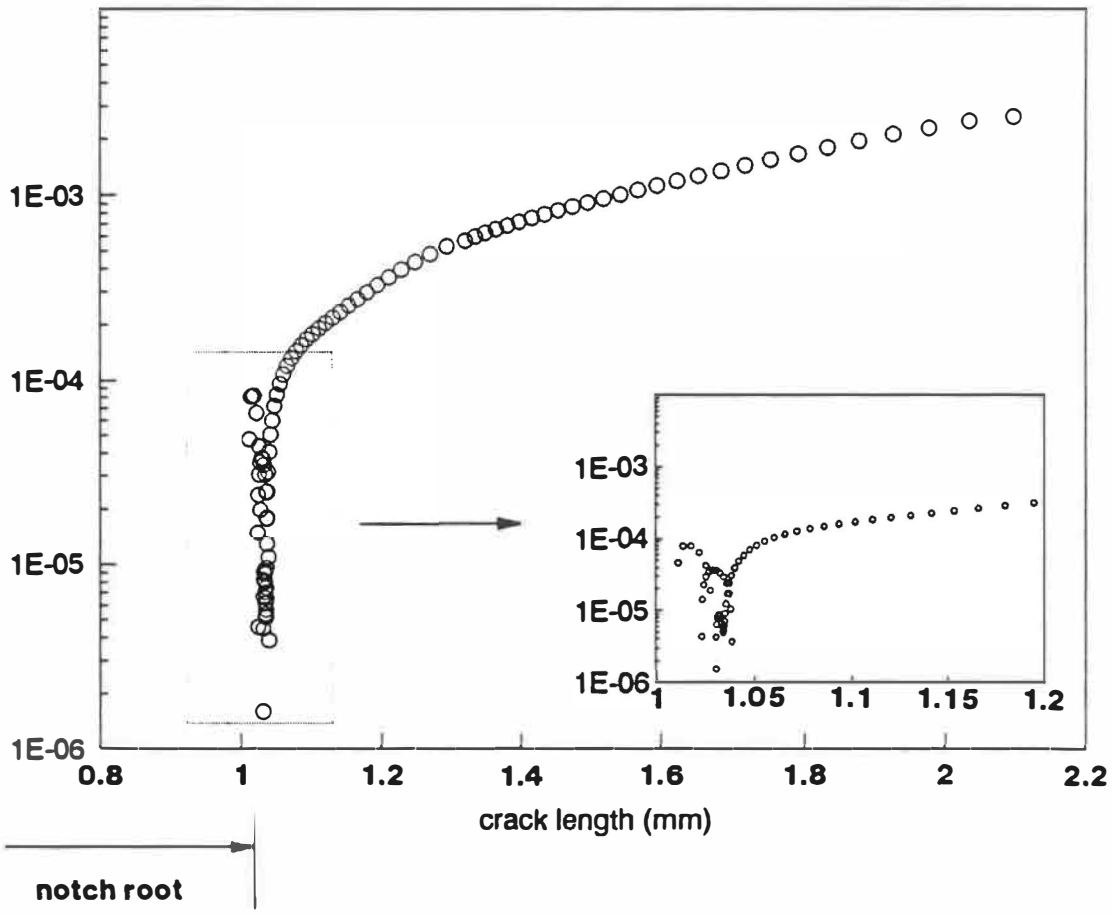

gure 3.19 Crack growth rate as a function of crack length. Note that the da/dN anges irrationally when $\Delta a < 60\mu m$ which is the about the average size of equaxied phase particles. (Ti64, 400°C).

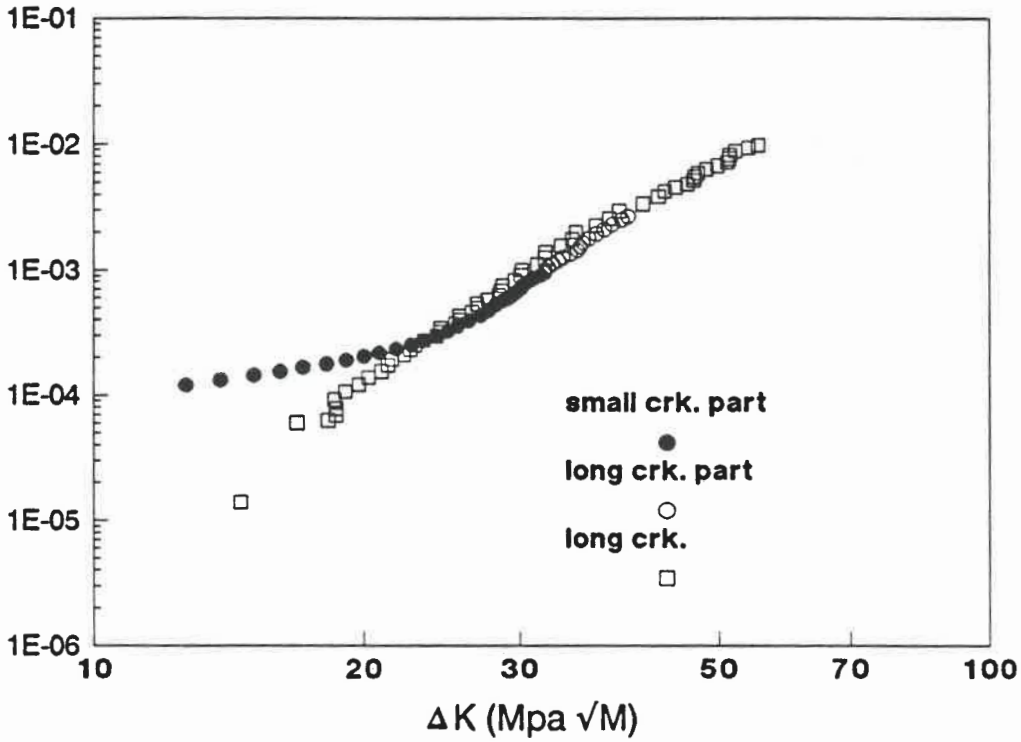

ure 3.20 A typical crack growth data for the SEN specimen. The crack growth e is higher than that of long crack data for $\Delta a < 130\mu m$ as a result of the notch stic strain field. (Ti64, 400°C).

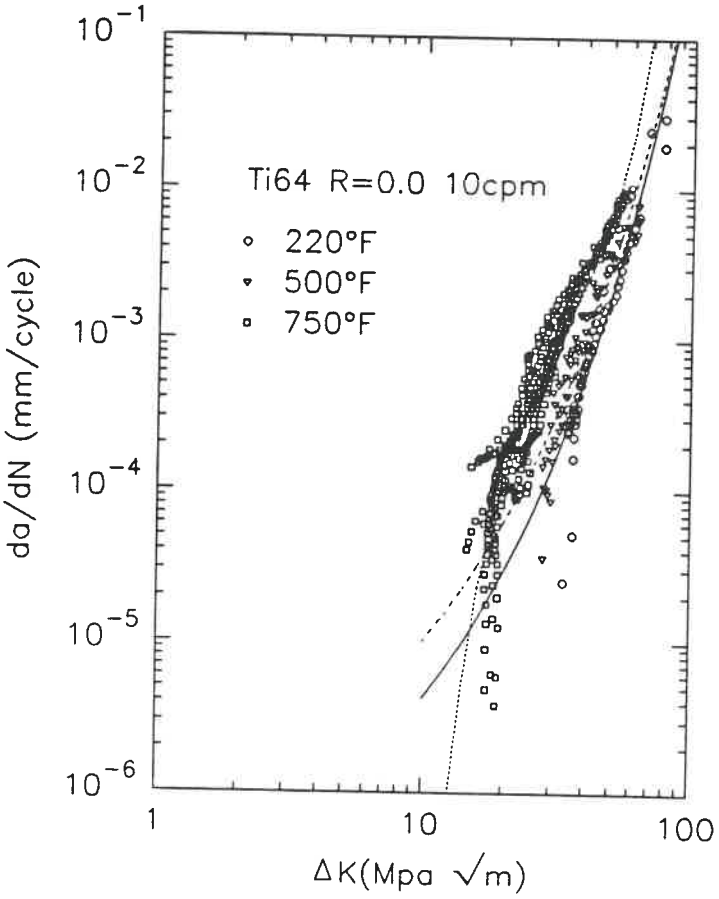

ure 3.21 The influence of temperature effect on the fatigue crack growth rates of
64.

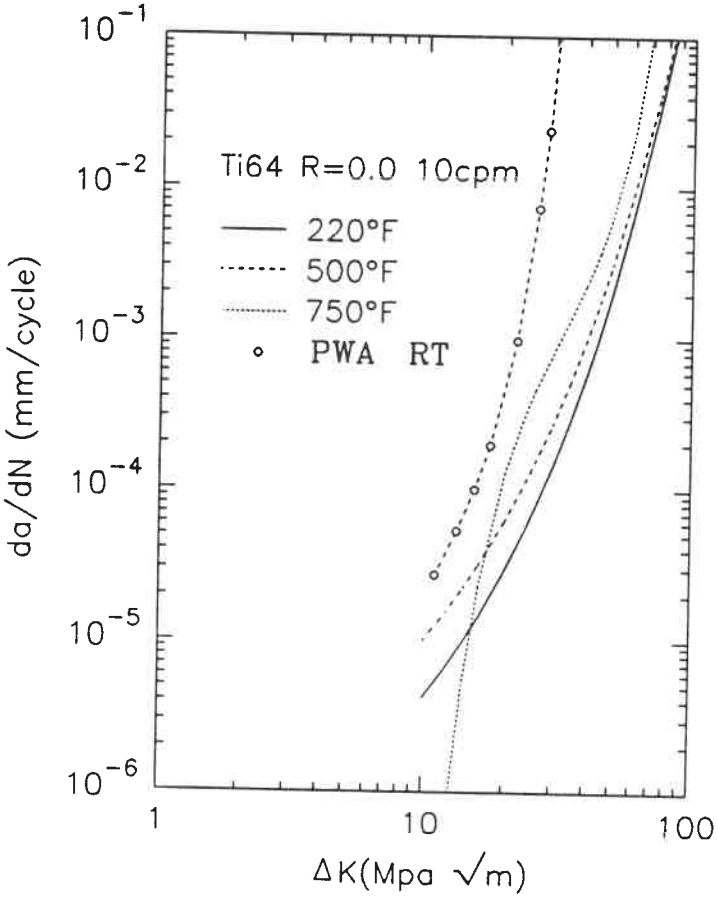

igure 3.22 A comparison between the FCG data at three test temperatures and the istorical data of PWA. (Ti64).

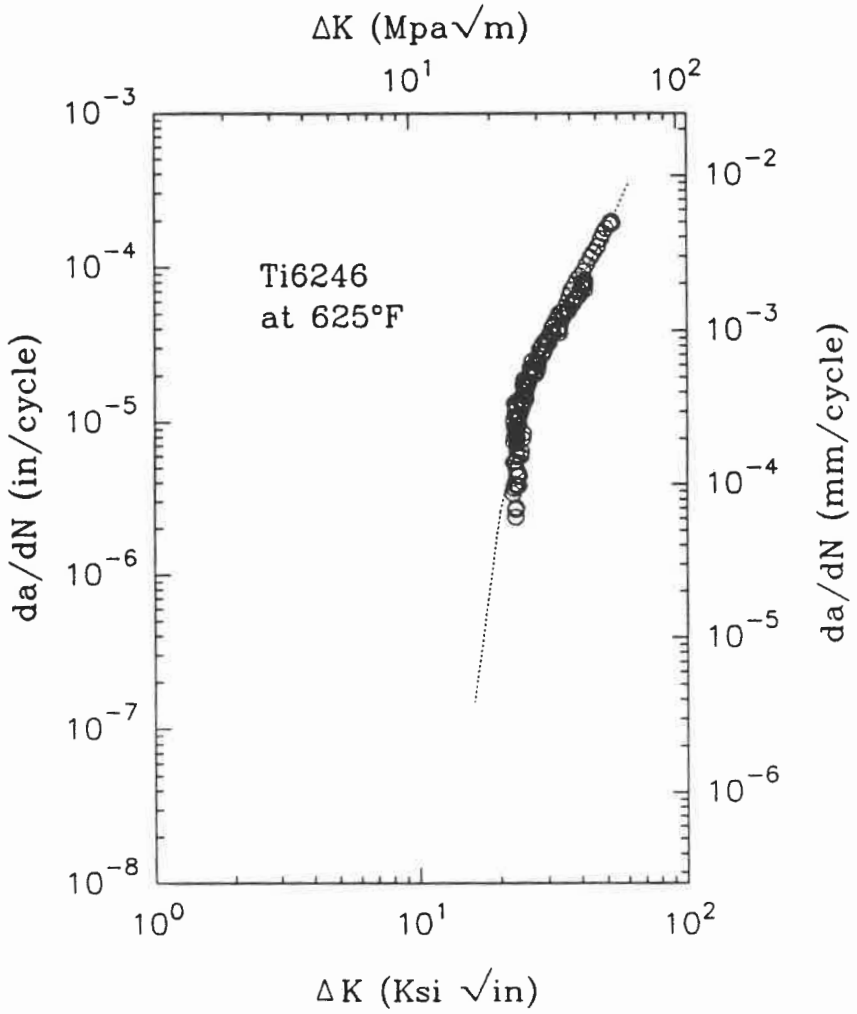

igure 3.23 Fatigue crack growth rate data of Ti6246 at 330°C. This data can be very ell fitted using a sinh function.

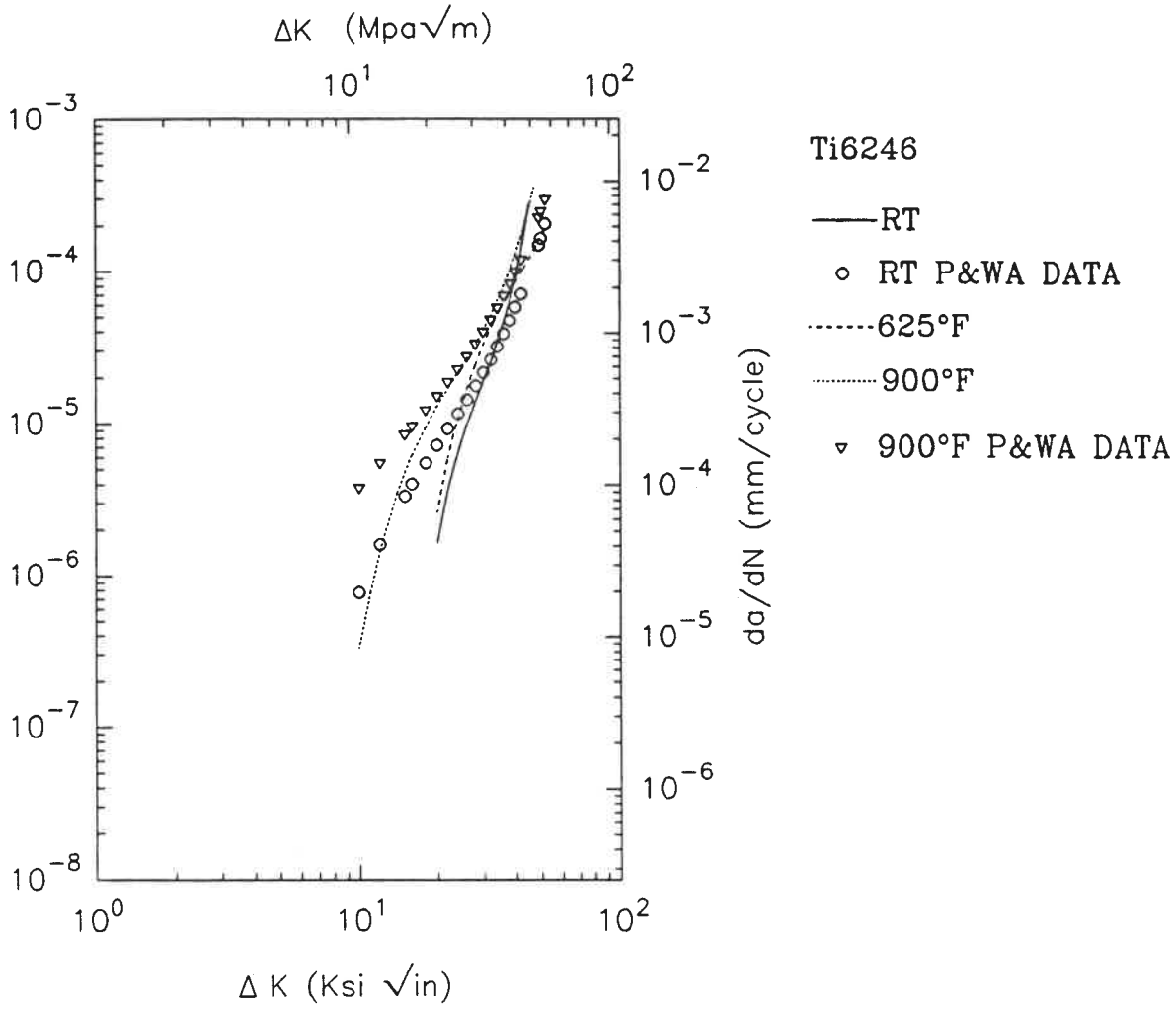

igure 3.24 Fatigue crack growth rate data for Ti6246 at three temperatures ɔmpared to the P&WA historical data.

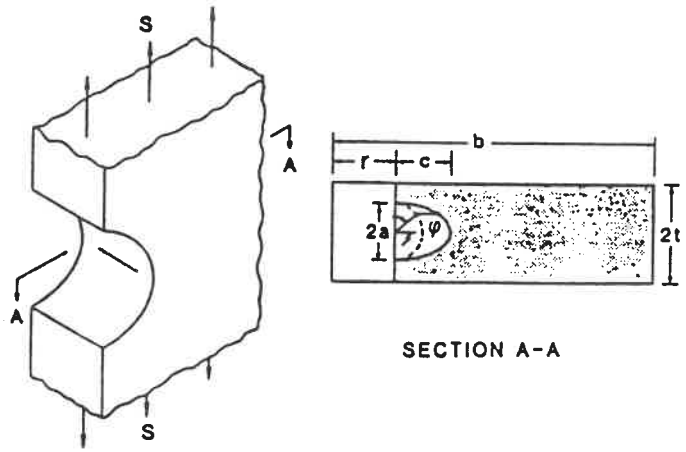

$$K = S(\pi a/Q)^{1/2} F_m(a/t, a/c, r/t, \phi)$$

$$Q = 1 + 1.464(a/c)^{1.65} \quad \text{for } a/c \leq 1$$
$$Q = 1 + 1.464(c/a)^{1.65} \quad \text{for } a/c > 1$$

Figure 3.25 A stress intensity factor model proposed by Newman[148-150] for a surface crack at a semi-circular notch.

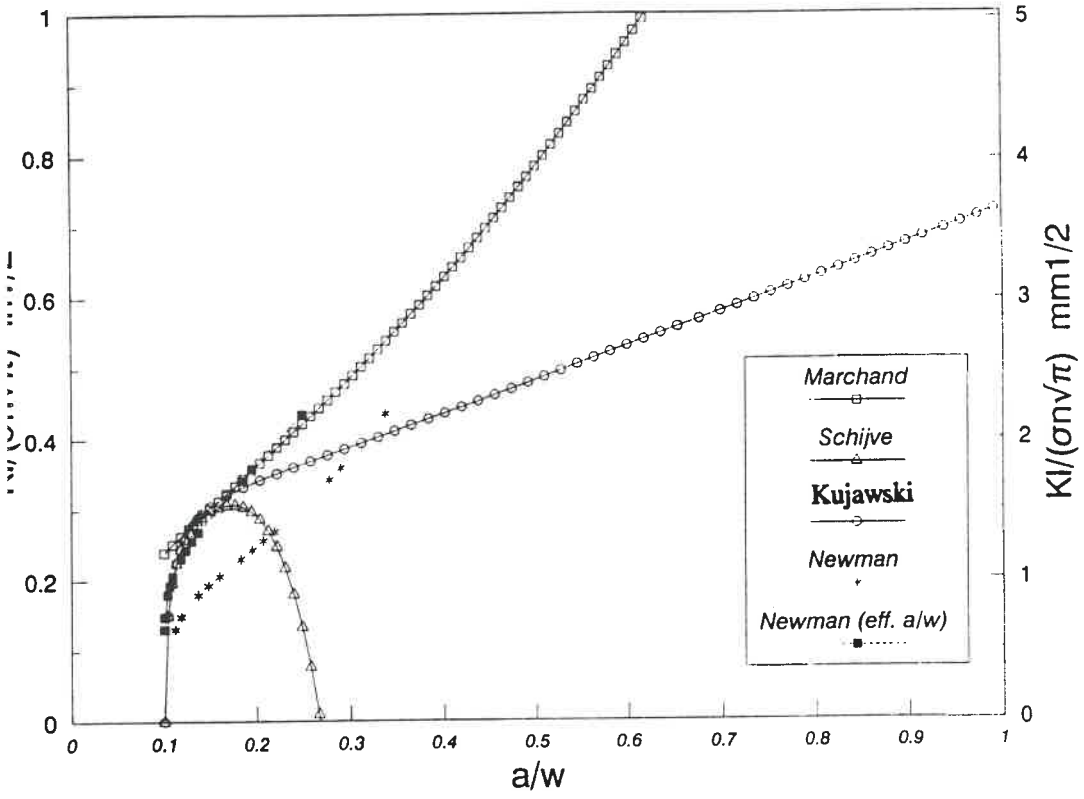

ıre 3.26 A comparison between the penny-shaped surface crack K_I model of ′man and the through-thickness crack models.

CHAPTER 4

THERMAL-MECHANICAL-FATIGUE CRACK GROWTH IN TITANIUM ALLOYS

4.1 INTRODUCTION

As the main objective of the joint research project, strain-controlled thermomechanical fatigue crack growth (TMFCG) tests have been performed on two titanium forgings, namely Ti64 and Ti6246. An advanced alternative current potential drop (ACPD) measurement technique has also been successfully employed to perform on-line monitoring of fatigue crack growth in specimen tested under isothermal and TMF conditions.

Thermal-mechanical fatigue cycling is expected to introduce a multitude of cyclic deformation and damage mechanisms. During the higher temperature portion of the TMF cycle, plastic deformation and various time-dependent creep mechanisms may be operative, along with aggressive environmental attack and metallurgical changes. At the lower temperature, these mechanisms are reduced in number or are excluded because of the lack of necessary thermal activation. This alternate activation of high and low temperature mechanisms can result in a combination of mechanisms not normally encountered in isothermal fatigue.

The influence of TMF cycle on the fatigue crack growth resistance (da/dN) is of great importance to the engine structural integrity program (ENSIP). The common procedure is to use isothermal data at the maximum temperature of a cycle or of a spectrum block to calculate the TMF crack growth rates. This procedure can often be extremely conservative and can lead to unrealistically low crack propagation life prediction. Moreover, there are instances where the procedure is non-conservative, that is TMF crack growth rates exceed those of the maximum temperature isothermal case[154]. Hence, there are needs to accurately model the TMF crack growth behavior.

In the following sections, the data correlation of the TMF tests is described. The emphasis is put on evaluating the effect of the interaction between strain and temperature on the crack growth rates.

4.2 TMFCG EXPERIMENTAL CONDITIONS

SEN specimens were used in the thermal-mechanical fatigue crack growth testing program. The specimens were fabricated from Ti64 and Ti6246 disc forgings, and were pre-cracked by EDM. The notch size is 0.38 mm in width and 0.5 mm in depth. Before TMF cycling, each specimen was cycled at 10Hz at one third of the testing load level for 1 h 30 min to obtain a sharpened fatigue crack tip. The TMF test matrixes for the two alloys are listed in Tables 4.1 and 4.2.

All the tests were performed under fully reversed (R=-1.0) strain cycling. This R value was chosen to enlarge the strain-temperature phasing effect. The cycling period was kept as t_c=100 sec, i.e. 0.6 cpm or 0.01 Hz, for all tests. The TMFCG data have been obtained for Ti64 with temperature cycling between 150°C (300°F, Tmin) and 400°C (750°F, Tmax), and Ti6246 with temperature cycling between 200°C (392°F, Tmin) and 480°C (900°F, Tmax). Three types of TMF cycles were selected, which included in-phase (IP), out-of-phase (OP) and counter-clockwise diamond (CCD) or faithful cycle. Isothermal FCG tests at the two extreme temperatures (Tmin and Tmax) under the same cycling frequency were also carried out for the sake of comparison. Detailed testing procedures have been explained in Chapter 2.

4.3 FRACTURE MECHANICS PARAMETERS

During a TMF test, the far-field strain $\Delta\varepsilon$ was controlled, the nominal stress, which represents the material's response to the cycling, was measured by the load cell of the INSTRON 8500.

The stress intensity factor K_I is calculated by the equations suggested in Appendix 3 for the SEN specimen, which can be simplified as

$$K_I = \left(\frac{N}{BW}\right)\sqrt{\pi a}\, H(\varsigma, \eta, \eta_b) \quad . \tag{4.1}$$

where N the measured load, B the thickness of the specimen, W the width of the specimen, a the crack length measured from the specimen edge and $H(\varsigma\ \eta,\ \eta_b)$ a geometrical function which has been proposed by Marchand[51] .

Three types of fracture mechanics parameters, including stress intensity factor range, maximum stress intensity factor and strain intensity factor were used in the da/dN data correlation procedures. The stress intensity factor range ΔK_I, which is commonly used in FCG data correlation, is written as

$$\Delta K_I = (\frac{\Delta N}{BW}) \sqrt{\pi a}\, H(\varsigma, \eta, \eta_b) \ . \tag{4.2}$$

where ΔN is the measured load range during the strain-controlled cycling.

The maximum stress intensity factor K_{Imax} used in the data reduction can be written as

$$K_{Imax} = (\frac{N_{max}}{BW}) \sqrt{\pi a}\, H(\varsigma, \eta, \eta_b) \ . \tag{4.3}$$

where N_{max} is the peak values of the measured load. There exists a crack opening oad value N_{op} , and the effective stress intensity range ratio U is defined as

$$U = \frac{\Delta K_{eff}}{\Delta K} = \frac{(1 - R_{eff})}{(1 - R)}, \tag{4.4}$$

where $\Delta K_{eff}=K_{Imax}-K_{op}$, $R_{eff}=N_{op}/N_{max}=K_{op}/K_{Imax}$, and R the load ratio. The effective stress intensity range ΔK_{eff} controls the actual fatigue crack growth rate. Most literature studies suggest that U is a simple linear function of R and independent of K_{Imax}[155].

In the strain-controlled TMF tests, the R value is not a constant throughout a test. This complicates the calculation of U. Assuming that the crack is open as soon as the load becomes tensile, K_{Imax} is akin to the effective stress intensity factor range. Therefore K_{Imax} can be used to represent ΔK_{eff} in the following data correlation.

As discussed in Chapter 1, the strain intensity factor range ΔK_{ε} was also tried in the strain controlled type FCG testing despite the fact that it does not have a clear physical meaning. Here ΔK_{ε} is defined as

$$\Delta K_{\varepsilon}=\Delta\varepsilon\sqrt{\pi a}\,H(\varsigma,\eta,\eta_b)\ . \qquad (4.5)$$

where $\Delta\varepsilon$ is the far-field strain applied during the test.

4.4 TMFCG behavior of Ti46

Figure 4.1 shows the results of the thermal-mechanical fatigue crack growth data (da/dN) of Ti64, which have been correlated using the stress intensity factor range ΔK_I. It can be seen that the ΔK_I failed to relate the da/dN data from

different TMF and isothermal tests. The scatter in the data becomes even larger in the higher ΔK_I region. This is due to the fact that the compressive part of the load cycle which is affected by the temperature cycling, does not contribute to the crack growth.

From Figure 4.2, one sees that the strain intensity factor ΔK_ε also does not give a satisfactory correlation for the da/dN data. Larger scatter can again be observed at higher ΔK_ε . Particularly, the data from the in-phase TMF condition are much lower than other conditions, which contradict the experimental observations and the fractographic analysis presented in Chapter 5.

Good correlation is obtained using ΔK_{eff} (i.e. K_{Imax}) as plotted in Figure 4.3. It can be seen that the da/dN data from all the three TMF conditions fall in a narrow scatter band. More precisely, the cracks grew slightly faster in the in-phase TMF tests than in the out-of-phase tests. Faithful TMF data is in between the in-phase and out-of-phase data and closer to the out-of-phase condition. When comparing with the respective isothermal FCG data shown in Figure 4.4, one can find that the in-phase data are quite close to the data obtained under isothermal tests at Tmax (400°C), while out-of-phase TMF test results are closer to the isothermal test data at Tmin. The slopes of all the curves are basically identical, indicating similar crack growth mechanisms. This has been confirmed by fractographic analysis in Chapter 5. Since the Ti64 forging has higher ductility which strongly depends on temperature, this scatter is believed to be attributed to a crack closure effect that is dependent on the strain vs. temperature relationships. As a result, the K_{Imax} cannot accurately represent the actual operating ΔK_{eff}.

Fractographic observation in Chapter 5 reveals evidence of crack tip closure and associated surface rubbing in Ti64 TMF tests. These closure processes are induced by combination of crack tip plasticity, oxide and crack surface roughness. The crack tip plasticity is the major factor affecting the crack opening, since the crack tip opening displacement (CTOD) and the plastic zone size are dependent on the yield stress, and the yield stress of Ti64 is reported to be strongly dependent on temperature[69].

As shown in Figure 4.5, the TMF data are compared with the isothermal FCG testing at Tmax (400°C) with 10 cpm loading frequency, which have been described in Chapter 3. It can be seen that the crack growth rates at higher loading frequency (the cycling rate was 16.7 times higher than 0.6 cpm used in TMF tests) tested at 400°C are quite close to out-of-phase TMF and to the isothermal test data at Tmin (150°C). This indicates that higher cycling rate will reduce the temperature dependence of FCG behavior for this alloy. The historical FCG data from the P&WA data base which were obtained using CT specimen under load cycling rate of 10 cpm also shows no significant temperature effects for FCG tests at RT and 400°C.

This is quite an interesting result and can be attributed to the strain rate effect on the material's stress-strain curve at elevated temperatures. In the same research program, a remarkably high stress relaxation rate immediately after straining (at $\dot{\varepsilon} \approx 1.33E-3 \sec^{-1}$) was observed in the stress relaxation tests of Ti64 at 400°C[156], which indicated high anelastic behavior of the titanium alloy due to

internal friction mechanisms[157]. The material's inelastic deformation is dependent on the strain rate. At a higher cycling rate, the crack tip plastic zone size becomes smaller. Thus the effect of crack closure becomes less important to an extent to affect the crack growth rates. As a matter of fact, the strong damping effect in Ti64 has been used in artificial human arthroses manufacture for many years.

4.5 TMFCG behavior of Ti6246

4.5.1 The fatigue crack growth data

Comparing Figure 4.1 and 4.2 for Ti64, Figures 4.6 and 4.7 show quite similar results obtained from the TMFCG tests on Ti6246 when the da/dN data are correlated to ΔK_I and ΔK_ε. This indicates again that ΔK_I and ΔK_ε are not the crack tip controlling parameters during the crack growth. Therefore they cannot effectively be used to correlate the da/dN data from all the TMF testing conditions.

Satisfactory correlation has been obtained using ΔK_{eff}. The result is presented in Figure 4.8. As can be seen that the in-phase data are very close to the data from isothermal tests at Tmax (480°C), while out-of-phase TMF test results are closer to isothermal tests data at Tmin (200°C). Faithful TMF data is in between the in-phase and out-of-phase data and closer to the out-of-phase data. Remarkable effects of environmental (oxidation) assisted crack growth can be observed at 480°C isothermal FCG and in-phase TMF tests at lower growth rate (da/dN ~ 10^{-3} nm/cycle). Similar results have been reported by Specht[22] for IMI834 (see

Section 1.4.2). This accelerated crack growth due to environment are supported by the microfractographic study of the fractured surfaces in Chapter 5. It was found that the accelerated crack growth was due to oxygen induced embrittlement in the material near the crack tip at elevated temperatures. At higher crack growth rates, all the data merge to a smaller scatter band and the environmental effect becomes minor.

In Figure 4.9, the da/dN data from the two most detrimental cases (in-phase TMF and isothermal test at T_{max}) are plotted. Recalling the typical shape of stress corrosion cracking SCC type da/dN curves[158], the plateau-like shape of the curves appears attributable to a time-dependent da/dN component which is independent on the stress intensity factor.

4.5.2 A model for environmental assisted fatigue crack growth

In order to quantify the accelerated crack growth in Ti6246 at elevated temperatures, various mechanistic based modeling approaches[159-168] were studied.

Considering the engineering applicability, a simple model based on damage accumulation of different damage mechanisms is proposed. In the cases where there is strong environmental attack (typically oxidation) contribution, the total fatigue crack growth in material can be attributed to fatigue and oxidation, i.e.

$$\left(\frac{da}{dN}\right)^{t} = \left(\frac{da}{dN}\right)^{f} + \left(\frac{da}{dN}\right)^{ox} \quad . \tag{4.6}$$

where $(da/dN)^f$ is controlled by cycling cycle-dependent processes which can be correlated by ΔK_I-based fracture mechanics parameters, and $(da/dN)^{ox}$ is controlled by time-dependent processes which are strongly dependent on temperature and related to oxidation kinetics and the thermal activation energy. It is more convenient to write $(da/dN)^{ox}$ as

$$\left(\frac{da}{dN}\right)^{ox} = \left(\frac{da}{dt}\right)^{ox} \bullet t_{eff} \tag{4.7}$$

where the t_{eff} is the effective period in which the oxidation-assisted cracking mechanisms operate. In the analysis of the Ti6246 TMF data, it is assumed that these mechanisms only operate when the load N is positive, since compressive stresses would close the crack and prevent the adsorption of oxygen on the crack surface at crack tip. The oxidation cracking rate $(da/dt)^{ox}$ is assumed to be controlled only by oxygen diffusion processes along interfaces and grain boundaries in the material. As explained in Section 1.4.3, $(da/dt)^{ox}$ can be written as

$$\left(\frac{da}{dt}\right)^{ox} = \left(\frac{da}{dt}\right)_0^{ox} \bullet \exp\left(\frac{-Q}{RT}\right) , \tag{4.8}$$

where $(da/dt)_0^{ox}$ is a constant, Q the apparent activation energy, R the universal gas constant and T the temperature in °K. From Eq.(4.7), we also have

$$\left(\frac{da}{dN}\right)^{ox} = \left(\frac{da}{dN}\right)_0^{ox} \bullet \exp\left(\frac{-Q}{RT}\right) , \qquad (4.9)$$

where $(da/dN)_0^{ox}$ is a constant for a specified effective period t_{eff}.

The constants can be determined from isothermal FCG tests at Tmax and Tmin, as they are shown in Figure 4.10. One can obtain

$$(da/dt)_0^{ox} = 2.36E\text{-}4 \text{ mm/sec } (9.295E\text{-}6 \text{ in/sec})$$

and

$$Q = 16.9 \text{ kj/mol.}$$

The oxidation crack growth component $(da/dN)^{ox}$ (mm/cycle) for isothermal tests can therefore be written as

$$\left(\frac{da}{dN}\right)^{ox} = 1.18E-2 \exp\left(\frac{-16.9}{RT}\right) . \qquad (4.10)$$

Using Eq.(4.6), the fatigue crack growth component $(da/dN)^{f}$ can be obtained and plotted as a function of K_{eff} as illustrated in Figure 4.11. It can be seen that the da/dN data due to fatigue damage follows very well the Paris' law of fracture mechanics and does not depend on the test temperatures.

The same principle can be applied to TMF tests. Considering the temperature was varying during the TMF cycling, an integral type equation can be written as

$$\left(\frac{da}{dN}\right)^{ox} = \int_{t_1}^{t_2} \left(\frac{da}{dt}\right)_0^{ox} \exp\left(\frac{-Q}{RT(t)}\right) dt \quad , \tag{4.11}$$

where t_1 and t_2 pertains to the starting and finishing time in one cycle between which the oxidation assisted cracking mechanisms operate. We assume that these times also indicate the crack opening and closing process. The crack is treated as opening when the load N is positive and closing when N goes to compressive. The constants in Eq.(4.11) are the same as those in Eq.(4.8) which were determined by the isothermal data tested at the two extreme temperatures.

After partition of the oxidation assisted crack growth rate, the fatigue crack growth data for Ti6246 at 480°C°, 200°C and three TMF conditions are plotted in Figure 4.12. All the data can be reasonably fitted by a hyperbolic sine function.

As an attempt to directly relate the apparent activation energy Q measured to the activation energy of oxygen diffusion Q_{OX} in the titanium alloy, a parabolic oxidation law is used, i.e

$$l_0 = \sqrt{Dt_{eff}} \quad , \tag{4.12}$$

where l_0 is the length of the diffusion path after effective time t_{eff} of exposure. The diffusivity D can be written as

$$D = D_0 \exp(\frac{-Q_{ox}}{RT}) \quad . \tag{4.13}$$

Here D_0 is a pre-exponential frequency factor and Q_{ox} the activation energy of oxygen diffusion in the titanium alloy. It is very difficult to determine the fraction of the material with diffused depth l_0 that will actually break at the crack tip after each load cycle as a result of oxygen-induced embrittlement. However, from Eq.(4.12) and Eq.(4.13), the Eq.(4.9) can be modified into:

$$\left(\frac{da}{dN}\right)^{ox} = \left(\frac{da}{dN}\right)_0^{ox} \bullet \exp\left(\frac{-Q_{ox}}{2RT}\right) \quad . \tag{4.14}$$

Then, compare to Eq.(4.10), one can estimate that Q_{ox} is about 33.9 kJ/mol.

Since the time-dependent component can also be possibly attributed to creep crack growth. Additional analysis must be performed to evaluate this possibility. The activation energy for creep Q_c in the particular alloy can be obtained through extrapolation of the creep and creep-raputre data[169,170]. According to Dorn[157], the creep strain ε_c can be correlated by the parameter

$$\theta = t \exp(\frac{-Q_c}{RT}) \tag{4.15}$$

and $$\varepsilon_c = f(\theta, \sigma) . \quad (4.16)$$

where the instantaneous creep strain ε_C is a function of θ and stress. If this is valid up to fracture, the strain at rupture depends on the applied stress, for Q_C constant. Thus

$$\varepsilon_r = \theta(\sigma)$$

or

$$\theta_r = t_r \exp(\frac{-Q_c}{RT}) . \quad (4.17)$$

Hence, for a given stress, i.e the maximum nominal stress of the TMF tests, and two rupture points t_r at Tmax and Tmin, we have

$$Q_c = [RLn(t_{r1}/t_{r2})]/(1/T_{max} - 1/T_{min}) . \quad (4.18)$$

Based on the data published in Ref. [169], the value of Q_C is calculated as 307 KJ/mol for Ti6246.

4.6 DISCUSSION AND CONCLUSIONS

Figure 4.13 shows very good agreement between the modified TMFCG data n Figure 4.12 and the isothermal FCG data at Tmax (480°C) with 10 cpm loading requency. This can be explained by the fact that higher cycling frequency will

reduce the t_{eff} in Eq. (4.7), which is the effective period in which the oxidation assisted cracking mechanisms operate during one cycle. As a result, the oxidation components $(da/dN)^{ox}$ becomes less important as compared with the fatigue damage component $(da/dN)^{f}$. In Figure 4.14, the fitted TMFCG data is also compared with the P&WA historical data for this material, which were obtained from CT specimen fatigue testing with 10 cpm loading frequency at RT and 480°C (900°F). It can be seen that the modified TMFCG data are reasonably close to the P&WA data at 480°C in the range $da/dN = 5.0x10^{-4} \sim 1.0x10^{-2}$ mm/cycle. The slight difference to the P&WA data at RT can be attributed to the differences in crack tip plastic zone sizes at RT and 480°C. This will affect the effective ΔK.

For the convenience of design, the fatigue crack growth data for Ti6246 at 200°C and three TMF conditions in Figure 4.3 are plotted with reference to the isothermal FCG data at 480°C. That is the $(da/dN)^{f}$ data are added to their oxidation crack growth terms which are equivalent to the test condition at 480°F (the worst environment case) and plotted in Figure 4.15. This is a proposed form of da/dN data reduction in the conditions of strong environment effects. These data can be more effectively fitted by a hyperbolic sine function to yield a design curve.

Comparing the fitted design curve with the P&WA data again, as shown in Figure 4.16, one can find that the P&WA curve can underestimate the crack growth rate in the TMF conditions.

The differences observed in the environmental effects on these two Ti-base alloys can be attributed to the differences in their microstructures. It has been

discussed in Chapter 1 that there are significant differences in the microstructure of the two titanium alloys. Ti6246 has a coarse acicular α-phase microstructure with straight α/ß interfaces which promote localized oxygen diffusion and thus making it more vulnerable to environment attack. While Ti64 has a fine equiaxed α-phase microstructure with curved α/ß interface which reduces the effective oxygen diffusion coefficient and therefore is more resistant to environment attack.

It is worthwhile to note that the low cycling frequency (0.6 cpm) used in the TMF tests puts specimens under possible transition regime between fatigue and creep. However, the measured apparent activation energy, Q of 16.9 KJ/mol is much smaller than the value 307 KJ/mol that is found in creep conditions. Therefore the crack growth due to creep should be negligible.

The thermodynamic energies are also analyzed to support the conclusion that the time dependent crack growth found in the tests are in fact dominated by the oxidation mechanisms. As has been discussed in Section 1.3.1, using a parabolic oxidation law, the average activation energy for oxygen diffusion in titanium Q_{ox} is found to be about 33.8 KJ/mol. This value is lower than 213 KJ/mol which is a value reported by Liu and Welsch[21] in the study of bulk diffusion of oxygen to α-Ti at the range ~ 410°C. However the fractographic study shows strong evidence of interfacial cracking due to oxygen diffusion along interface boundaries. It is believed that the calculated Q_{ox} is closer to the value of the interfacial diffusion energy. Unfortunately, this data was not found for the titanium alloys.

The main conclusions drawn from this study can be summarized as follows:

- The ΔK and ΔK_{ε} are not appropriate fracture mechanics parameters to correlate TMFCG data for the titanium alloys;

- The K_{max} value taken as equal to ΔK_{eff} was found to correlate all the various isothermal and TMF crack growth rate data;

- The major time-dependent contribution to cracking was found to be oxygen-induced embrittlement;

- A model was developed to predict the TMF crack growth rate based solely on the isothermal data.

TS_NAME	Sp. No.	δE %	R_ratio	$\dot{E}$ sec-1	waveform	Temp. (°F)	Remarks
TMF51	TIA51	0.40	-1	1.6E-4	triangular	750 <---> 300	in-phase TMFCG
TMF52	TIA52	0.40	-1	1.6E-4	triangular	750 <---> 300	in-phase TMFCG *F
TMF53	TIA53	0.35	-1	1.4E-4	triangular	750 <---> 300	in-phase TMFCG
TMF54	TIA54	0.35	-1	1.4E-4	triangular	750 <---> 300	in-phase TMFCG
TMF58	TIA58	0.35	-1	1.4E-4	triangular	750 <---> 300	in-phase TMFCG
TMF55	TIA55	0.35	-1	1.4E-4	triangular	750 <---> 300	out-of-phase TMFCG
TMF56	TIA56	0.40	-1	1.6E-4	triangular	750 <---> 300	out-of-phase TMFCG
TMF81	TIA81	0.35	-1	1.4E-4	triangular	750 <---> 300	out-of-phase TMFCG
TMF57	TIA57	0.35	-1	1.4E-4	triangular	750 <---> 300	diamond TMFCG
FCG58	TIA58	0.35	-1	1.4E-4	triangular	300	isothermal
FCG83	TIA83	0.35	-1	1.4E-4	triangular	300	isothermal
FCG59	TIA59	0.35	-1	1.4E-4	triangular	750	isothermal
FCG84	TIA84	0.35	-1	1.4E-4	triangular	750	isothermal

TS_NAME	Sp. No.	δE %	R_ratio	$\dot{E}$ sec-1	waveform	Temp. (°F)	Remarks
TMF61	TIB61	0.300	-1	1.2E-4	triangular	900 <--> 392	in-phase TMFCG *F
TMF62	TIB62	0.350	-1	1.4E-4	triangular	900 <--> 392	in-phase TMFCG
TMF65	TIB65	0.375	-1	1.5E-4	triangular	900 <--> 392	in-phase TMFCG
TMF63	TIB63	0.350	-1	1.4E-4	triangular	900 <--> 392	out-of-phase TMFCG
TMF66	TIB66	0.375	-1	1.5E-4	triangular	900 <--> 392	out-of-phase TMFCG
TMF64	TIB64	0.375	-1	1.5E-4	triangular	900 <--> 392	diamond TMFCG
FCG61	TIB61	0.350	-1	1.4E-4	triangular	392	isothermal
FCG67	TIB67	0.375	-1	1.5E-4	triangular	900	isothermal

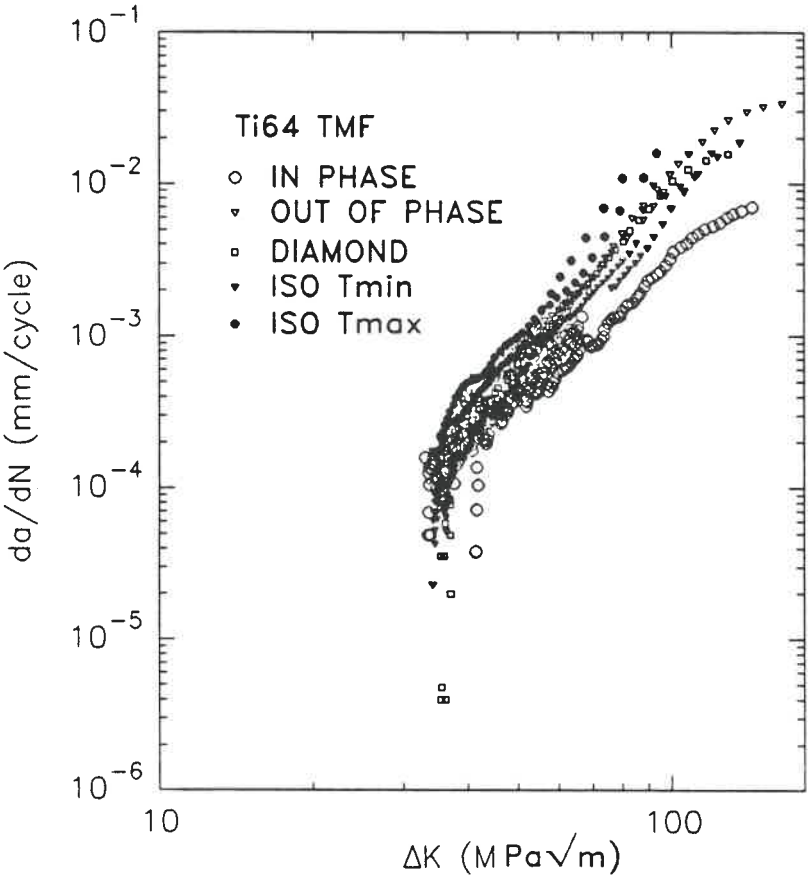

Figure 4.1 TMFCG data of Ti64 as they are correlated to the stress intensity factor range ΔK.

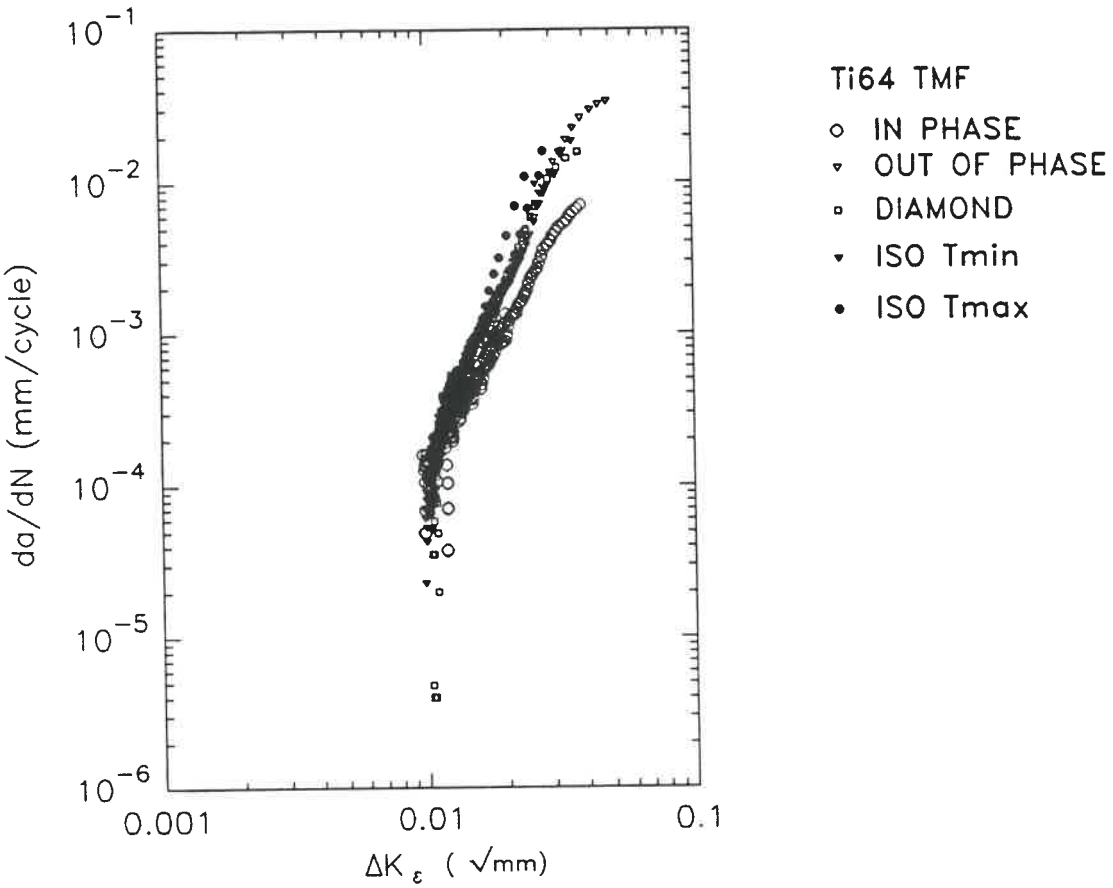

Figure 4.2 TMFCG data of Ti64 as they are correlated to the strain intensity factor range ΔK_ε.

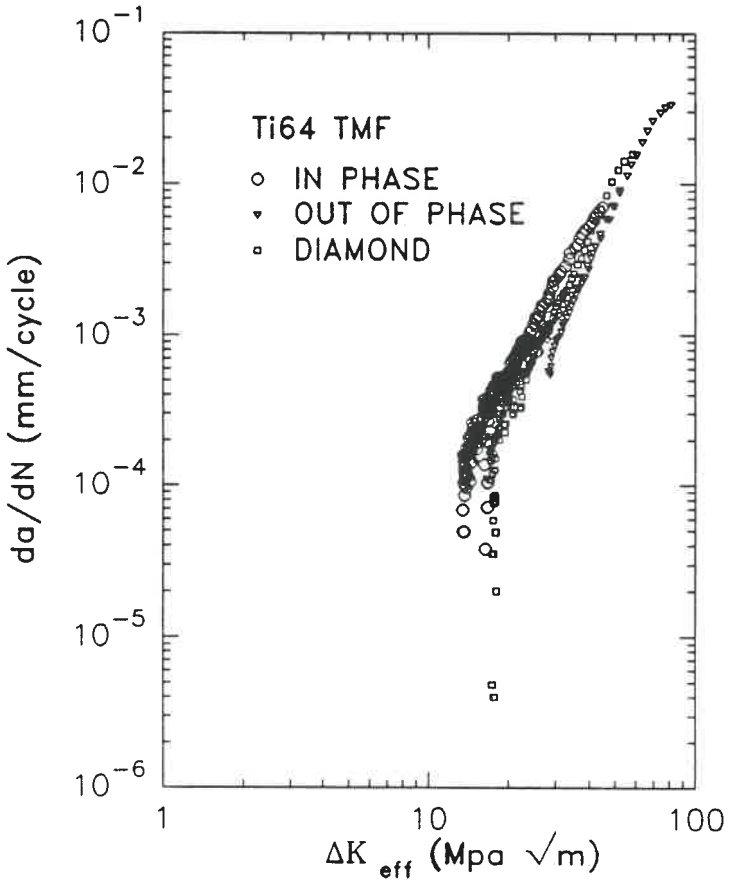

Figure 4.3 TMFCG data of Ti64 correlated to the effective stress intensity factor range ΔK_{eff}.

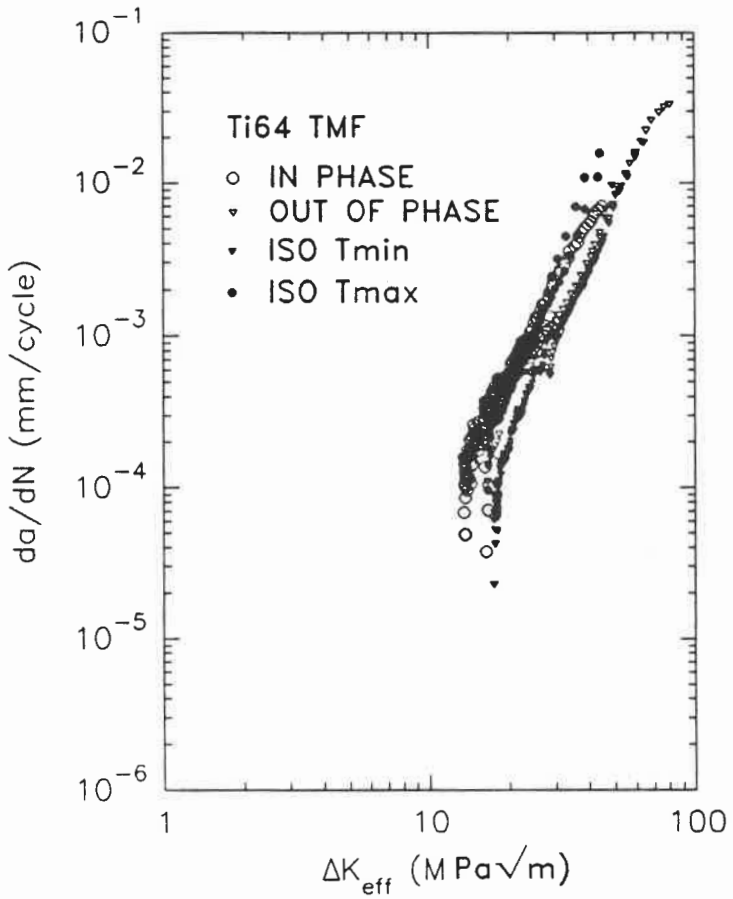

igure 4.4 A comparison between TMFCG data and isothermal FCG data of Ti64
; they are correlated to the effective stress intensity factor range ΔK.

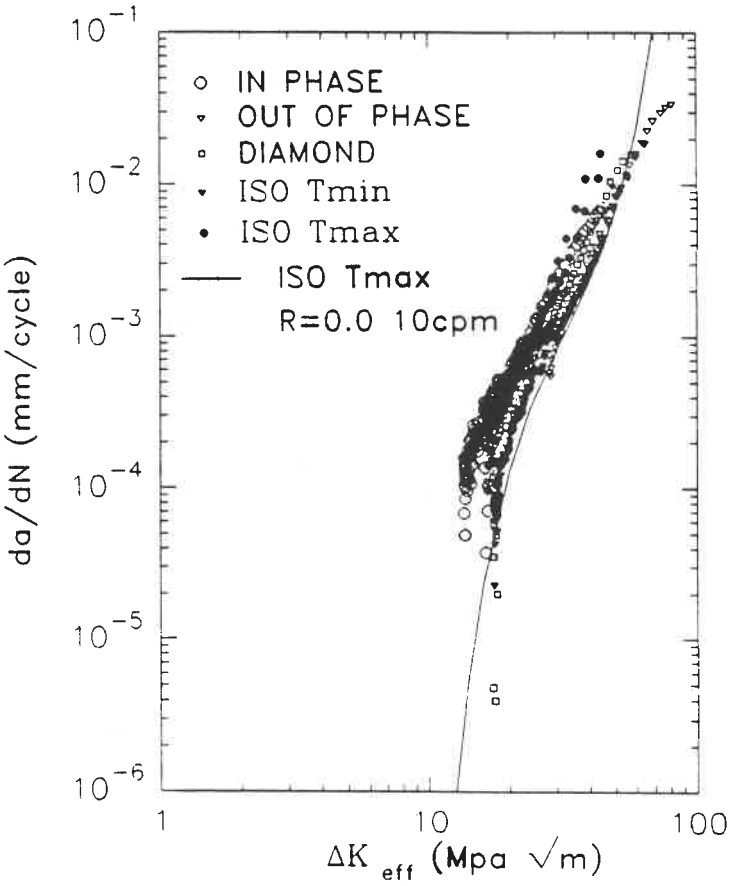

Figure 4.5 A comparison between TMFCG data (0.6cpm) and the isothermal FCG data of Ti64 tested at higher frequency (10cpm).

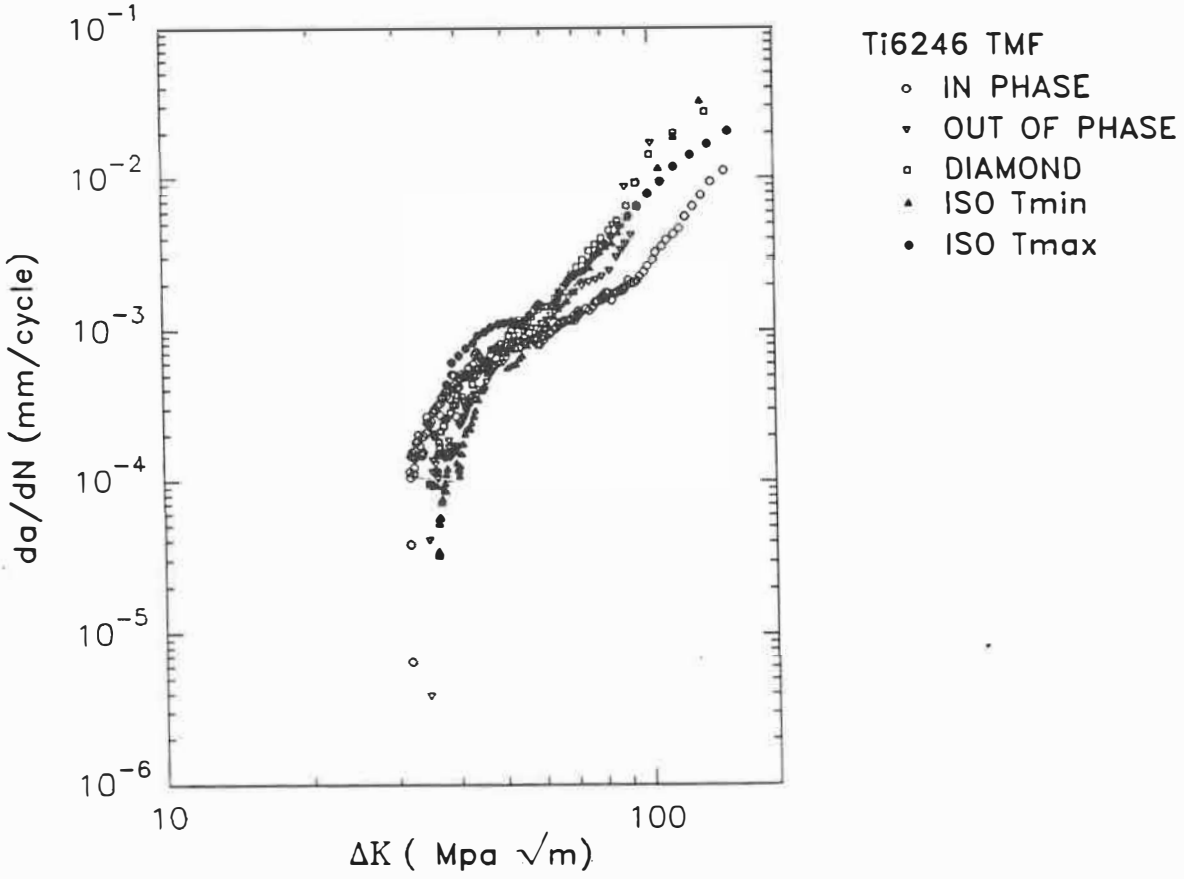

igure 4.6 TMFCG data of Ti6246 when plotted as a function of the stress intensity ıctor range ΔK.

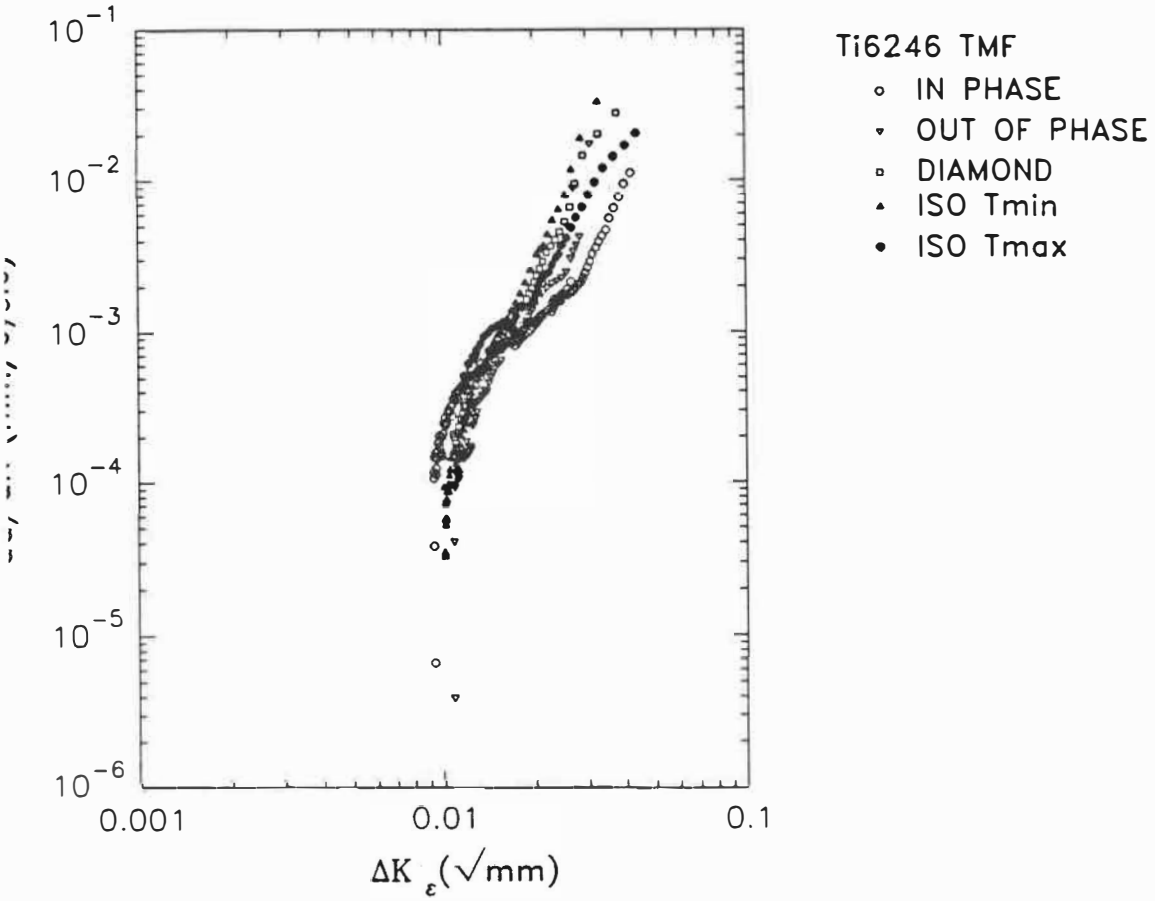

ure 4.7 TMFCG data of Ti6246 when plotted as a function of the strain intensity tor range ΔK_{ε}.

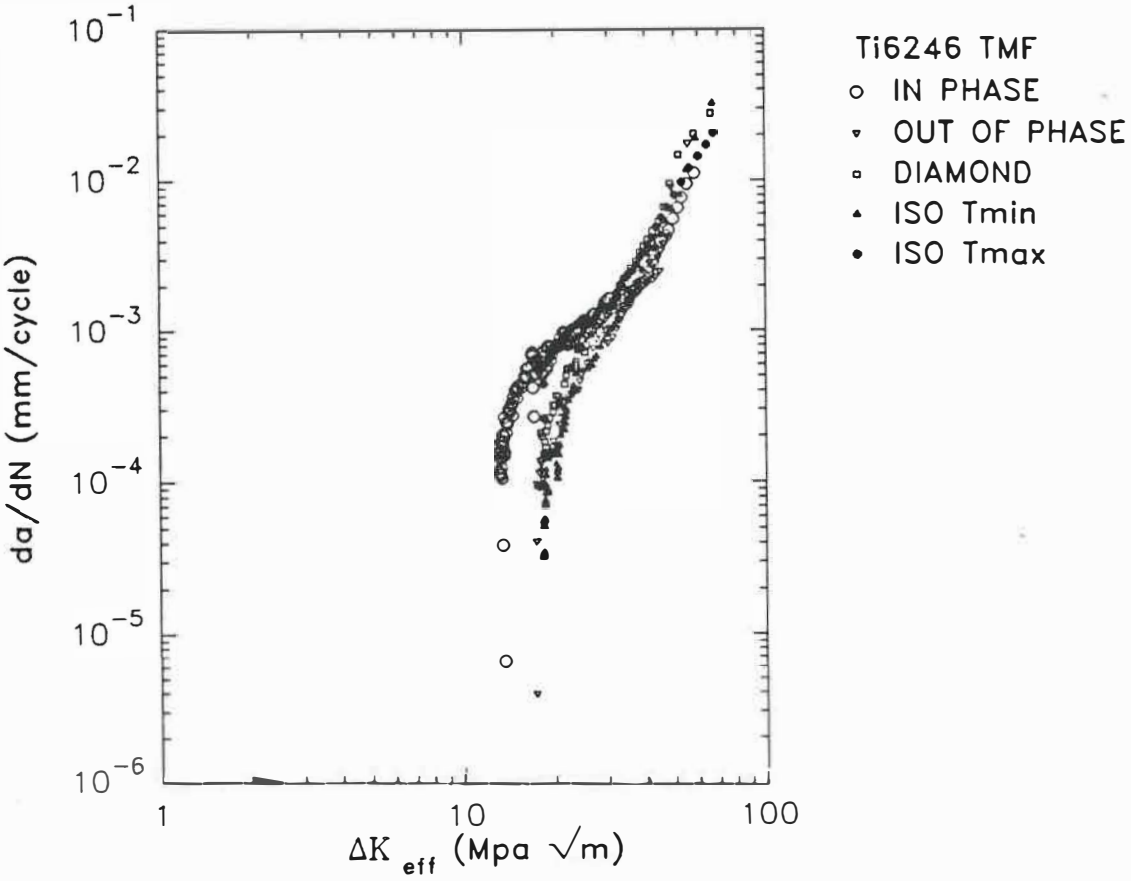

igure 4.8 TMFCG data of Ti6246 when plotted as a function of the effective stress tensity factor range ΔK_{eff}.

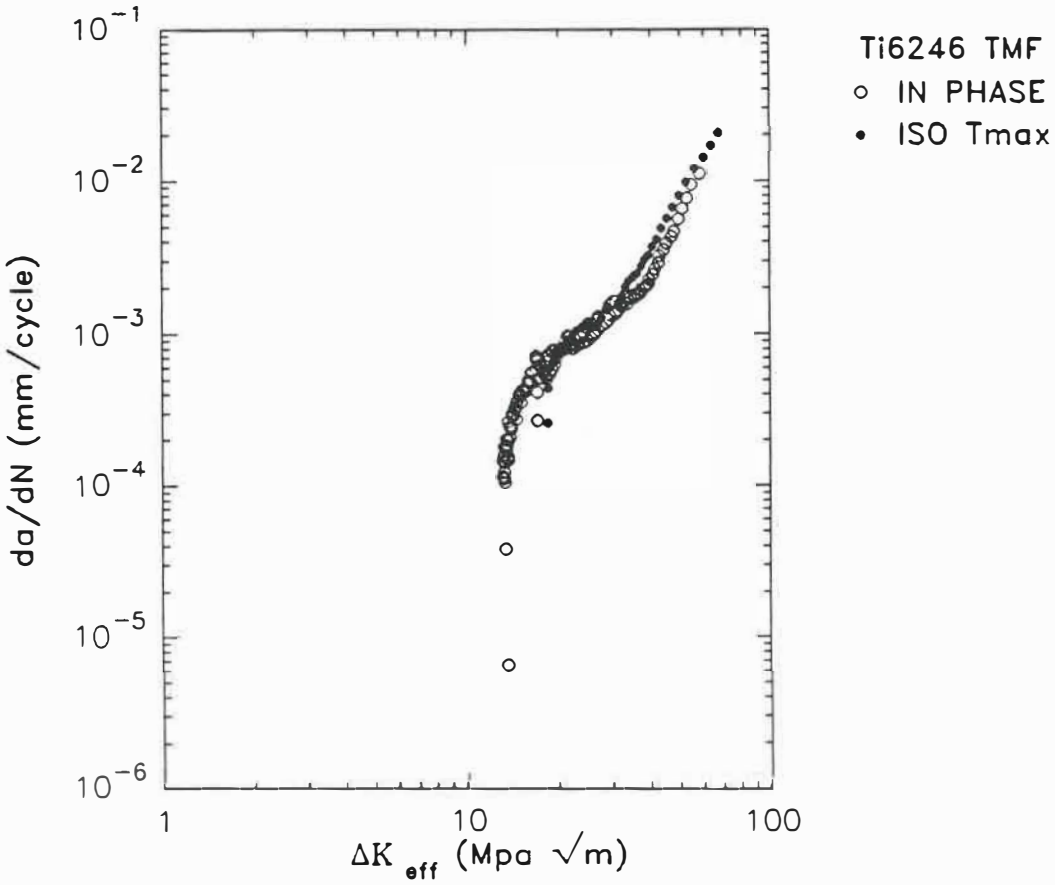

igure 4.9 A comparison between the in-phase TMFCG data of Ti6246 and FCG ata tested at T_{max} when plotted as a function of the effective stress intensity ctor range ΔK_{eff}.

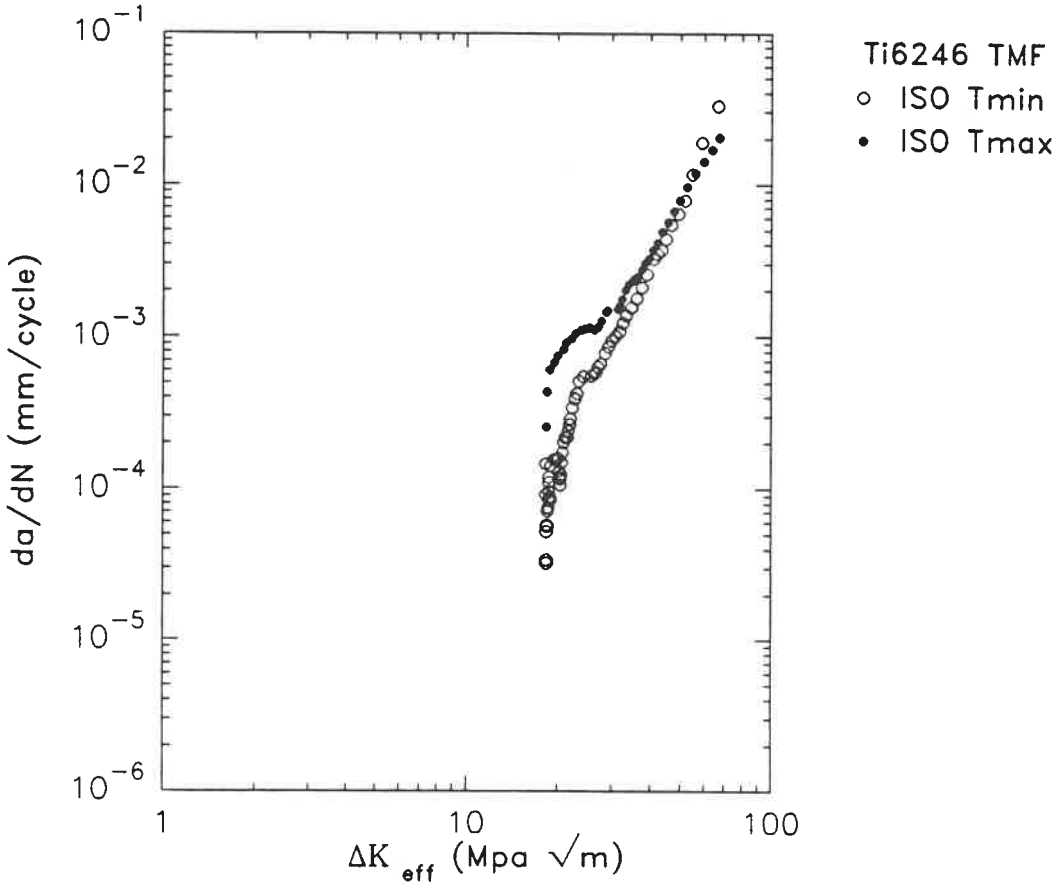

Figure 4.10 A comparison between the FCG data of Ti6246 tested at T_{max} and that tested at T_{min}, when plotted as a function of the effective stress intensity factor range ΔK_{eff}.

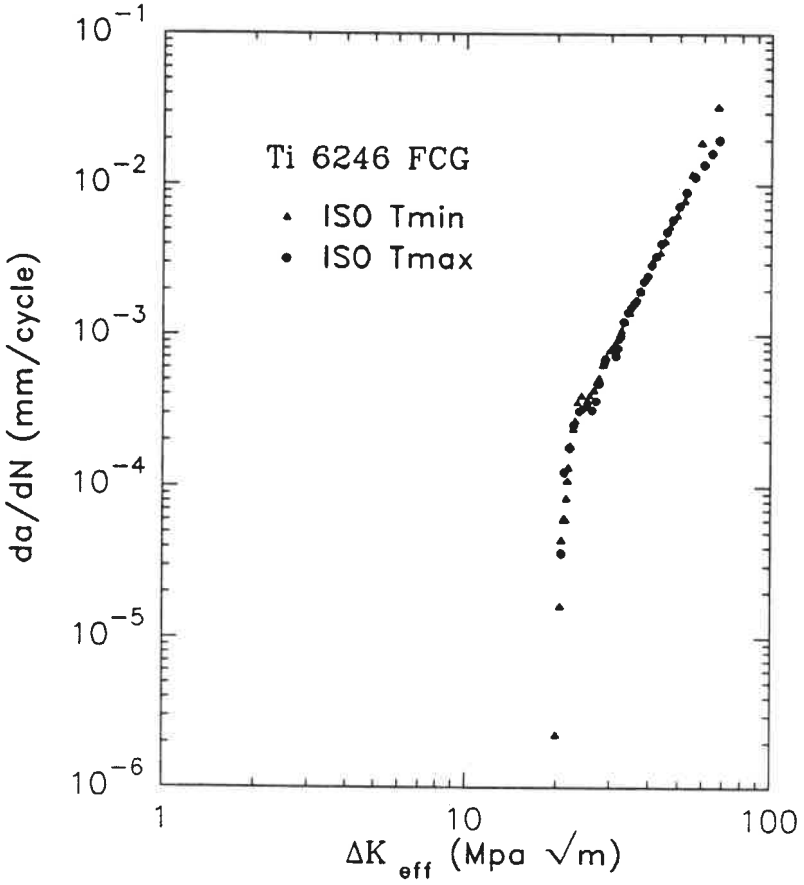

ure 4.11 A comparison between the FCG data of Ti6246 tested at T_{max} and that ted at T_{min}, as they are correlated by the effective stress intensity factor range Δ ff after partitioning of the components to remove the environment-assisted cking component.

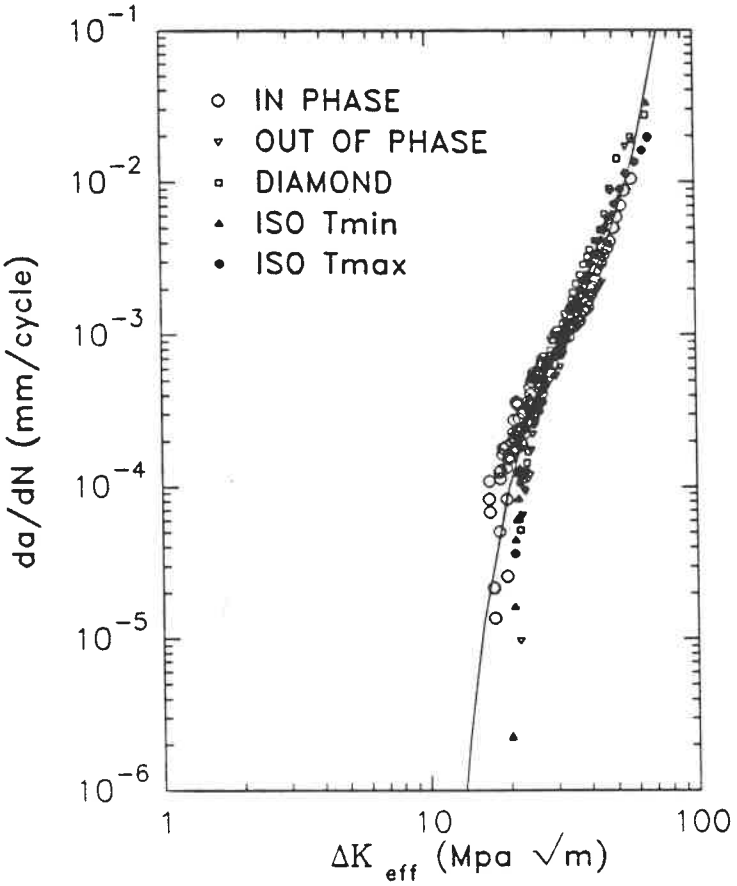

Figure 4.12 TMFCG and isothermal FCG data of Ti6246 when plotted as a function of the effective stress intensity factor range ΔK_{eff} after partitioning of the components due to the environment assisted cracking.

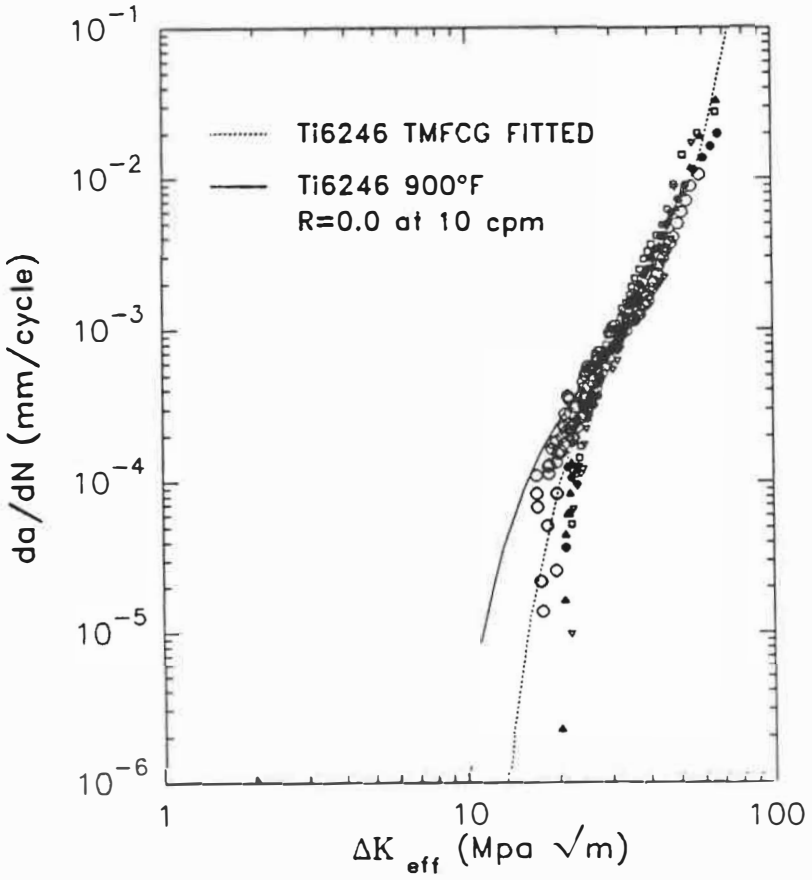

Figure 4.13 A comparison between TMFCG data of Ti6246 (0.6cpm) and the FCG data tested at higher frequency (10cpm), when plotted as a function of the effective stress intensity factor range ΔK_{eff} after partitioning of the components due to the environment assisted cracking.

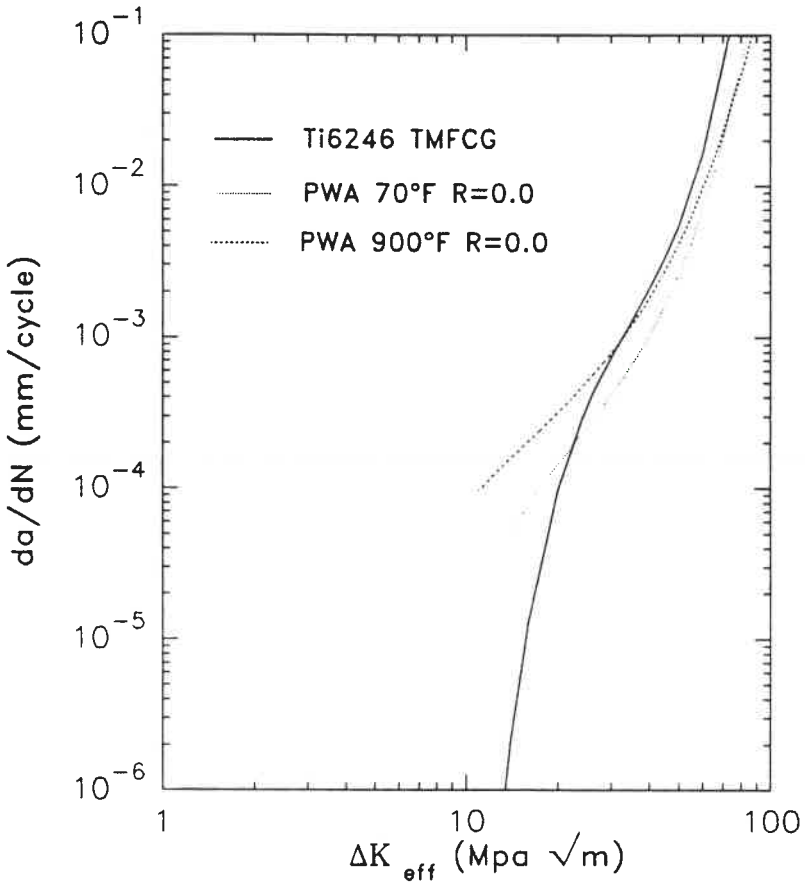

Figure 4.14 A comparison between TMFCG data of Ti6246 and the PWA historical FCG data.

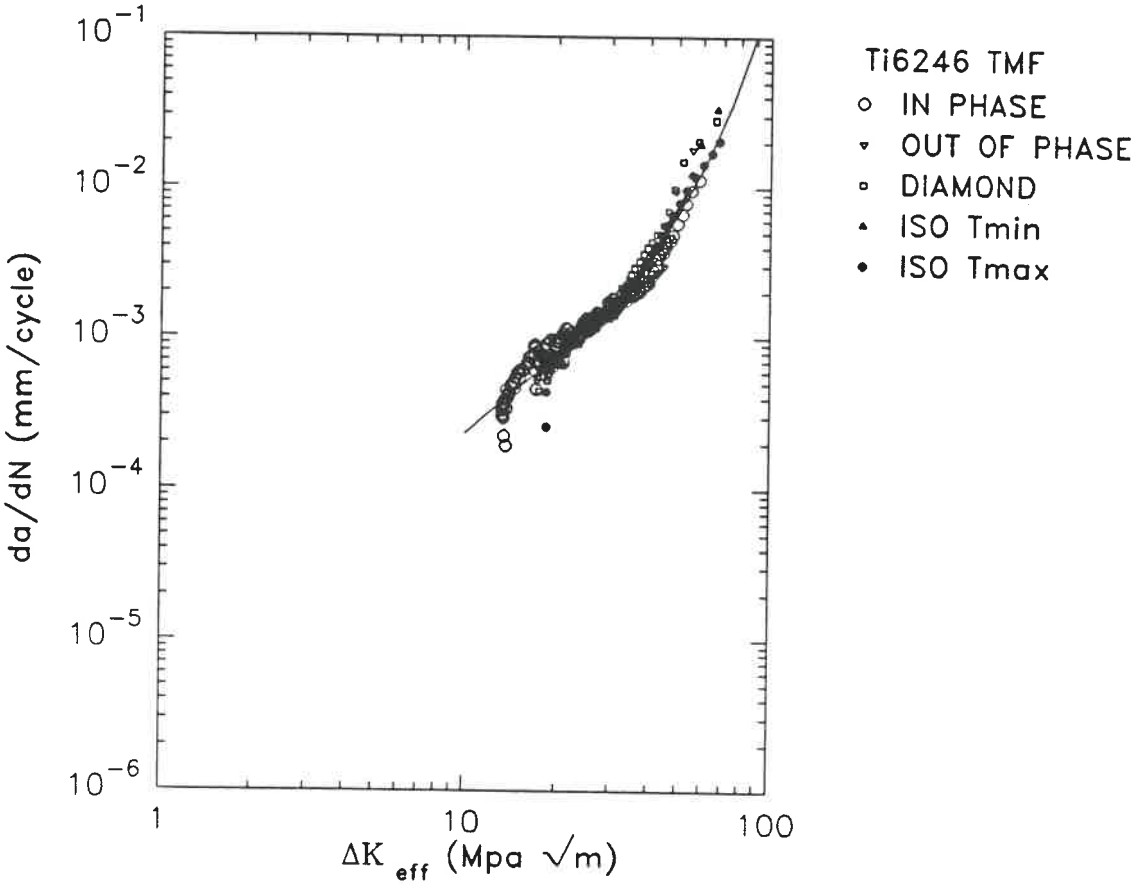

gure 4.15 A "worst" case reduction of the TMFCG data for Ti6246, in which all the
:G rate data from different test conditions are added to their respective oxidation
ıck growth terms that are equivalent to the test condition at 480°C.

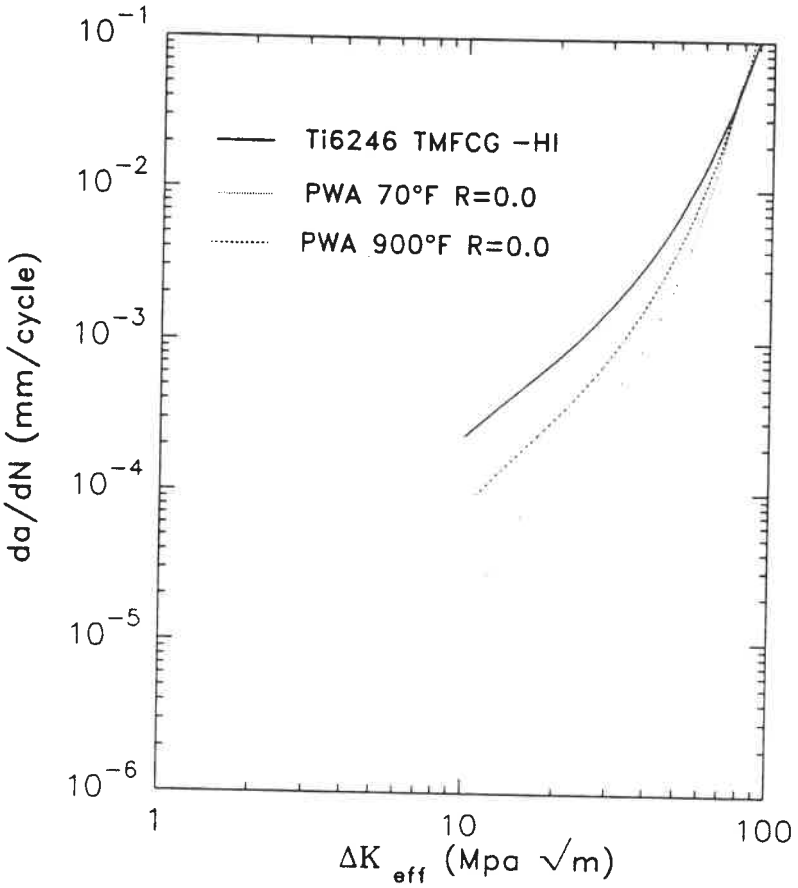

Figure 4.16 A comparison between TMFCG data (0.6cpm) with oxidation cracking components at 480° and the PWA historical FCG data (10cpm) at 480°C and RT. Ti6246).

CHAPTER 5

FRACTOGRAPHIC STUDIES ON FATIGUE CRACK GROWTH MECHANISMS OF TITANIUM ALLOYS

5.1 INTRODUCTION

The microscopic aspects of fatigue crack growth in the two $\alpha+\beta$ titanium alloys at RT and elevated temperatures were studied using SEM. The microscopic features of the fracture surfaces at different stages of fatigue crack growth were observed and analyzed. The SEM observations were centered on the relationship between the fracture morphology and the microstructural phases, and the effect of the α/β interfaces on the resistance to fatigue crack growth.

As summarized in Chapter 1, several mechanisms of fatigue crack initiation in $\alpha+\beta$ titanium alloys have been studied, including α/β interface cracking, primary α cracking at slip bands or slipless cracking, cleavage-like subsurface cracking, and grain egression. In addition to the effects of microstructure, the operative mechanism of crack initiation is also affected by a variety of mechanical and environmental conditions such as cycling frequency, load ratio (R-ratio), temperature and corrosive environment.

In the following sections, the typical results of SEM fractographic analyses on the LCF and TMF tests are summarized. The observations were focused on crack initiation sites at the root of the notch for the LCF (or FCI) tests. While for TMF tests, more efforts were made in comparing the fracture topography and explaining the crack growth mechanisms under the different types of TMF cycling.

5.2 THE FRACTURE MORPHOLOGY IN LCF TESTS

Recalling that the microstructure of an $\alpha+ß$ forged Ti64 forging and a ß forged Ti6246 forging shown in Figure 2.3 and Figure 2.4, composition analyses were performed on the fracture surfaces of specimens using a JOEL 840 SEM with LINK spectrum analyzer. The chemical compositions of beta stabilizers (V in Ti64 and Mo in Ti6246) were found to vary between microregions. Using the reference compositions obtained from the polished microstructure samples, the fracture morphology associated with the different phases could then be confidently identified.

As a typical example, Figure 5.1 shows the chemical content of vanadium in several featured microregions in a Ti64 SEN specimen tested at 400°C. These content values were measured by zooming in the microregions and taking the average measurement by the spectrum analyzer. Here, the zone 4, 5 and 8 with cleavage-like facet morphology have relative low V contents and are identified as primary α-particles. While zones 6, 7 and 9 with more ductile features have higher V contents and are identified as $\alpha+\beta$ matrix of the material.

The LCF crack initiation and growth test conditions have been described in Chapter 3. The following SEM observations indicate the fractographic features at the root of a notch, and the role of α/β interfaces during fatigue crack growth.

5.2.1 Ti64 tested at 400°C

Figure 5.2a shows the fracture surface near the root of the notch for a Ti64 specimen tested at 400°C. Here the notch is at the bottom of the photograph, the crack propagates upwards. This rule of presentation (crack propagation from bottom to top) is used for all the following micrographs. Evidence of a cleavage-like facet morphology associated with the α-phase can be identified. The $\alpha+\beta$ matrix appears to have higher ductility. Tearing-like areas can be found between α-phase grains. Fatigue striations become evident and the well defined in the equiaxed α-phase particles when cracks grow approximately 15~20 (μm) from their initiation sites along the notch. In these regions, the crack growth rates da/dN measured through striation counting are in a range of 1.0~5.0E-4 (mm/cycle). This is fairly closed to the macro da/dN measured by ACPD technique in Figure 3.19 of Chapter 3. Cleavage-like facets of α-phase can still be found in these regions in some local cracking planes that apparently have certain angles with the principal crack planes which presents well formed fatigue striations.

In Figure 5.2b, a fatigue initiation site (lower center of the photo) in the same specimen is studied. The crack apparently was initiated in an α-phase grain

with cleavage-like features. Analyses of the stereofractographic pairs of this micro region indicate that the crack nucleation planes coincide with the plane of maximum shear stresses obtained from the FEM results of Chapter 3. The $\alpha+\beta$ regions around the equiaxed facets have a rough and less crystallographic feature.

No cyclic cleavage striations can be observed on the cleavage-like facet from a closer view of the initiation zone right at the tip of the notch, as shown in Figure 5.3a. This indicates that the fracture initiates as a result of slip caused by shear stress. This point becomes more evident in the interface regions between α-phase particles and its $\alpha+\beta$ matrix shown in Figure 5.3b. The slip lines parallel to the crack growth direction can be observed in the α-grain while very fine striations vertical to crack growth direction start forming in $\alpha+\beta$ matrix. The average microscopic da/dN is about 0.1μm/cycle. Furthermore, analysis of several other crystallographic facets showed that fracture began near or at the α/ß interface and proceeded toward the interior of the equiaxed α-phase particles. All this evidence suggests that the α-phase islands failed first and that the surrounding α+ß matrix fractured under considerably higher cyclic strains as confirmed by the presence of coarse striations and faint crystallographic features in the α+ß matrix. As compared with specimens tested at other temperatures, the above observations which pertains to the initiation zone were found to be more pronounced with increasing temperature.

As can be expected, see Figure 5.4a, when the cracks grew outside the zone of influence of the notch, well-defined fatigue striations mostly on α-phase grains are observed with secondary cracking forming along the α/ß interface and becoming

more prevalent with increasing ΔK. For these regions, the measured microscopic da/dN are in agreement with the macroscopic values measured by the ACPD technique. These results are also consistent with the observation made by Rhodes et al[26].

Finally at ΔK ~ 50 Mpa√m, the mixture of coarse striations in the α-phase and ductile dimples on α+β matrix can be observed. See Figure 5.4b. The micro da/dNs, which is around 2.0E-3 mm/cycle, are found in excellent agreement with ACPD measured values given in Figure 3.20.

5.2.2 Ti6246 tested at 480°C

Due to the coarse microstructure of the Ti6246 forging, the overall fractographic aspects of the surfaces appears relatively rough as compared with Ti64. The same methodology has been used to identify phase relations on the fracture surfaces for this double phase material. The chemical contents of β-stabilizer molybdenum were used as reference.

The fractured Ti6246 specimens tested at 480°C displayed numerous cleavage-like (or crystallographic) facets near the root of the notch, i.e. in the initiation zones (see Figure 5.5a). These facets were found to be on the acicular α-phase grains. Figure 5.5b reveals the crack propagation history at an initiation site. This is one of the stereofractographic pairs of this microregions. The observations indicated that the facet cracking plane at the root of the notch also coincides with

the notch maximum shear stress plane. Fatigue striations started forming outside the cleavage-like facet zone which is ~ 4μm from the notch. They are more pronounced alone several acicular α-phase particles. Additionally, in some other areas subsurface cracking with cleavage-like facet features were observed in the tests at 480°C.

At a moderate $\Delta K \sim 25$ (Mpa$\sqrt{m}$), outside the zone influenced by the notch, delamination of acicular α-phase from the its transformed ß matrix are important features of the fracture surfaces, as shown in Figure 5.6a. These become much clearer at $\Delta K \sim 35$ (Mpa$\sqrt{m}$) in Figure 5.6b. As a stronger evidence of the interfacial fatigue crack growth, a cross section parallel to crack growth direction is shown in Figure 5.7a. Here the left hand side of the photograph shows the microstructure of the material and the right hand side shows the fracture surface. The crack can be seen altering its direction to follow the preferential path along α/β interface. Comparing the geometry of the accicular α-phase particles on the left and the shape a crack growth wake on the right, one can conclude that the crack propagates along α/β interface instead of in the accicular α-phase. The crack growth proceeded through concurrent delamination of the α/ß interfaces along the crack front. As a result, depending on the relative orientation of the α/ß interfaces with respect to the loading axis, either striations along the delaminated areas or secondary cracking along the α/ß interfaces were produced. See Figure 5.7b.

With increasing ΔK, interfacial secondary cracking becomes more pronounced since it is the most efficient mechanism to reduce the actual stress field a head of the main crack. This is supported by the fact that secondary cracks

coincide with the striations at higher ΔK levels. Mixture of tearing dimples and α/β separation can be observed near final fracture regions (see Ref. [171,172]).

5.3 TMF CRACK GROWTH MECHANISMS

The TMF tests have been described in Chapters 2 and 4. All the TMF crack growth tests were performed under fully reversed strain cycling at 0.01 Hz (0.6 cpm). The maximum tensile strain coincides with the maximum temperature in the in-phase (IP) condition, while maximum compressive strain coincides with the maximum temperature in the out-of-phase (OP) conditions. In order to explain the differences in crack growth rates under different TMF cycles, the following SEM observations were made up on comparing the fractographic features of specimen tested under the IP, OP and CCD (count-clockwise-diamond) TMF cycles.

5.3.1 TMFCG in Ti64

Figure 5.8 shows a montage of fracture surfaces of Ti64 obtained under IP TMF condition with $\Delta K \sim 22$ (Mpa$\sqrt{m}$). It can be seen that the overall fractographic features are quite crystallographic and can be easily associated with the material's microstructure. Similar to Figure 5.3a, the equiaxed α-phase grains display islands with relative flat surfaces and well-defined fatigue striations. Some secondary cracks are seen at α/β interfaces.

The fracture surfaces obtained under OP conditions at the similar ΔK present pronounced rubbing lines parallel to the crack growth direction and depression areas where fatigue striation lines appear faint (see Figure 5.9). The overall fractographic features are flat and less crystallographic. These are the indications of crack surface mating and crack tip closure. In this test condition, the compressive stress was applied at the maximum temperature and therefore at a relatively low yield strength, favoring the plastic deformation on the crack surface during crack closure. As well, the secondary cracking is less prominent.

As shown in Figure 5.10a and Figure 5.10b, these interesting differences in the fractographic features associated with IP and OP TMF conditions remain at higher ΔK ($\sim$ 35 (Mpa$\sqrt{m}$) values.

In the CCD condition, Figure 5.11, the morphology of the fracture surface is in between the situations found for IP and OP conditions. Here, the α-phase islands with well-defined striations are lightly affected by local depression and rubbing, although there are some heavily rubbed areas. No continuous rubbing lines can be observed in the case of OP. However, the overall fracture surfaces are less crystallographic than for the IP conditions, and the secondary cracking is also less pronounced.

Fracture surfaces of isothermal FCG test with the same loading frequency at the maximum temperature were also studied. As shown in Figure 5.12, the overall fractographic features are close to those in the IF condition. The secondary cracking

also appears prominent. However there are some depressed areas as a result of compressive part of the load cycles.

5.3.2 TMFCG in Ti6246

The typical fractographic results of Ti6246 tested under IP TMF conditions (with $\Delta K \sim 20$ Mpa$\sqrt{m}$) are presented in Figure 5.13. The overall fractographic features appear relatively crystallographic and can be easily associated with the microstructure. Some acicular α-phase packets form many flat facets with fine and well-defined striations. Other acicular α-phase particles with certain orientations were delaminated from their β matrix leaving parallel traces or channels on the fracture surface. These indicate that cracks propagate following certain preferential microstructural planes, notably the α/β interfaces.

Remarkably different fracture surfaces were obtained from the OP TMF conditions with similar ΔK. As shown in Figure 5.14, the overall fractographic features appear eminently flat and less crystallographic. Their relationship with the microstructural features become less evident. Since the crack propagates without following certain crystallographic planes, it is locally stopped by certain microstructural barriers, notably at grain boundaries, and has to re-initiate to proceed continuously.

However, comparing Figure 5.15a and Figure 5.15b, the differences in terms of fracture morphology in IP and OP tests become minor at higher crack growth

rates under $\Delta K \sim 35$ (Mpa$\sqrt{m}$). This can be also observed from the measured macro crack growth da/dN data obtained using the ACPD technique (see Figure 4.8).

The TMFCG test under CCD TMF condition presents a fracture morphology (Figure 5.16) in between what found for the IP and OP conditions. The interfacial crack growth is not as dominating as in the IP condition, and the overall morphology is still less crystallographic. The cracks basically do not appear to follow certain preferential crystallographic paths as they do in IP conditions. This is consistent with the macroscopic FCG behavior (da/dN data) in CCD being closer to that for OP conditions, as shown in Figure 4.8.

From the SEM observations above, it is clear that the temperature at the maximum stress intensity factor value (K_{Imax}) plays an important role in the FCG mechanisms in the Ti6246 forging. To further stress this point, the SEM analyses were also performed on an isothermal FCG test at T_{max} with the same cycling frequency. The results are shown in Figure 5.17a which presents the specimen's fracture surface at $\Delta K \sim 15$ (Mpa$\sqrt{m}$). At this ΔK value which is lower than in the cases shown in Figure 5.13-14, stronger environment effect on FCG (refer to Figure 4.8) can be observed. Oxidation deposits, cleavage-like fracture and secondary cracking at α/β interfaces can be seen on the fracture surfaces. Figure 5.17b provides a closer view on the oxidation embrittled facets and interfaces, and secondary cracks. The fatigue striations have become less visible. This indicates that the crack growth due to fatigue is no longer a dominating component. The environment-assisted cracking has become more important.

Still at the same ΔK level, Figure 5.18a shows some of the other microscopic regions. These are featured by numerous α-phase separation traces that are basically parallel to the crack growth direction. This can be attributed to the weakened α/β interfaces by oxidation.

On the contrary, the environment effects are much smaller in the OP TMF condition. At the similar ΔK level, interfacial crack growth become less dominating and well defined fatigue striations can be clearly observed (see Figure 5.18b).

5.4 DISCUSSION AND CONCLUSIONS

Fatigue crack initiation (FCI) at the primary α-phase is also consistent with the other reported initiation sites in Al-rich regions[31]. The Al content for both alloys was found to be higher in the α-phase than in the transformed ß matrix. The crack initiation and growth at the α+ß interfaces (especially observed in Ti6246 tests at 480°C) indicate that elongated preferentially oriented α+ß interfaces (with respect to the notch) can be detrimental to the material's FCI and FCG resistance. As suggested by Eylon[28], the surface connected interfacial cracking is an indication of environmental effects on the fatigue crack initiation processes. Diffusion of oxygen (at elevated temperatures) from the surface into the material is enhanced along the α/ß interfaces either by lattice mismatch between the hexagonal α and cubic ß phases or by the interface stresses developed during the load cycles. Interfacial diffusion is also promoted by the higher surface to volume ratio associated with the acicular α-phase and higher dislocation density. The resulting

higher interstitial contents embrittle the interface zone[29] and reduce its ability to plastically deform. This preferential oxygen diffusion along α/β interface causes the so called "oxygen induced embrittlement" at elevated temperatures. As a result, the material's resistance to fatigue crack growth is decreased.

From these fractographic studies, the following conclusions can be made:

-The crack initiation sites for both alloys were found to be in the α-phase particles or at α/β interfaces, with cleavage-like facet fracture morphology.

-A good agreement between the microscopic da/dN and the measured ACPD da/dN (in the ΔK controlled - Paris' region) can be observed.

-Preferential α/β interfacial cracking assisted by environmental embrittlement at high temperature is particularly important to Ti6246. It controls the FCI and FCG resistance of the alloy.

-Differences in crack tip plasticity are observed in the in-phase and out-of-phase TMF tests on Ti64.

-Differences in crack growth morphologies are found the in-phase and out-of- phase TMF tests on Ti6246, as a result of oxidation assisted embrittlement.

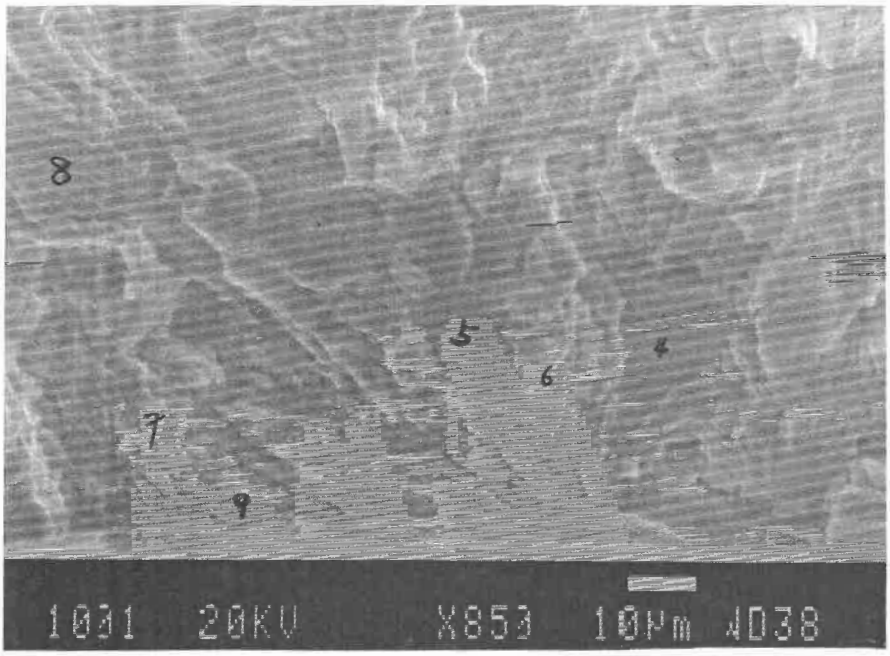

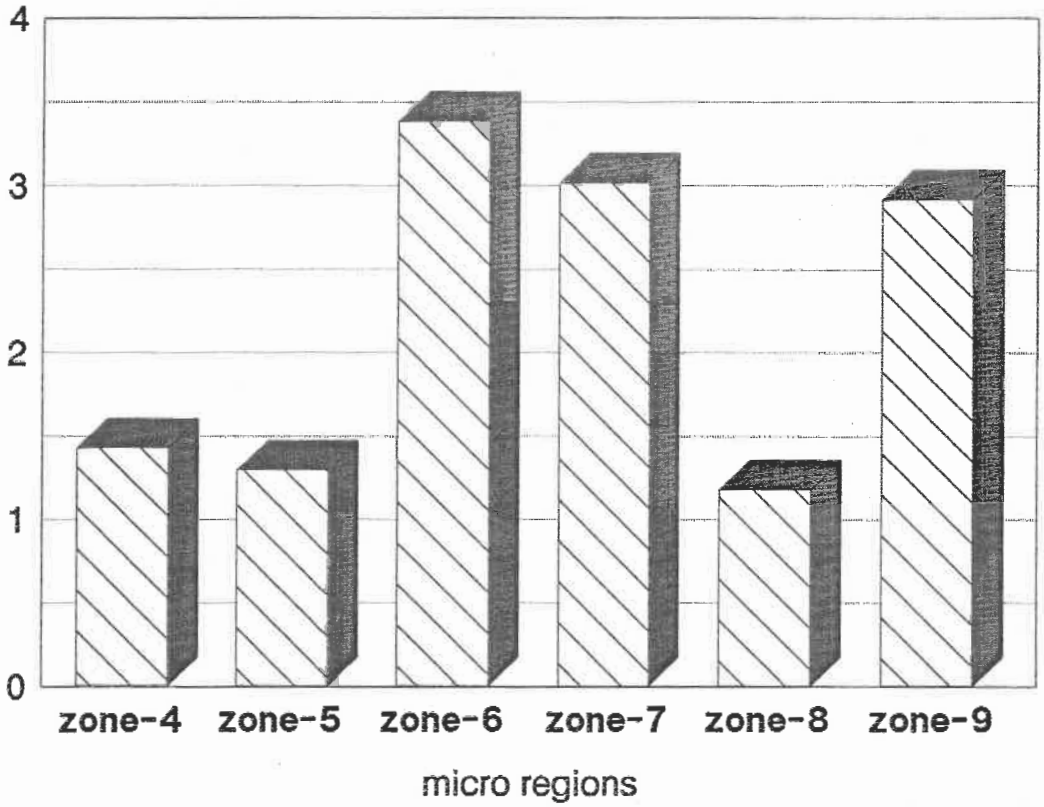

e 5.1 Typical relationship between β-stabilizer compositions in Ti64 and its graphic features (region near the root of the notch of an SEN specimen)

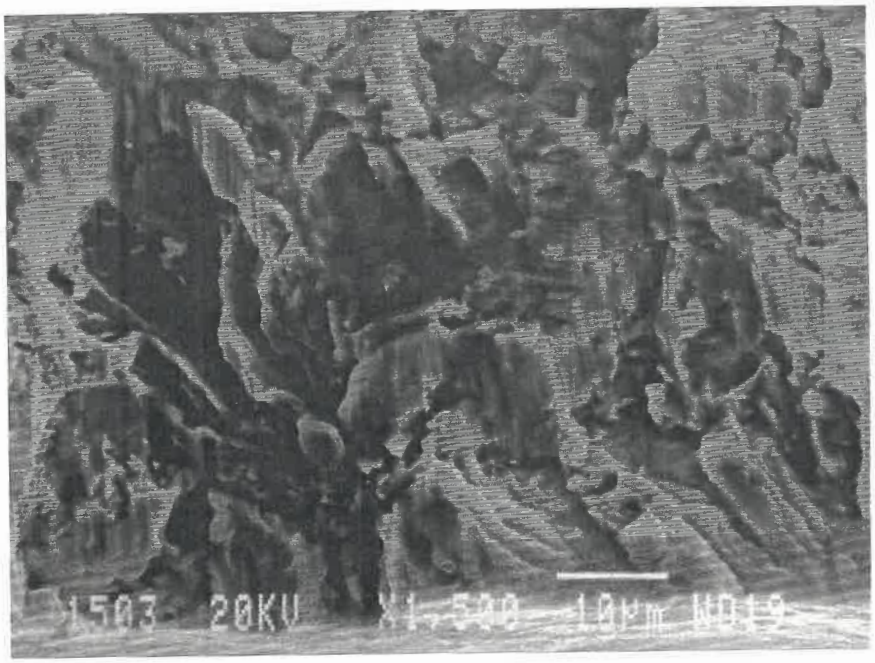

e 5.2a An overview of the fatigue crack initiation zone at the root of the notch.
, 400°C)

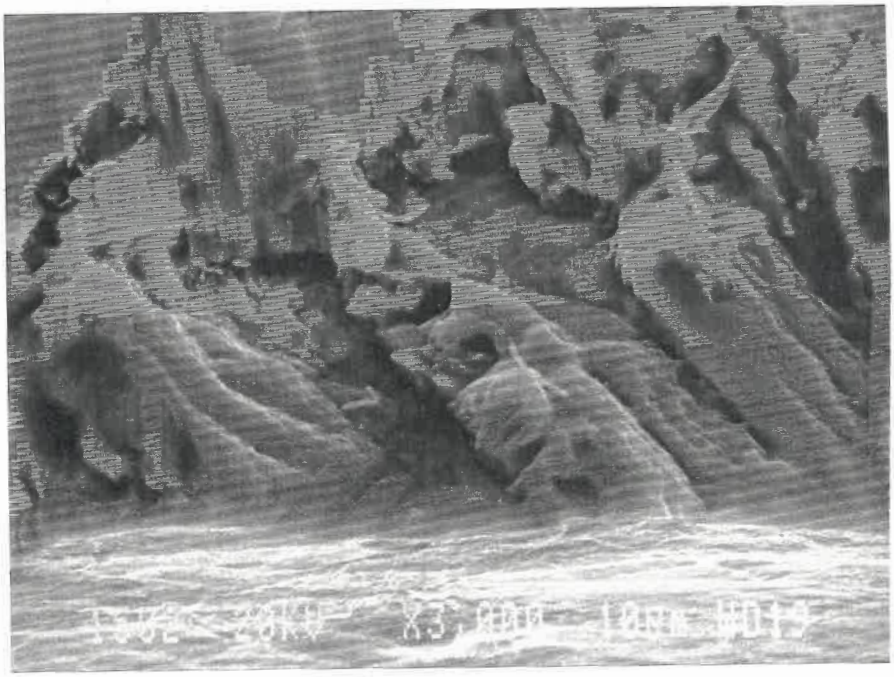

ɜ 5.2b A closer view of a fatigue crack initiation site in an α-phase grain right
root of the notch.

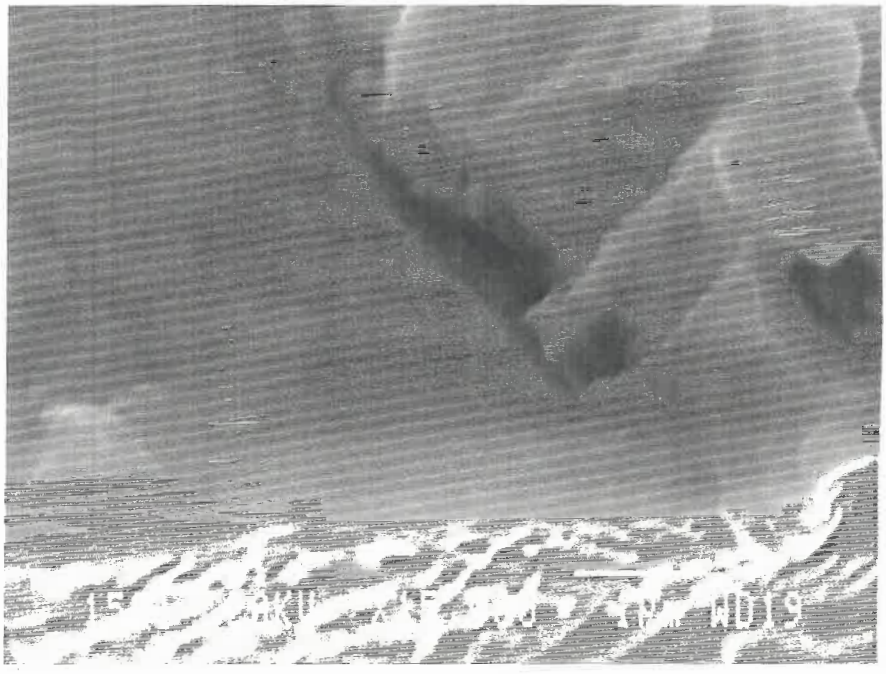

ıre 5.3a A more detailed observation on the cleavage-like facet type initiation at the root of the notch.

re 5.3b A transition from cleavage-like facet in an α-phase grain to striation ‹ growth type near α/β interface.

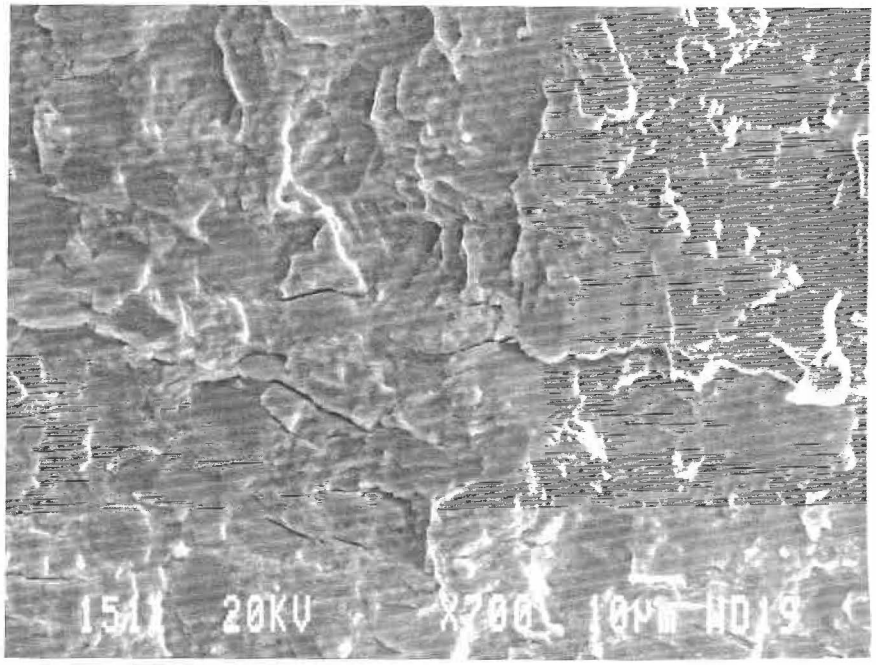

re 5.4a Well defined striations mostly in the α-phase grains and secondary ks occurring along α/β interfaces. (region outside the notch influence zone).

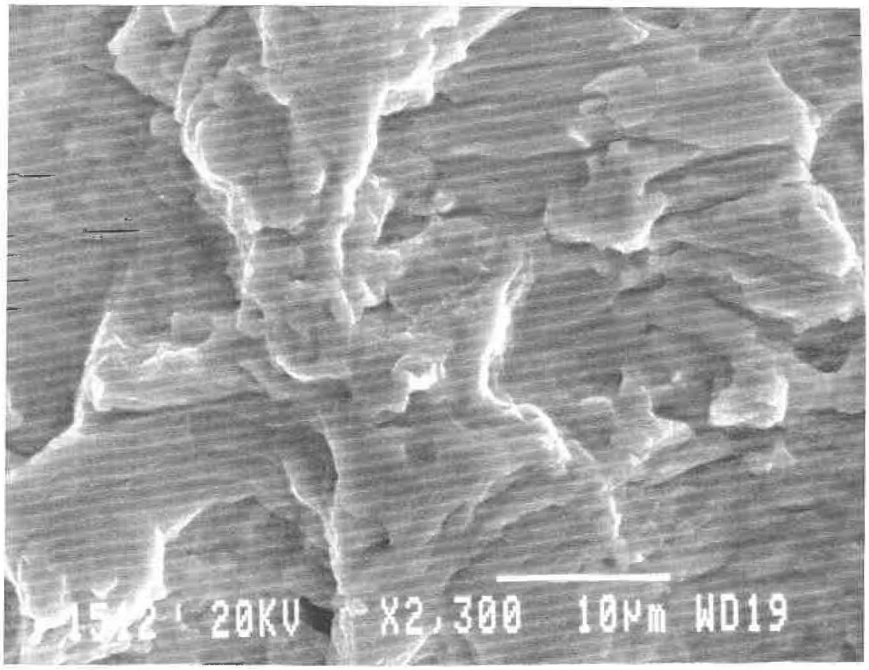

re 5.4b Mixture of coarse striations and ductile tearing dimples at final stage of k growth ($\Delta K \sim 50$ Mpa$\sqrt{m}$).

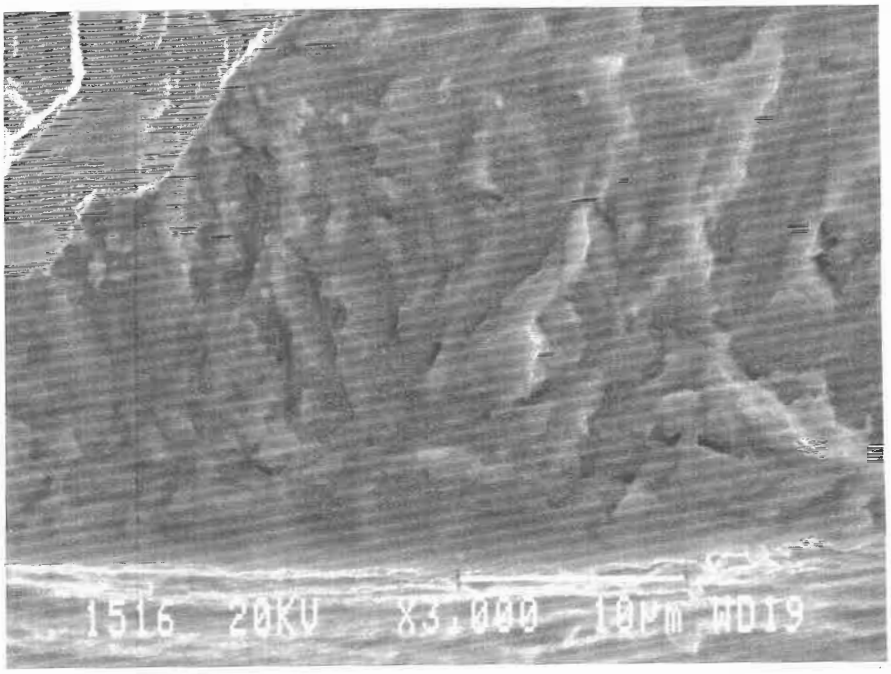

:e 5.5a An overview of the fatigue crack initiation zone at the root of the notch.
'46, 480°C)

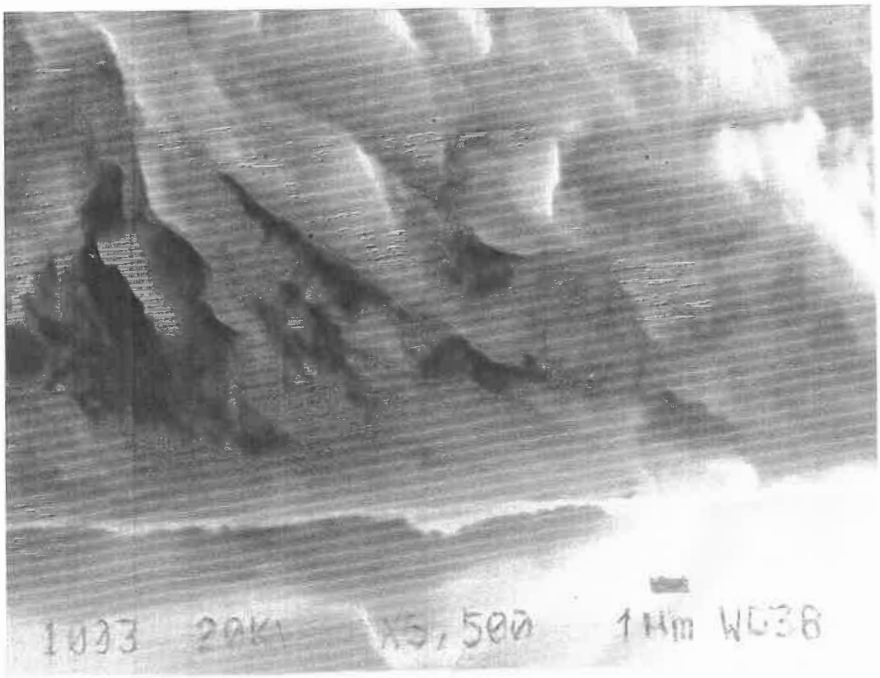

ıre 5.5b A closer view of a fatigue crack initiation site in an acicular α-phase
ı right at the root of the notch.

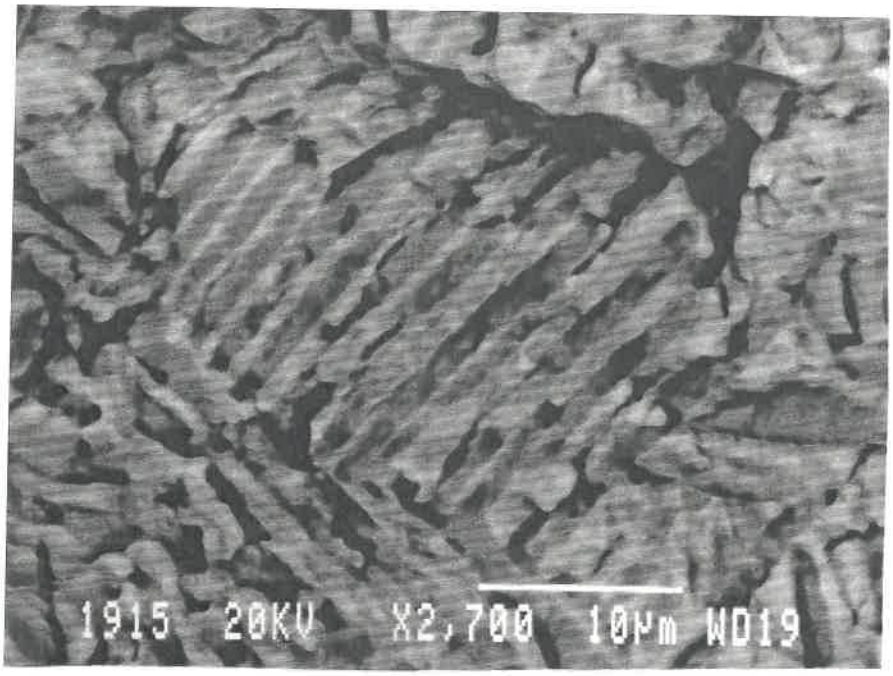

re 5.6a Delaminations of acicular α-phase from its transformed β matrix as a lt of fatigue crack propagation. ($\Delta K \sim 25$ (Mpa$\sqrt{}$m), outside the notch influence)

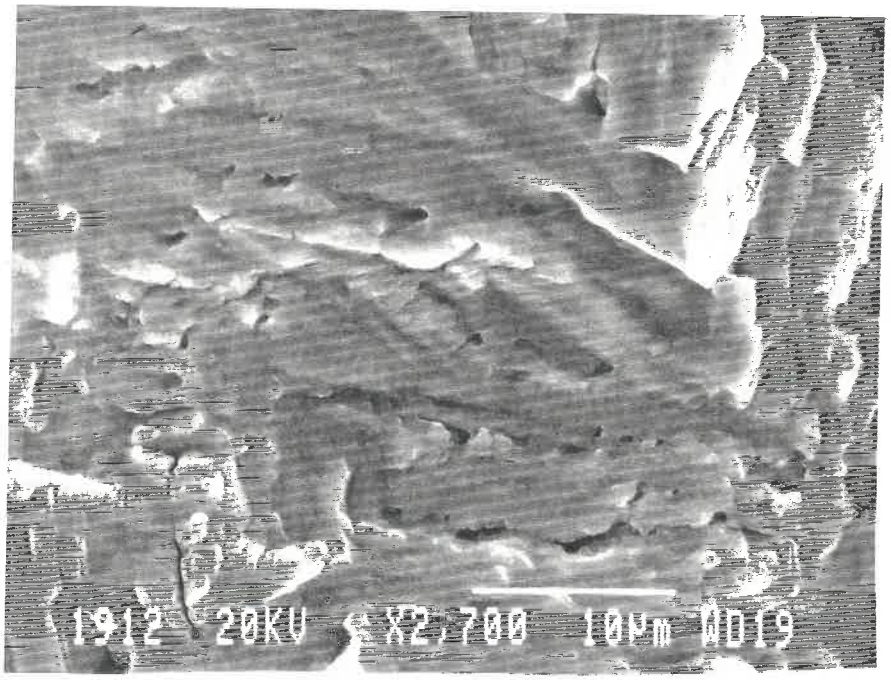

ıre 5.6b A stronger evidence of the interfacial fatigue crack growth. Striations be seen vertical to the accicular α-phase axis. ($\Delta K \sim 35$ (Mpa$\sqrt{}$m)).

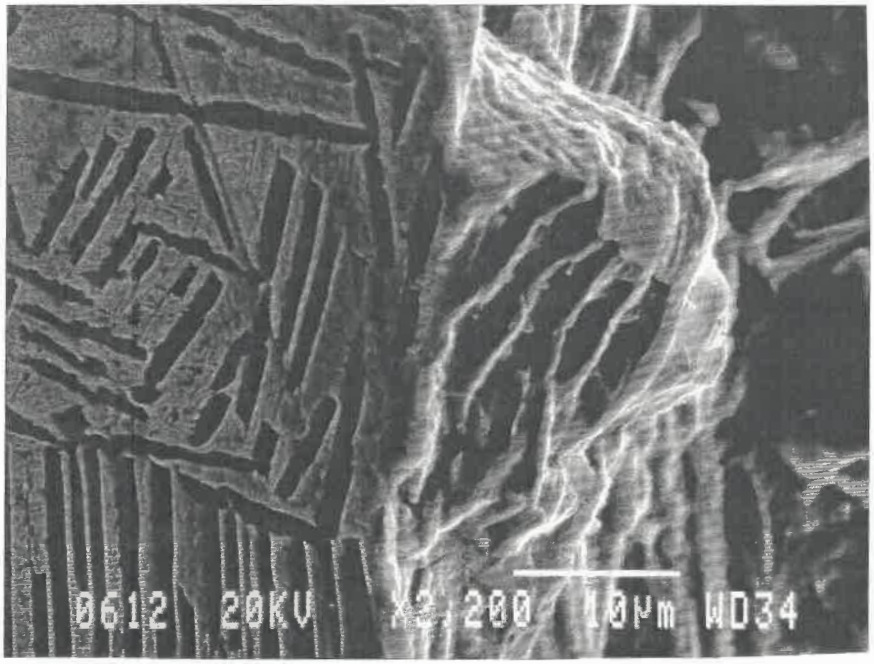

ure 5.7a A cross sectional view of interfacial crack growth showing clearly the ıtionship between the material's microstructures and fractographic features.

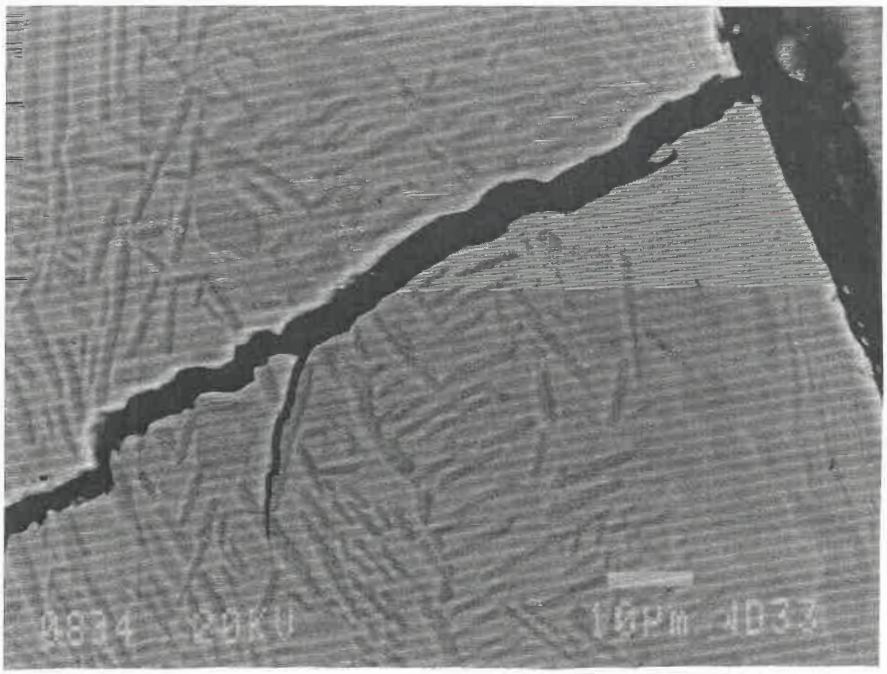

Figure 5.7b A secondary crack formed along α/β interface. (Ti6246 at 480°C)

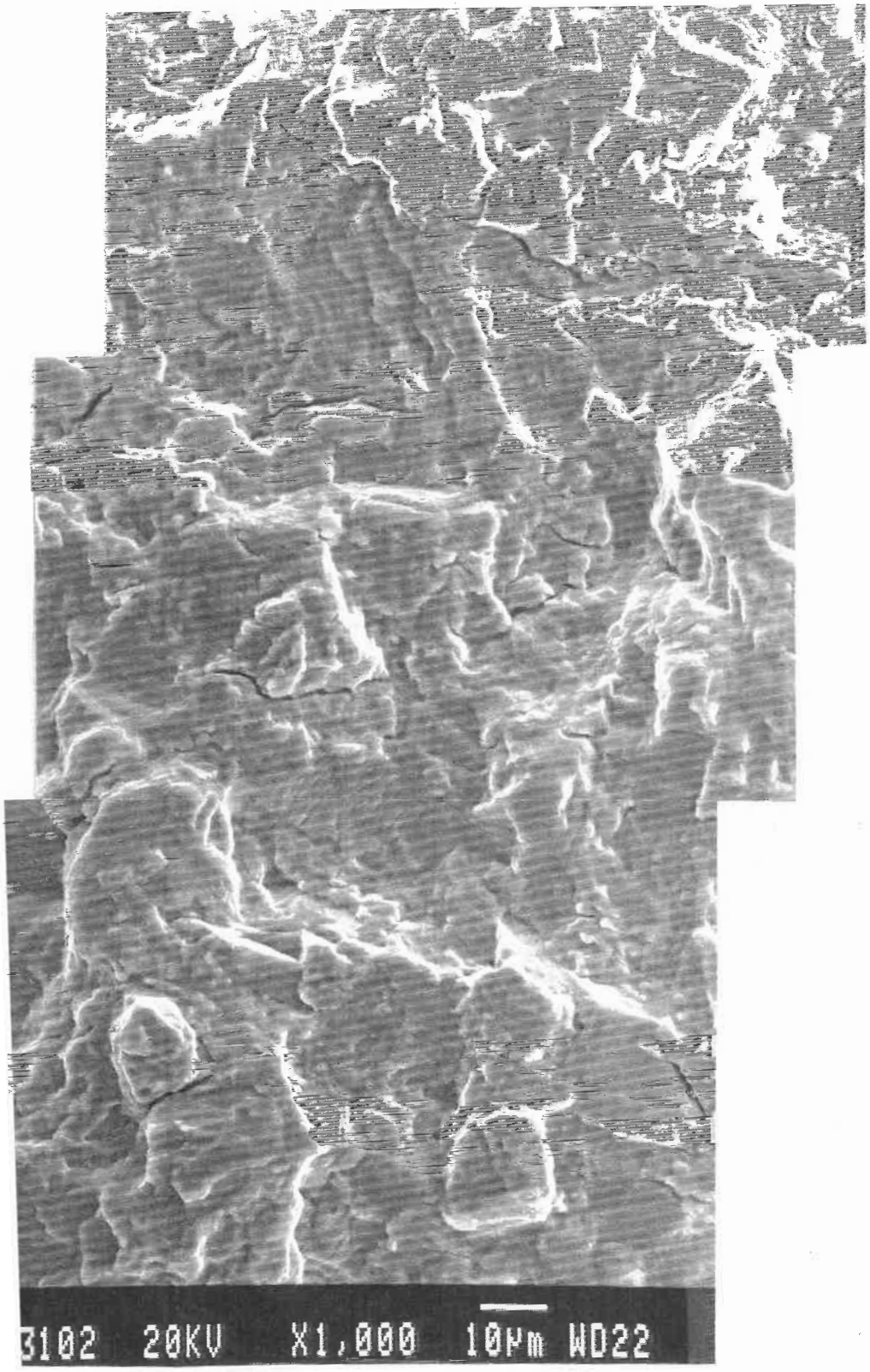

re 5.8 Microfractograph of Ti64 tested under in-phase TMF cycling.
-22 (Mpa√m).

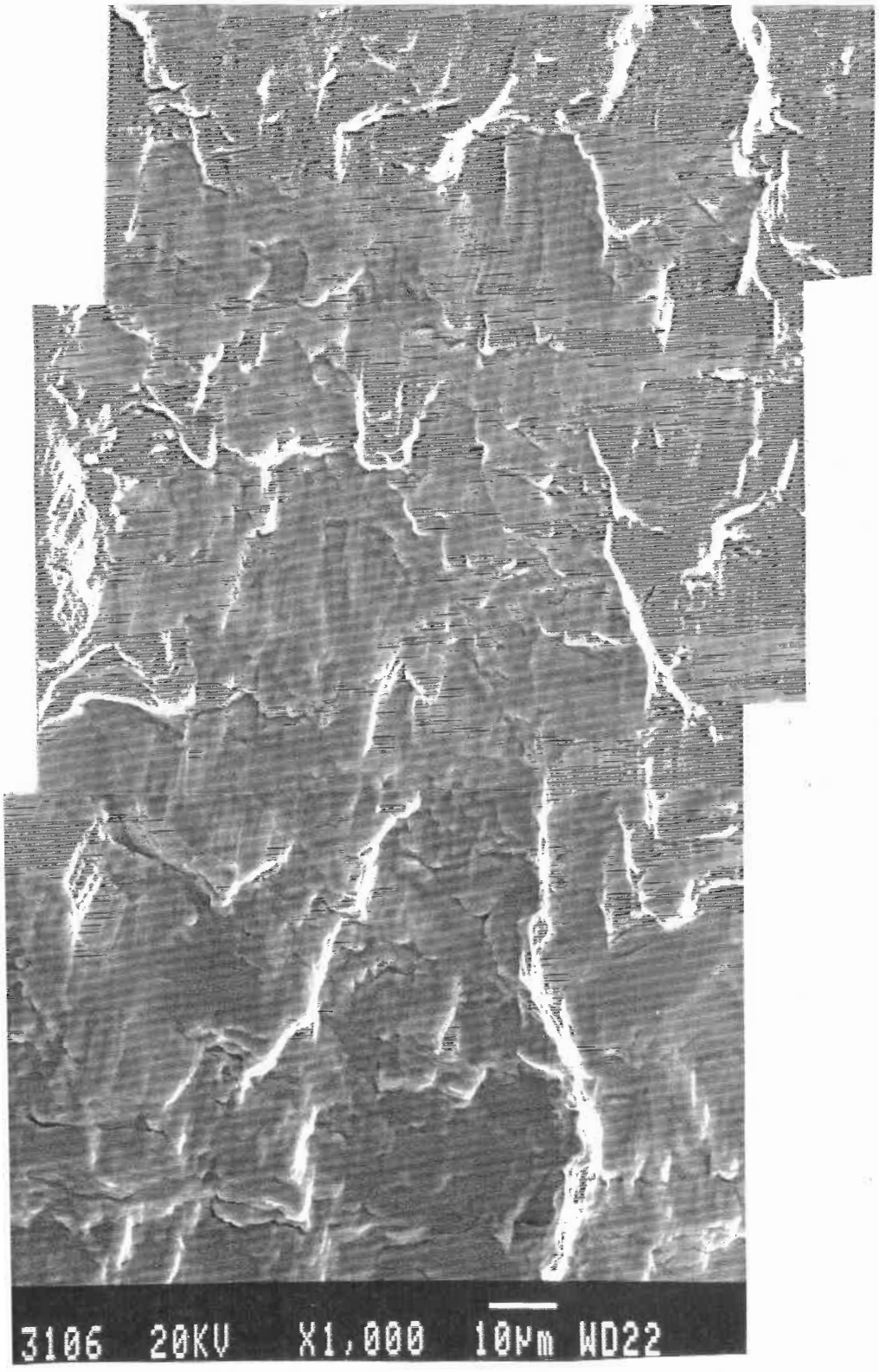

e 5.9 Microfractograph of Ti64 tested under out-of-phase TMF cycling.
22 (Mpa√m).

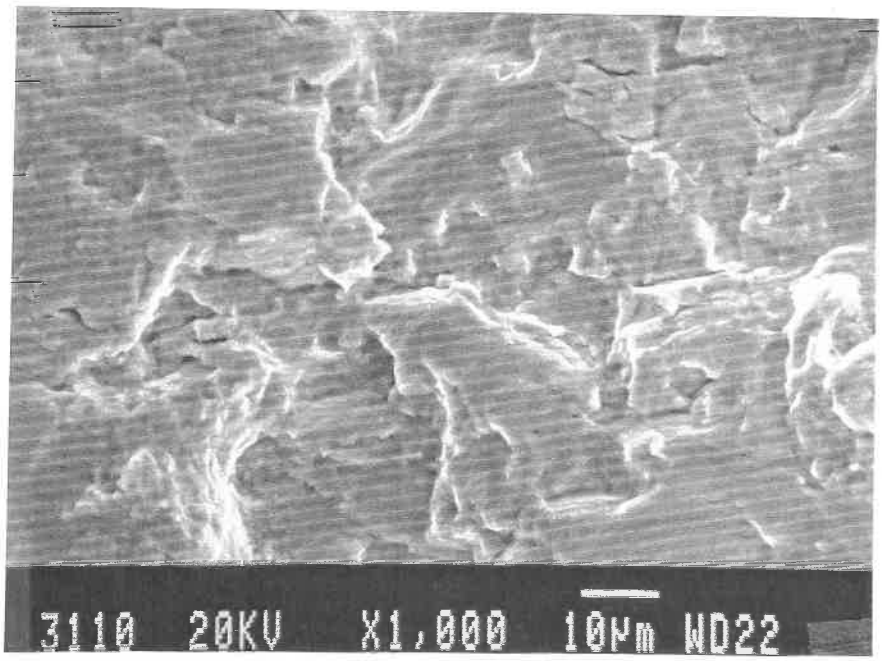

gure 5.10b Microfractograph of Ti64 tested under out-of-phase TMF cycling.
$\Delta K \sim 35$ (Mpa$\sqrt{m}$).

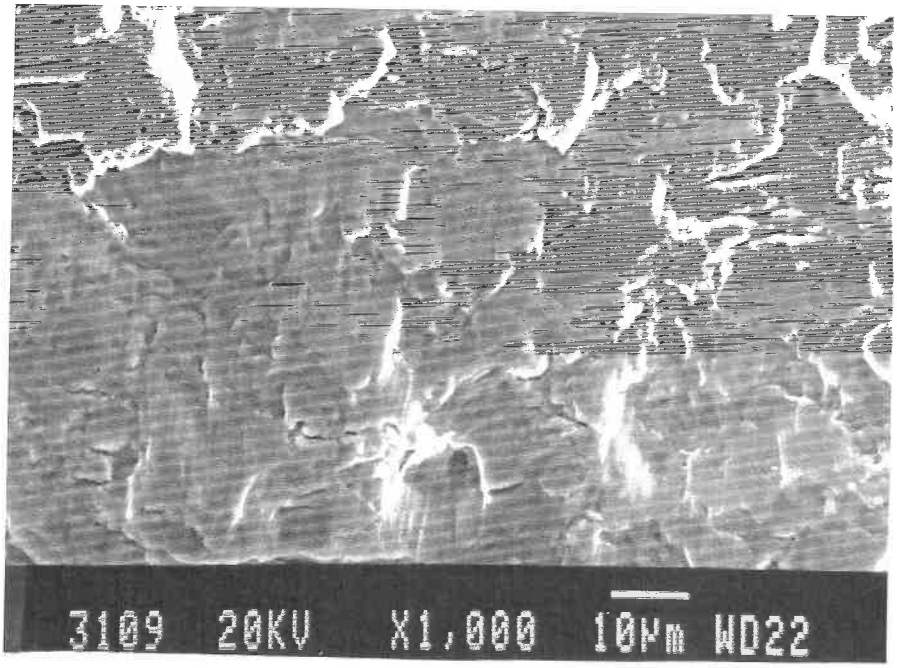

ıre 5.10a Microfractograph of Ti64 tested under in-phase TMF cycling.
$\Delta K \sim 35$ (Mpa$\sqrt{m}$).

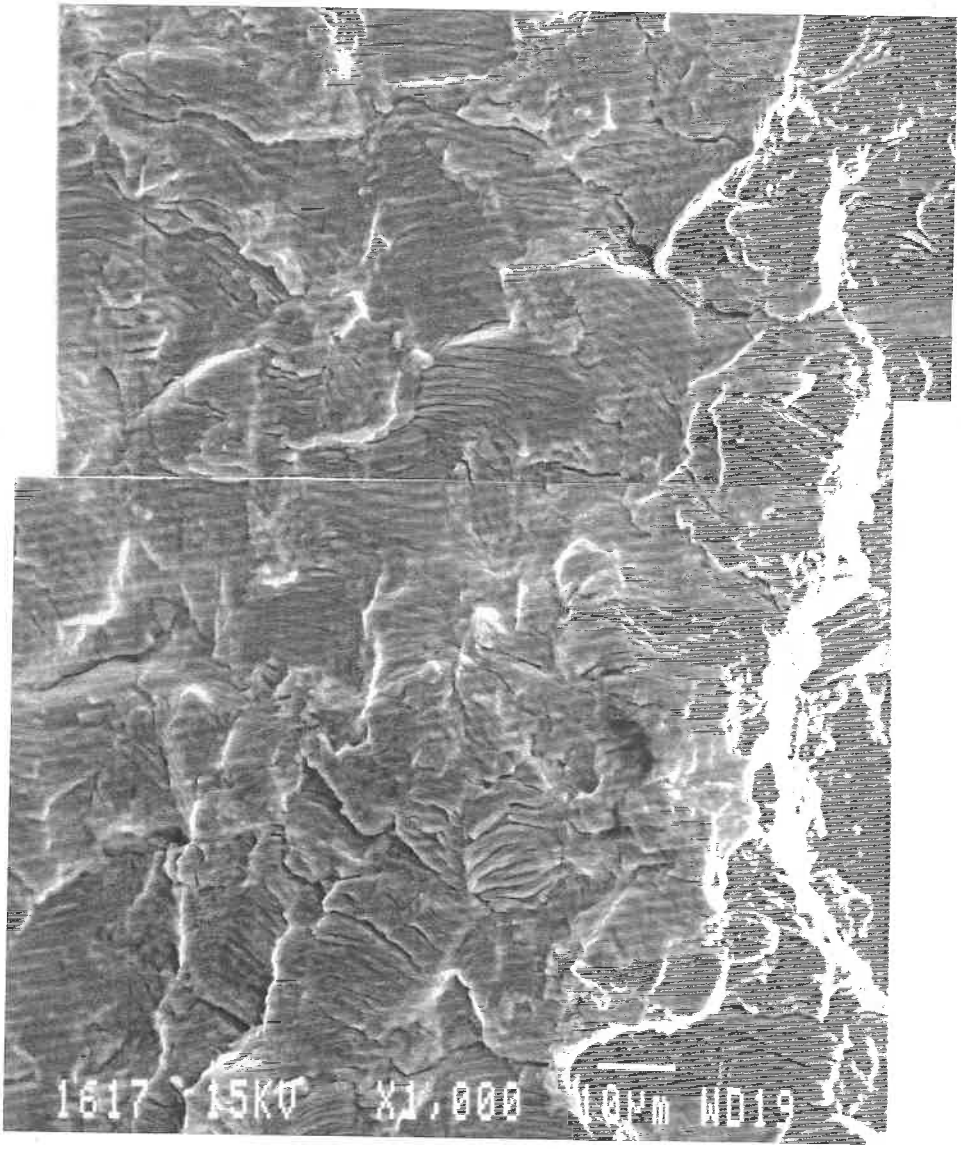

re 5.11 Microfractograph of Ti64 tested under counter-clockwise-diamond TMF
ng. $\Delta K \sim 22$ (Mpa$\sqrt{m}$).

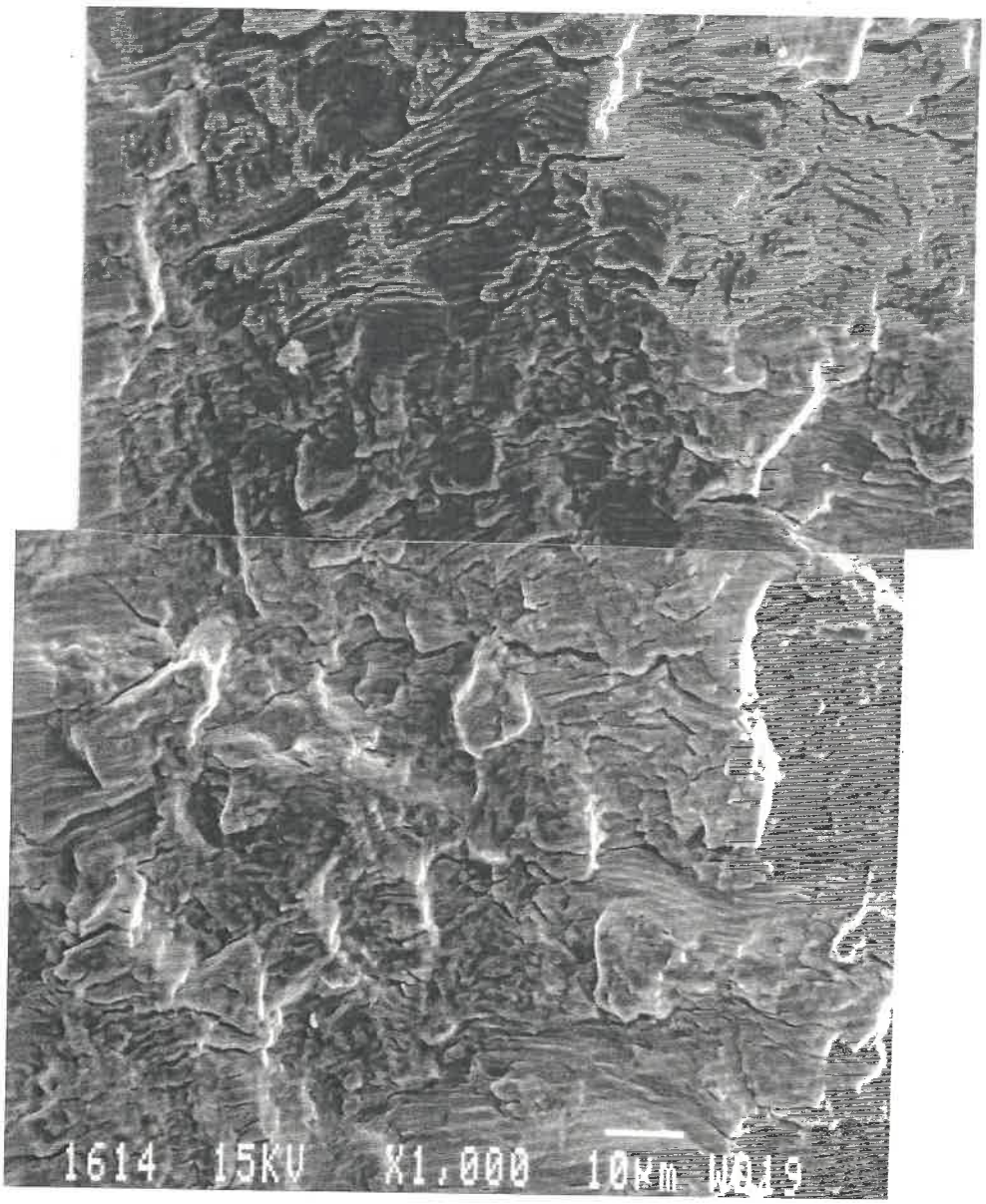

re 5.12 Microfractograph of Ti64 tested under isothermal fatigue cycling at x. $\Delta K \sim 22$ (Mpa$\sqrt{m}$).

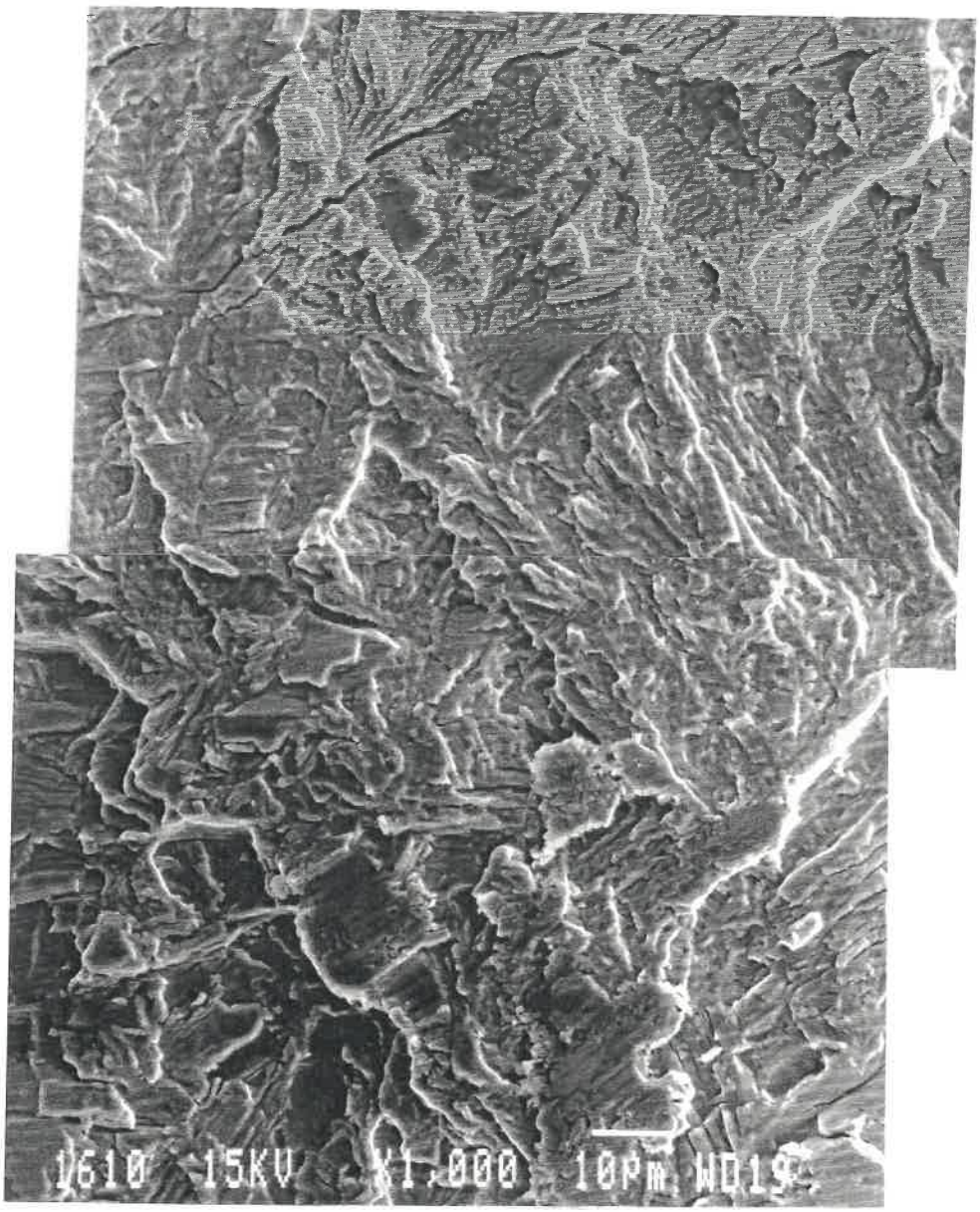

ıre 5.13 Microfractograph of Ti6246 tested under in-phase TMF cycling.
~ 20 (Mpa$\sqrt{}$m).

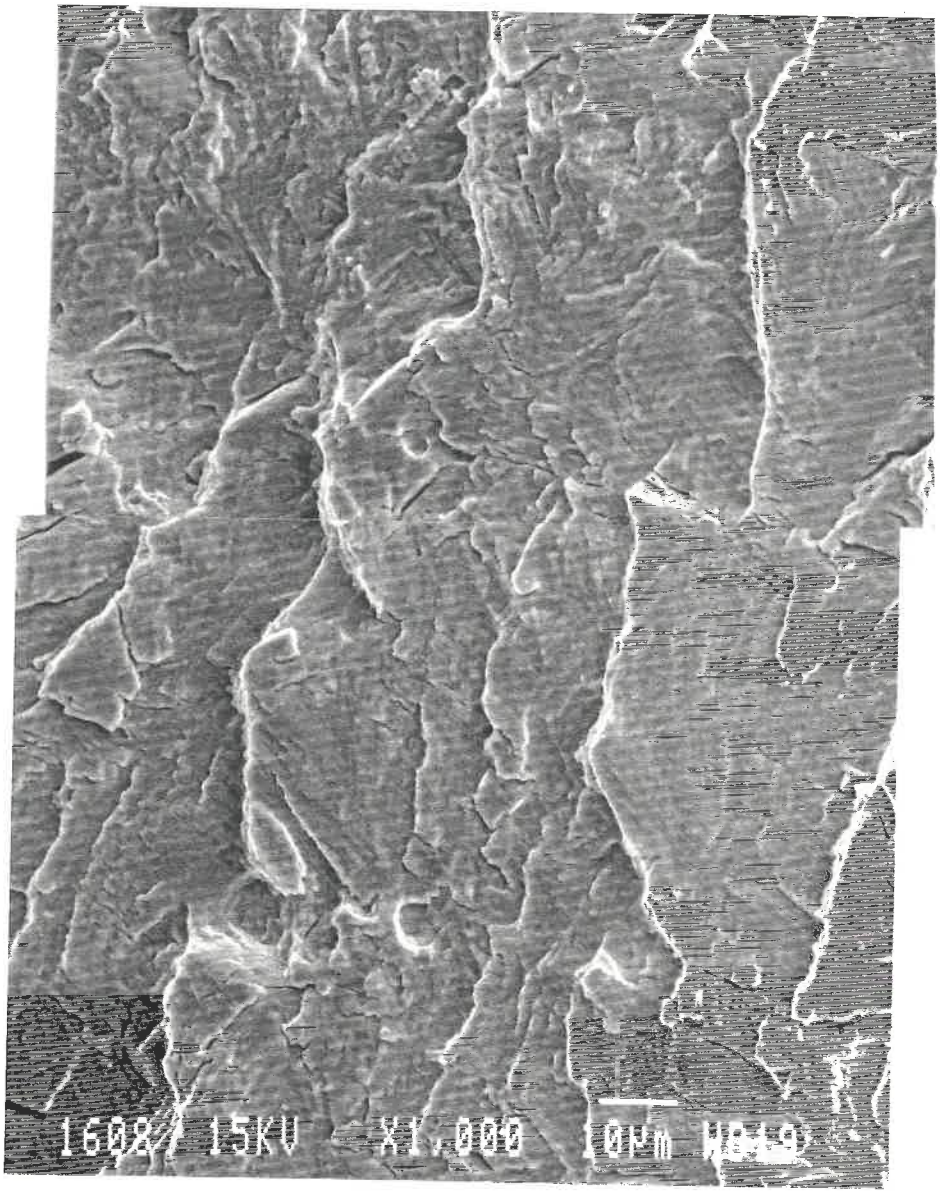

e 5.14 Microfractograph of Ti6246 tested under out-of-phase TMF cycling.
20 (Mpa√m).

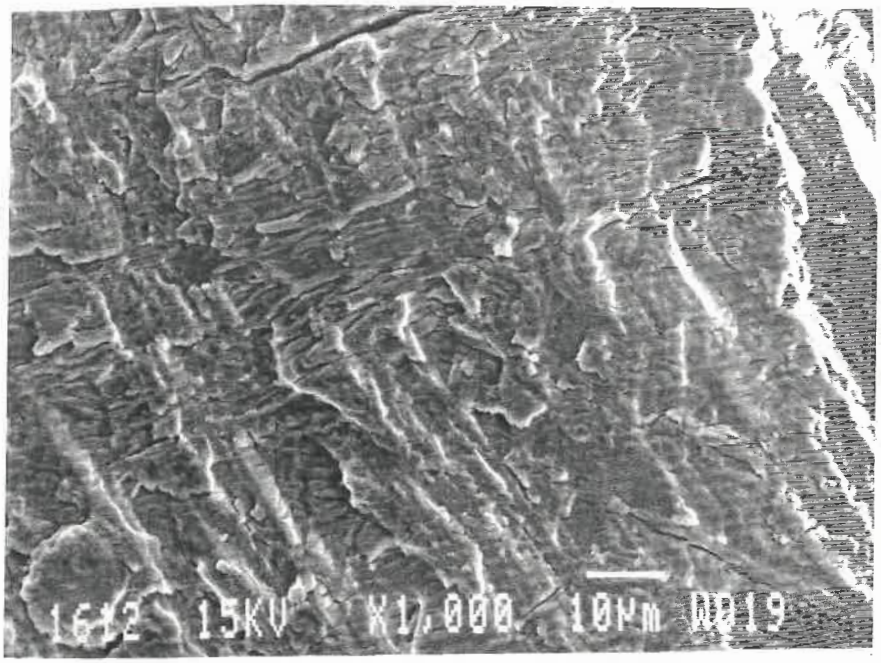

ure 5.15a Microfractograph of Ti6246 tested under in-phase TMF cycling.
~35 (Mpa√m).

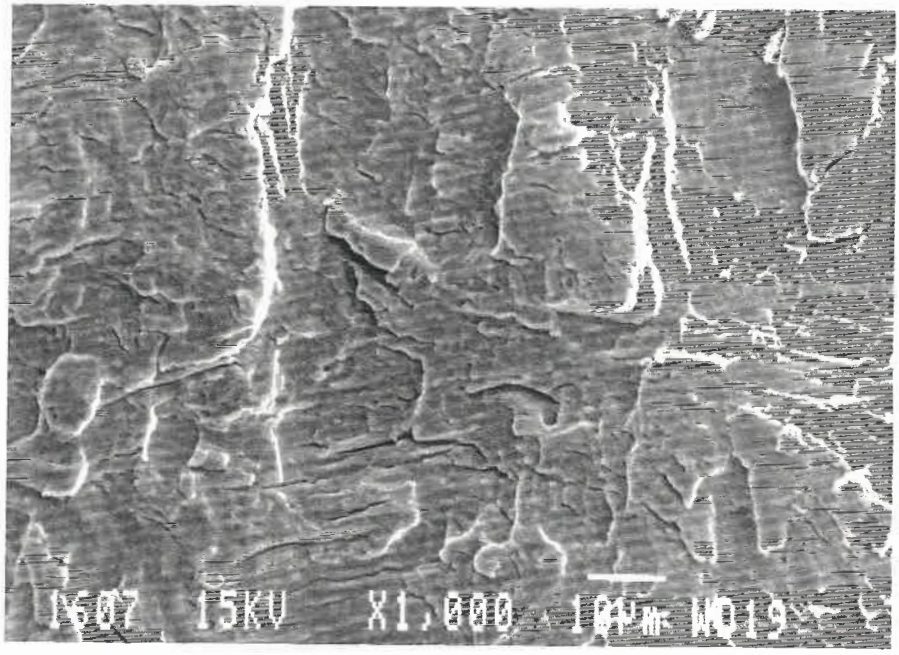

ure 5.15b Microfractograph of Ti6246 tested under out-of-phase TMF cycling.
~35 (Mpa√m).

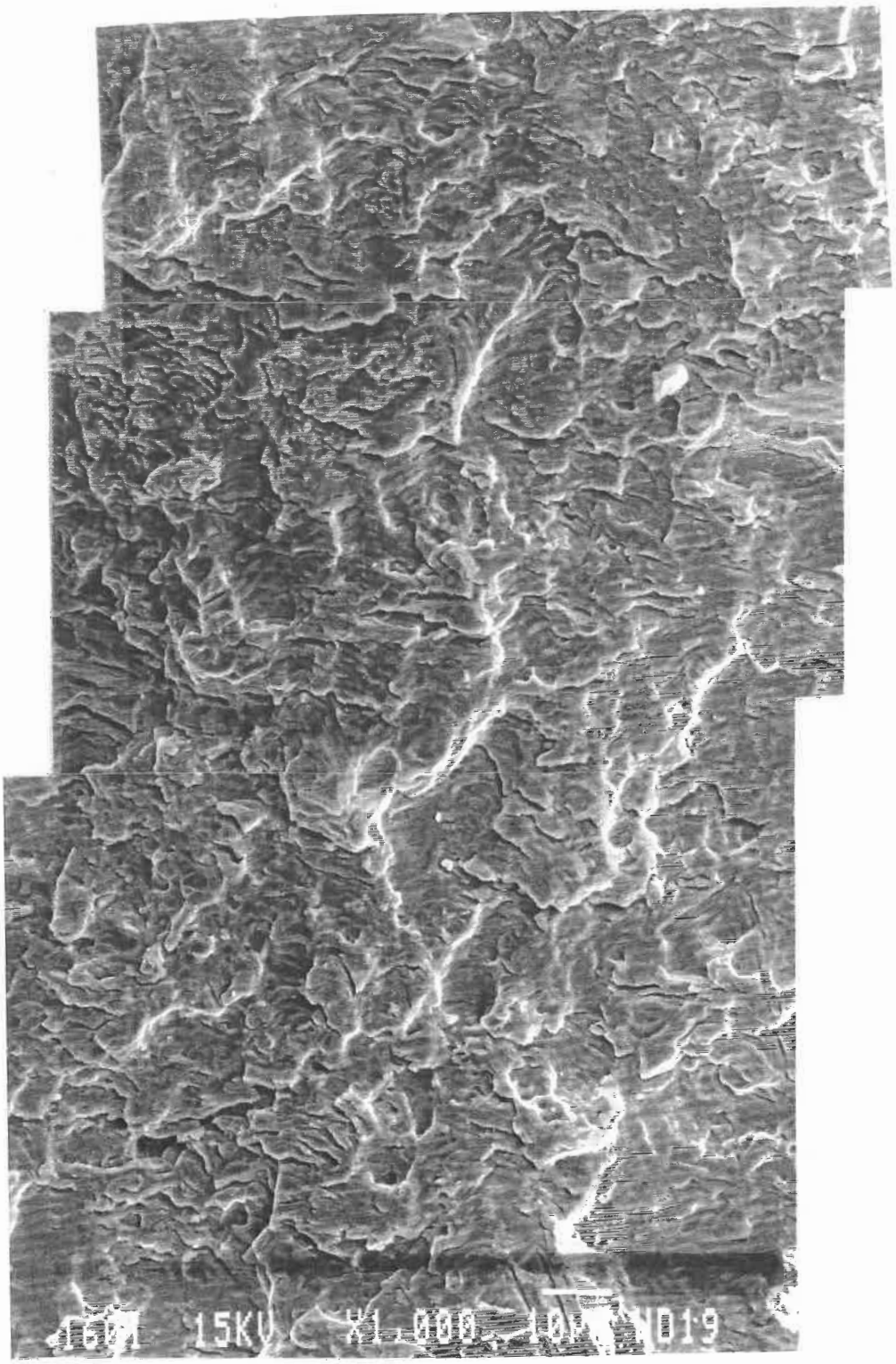

: 5.16 Microfractograph of Ti6246 tested under counter-clockwise-diamond
:ycling. $\Delta K \sim 20$ (Mpa$\sqrt{m}$).

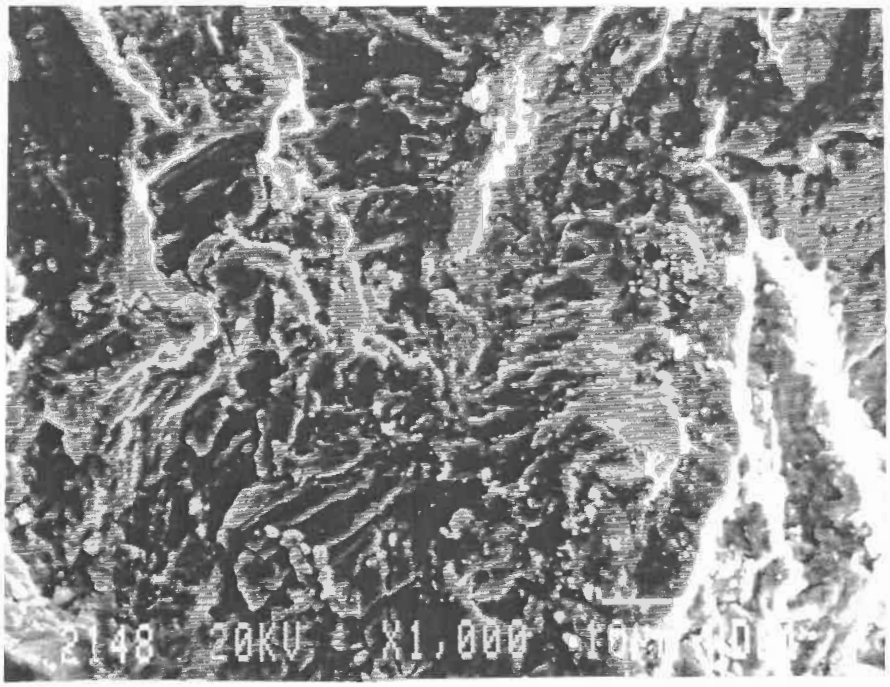

ure 5.17a Microfractograph of Ti6246 tested at 480°C showing oxidation deposits, tle fracture marks and secondary cracks. (ΔK ~ 15 (Mpa√m), 1000 X)

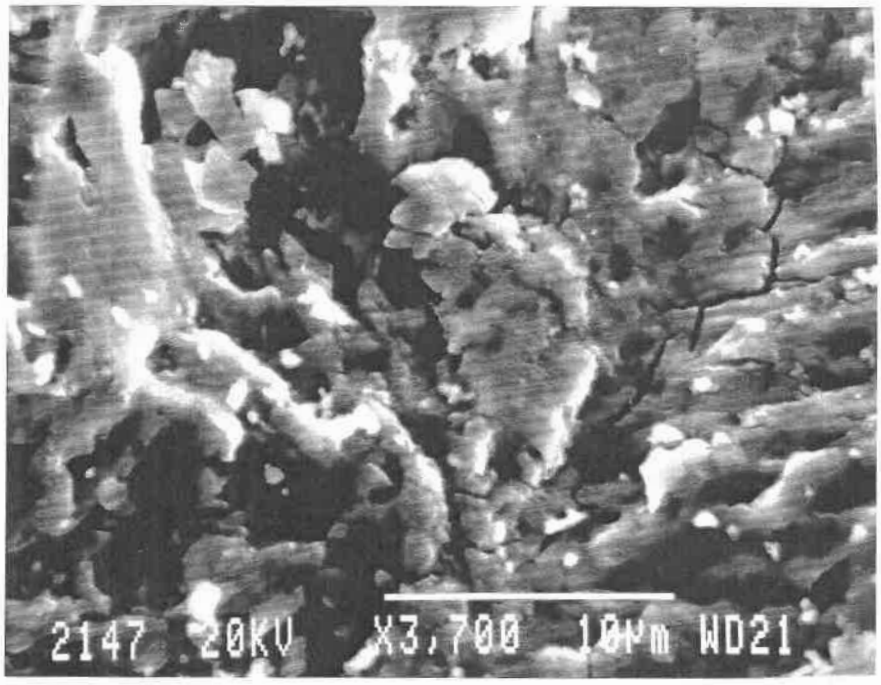

ıre 5.17b Microfractograph of Ti6246 tested at 480°C showing oxidation ɔsits, cleavage-like facets and secondary cracks. (ΔK ~ 15 (Mpa√m), 3700 X)

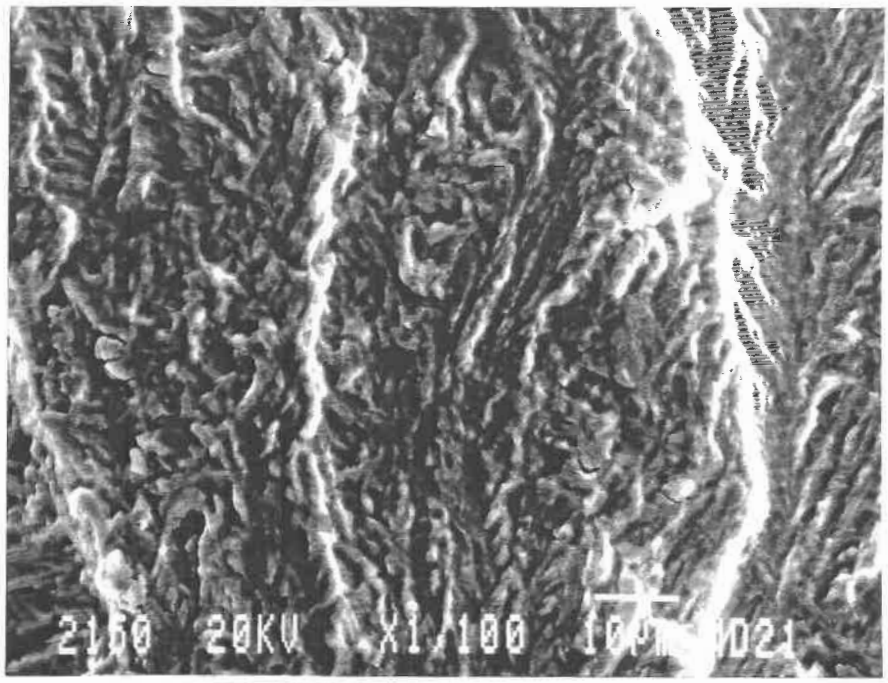

e 5.18a Microfractograph of Ti6246 tested at 480°C showing traces of α-phase
ination as a result of oxidation weakend α/ß interfaces. (ΔK ~ 15 (Mpa√m),
X)

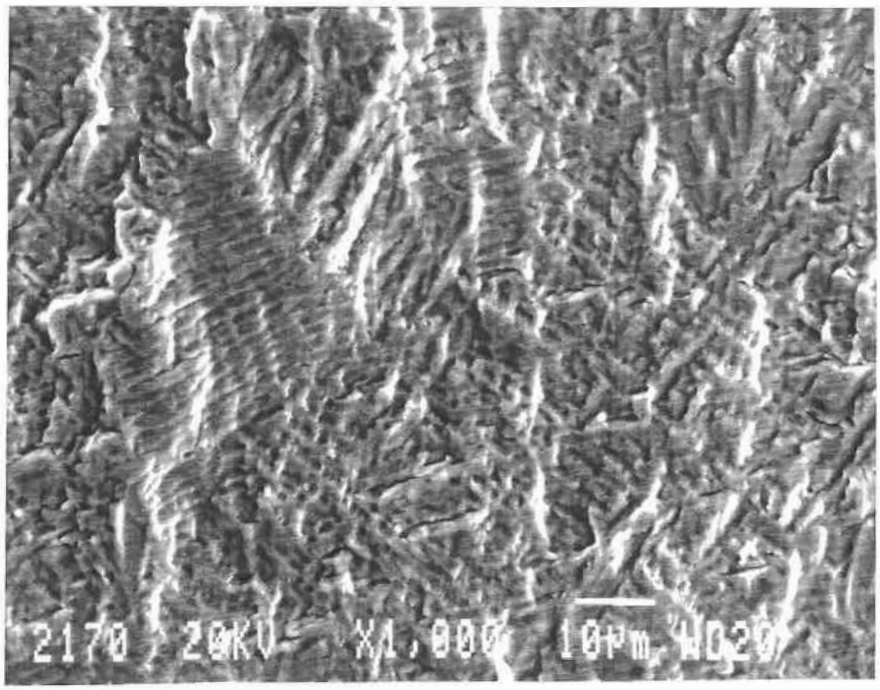

re 5.18b Microfractograph of Ti6246 tested in out-of-phase TMF condition in
h environment effects are much smaller so that well defined fatigue striations
)e observed. (ΔK ~ 15 (Mpa√m), 1000 X)

CHAPTER 6

SINGLE TOOTH FIRTREE SPECIMEN LCF TESTING

OF PWA1480 AT 1200°F

6.1 INTRODUCTION

As a part of the verification test plan, Low Cycle Fatigue (LCF) testing of Single Tooth Firtree (STFT) specimen of unpeened single crystal PWA1480 has been performed at 650°C (1200°F) in the TMF rig. Computerized testing procedures including fatigue crack growth measurements and inductive heating of the specimen were developed for the STFT testing. The data for fatigue Crack initiation life N_i (to 1/32" crack) and life to final failure of specimen N_f for PWA1480 were obtained. The results were compared with the respective data of P&WA database, and good agreement was observed.

This test plan was set to develop P&WA STFT LCF testing capability on the P&WC TMF rig, similar to that in CEB (commercial engine board) and GESP[177]. A close view of the STFT LCF test setup is given in Figure 6.1. Like the SEN specimen tests, STFT specimen test is also a type of "substructure" test, in which the specimen is designed to have certain component geometrical features at critical locations. This type of test is used to bridge the gap between the pure material

mechanical property test and high cost full-scale component tests such as spin pit test. In many cases, STFT test will help to reduce the number of full-scale component tests. Furthermore, STFT test can be used to rate blade/disc materials and blade/disc surface processing techniques (such as shot penning) and to calibrate structural FEM analysis and LCF life prediction. The STFT LCF test is more flexible and can be easily performed under simulated loading conditions (e.g. spectrum loading, cycling with dwell times, etc.) and at various elevated temperatures.

6.2 EXPERIMENTAL PROCEDURES

The single tooth firtree (STFT) specimens are fabricated from P&WA 1480 single crystal bars used in the turbine blade manufacture. The specimen crystal orientations are $\alpha = 6 - 10°$, $\beta = 45°$ and $\theta = 0°$, as indicated in Figure 6.2. Clear crystal dendrites can be observed from the low magnification microstructure photograph (of cross sections of the specimen) as shown in Figure 6.3. The direction of crystal dendrites indicate the two secondary orientation of the specimen.

The test matrix of the test performed is listed in Table 6.1. As can be seen, the material is unpeened single crystal PWA1480, the test temperature is 650°C (1200°F), and the test mode is in load control with a loading frequency of 1.0 Hz (60cpm). Three stress levels were chosen for the tests. The minimum stress was kept at 2 or 3 Ksi (15Mpa) in order to maintain the contact orientation of the fir tree root

with its STFT grip during the test. The alignment of the load train shown in Figure 6.4 was carefully checked using the procedures proposed by P&WA[177].

The test temperature was controlled by an inductive heating system. An inductive coil made from 3/16" (o.d) cooper tubing was designed to achieved an uniform temperature profile in the test area of STFT specimen (0.375" from the bottom). The maximum temperature deviation within the test area was measured to be less than 15°C (70°F) at 650°C (1200°F). The temperature control accuracy was ±1°C.

Fatigue crack initiation and growth at the fir tree roots were monitored on line by the advanced ACPD technique which has been described in Chapters 2 and 3. Some modifications were made for the STFT specimen. As can be seen in Figure 6.5, two sets of working probes were used for both sides of the STFT specimen to pick up the potential signals. Since the current ACPD measurement system CGM5 has only one working probe channel, a digital switch system (with 20 channel switching capability) was used and incorporated into the test control software so that signals from both probe sets could be monitored. It was found that the ACPD system took 30 to 60 seconds to stabilize itself after each probe switching.

Typical ACPD signal output for a STFT specimen LCF test is shown in Figure 6.6. Here the maximum and minimum readings of potential in a sampled cycle are plotted as a function of number of cycles. The gradual increase of the signals indicated the fatigue crack initiation and propagation in the STFT specimen.

The change of the ACPD signal was assumed to be linearly related to the average crack depth across the specimen thickness[177]. Figure 6.7 shows how the crack initiation life (to 1/32" crack) were obtained from the curves of measured ACPD vs. number of cycles by the ACPD signal processing software "TMFCG". Here the crack aspect ratio was assumed to be a/c=1.0. Thus a 1/32" surface crack length gives a 1/64" crack depth.

6.3 TEST RESULTS

The LCF test results of the STFT specimens are summarized in Table 6.1 as well as in Figure 6.8. The crack initiation lives (to 1/32" crack) of different tests are correlated using the maximum load. Respective data from P&WA data base (average values of the scatter) are also plotted. Fairly good agreement between P&WC and P&WA data can be observed. Besides, narrower scatter of the data was achieved in P&WC STFT specimen LCF tests.

A comparison between the STFT crack initiation life and total life to specimen failure (final crack size indicated in Table 6.1) indicates that the remaining life after 1/32" crack initiation at the fir tree root takes more than 70% of the total life.

Preliminary study on fractured specimen was performed to help understand the fatigue crack initiation and growth mechanisms for the single crystal PWA1480 and crack growth profiles of the STFT specimen.

A Front view of a fractured specimen is given by Figure 6.3. Overall fatigue crack initiation locations and propagation directions can be observed. A closer view of the fatigue crack profiles are given in Figure 6.9. The cracks were initiated near the mid thickness at the fur tree root. The crack growth at both sides of the STFT specimen were found not even in most of the test.

6.4 CONCLUSIONS

Through this verification test plan, experiences on STFT specimen LCF testing were obtained in P&WC TMF rig. Following important technical achievements can be summarized:

- Testing control and data requisition software based on HP9000 300 series system;

- Inductive heating and temperature control system for STFT specimen (P&WA use closed radiation furnace);

- Application of ACPD technique in crack initiation and growth monitoring in STFT specimen LCF test for the first time. No test interruptions were needed for specimen damage assessments.

The main conclusions of this Chapter can be summarized as :

a). The capability of TMF rig in performing STFT specimen LCF tests at elevated temperatures has been demonstrated.

b). Computerized testing procedures for STFT tests including fatigue crack initiation and growth measurement using ACPD techniques have been developed.

c). The ability to replicate the historical P&WA STFT data on unpeened single crystal PWA1480 at 650°C (1200°F) has been demonstrated.

d). A comparison of fatigue crack initiation life N_i with the life to failure (N_f) for the STFT specimen indicates considerable remaining life after 1/32" crack initiation.

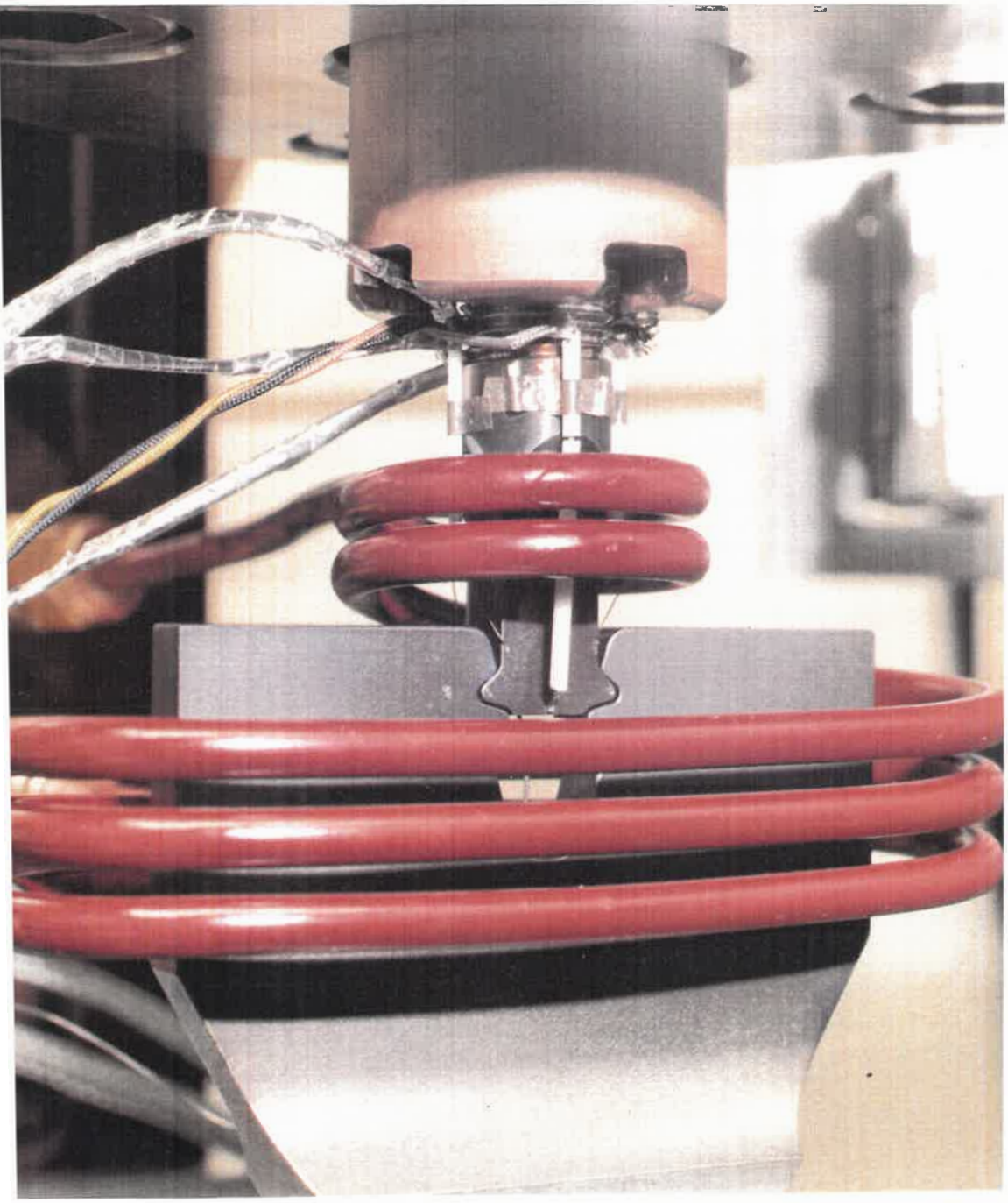

Figure 6.1 An overview of the STFT LCF testing set-up.

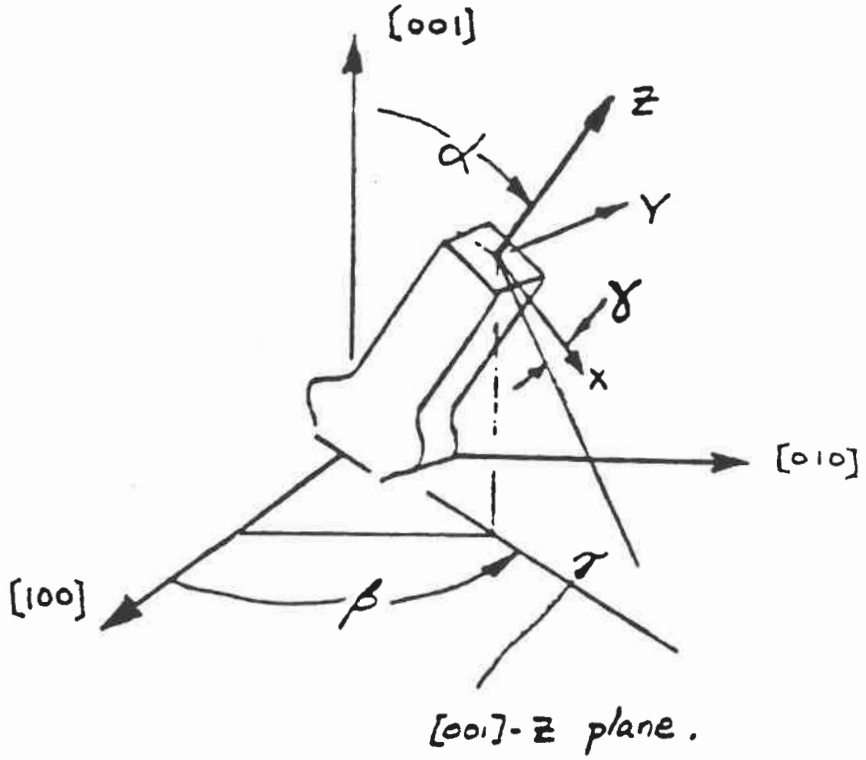

Figure 6.2 The crystal orientation of the PWA 1480 STFT specimen.

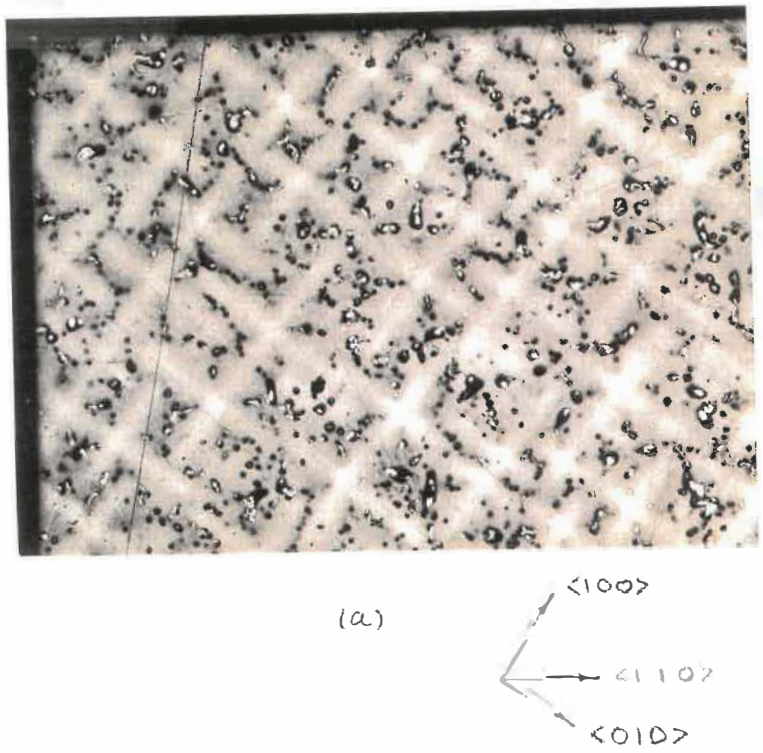

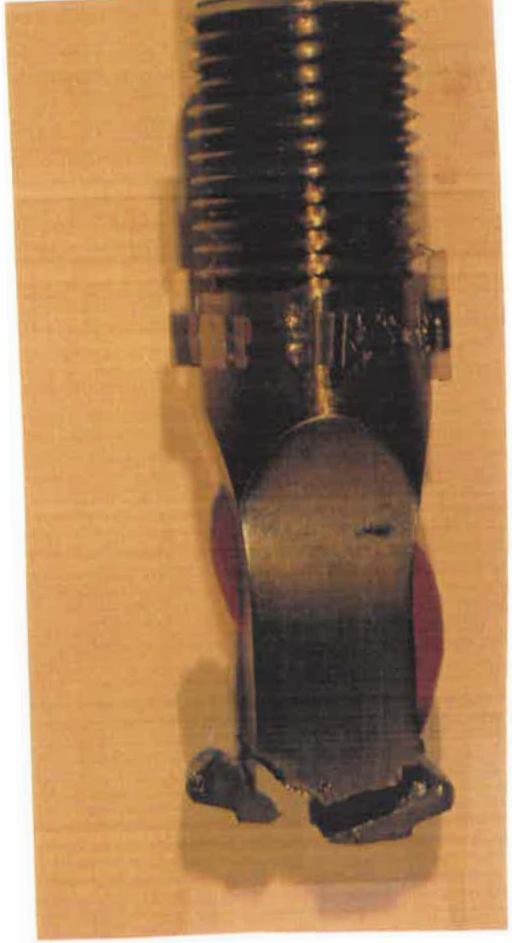

Figure 6.3 (a). A cross sectional view of a PWA 1480 STFT specimen microstructures; (b). A photograph of a tested specimen.

gure 6.4 An illustration of the load train and specimen grips of the STFT test.

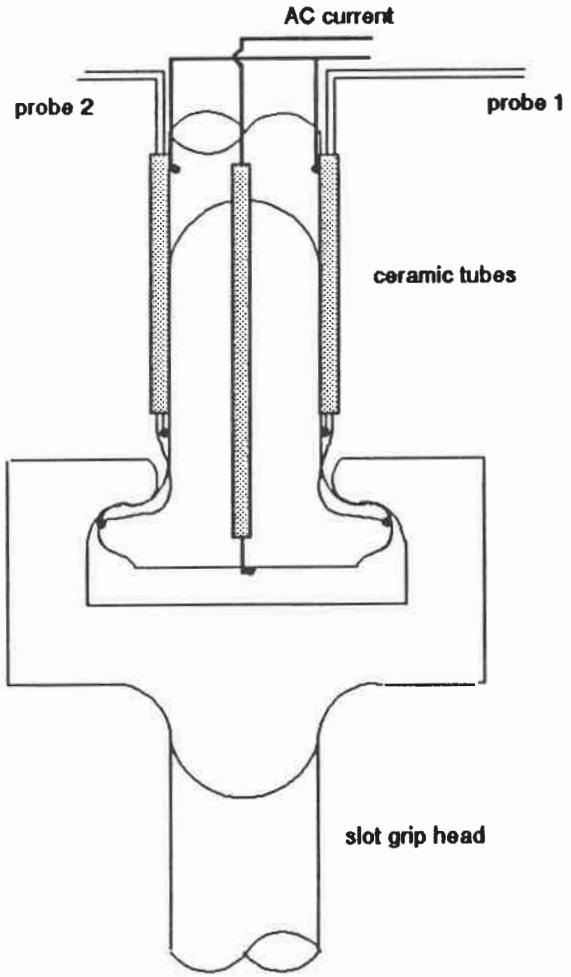

Figure 6.5 A schematic illustration of ACPD probe set-up for the STFT specimen.

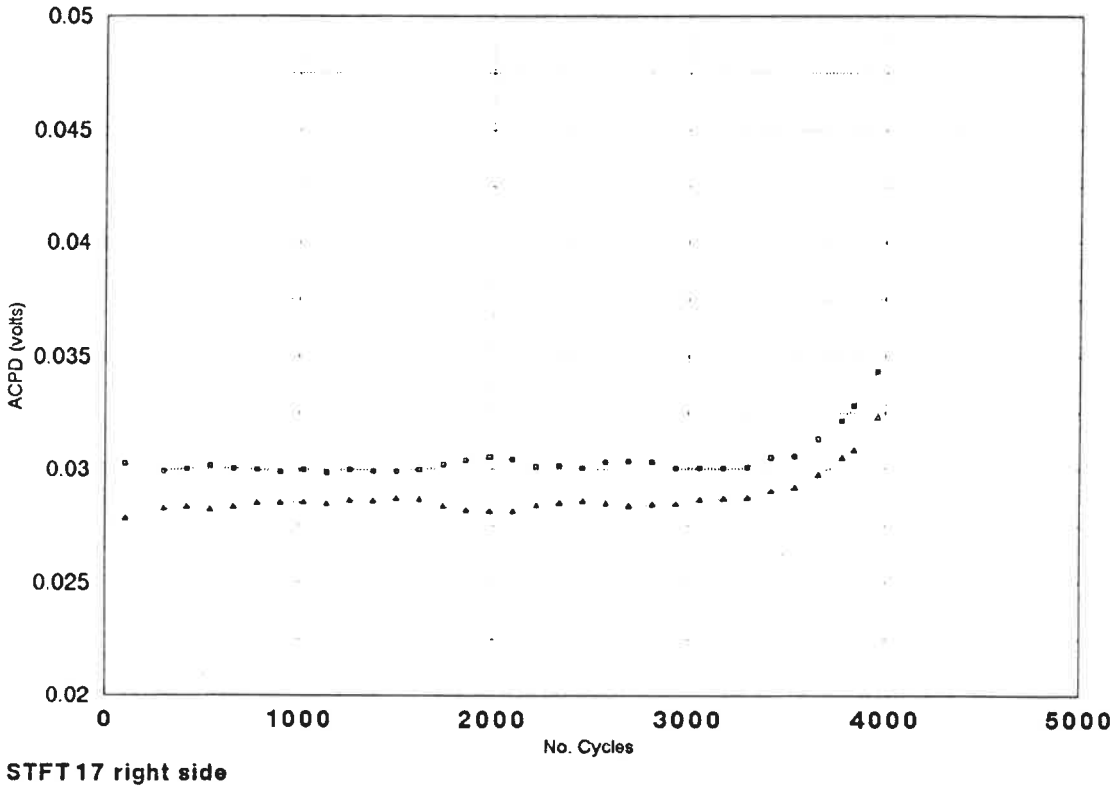

Figure 6.6 Typical ACPD signal output for a STFT specimen LCF test. Here the maximum and minimum values of PD readings in sampled cycles are plotted as functions of number of cycles.

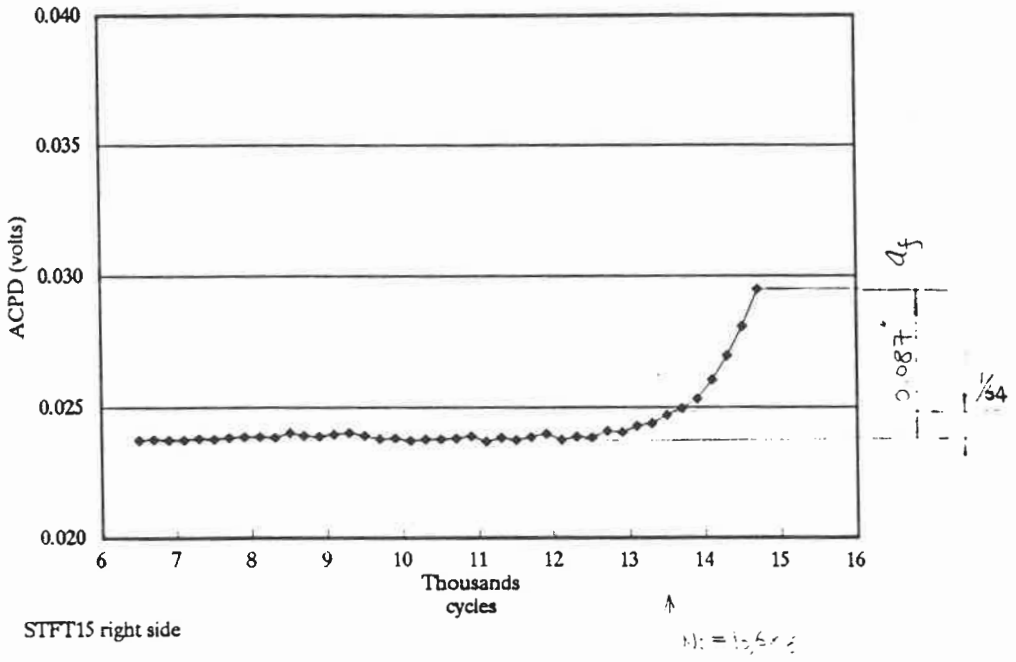

Figure 6.7 A schematic illustration of the ACPD signal processing showing how the crack initiation life (to 1/32" crack) were obtained from the measured ACPD vs. No. of cycle curves.

Table 6.1 The test matrix and main results of STFT LCF tests on PWA1480.

	Specimen Series No.	Stress σmax (Ksi)	Stress σmin (Ksi)	R-ratio σmin/σmax	Peak load (lbs) (actually measured)	Ni life to 1/32"	Nf life at test stop	max. crack length at test stop
STFT14	SKN70050799311	24.66	3.021	0.1224	2690.1	19378	20701	0.1915
STFT15	SKN70050799311	24.66	3.021	0.1224	2691.5	13688	14701	0.0880
STFT16	SKN70050799311	24.66	3.021	0.1224	2695.0	17126	18301	0.1150
STFT06	SKN70050799310	29.20	2.014	0.0688	3200.9	6565	7080	0.0910
STFT07	SKN70050799310	29.20	3.021	0.1032	3122.9	3995	4697	0.0905
STFT08	SKN70050799309	29.20	3.021	0.1032	3147.1	2318	2499	0.0435
STFT09	SKN70050799310	29.20	3.021	0.1032	3145.5	2464	3041	0.0945
STFT17	SKN70050799306	29.20	2.014	0.0688	3147.0	3602	3961	0.0685
STFT18	SKN70050799306	29.20	2.014	0.0688	3156.8	3546	3867	0.0910
STFT11	SKN70050799309	33.72	3.021	0.0893	3686.9	1411	1543	0.0470
STFT12	SKN70050799309	33.72	3.021	0.0893	3698.3	1188	1387	0.0440
STFT19	SKN70050799306	33.72	3.021	0.0893	3640.8	1539	1785	0.0600

Material: PWA1480
Test Temperature 1200°F
Loading Frequency 1.0 Hz

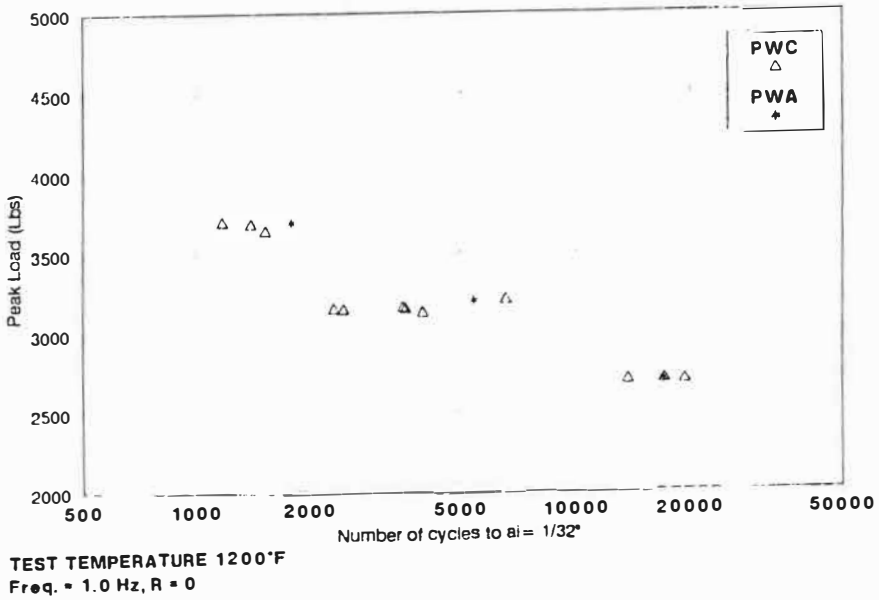

Figure 6.8 Correlation of STFT crack initiation life data using the maximum tensile load. The respective data from PWA historical data base (average values) are also plotted.

ıre 6.9 The fatigue crack propagation profiles for both side of a STFT specimen.
'A1480, 1200°F)

SUMMARY

In this chapter, a summation of major progress made towards achieving the objectives of the project is presented.

- THERMAL-MECHANICAL TESTING SYSTEM

the system is composed of two independent closed loop control units. One loop is for temperature control, while the other is for mechanical loading control. The specimens are heated by an inductive heating system with its output power regulated by a digital temperature control unit. The cooling part of a thermal cycle is realized by an air convection cooling system. Stable and accurate temperature control was achieved by well designed induction coils and cooling air distributor, and also by fine tuning of the controlling parameters of the inductive heating system and temperature control unit. Mechanical cycling is performed by a 100 KN electro-hydraulic servo material testing system equipped with state-of-the-art digital control units and user computer interfaces. The testing control and data acquisition are carried out by HP digital units.

Testing control procedure and data acquisition software (TMF-1), based on the HP9000 system, were developed. The system is capable of performing many structural material mechanical property tests including (1) monotonic loading stress-strain test; (2) cyclic loading stress-strain test; (3) isothermal LCF test; and (4) TMF

test. The main features of the system are (1) user-friendly testing parameter input and verification; (2) automatic testing system set-up and calibration; (3) live data display and monitoring; (4) background multi-channel high-speed (100,000 readings/sec) data collection and transfer; and (5) interactive overall testing control procedure (i.e. starting, sampling cycle, safety check, and stop criteria, etc.). Furthermore, the code is composed of structured modules which increase its versatility to accommodate any new test requirements.

Three typical TMF cycles were performed in the rig, which include out-of-phase (maximum strain at minimum temperature), in-phase (maximum strain at maximum temperature) and a faithful type TMF cycle (diamond).

By carrying out LCF and TMF testing on the titanium alloys, this system was proven capable of cycling specimens under various programmed thermal-mechanical histories (isothermal and anisothermal conditions) with a high degree of accuracy and reliability.

- ACPD CRACK GROWTH MONITORING SYSTEM

The fatigue crack initiation and growth were measured using an Alternative Current Potential Drop (ACPD) measurement unit CGM5. Optimum instrument set-up, probe spot welding procedures and probe configurations were developed for several geometries of titanium specimens including the SEN geometry (for isothermal

and TMF conditions). The materials response to different frequencies and amplitudes of AC currents were characterized.

The system's sensitivity and linearity with respect to the measurement of crack length are enhanced by the skin effect which results from passing a high frequency AC current (>30KHz) through the specimen. This has been verified by several test results. With the present ACPD system, the crack growth as a function of number of cycles (a-N curve) can be easily obtained for room and elevated temperatures. .

The actual ACPD system has achieved an average crack initiation detection limit of about 50 μm with a probability of detection (POD) better than 95%. This is well below the crack initiation size specified by the Engine Structural Integrity Program (ENSIP) used in component life management planning for P&WC commercial engines, in which a_i = 1/32" (0.8 mm). Hence the system can be used to measure the crack initiation life of specimens and component like coupons. In turn, the long crack growth (average) can be monitored by the system with an accuracy of about 2 μm per 1 mV ACPD change at RT and 18 μm per 1 mV at high temperature. This is also well below the ASTM requirements for fatigue crack growth testing. Furthermore, the system was shown to be ideal for studying the closure mechanisms for short and long cracks.

- STUDY OF FATIGUE CRACK INITIATION

Fatigue crack initiation tests were performed on Ti64 and Ti6246 at room and elevated temperatures (400°C for Ti64, 480°C for Ti6246). Single Edge Notched (SEN) specimens were used. The notch was semi-circular in shape and designed to match the notch features (i.e. the stress concentration factor K_t) of bolt holes encountered in P&WC turbine compressor disc. .

The crack initiation lives in the SEN specimens were detected by the ACPD technique. The relationship between the measured ACPD signal and notch fatigue cracking pattern were studied. Fatigue crack initiation life N_i was defined as the cycles to form a crack with an average depth of 1/64" at the root of the notch. With this definition, N_i can be easily obtained from a measured a-N curve.

A notch strain analysis procedure based on Gemma's model were developed, which establishes the functions that relate the far-field controlled strain and the notch strain/stress parameters including total strain, maximum plastic strain and cyclic plastic strain range at the root of the notch. These strains were used to correlate the crack initiation data. To obtain the material's cyclic constants, high temperature cyclic stress-strain tests were also performed.

The typical LCF results obtained with SEN specimens indicated that:

- a new methodology to predict LCF lives of components using low cost "substructural" (component-like) LCF test data is possible and reliable;

- the fatigue crack initiation (FCI) resistance of Ti64 forging at RT and 400°C, which is mainly caused by cyclic plasticity, is good;

- the fatigue crack initiation resistance of Ti6246 forgings at high temperature (480°C), where the FCI is greatly affected by environment-assisted embrittlement, is low.

These data confirmed the LCF results observed in the field and in full-scale component testing.

- SHORT AND LONG CRACK GROWTH ANALYSIS

As soon as cracks initiate, crack growth becomes of significant concern. In this project, fracture mechanics parameters based on various solutions for the stress intensity factor (K) were investigated in analyzing the crack growth kinetics. The effect of notch stress field on the crack growth rates were addressed. The stress intensity factors for small cracks emanating from notches and long cracks growing out of the affected zone were also calculated separately. The FCG test program has achieved:

- a quantification of three transitional (critical) crack lengths which separate microstructural growth controlled (<60μm), inelastic notch field growth controlled (<130μm), elastic notch field growth controlled (<420μm) and far-field growth controlled regions for the SEN specimen studied;

- the crack growth rate data for Ti64 at RT, 220,500, 750°F; which can be used to predict crack growth lives of actual components;

- the crack growth rate data for Ti6246 at RT, 300, 625 and 900° F; which can be used to predict crack growth lives of actual components;

- a quantification of the effect of temperature and microstructure on the crack growth rates in titanium alloys.

These data were also used in understanding the fatigue crack growth mechanisms of the titanium alloys.

- THERMAL MECHANICAL FATIGUE CRACK GROWTH

TMF crack growth tests were performed on Ti64 and Ti6246 forgings. SEN specimens were used for all tests. The notches were machined (as a pre flaw) by EDM. The specimens were cycled under mechanical strain controlled conditions with a cycle period of 100 sec (0.01 Hz). Three TMF conditions were investigated. The

TMF testing capabilities of the rig and the application of the ACPD technique to anisothermal conditions were verified.

Thermal mechanical fatigue crack data were obtained for Ti64 with temperature cycling between 300°F (T_{min}) and 750°F (T_{max}), and for Ti6246 with temperature cycling between 392°F (T_{min}) and 900°F (T_{max}). Isothermal FCG tests at T_{min} and T_{max} and at the same cyclic frequency were also performed for the sake of comparison.

From TMF test results, the following conclusions can be drawn:

- The TMFCG data for Ti64 and Ti6246 fell in-between the isothermal FCG curves at the two extreme temperatures. More precisely, the in-phase TMF data were close to FCG data at T_{max} while the out-of-phase data TMF data close to FCG data at T_{min};

- Strong crack closure effects were observed in the Ti64 TMFCG tests;

- Strong environmental effects (oxidation-assisted cracking) were found with Ti6246 tested in in-phase TMF cycling conditions and at T_{max} ;

A simple model based on a mechanistic analysis, which incorporates the time-dependent damage caused by environment attack in isothermal and TMF conditions, was proposed for Ti6246.

Furthermore, the accelerated crack growth observed in the in-phase TMF tests explained the FCG data obtained in the field and in the spin pit tests of the Ti6246 forgings. These results are found to be in excellent agreement with the results recently published by an independent study[22] on a similar titanium forging (Ti6242) tested at high temperatures.

- FRACTOGRAPHIC STUDY OF THE FCG MECHANISMS

Extensive microscopic observations of the fractured surfaces obtained under different testing conditions were conducted using Scanning Electron Microscopy (SEM). To study the effect of microstructure on fatigue, the microstructural differences between the two titanium forgings were addressed. Composition analyses were performed using a spectrum analyzer, which were used as references to identify the fracture morphology associated with different phases during the fractographic analyses.

For the fatigue crack initiation tests, the SEM analyses were focused on the micro crack initiation sites at the root of the notches. It was found that,

- the crack initiation sites for both alloys were at the α-phase particles or/and at the $\alpha/ß$ interfaces, with cleavage-like facet fracture morphology;

- the large quasi-cleavage facet packets in Ti6246, observed in the high temperature LCF tests, resulted from environment assisted embrittlement of the $\alpha/ß$ interfaces;

- the high FCI resistance of Ti64 is associated with its fine equiaxed α-phase structure;

- the low FCI resistance of Ti6246 is associated with its coarse accicular α-phase structure.

The fractographic observations pertaining to crack growth obtained in isothermal and TMF conditions were focused on (1) the relationship between the microscopic da/dN (using striation count techniques) and the macroscopic experimentally measured data; (2) the effects of microstructures on the crack growth paths; (3) the comparison of the overall fracture morphologies associated with different test conditions.

The results indicate the following:

- a good agreement between the microscopic da/dN and the measured ACPD da/dN (in the ΔK controlled regions - Paris' region);

- secondary cracking along the $\alpha/ß$ interfaces at moderate ΔK's in Ti64 tested at high temperatures;

- preferential α/ß interfacial cracking assisted by high temperature environmental embrittlement in Ti6246;

- differences in crack tip plasticity featured with the in-phase and out-of-phase TMF testing for Ti64;

- differences in crack growth morphologies between the in-phase and out-of- phase TMF testing for Ti6246, as a result of oxidation assisted embrittlement.

These observation resulted in a mechanistic understanding of crack growth for the two titanium alloys, and, in particular, helped the development of a fatigue-assisted and environment-assisted cracking model for Ti6246 and explained the strong crack closure effects found in Ti64 TMF testing.

- LCF TESTS FOR STFT PWA1480 SINGLE CRYSTAL ALLOY

Low cycle fatigue testing of Single Tooth Firtree (STFT) specimens of PWA1480 single crystal were performed at 1200°F. These tests were also used as a verification test plan set to develop STFT LCF testing capabilities at P&WC, similar to the ones available at CEB and GESP (P&WA). This test program has permitted:

- to establish the capability of the TMF rig for performing STFT LCF tests at elevated temperatures;

- to establish a (fully automatic) computerized testing procedure for STFT testing which includes fatigue crack initiation and growth measurements using the ACPD technique. Unlike the testing facilities used at P&WA, the testing procedure developed here at P&WC does not require test interruptions and dismantling of the specimens at regular intervals by technicians.

- to duplicate and verify the historical P&WA STFT data on unpeened single crystal PWA1480 at 650° C.

REFERENCES

[1] M. J. Donachie, Jr.,"TITANIUM AND TITANIUM ALLOYS", Source Book, ASM, 1982.

[2] M. J. Donachie, Jr.,"SUPERALLOYS", Source Book, ASM, 1984.

[3] R. L. Thompson, "Structural Analysis Method Development for Turbine Hot Section Components", J. of Engng for Gas Turbines and Power, ASME Trans. Vol. 111, April 1989, pp. 287-300.

[4] E. W. Collins, "The Physical Metallurgy of Titanium Alloys", ASM, 1984.

[5] J. C. Chesnutt, et al, "Relationship Between Mechanical Properties, Microstructure, and Fracture Topography in $\alpha+\beta$ Titanium Alloys", ASTM STP 600, 1976, pp. 99-138.

[6] T. Matsumoto, et.al, "Fatigue and fracture toughness properties of Ti-6Al-4V with acicular aplpha microstructures", Proc. of 7th Int. Conf. on Titanium, June, San Diego, USA, 1992.

[7] H. J. Frost and M. F. Ashby, "Deformation Mechanism Maps", PERGAMON PRESS, 1982.

[8] N. J. Marchand and J. C. Moosbrugger, "Non-linear Structural Modeling for Life Predictions: Physical Mechanisms and Continuum Theories", Int. J. Pres. Ves. & Piping, vol.47, 1991, pp. 79-112.

[9] N. J. Marchand and W. Dorner, "The Mechanical Processes of Thermal Fatigue Degradation In Cast Turbine Blades", Canadian Aeronautics and Space Journal, Pub. by CASI, Vol. 36, No.2, June, 1990, pp. 72-80.

[10] S. S. Chiu, J. Eftis, D. L. Jones, "Prediction of Fatigue Life With and Without Hold Times Using the Chaboche Viscoplastic Constitutive Theory", J. of Engr. Mat. and Tech., Vol. 112, 1990, pp. 189-197.

[11] R. E. Hill, "Physical Metallurgy Principles", Second Edition, D. Van Nostrand Co., 1973.

[12] M. A. Meyers and K. K. Chawla, "Mechanical Metallurgy , principles and application", Prentice-Hall, Inc., 1984.

[13] Y. Krishna et al, "Fracture Mechanism Map For Alloy Ti-6Al-4V", Proc. of 4th Inter. Conf. on Titanium, May 19-22, 1980, pp. 1701-1707.

[14] A. K. Miller and T. G. Tanaka, "A New Method for Integrating Unified Constitutive Equations Under Complex Histories", J. of Engng Mater. and Tech., Vol. 110 July 1988, pp. 205-211.

[15] K. S. Chan, U. S. Lindholm, "Inelastic Deformation Under Nonisothermal loading", J. of Engr. Mat. and Tech., Vol. 112, 1990, pp. 15-25.

[16] K. S. Chan, U. U. S. Lindholm et al, "High Temperature Inelastic Deformation of the B1900+Hf Alloy Under Multiaxial Loading: Theory and Experiment", J. of Engr. Mat. and Tech., Vol. 112, 1990, pp. 7-14.

[17] V. G. Ramaswamy et al, "A Unified Constitutive Model for the Inelastic Uniaxial Response of René 80 at Temperatures Between 538° C and 982° C", J. of Engr. Mat. and Tech., Vol. 112, 1990, pp. 281-286.

[18] W. J. Plumbridge and E. G. Ellison, "Stress Response Behaviour of A Cast Nickel Base Superalloy Subject to Combined Creep-Fatigue", Fatigue Fract. Engng. Mater. Struc., Vol.14, No.4, 1991, pp. 373-389.

[19] "Oxidation of metals and alloys", Seminar of ASM, Oct . 1970.

[20] "Oxidation of metals", by Karl Hauffe, CN63-1768, Plenum Press, 1965.

[21] Z. Liu and G. Welsch, "Literature survey on diffusivities of oxygen, Aluminum, and Vanadium in Alpha Titanium, Beta Titanium, and in Rutile", Met. Trans. A, Vol. 19A, April 1988, pp. 1121-1125.

[22] J. U. Specht, "The low cycle fatigue behaviour of titanium alloys", Proc. of LCF-3, Sept. 5-10, Berlin, Germany, 1992, pp.19-24.

[23] M. Niinomi et.al., "Micromechanism of improvement in crack initiation and propagation toughness of a Ti-AL-Sn-Zr-Mo alloy by coarsening prior β-grains", Materials Science and Technology, Vol.4 , Sept., 1988.

[24] M. Niinomi and T. Kobayashi, "Toughness and strenght of microstructurally controlled titanium alloys", ISIJ Int., Vol. 31, No. 8, pp.848-855.

[25] G. Sridhar, et. al., "The influence of heat treatment on the structure and properties of a near-α titananium alloy", Met. Trans. A, Vol. 18A, 1987, pp. 877-885.

[26] C. G. Rhodes, "Influence of α/β Interface Phase on Fracture Toughness and Fatigue Crack Growth Rate in Ti-6Al-4V", Proc. of 4th Inter. Conf. on Titanium, May 19-22, 1980, pp. 1692-1700.

[27] M. Niinomi, et.al., "Improvement in mechanical properties of $\alpha+\beta$ type titanium alloys by microstructual control using thermochemical processing", Proc. of 7th Int. Conf. on Titanium, June, San Diego, USA, 1992.

[28] D. Eylon et al, "High Temperature Low Cycle Fatigue Behaviour Of Near Alpha Titanium Alloys", Proc. of 4th Inter. Conf. on Titanium, May 19-22, 1980, pp. 1845-1854.

[29] G. Welsch and W. Bunk, "Deformation modes of the α-phase of Ti-4Al-4V as a function of oxygen concentration and aging temperature", Met. Trans. A, Vol. 13A, 1982, pp. 889-899.

[30] G.T. Gray III, G. Luetjering, and J. C. Williams, "The influence of oxygen on the structure, fracture, and fatigue crack propagation behavior of Ti-8.6 Wt Pct Al", Met. Trans. A, Vol. 21A, 1990, pp. 95-105.

[31] J. L. Gilbert and H. R. Piehler, "Grain Egression: a new mechanism of fatigue-crack initiation in Ti6Al-4V", Met. Trans. A, Vol. 20A, 1989, pp. 1715-1725.

[32] Y. Mahajan and H. Margolin, "Low cycle fatigue behavior of Ti-6Al-2Sn-4Zr-6Mo: Part1. The role of microstructure in low cycle crack nucleation and early crack growth", Met. Trans. A, Vol. 13A, 1982, pp. 257-267.

[33] A. Dowson, C.J. Beevers, and L. Grabowski, "The microstructure features associated with the growth of short fatigue cracks in a Near-Alpha Ti alloy", Proc. of 7th Int. Conf. on Titanium, June, San Diego, USA, 1992.

[34] J. E. Heine, J. R. Warren and B. A. Cowles, "Thermal Mechanical Fatigue of Coated Blade Materials", WRDC-TR-89-4027, internal report, June 1989.

[35] D. A. Boismier and H. Sehitoglu, "Thermo-Mechanical Fatigue of Mar-M247: Part 1- Experiments", Trans. of ASME, Vol. 112, Jan. 1990, pp. 68-79.

[36] H. Sehitoglu and D. A. Boismier, "Thermo-Mechanical Fatigue of Mar-M247: Part 2- Life Prediction", Trans. of ASME, Vol. 112, Jan. 1990, pp. 80-89.

[37] P. K. Wright, "Oxidation-Fatigue Interactions in a Single-Crystal Superalloy", ASTM STP 942, 1988, pp. 558-575.

[38] F. Rezai-Aria and L . Rémy, "An Oxidation Fatigue Interaction Damage Model For Thermal Fatigue Crack Growth", Engng. Fract. Mech. Vol. 34, No. 2, pp. 283-294, 1989.

[39] M. François and L. Rémy, "Thermal-Mechanical Fatigue of MAR- M509 Superalloy. Comparison With Low-Cycle-Fatigue Behaviour", Fatigue Fract. Engng Mater. Struct. Vol. 14, No. 1, 1991, pp. 115-129.

[40] J. L. Malpertu and L. Rémy, "Influence of Test Parameters on the Thermal-Mechanical Fatigue Behaviour of Superalloy", Metallurgical Trans. A, Vol. 21A, Feb. 1990, pp. 389-399.

[41] H. L. Berstein and J. M. Allen, "Analysis of Cracked Gas Turbine Blades", ASME, 91-GT-16, 1991.

[42] N. Ohno, Y. Takahashi and K. Kuwabara, "Constitutive Modeling of Anisothermal Cyclic Plasticity of 304 Stainless Steel", J. of Engng Mater. and Tech. Vol. 111, Jan. 1989, pp. 106-114.

[43] N. J. Marchand, "Thermal-Mecanical Fatigue of combustors, Vanes and Blades Components", Research Proposal, 1989.

[44] N. Marchand, G. L'Esperance, and R. M. Pelloux, "Thermal-Mechanical Cyclic Stress-Strain Responses of Cast B-1900+Hf", ASTM STP 942, 1988, pp. 638-656..

[45] N. J. Marchand and R. M. Pelloux, "High Strain Fatigue Crack Growth in Nickel-Base Alloys", Res. Mechanica, Vol. 27, 1988, pp. 285-308..

[46] N. J. Marchand, R. M. Pelloux and B. Ilschner, "Non-isothermal fatigue crack growth in Hastelloy-X", Fatigue Fract. Engng Mater. Struct. Vol. 10, No.1 1987, pp. 59-74..

[47] N. Marchand and R. M. Pelloux, "Thermal-Mechanical Fatigue Crack Growth in Inconel X-750", NASA Contractor Report 174740, Oct. 1984.

[48] N. Marchand and R. M. Pelloux, "Thermal-Mechanical Fatigue crack growth in B-1900+Hf", in High Temperature Alloys For Gas Turbines And Other Applications [Vol. II], ed. by Betz et al. 1986, pp. 1543-1558.

[49] N. Marchand and R. M. Pelloux, "A Computerized Test System For Thermal-Mechanical Fatigue Crack Growth", J. of Testing and Evaluation, JTEVA, Vol. 14, No.6, Nov. 1986, pp.303-311.

[50] N. Marchand, R. M. Pelloux and B. Ilschner, "A Fracture Mechanics Criterion For Thermal-Mechanical Fatigue Crack Growth of Gas Turbine Materials", Engng Fract. Mech. Vol. 31, No. 3 1988, pp. 535-551.

[51] N. Marchand, D. M. Parks and R. M. Pelloux, "KI-solutions for single edge notch specimens under fixed end displacements", Int. J. of Fracture Vol.31 1986, pp.53-68.

[52] D. A. Wilson and J. R. Warren, "Thermal Mechanical Crack Growth Rate of a High Strength Nickel Base Alloy", J. of Engng. for Gas Turbines and Power", ASME Trans., Vol. 108 April 1986, pp.396-402.

[53] D. A. Wilson and J. R. Warren, "Thermal Mechanical Fatigue Crack Growth", AFWAL-TR-84-4185, March 1985.

[54] H. Sehitoglu, "Constraint Effect in Thermo-Mechanical Fatigue", J. of Engng Materials and Technology, Vol. 107, July 1985, pp. 221-226.

[55] D. Slavik and H. Sehitoglu, "Constitutive Models Suitable for Thermal Loading", J. of Engng Material and Technology, Vol. 108 Oct. 1986, pp. 303-226.

[56] H. Sehitoglu and D. Slavik, "Critical Experiments in Thermo-mechanical Loading", "Low cycle Fatigue and Elasto-Plastic Behaviour of Material", edited by K. T. Rie, Elsevier Applied Science Publication LTD., 1987.

[57] H.Sehitoglu and M. Karasek, "Observations of Material Behaviour Under Isothermal and Thermo-Mecanical Loading", J. of Engng Material and Technology, Trans. of ASME, Vol. 108, April 1986, pp.192-198.

[58] H. Sehitoglu, "Crack-Growth Studies Under Selected Temperature-Strain Histories", Eng. Frac. Mechanics, Vol. 26, No. 4, 1987, pp. 475-489.

[59] M. L. Karasek, H. Sehitoglu, and D. C. Slavik, "Deformation and Fatigue Damage in 1070 Steel under Thermal Loading", ASTM STP 942, 1988, pp. 184-205.

[60] H. Sehitoglu, "Changes in State Variables at Elevated Temperatures" J. of Engng Material and Technology, Trans. of ASME, Vol. 111, April 1989, pp. 192-203.

[61] R. W. Neu and H. Sehitoglu, "Thermomechanical Fatigue, Oxidation, and Creep: Part I. Damage Mechanisms", Metallurgical Transactions A, Vol.20A, Sept. 1989, pp. 1755-1767.

[62] R. W. Neu and H. Sehitoglu, "Thermomechanical Fatigue, Oxidation, and Creep: Part II. Life Prediction", Metallurgical Transactions A, Vol. 20A, Sept. 1989, pp. 1769-1783.

[63] M. C. Fec and H. Sehitoglu, "Thermal-Mechanical Damage in Rairoad Wheels Due To Hot Spotting", Wear, 102, 1985, pp.31-42.

[64] M. Karayaka and H. Sehitoglu, "Thermo-Mechanical Fatigue of Particulate-Reinfored Aluminum 2xxx-T4", Met. Trans. A, Vol. 22A, Mar. 1991, pp. 697-707.

[65] H. Sehitoglu and M. Karayaka, "Prediction of thermomechanical fatigue lives in Metal Matrix Composites", Met. Trans. A, Vol. 23A, July 1992, pp. 2029-2038.

[66] M. Karayaka and H. Sehitoglu, "Thermo-Mechanical Fatigue of Metal Matrix Composites", Proc. of LCF-3, Sept. 5-10, Berlin, Germany, 1992, pp.13-18.

[67] J. J. Pernot and S. Mall, "A Thermal-Mechanical Fatigue Crack-Growth Testing System", Experimental Techniques, Vol. 13, Number 2, 1989.

[68] J. J. Pernot, "Thermal-Mechanical Fatigue Testing of A Titanium-Aluminide Alloy", M.S. Thesis, AFIT/GAE/AA/87D-18, Dec. 1987.

[69] A. Gysler and G. Lutjering, "Influence of test temperature and microstructure on the tensile properties of titanium alloys", Met. Trans. A, Vol. 13A, July 1982, pp. 1435-1443.

[70] K. P. Walker and D. A. Wilson, "Creep Crack Growth Predictions in Inco 718 Using A Continuum Damage Model", private communication.

[71] K. P. Walker, "Research and Development Program For Nonlinear Structure Modeling with Advanced Time-Temperature Dependent Constitutive Relationships", NASA. CR-165533, 1981.

[72] E. H. Jordan and G. J. Meyers, "Fracture Mechanics Applied to Elevated Temperature Crack Growth", J. of Engng Mater. and Tech., ASME Trans., Vol. 111, July 1989, pp306-313.

[73] G. J. Meyers, "Fracture Mechanics Criteria For Turbine Engine Hot Section Components", NASA, CR-167896, 1982.

[74] J. L. Malpertu and L. Remy, "Thermomechanical Fatigue Behaviour of a Superalloy", ASTM STP 942, 1988, pp. 657,671.

[75] G. R. Halford, et al, "Bithermal Fatigue: A Link Between Isothermal and Thermomechanical Fatigue", ASTM STP 942, 1988, pp. 625-637.

[76] E. H. Jordan and G. J. Meyers, "Fracture Mechanics Applied to Nonisothermal Fatigue Crack Growth", Engng Fract. Mechanics Vol.23, No.2, 1986, pp.345-358.

[77] G. Engberg and L. Larsson, "Elevated-Temperature Low Cycle and Thermomechanical Fatigue Properties of AISI H13 Hot-Work Tool Steel", ASTM STP 942, 1988, pp. 576-587.

[78] K. Kuwabara and A. Nitta, "Thermal-Mechanical Low-Cycle Fatigue Under Creep-Fatigue Interaction on Type 304 Stainless Steels", Fatigue of Engineering Materials and Structures Vol. 2, pp. 293-304.

[79] K. Kuwabara, A. Nitta and T. Kitamura, "Thermal-Mechanical Fatigue Life Prediction in High-Temperature Component Materials For Power Plant", ASME Conf. on Advances in Life Prediction Methods, New York, April 18-20, 1983. pp. 131-141.

[80] T. S. Cook, K. S. Kim, and R. L. Mcknight, "Thermal Mechanical Fatigue of Cast Rene 80", ASTM STP 942, 1988, pp. 692-708.

[81] R. Ohtani, T. Kitamura and N. Tada, "Crack Propagation of Varying Temperature Low-Cycle Fatigue Simulation Thermal Fatigue", Proceeding of ICM-5, Beijing, 1987, pp.1101-1108.

[82] A. E. Gemma, F. X. Ashland, and R. M. Masci, "The Effects of Stress Dwells and Varying Mean Strain on Crack Growth During Thermal Mechanical Fatigue", J. of Testing and Evaluation, JTEVA, Vol. 9, No. 4, July 1981, pp. 209-215.

[83] D. F. Mowbray and G. G. Trantina, "Thermal Fatigue Analysis", ASTM STP 612, 1976, pp. 329-352.

[84] A. Krajczyk and Zuchowski, "Specific Strain Work As A Measure of Material Damage Under Creep And Thermal Cycling", Proc. of ICM5, Beijing, 1987, pp. 1095-1100.

[85] G. R. Halford, et.al, "Fatigue Life Prediction Modeling For Turbine Hot Section Materials", J. of Engng for Gas Turbines and Power, ASME Trans. Vol. 111, April 1989, pp. 279-285.

[86] V. Moreno, G. J. Meyers, et al, "Nonlinear Structural And Life Analysis of A Combustor Liner", NASA TM-82846, 1982.

[87] G. R. Halford and S. S. Manson, "Life Prediction of Thermal Mechanical Fatigue Using Strainrange Partitioning", ASTM STP 612, 1976, pp.239-254.

[88] A. A. Sheinker, "Exploratory Thermal-Mechanical Fatigue Results For Rene'80 In Ultrahigh Vacuum", NASA, CR-159444, 1978.

[89] A. Nitta, K. Kuwabara, T. Kitamura and T. Ogata, "The Characteristics of High-Temperature Fatigue Strength in Fe-Base Forged Superalloy A286 Used for Gas Turbine Disk", CRIEPI Report [Japan] E284017, Jan. 1985.

[90] S. Crutzen, R. W. Nichols, "Developments in fracture mechanics and non-destructive examination", Nuclear Engineering and Design 134, 1992, pp. 59-86.

[91] A. E. Gemma, B. S. Langer, and G. R. Leverant, "Thermomechanical Fatigue Crack Propagation in an Anisotropic [Directionally Solidified] Nickel Base Superalloy", ASTM STP 612, 1976, pp. 199-213.

[92] D. F. Mowbray and D. A. Woodford, "Observations and Interpretation of Crack Propagation Under Conditions of Transient Thermal Strain", Conf. Publication No.13 of Int. Conf. on Creep and Fatigue in Elevated Temperature Applications, Philadelphia, Sept. 1973, pp. 179.1-179.7.

[93] T. Koizumi and M. Okazaki, "Crack Growth and Prediction of Enduance in Thermal-Mechanical Fatigue of 12Cr-Mo-V-W Steel", Fatigue of Engng Mater. and Structures, Vol. 1, 1979, pp. 509-520.

[94] D. F. Mowbray, "Derivation of a Low-Cycle Fatigue Relationship Employing the J-Integral Approach to Crack Growth", ASTM STP 601, 1976, pp. 33-46.

[95] M. S. Starkey and R. P. Skelton, "A Comparison of The Strain Intensity and Cyclic J Approaches To Crack Growth", Fract. of Engng Mater. and Struct. Vol.5, No. 4, 1982, pp. 329-341.

[96] N. E. Dowling, "Geometry Effects and the J-Integral Approach to Elastic-Plastic Fatigue Crack Growth", ASTM STP 601, 1976, pp. 19-32.

[97] M. Okazaki and T. Koizumi, "Relationship of Crack Growth Between Thermal-Mechanical and Isothermal Low-Cycle Fatigue at Elevated Temperatures", J. of Engng Mater. and Tech., Trans. of ASME, Vol. 109, April 1987, pp. 114-118.

[98] M. Okazaki and T. Koizumi, "Crack Propagation of Steel During Low Cycle Thermal-Mechanical and Isothermal Fatigue at Elevated Temperatures", Metallurgical Transactions A, Vol. 14A, Aug. 1983, pp.1641-1648.

[99] J. F. Yau and S. N. Malik, et al, "Elevated Temperature Crack Growth", CR174957, Aug. 1985.

[100] W. K. Wilson and I. W. Yu, "The Use of The J-integral in Thermal Stress Crack Problems", Int. J. of Fracture, Vol. 15, No.4, Aug. 1979, pp. 377-387.

[101] M. E. Gurtin, "On A Path-Independent Integral For Thermoelasticity", Int. J. of Fracture 15, 1979, pp. R169-R170.

[102] A. K. Wong and R. Jones, "A Numerical Study of Two Integral Type Elasto-Plastic Fracture Parameters Under Cyclic Loading", Engng Fract. Mechanics, Vol. 26 No.5, 1987, pp. 741-752.

[103] V. Kumar, B. I. Schumacher, and M. D. German, "Development of A Procedure For Incorporating Secondary Stresses in The Engineering Approach", EPRI Handbook, 1984, pp. 7.1-7.37.

[104] Y. Oshida and H. W. Liu, "Grain Boundary Oxidation and an Analysis of the Effects of Oxidation on Fatigue Crack Nucleation Life", ASTM STP 942, 1988, pp. 1199-1217.

[105] R. P. Skelton, "Environmental Crack Growth in 0.5Cr-Mo-V Steel During Isothermal High Strain Fatigue and Temperature Cycling", Materials Science and Engineering, Vol. 35, 1978, pp. 287-298.

[106] Heil, "Crack Growth in IN Alloy 718 Under Thermal-Mechanical Cycling", Dissertation Abstracts International Vol. 47 No. 10 April 1987, PP. 4275-B.

[107] H. -J. Christ, H. Mughrabi, "Microstructure and fatigue", Proc. of LCF-3, Sept. 5-10, Berlin, Germany, 1992, pp. 56-69.

[108] E. Vasseur and L. Remy, "Mechanical behaviour and microstructure of an ODS-superalloy tested under LCF and TMF loading". Proc. of LCF-3, Sept. 5-10, Berlin, Germany, 1992, pp.204-209.

[109] J. J. McGowan and H. W. Liu, "A Kinetic Model of High Temperature Fatigue Crack Growth", ASTM STP 612, 1976, pp. 377-389.

[110] A. Levy, "High-Temperature Inelastic Analysis", Computers and Structures, Vol.13, 1981, pp. 249-256.

[111] D. Assaker and M. Hogge, "Finite Element Analysis of Thermo-Mechanically Loaded Structures", Pub. by MECAMAT, in The Inelastic Behaviour of Solids, Models and Utilization, ed. by G. Cailletaut et al. 1988 pp. 389-403.

[112] N. J. Marchand, W. Dorner, and B. Ilschner, "Elastic-Plastic Finite Element Analysis of Thermally Cycled Double-Edge Wedge Specimens", Pub. by MECAMAT, in The Inelastic Behaviour of Solids, Models and Utilization, ed. by G. Cailletaut et al. 1988 pp. 427-443.

[113] K. T. Kim, "A Temperature Dependent Strain Hardening Law", Res Mechanica 26, 1989, pp. 371-382.

[114] M. Geradin, et al, "Three Dimensional Turbine Blade Analysis in Thermo-viscoplasticity", in The Inelastic Behaviour of Solids, Models and Utilization, ed. by G. Cailletaud et al. pub. by Mecamat, 1989, pp. 600-609.

[115] R. A. Miller, "Life Modeling of Thermal Barrier Coatings for Aircraft Gas Turbine Engines", J. of Engng for Gas Turbines and Power, ASME Trans. Vol. 111, April 1989, pp. 301-305.

[116] Y. Dai, "Some Notes on J-integral Under Combined Thermal and Mechanical Loading", Int. J. of Fracture, Vol.41, 1989, R77-R81.

[117] H. Shimada and Y. Furuya, "Local Crack-Tip Strain Concept for Fatigue Crack Initiation and Propagation", J. of Engng Materials and Technology, Vol. 109, April 1987, pp. 101-106.

[118] D. Kujawski and F. Ellyin, "On The Size of Plastic Zone Ahead of Crack Tip", Engng Fract. Mech., Vol. 25, No.2, 1986, pp. 229-236.

[119] D. Kujawski and F. Ellyin, "A Fatigue Crack Propagation Model", Engng Fract. Mech. Vol. 20, No. 5/6, 1984, pp. 695-704.

[120] K. T. Rie and R. M. Schmidt, "Life Prediction For Low-Cycle Fatigue Under Creep-Fatigue Interaction", Proc. of ICM-5, Beijing, 1987, pp. 1022-1029.

[121] N. J. Marchand, Y. Dai and M. Hongoh, "Thermal-Mechanical Fatigue Crack Growth in Aircraft Engine Materials", Interim Report, April 1990 to Feb. 1991, WY-910069, 1991.

[122] Douglas H. Norrie and Gerarg de Vries, "The Finite Element Method", Academic Press, 1973.

[123] C. A. Brebbia, "The Boundary Element Method for Engineers", A HALSTED PRESS BOOK, JOHN WILEY & SONS, New York, 1978.

[124] M. Hongoh, "General comments on boundary element method", Pratt & Whitney Canada, 8-F.3, Nov. 29, 1989, [48 pages].

[125/ F. Kolkailah and A. J. Mcphate, "Bodner-Partom Constitutive Model and Nonlinear Finite Element Analysis", J. of Engng. Mater. and Tech., Vol.112, July, 1990, pp. 287-291.

[126] C. L. Chow and K. Y. Sze, "Characterization of Notched Ductile Failure With Continuum Damage Mechanics", J. of Engr. Mat. and Tech., Vol. 112, 1990, pp. 412-421.

[127] J. Lemaitre, "Micro-mechanics of crack initiation", Int. J. of Fract., Vol. 42, 1990, pp. 87-99.

[128] A. Chulya and K. Walker, "A new uniformly valid asymptotic integration algorithm for elasto-plastic creep and unified viscoplastic theories including continuum damage", Int. J. for Num. Meth. in Engr. Vol.32, 1991, pp. 385-418.

[129] N. J. Marchand, W. Dorner, and B. Ilschner, "A novel procedure to study crack initiation and growth in thermal fatigue testing", ASTM STP 1060, pp.237-259, 1990.

[130] N. J. Marchand,"Feasibility study of a damage measurement sensor based on the ACPD technique", final report, prepared for the Dept. of National Defense, DAS ENG 6-6, Ottawa, Ontario, Dec. 1990, (45 pages).

[131] I. Verpoest et al, "An improved AC potential drop method for detecting surface microcracks during fatigue tests of unnotched specimens", Fatigue Eng. Mater. Struct. 3, 203-17, 1981.

[132] M. C. Lugg, "The analysis of sparse data in ACPD crack growth monitoring", NDT International Vol. 21, No. 3, June 1988.

[133] K. Ikeda, et al., "Electrical potential drop method for evaluating crack depth", Int. J. of Fracture 47: 25-38, 1991.

[134] I. S. Hwang and R. G. Ballinger, "A multi-frequency AC potential drop technique for the detection of small cracks", Meas. Sci. Technol. 3, pp.62-74, 1992.

[135] A. C. Pickard, et al , "Crack detection and crack length measurement in the gas turbine industry", Fatigue crack measurement: techniques and applications, editors K.J. Marsh, R. A. Smith and R. O. Ritchie, EMAS, 1992.

[136] Y. Dai, N. Marchand and M. Hongoh, "Study of fatigue crack initiation and propagation in Titanium alloys by ACPD techniques", 39th Annual Conf. of CASI, 6th Symposium on Aerospace structures & Materials, Ottawa, May 4, 1992 (submitted to CASI journal).

[137] N. Marchand, Y. Dai and M. Hongoh, "Thermal-mechanical fatigue crack growth in aircraft engine materials", INTERIM REPORT _2, May, 1990 to Feb. 1991, Prepared for the National Research Council, Canada, WY-910069, 106 pages, April, 1991.

[138] "Standard test method for measurement of fatigue crack growth rates", ASTM E647-91 , ASTM 91 annual book V0l. 3.

[139] "Engine Structural Integrity Program (ENSIP)", MIL-STD-1783, USAF, Nov. 30, 1984.

[140] K. J. Miller, "The short crack problem", Fract. of Engng. Mat. and Struc. Vol. 5. No.3. pp.223-232, 1982.

[141] K. J. Miller, "Metal fatigue - past, current and future", Twenty-seventh John Player Lecture, March 27, 1991.

[142] K. Rezai and R. N. Tadros, "Life management planning", AGARD R-732, 1988.

[143] P. R. Frise and R.Bell, "Fatigue crack growth and coalescence at notches", Int. J. Fatigue 14 No.1, pp. 51-56, 1992.

[144] A. E. Gemma, "An approximate elastic analysis of the effect of plane strain at the surface of a notch", Engng. Fract. Mech. vol. 21 No. 21, pp.495-501, 1985.

[145] E. Balanger, N. Marchand and Y. Dai, "3D elasto-plastic FE modeling for SEN specimen", Internal Report, Ecole Polytechnique de Montreal, Canada, 1992, 43 pages.

[146] M. Ohnami, et al, "Notch effect on Low Cycle Fatigue in creep-fatigue at high temperatures: Experiment and Finite Element Mothod Analysis", ASTM STP 942, pp. 1066-1095, 1988.

[147] J. Schijve, "The stress intensity factor of small crack at notches", Fract. of Mater. and Struct., vol. 5, pp. 77-90, 1982.

[148] J. C. Jr. Newman, et al, "Short-crack growth behaviour in an Aluminium Alloy-An AGARD cooperative Test Program", AGARD R-732, 1988.

[149] J. C. Jr. Newman and I. S. Raju, "An empirical stress-intensity factor equation for the surface crack", Eng. Fract. Mech. Vol. 15, No. 1-2. pp. 185-192, 1981.

[150] P. W. Tan, I. S. Raju, et al, "Evaluation of finite-element models and stress-intensity factors for surface cracks emnating from stress concentrations", ASTM STP 1060, pp. 34-48, 1990.

[151] D. Kujawaski, "Estimations of stress intensity factors for small cracks at notches", Fatigue Fract. Engng Mater. Struct. Vol. 14, No. 10, pp. 953-965, 1991.

[152] T. Fett, "The stress intensity factor for small cracks at the root of a notch", Int. J. of Fracture 54: R57-R64, 1992.

[153] N. E. Dowling, "Fatigue at notches and the local strain and fracture mechanics approaches", ASTM STP 677, pp. 247-273, 1979.

[154] T. Nicholas, et al, "Predicting crack growth under thermo-mechanical cycling", Int. J. of Fracture 41, pp. 157-176, 1989.

[155] D. Broek, "Elementary Engineering Fracture Mechanics", Matinus Nijhoff Publishers, 1987.

[156] B. Godin "Stress relaxation test of Ti46 at RT and elevated temperatures", interal report (PFE-2), Department of materials engineering, Ecole Polytchnique de Montreal, 50 pages, Sept., 1990.

[157] I. Le May, "Principles of Mechanical Metallurgy", Elsevier, 1990.

[158] A. J. Russel and D. Tromans,"A Fracture Mechanics Study of Stress Corrosion Cracking of Type-316 Austenitic Steel", Met. Trans A, Vol. 10A, Sept., 1979.

[159] T. Nicholas and J. M. Larsen, "Life Prediction For Turbine Engine Components", ASTM STP 612, 1976, pp. 353-375.

[160] A. Plumtree and B. P. D. O'Connor, "Damage Accumulation and Fatigue Crack Propagation in a Squeeze-formed Aluminium Alloy", Int. J. Fatigue, Vol.11, No 4, 1989, pp. 249-254.

[161] G. R. Romanoski, et al, "A Model for Life Predictions of Nickel-Base Superalloys in High-Temperature Low Cycle Fatigue", ASTM STP 942, 1988, pp. 456-469.

[162] B. N. Leis, "A Nonlinear History-Dependent Damage Model for Low Cycle Fatigue", ASTM STP 942, 1988, pp. 143-159.

[163] T. Nicholas, T. Weerasooriya, and N. E. Ashbaugh, "A Model for Creep/Fatigue Interactions in Alloy 718", ASTM STP 868, 1985, pp. 167-180.

[164] K. Y. Hour and J. F. Stubbins, "The Effects of Hold Time and Frequency on Crack Growth in Alloy 800H at 650°C", Metallurgical Transactions A, Vol. 20A, Sept. 1989, pp.1727-1734.

[165] M. Fujino and S. Taira, "Effect of Thermal Cycle on Low Cycle Fatigue Life of Steels and Grain Boundary Sliding Characteristics", Vol. 2, ICM 3, Cambridge, England, Aug. 1979.

[166] S. Taira and M. Fujino, "A Damage Analysis in High Temperature Thermal Fatigue", Transactions ISIJ, Vol. 19, 1979.

[167] F. Gabrielli and R. M. Pelloux, "Effect of Environment on Fatigue and Creep Crack Growth in Inconel X-750 at Elevated Temperature", Metallurgical Transactions A, Vol. 13A, June 1982, pp. 1083-1090.

[168] S. Mall, et al, "Investigation of Creep/Fatigue Interaction on Crack Growth in Titanium Aluminide Alloy", J. of Engng. Mater. and Tech., Vol.112, Oct, 1990, pp. 435-441.

[169] H. E. Boyer, "Atlas of creep and stress - rupture curves", ASM International, ISNB: 0-87170-322-X, 1988.

[170] B. Dogan, A. Saxena and K. H. Schwalbe, "Creep crack growth in creep-brittle Ti-6242 alloys", Materials in High Temperatures, Vol. 10, No.2 May 1992.

[171] Y. Dai, N. Marchand and M. Hongoh, "Low cycle fatigue crack initiation and growth at room and elevated temperatures", Proc. of Third Int. LCF conf. Berlin, Sept. 1992, pp. 586-600.

[172] Y. Dai, N. Marchand and M. Hongoh, "Fatigue crack growth mechanisms of two titanium alloys at room and elevated temperatures", Proc. of 7th World Conf. on Titanium, San Diego, USA, June 28, 1992, in press.

[173] Y. Dai and N. Marchand, "Fatigue crack initiation study of CPW41 at 750° F using SEN specimen", Memo to M. Hongoh, SSF# S-5668, SSF# S-5746, Code 400-3-4, P&W C, Nov. 20, 1991.

[174] Y. Dai and N. Marchand, "Fatigue crack growth data for CPW41 at 220, 500, 750° F using SEN specimen", Memo to M. Hongoh, SSF# S-5668, SSF# S-5746, Code 400-3-4, P&W C, Nov. 20, 1991.

[175] Y. Dai and N. Marchand, "Cyclic behaviour of CPW41 and CPW459 at 750°F and 900°F respectively", Memo to M. Hongoh, SSF# S-5668, SSF# S-5746, Code 400-3-4, P&W C, Nov. 20, 1991.

[176] Y. Dai and N. Marchand, "Thermal-Mechanical-Fatigue Crack Growth data of CPW41 and CPW459", Memo to M. Hongoh, SSF# S-5668, SSF# S-5746, Code 400-3-4, P& W C, June 19, 1992.

[177] Y. Dai, "Summary of Single Tooth Fir Tree Specimen Testing of PWA1480 at 1200°F", Memo to N. Saad, June 24, 1992.

APPENDIX I

SOME IMPORTANT ASPECTS ON TMF TESTING SYSTEM

The following notes are presented to facilitate the future operation and trouble shooting of the TMF rig. Some notes are important for safety and maintenance.

A1.1 Temperature control system

The temperature is controlled by an universal digital controller UDC3000 (Honeywell) which regulates the power output of the 3P (HALMAR) SCR power controller. The control signal is output through the OUT port which is configured as current output mode (5-20 mA). The wiring for 3P is configured as ISO mode (with 750Ωm option). The feed back signal is measured by HP3852 through Auxiliary output that has been set as LINEAR.

A1.2 Inductive heating system

The 3P (HALMAR) SCR controls the 15KW TOCCO induction RF power generator. The secondary power transformer has been removed to reduce the working coil voltage thus the emf radiation. By doing so, the cooling water volume is restricted by the long coaxial RF cable and its connection to the working coil. Although a cooling water jumper is used, it is very important not to operate the

system over 50% as indicated by the UDC3000 OUT to protect the cable from over heating.

A1.3 Convection cooling control

The cooling air flow can be adjusted separately for upper and lower distributor rings. The flow delay is adjusted by the air buffer connected immediately after the pressure source. The on / off switch of the air valve is controlled by alarm-1 and alarm-2 of the UDC 3000, which can be set digitally at desired temperature points.

A1.4 Data acquisition and control system

The HP3852A data acquisition/control unit consist of a main frame and several plug-in accessories including HP44702B DVM, HP44713A high speed multiplexer, HP44726A DAC programmable function generator, HP44713A digital switch card and HP44715A events counter. This data acquisition and control unit is used to (1) collect/transfer multi-channel data from INSTRON 8500 tower and the UDC3000 to the HP9000 Series 300 workstation, (2) generate two synchronous temperature and mechanical load/strain signals to the two closed loop control units, and (3) control the testing procedures. The central controller (HP9000 series 300 system) is equipped with two 1.4 MB floppy disc driver and one 150MB (28 ms) hard disc. A 16 inch, 6 plane color, graphic monitor is used to plot and display the

testing data. This controller is used to program the testing software and control the whole testing processes.

The basic strategy for data acquisition and test control is pretty simple and straight forward. All the programs were written in HP-BASIC 5.1 installed in the HP9000 series 300. At the beginning of a test, the central controller reads the INSTRON status information. Knowing the readiness of the INSTRON system, the program sends commands to (1) set safety limits, (2) to configure and calibrate the machine. After setting of the data acquisition procedures, the controller triggers the machine to start the test. Program then runs in the main loop.

The "ON KEY EVENT " branching technique is frequently used in the program to allow modification of the on-going test parameters when necessary. The major testing parameters or variables (strain, stress, stroke, temperature, ACPD CH_A and CH_B) are sampled by 2500 point sets over two successive load cycles. The sampling can happen either at regular intervals (which is changeable during test) or any time when a pre-specified key is pressed. Cycles immediately before termination of test are always sampled.

At any time, these parameters can be monitored on the terminal or CRT. Live data scanned by the HP4407B DVM (from different analog output channels) are continuously entered to the controller and displayed. During the sampling, the DVM is configured in scanning mode and data are first stored in the DVM buffer and then transferred (when the "scan finish" interrupt occurs) through the GPIO interface directly to the hard disc at rate of 100,000 readings per second, producing

a binary data file which is named corresponding to the cycles being sampled. At the same time, the data are also read by the controller from the INSTRON 8500 live data buffer through the HP-IB interface, and displayed on CRT. Hence, the operator can know what is going on with the test at all time.

After terminating the test using a provided criterion such as load drop, percentage of ACPD signal changes or predicted life of the specimen, the INSTRON machine and the induction heating system are automatically put in a safety modes to protect the specimen. Then, by unpacking and digital filtering, 250 data point sets of the variables for each load cycles sampled are stored in the final file in ASCII. A major statistical data file is also generated at the end of test. The complete software package developed up to now is shown in the Appendix 4.

HP44713A digital switch card is used for multiple ACPD probe measurement. It can operate over 24 PD channels. The 2-channel HP44715A event counter is used to count mechanical and thermal cycles. It also provides the event trigger signal for data logging and INSTRON status control.

A well designed relay safety element is installed beside the UDC3000. It is used to energize the event detectors of INSTRON 8500, receive the trig signals from HP3852 system and send relay pulses to TOCCO and heating jack of the specimen grip.

APPENDIX II

CYCLIC BEHAVIOR OF TI64 AND TI6246 AT 750° F AND 900° F RESPECTIVELY

A2.1 Stress vs. Strain curves

The cyclic behavior of two titanium alloys Ti64 and Ti6246 was determined at 750° F and 900° F respectively under multiple step completely reversed cyclic straining with constant strain rate $\dot{\varepsilon}$ = 1.0E-3 sec^{-1}. The cyclic parameter k and n values were obtained from the tests, which were then used for FEM and theoretical notch strain analysis described in Chapter 3.

The strain controlled cyclic tests have led to the following :

a). Under fully reversed strain cycling with strain rate $\dot{\varepsilon}$ = 1.0E-3 sec^{-1} , the cyclic stress-strain curves for Ti64 at 750° F can be expressed as:

$$\varepsilon_t = \frac{\sigma}{13771.85} + \left(\frac{\sigma}{122.71}\right)^{1/0.0699} \qquad \text{(A2.1)}$$

for strain amplitude < 0.7% (see Figure A2.4); and

$$\varepsilon_t = \frac{\sigma}{13771.85} + \left(\frac{\sigma}{165.16}\right)^{1/0.1216} \qquad \text{(A2.2)}$$

for strain amplitude > 0.7% (see Figure A2.5).

b) The cyclic behavior of Ti64 at 750° F is between bilinear and power law. It is suggested to use two power law equations.

c) Under fully reversed strain cycling with strain rate $\dot{\varepsilon}$ = 1.0E-3 sec^{-1} , the cyclic stress-strain curves for Ti6246 at 900° F can be expressed as:

$$\varepsilon_t = \frac{\sigma}{14495.38} + \left(\frac{\sigma}{188.77}\right)^{1/0.1024} \qquad \text{(A2.3)}$$

d). Recommended that multiple specimen cyclic straining tests and tests with a positive mean strain be performed. This will be used to determine the scatter band of the cyclic curves and the effect of mean strain of material hardening at these temperatures.

A2.2 Cyclic Experiment and Data Processing

The general description of the test system can be found in Chapter 2. Smooth cylindrical specimens were used to study the materials' cyclic behavior at elevated temperatures. During the tests, the specimens were heated by the induction heating system, and cycled under the strain controlled mode. All the tests were performed under fully computerized testing procedures. The stabilized stress and strain loops at each strain amplitude were digitally recorded by 250 points per strain cycle.

Figure A2.1-2 and A2.7-8 show the typical stabilized loop data for different strain amplitudes. The test started cycling under low strain amplitude, when saturation was achieved, the strain amplitude was increased to a higher step. Cycling stopped at final amplitude of 1.2%. Then a monotonic loading tensile test was performed as shown in Figure A2.6 and A2.11.

The cyclic stress-strain curve of the two alloys are shown in Figure A2.3 and A2.9. The material cyclic parameter was determined from Figure A2.4-5 and A2.10 by the least square regression method.

From Figure A2.3 and A2.6, one can find that cyclic behavior of CPW41 at 750°F is between bilinear and power law curves. Figure A2.4-5 used two sets of K and N to fit the data points. The final tensile test showed that strain cycling has little influence on materials' Young's moduli E.

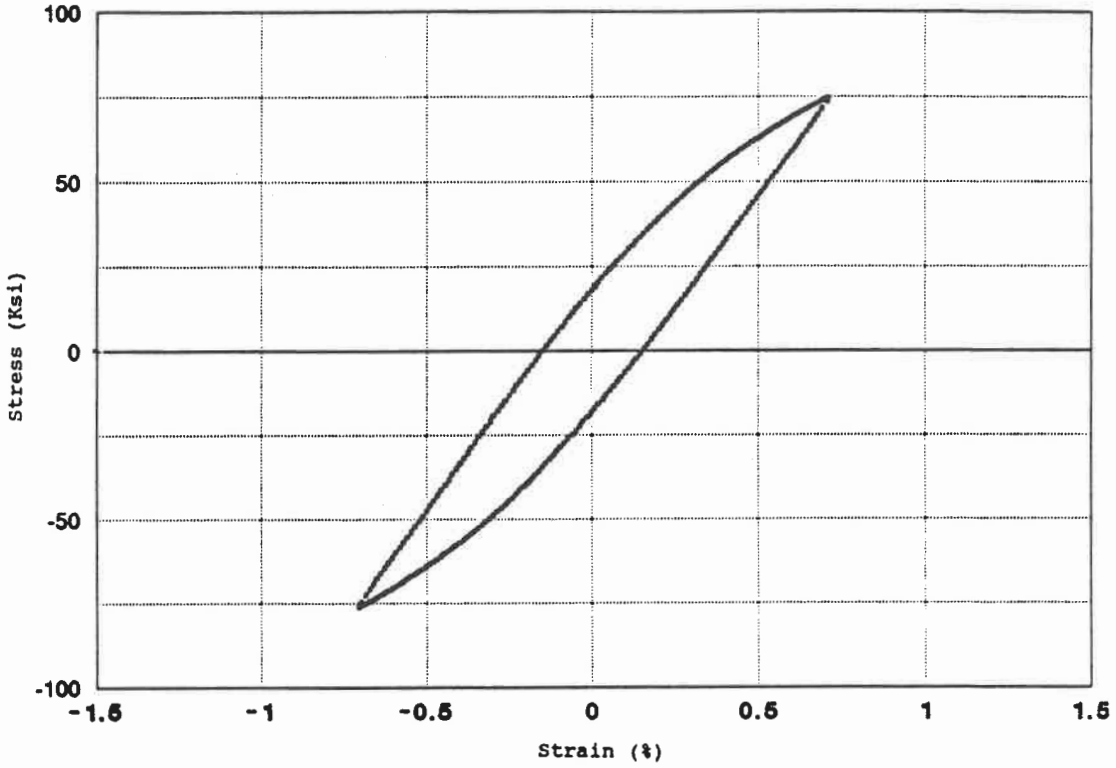

A2.1 The Cyclic stress-strain loops under 0.7% strain amplitude at 400 C. Ti64.

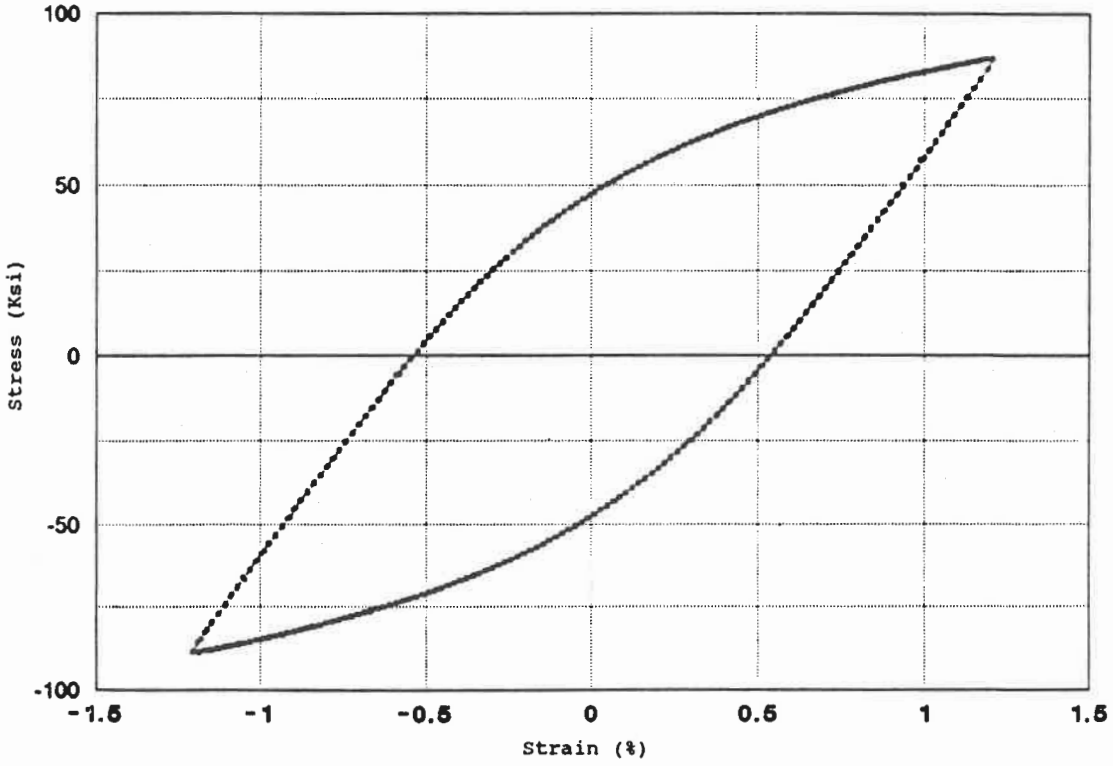

A2.2 The Cyclic stress-strain loops under 1.2% strain amplitude at 400 C. Ti64.

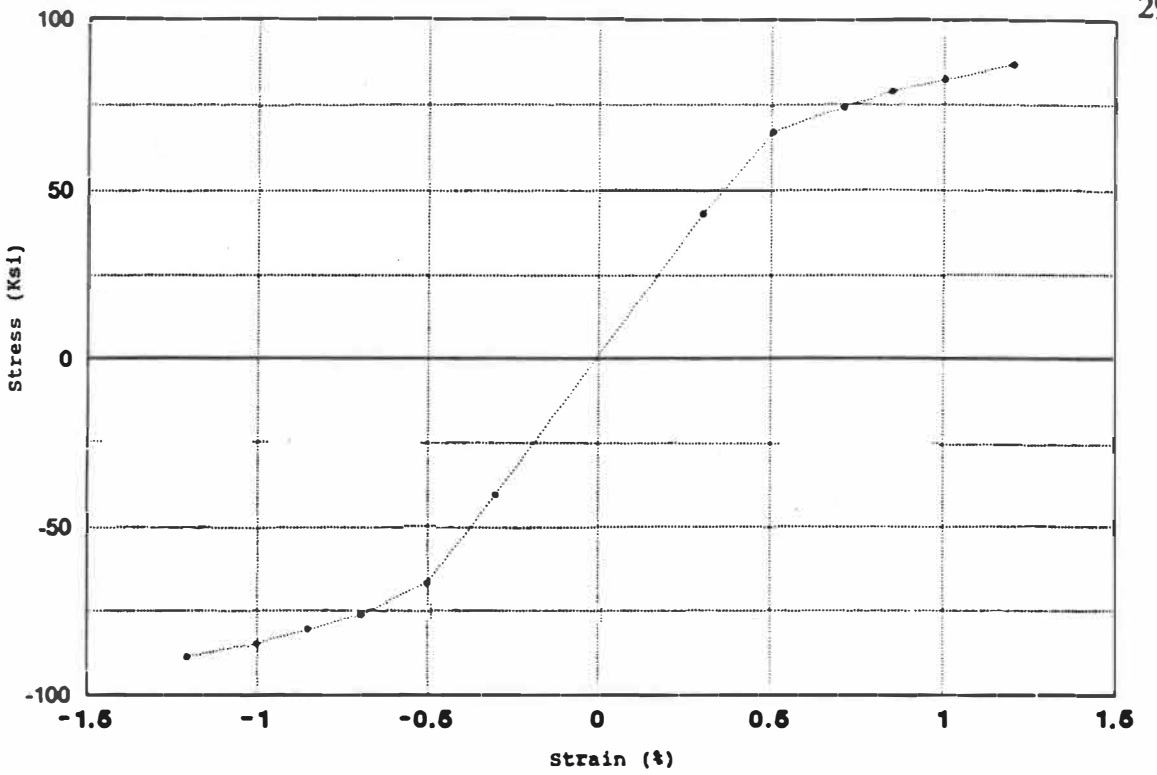

A2.3 A cyclic stress-strain curve of Ti64 at 400 C.

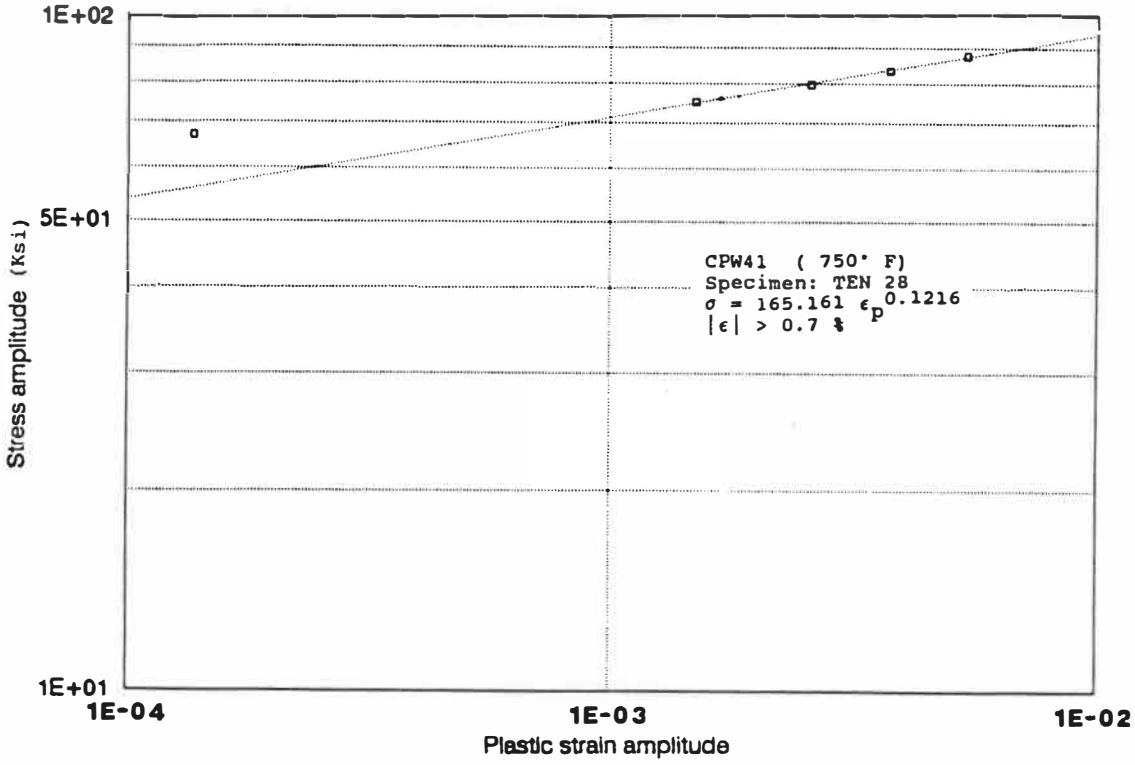

A2.4 A cyclic stress-strain curve of Ti64 at 400 C in logarithmic scale.

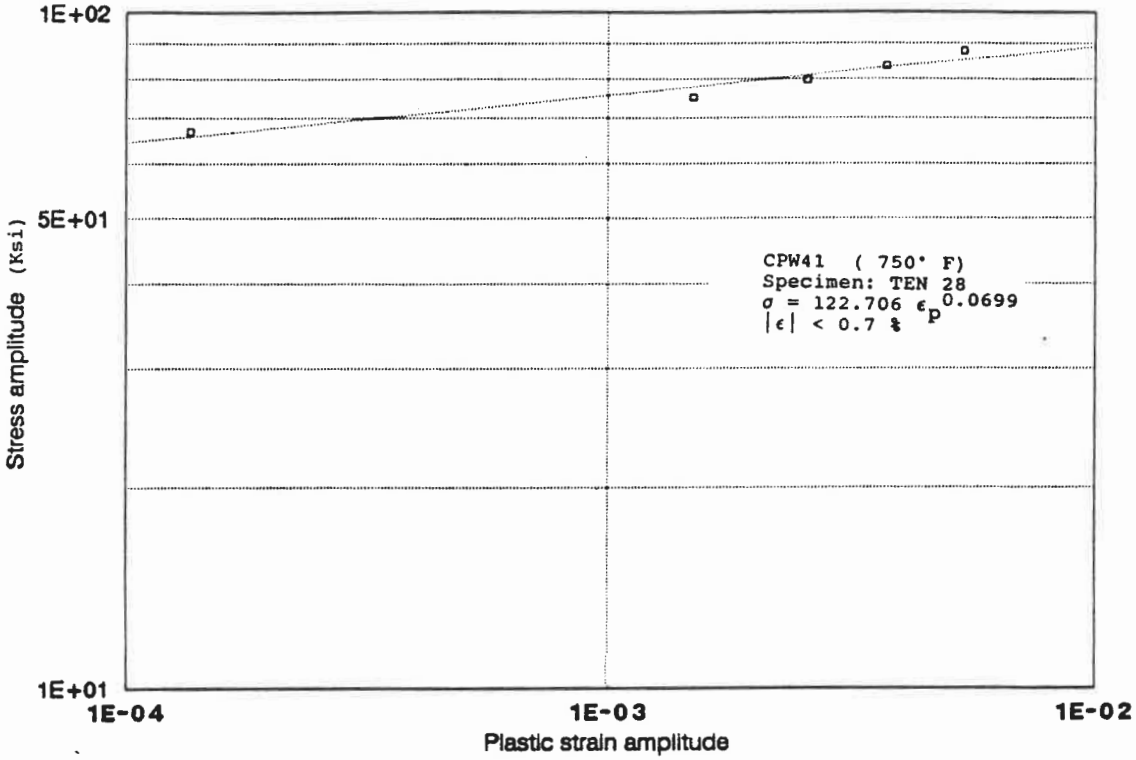

A2.5 A cyclic stress-strain curve of Ti64 at 400 C in logarithmic scale.

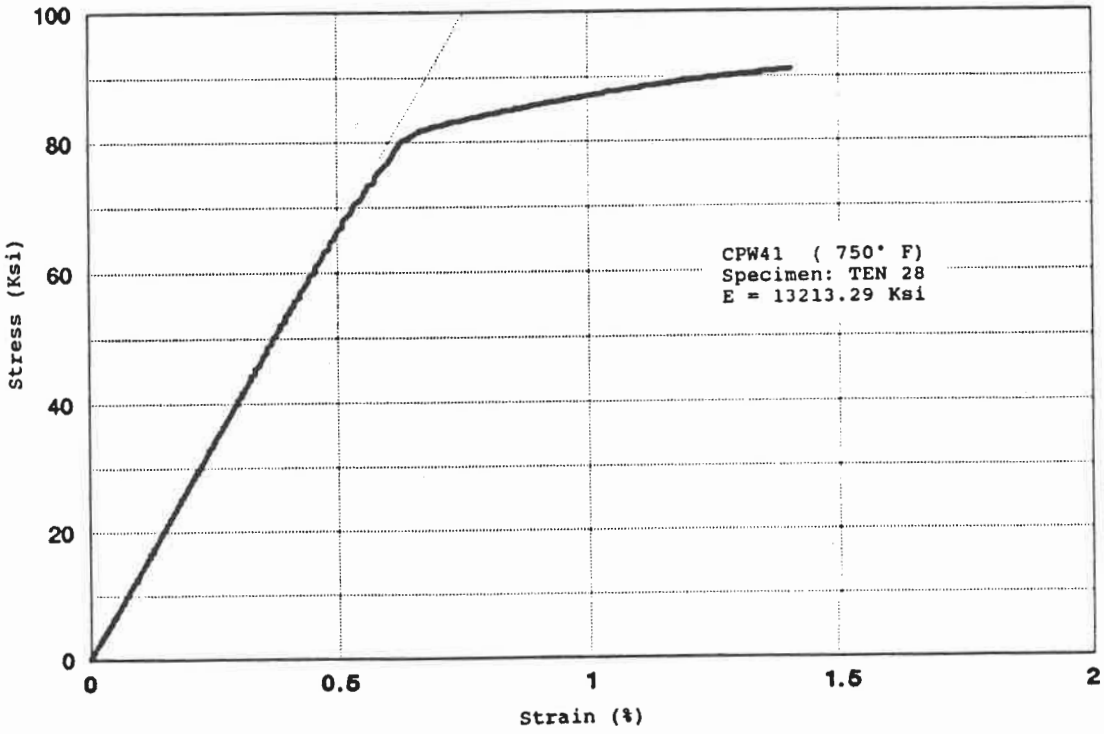

A2.6 A tensile stress-strain curve of Ti64 at 400 C after cyclic test.

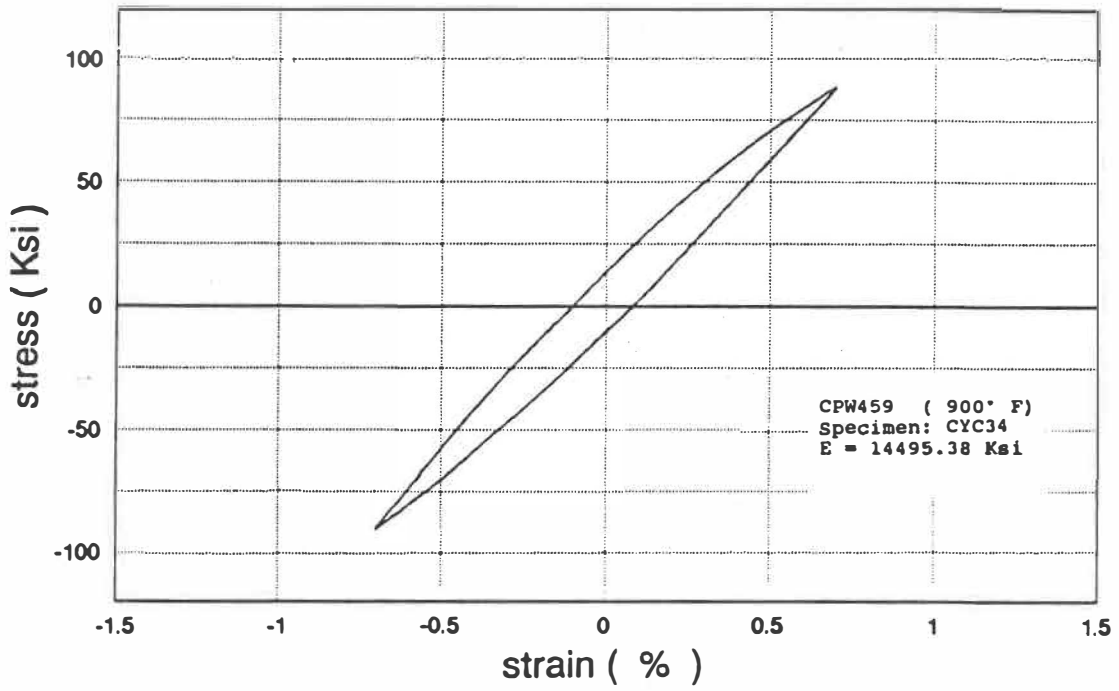

A2.7 The Cyclic stress-strain loops under 0.7% strain amplitude at 480 C. Ti6246.

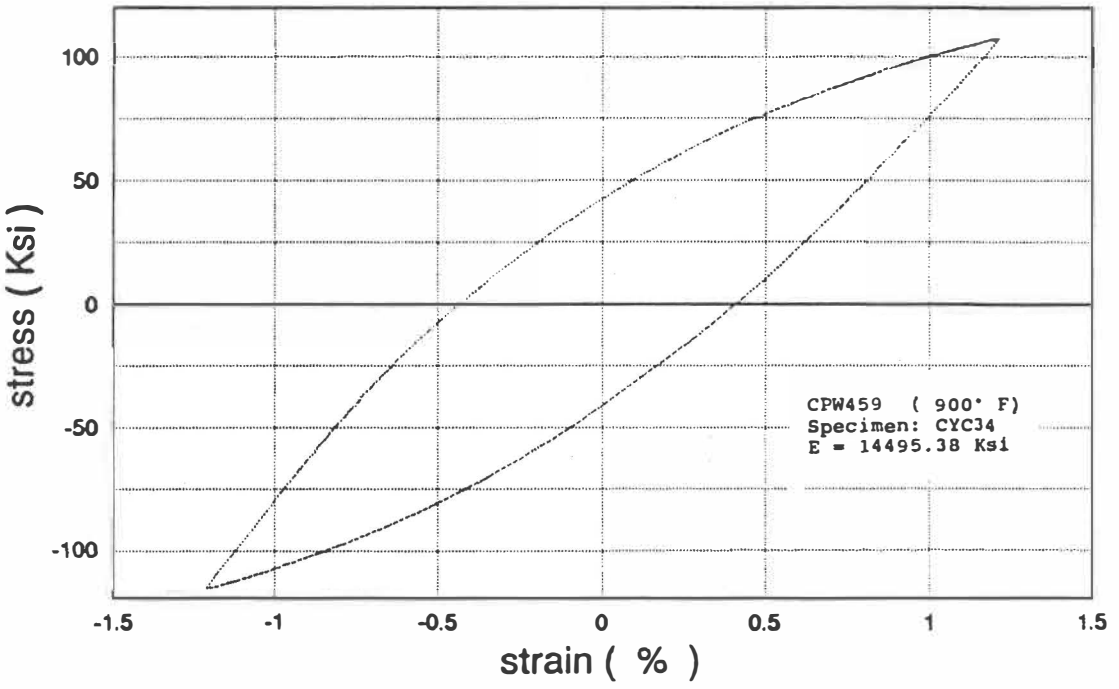

A2.8 The Cyclic stress-strain loops under 1.2% strain amplitude at 480 C. Ti6246.

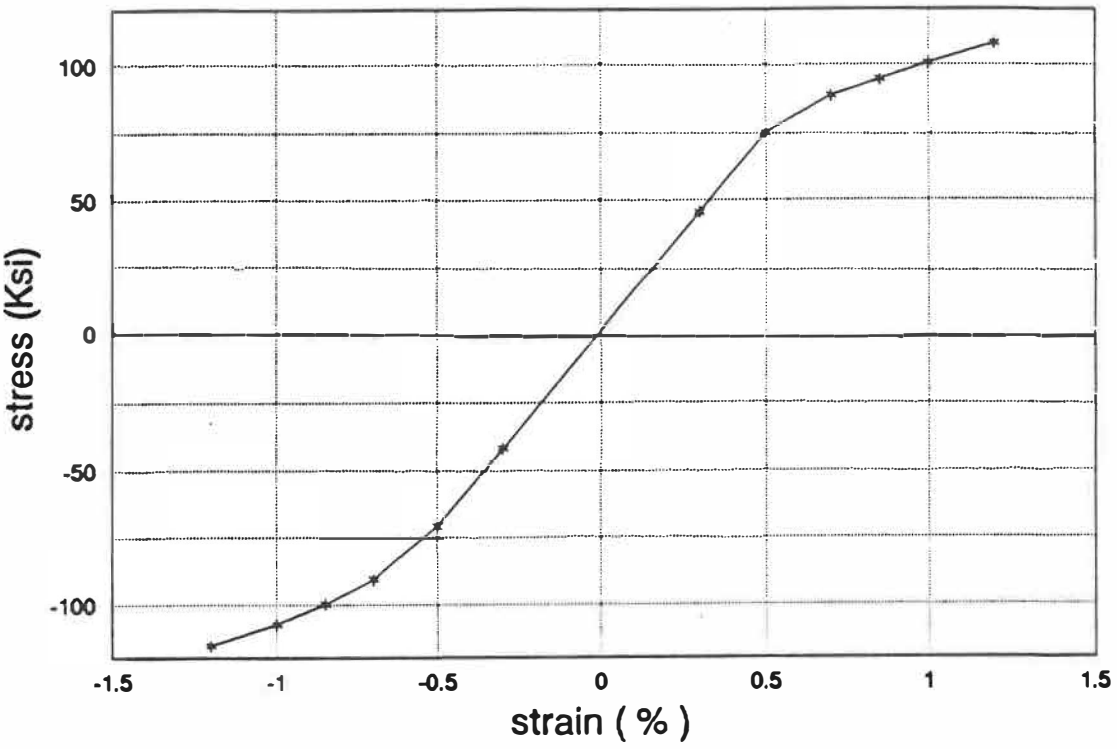

A2.9 A cyclic stress-strain curve of Ti6246 at 480 C.

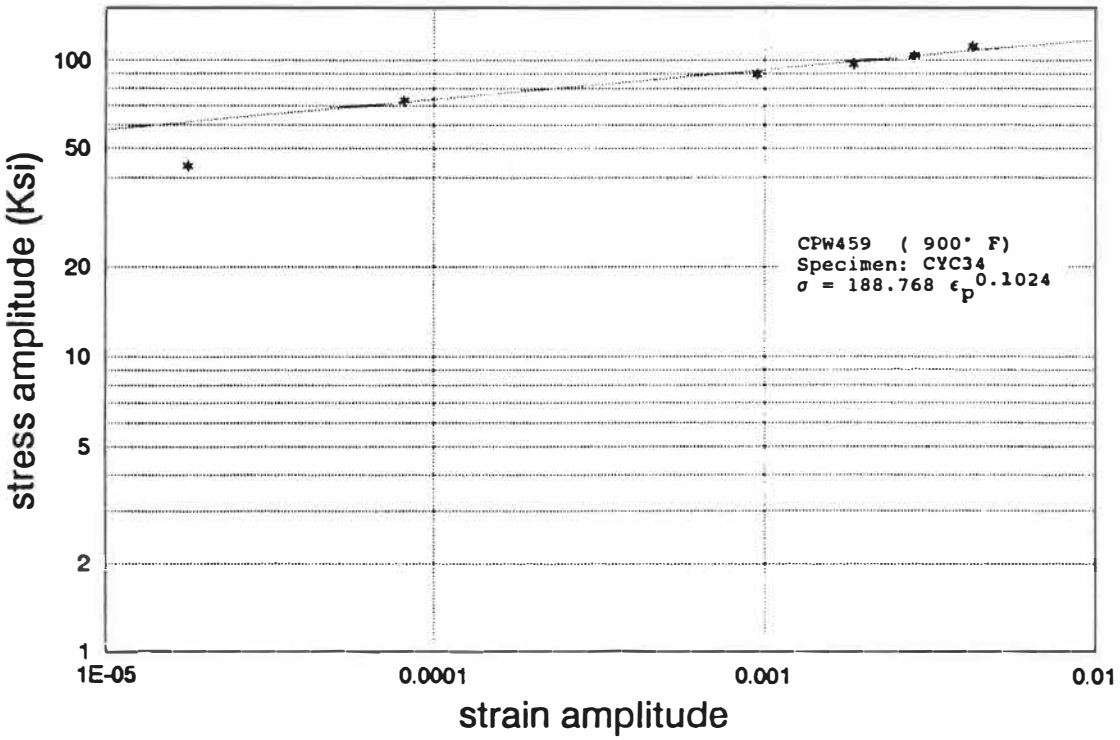

A2.10 A cyclic stress-strain curve of Ti6246 at 480 C in logarithmic scale.

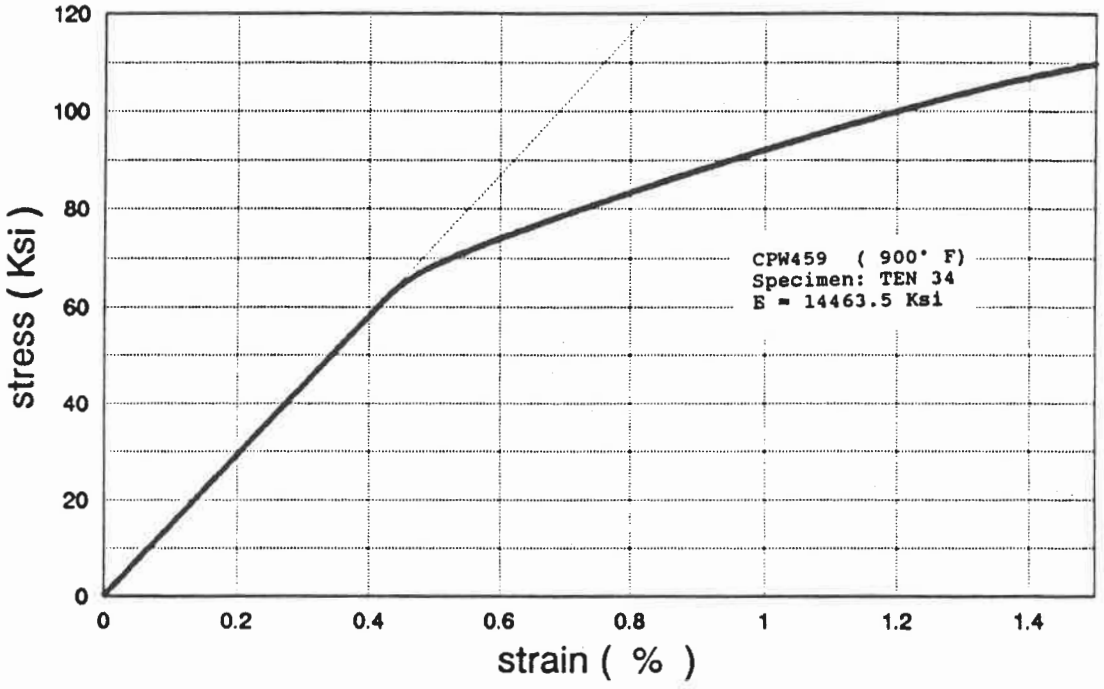

A2.11 A tensile stress-strain curve of Ti6246 at 480 C after cyclic test.

APPENDIX III

AN IMPROVED KI-SOLUTION FOR SINGLE EDGE NOTCHED SPECIMENS UNDER FIXED END DISPLACEMENT

Refer to the SEN specimen in Figure A2.2 and Figure A3.1. Considering the fact that the actual zero-rotation condition is imposed within the strain gauge length L, and that the strain is measured at back face instead of the centerline of the specimen, Marchand[51] introduced a converted length L_b where the zero-rotation condition holds. Hence the corrected K_I becomes

$$K_I = \frac{E'\delta}{L}\sqrt{\pi a}\, G(\xi,\eta,\eta_b) \quad , \tag{A3.1}$$

or

$$K_I = \frac{E'\delta}{L}\sqrt{\pi a}\, H(\xi,\eta,\eta_b) \, . \tag{A3.2}$$

Here the E'=E(Young's modules) for plane stress and $E/(1-\nu^2)$ for plane strain.

It was shown that the value of L_b/W ($\eta_b=L_b/W$, $\eta=L/W$) significantly affect the K_I value when crack length $\xi=a/W$ approaches 0.5. However there was no solution given to estimate L_b. Obviously, the chosen value of L_b will only influence the "no-crack" terms in the analysis, i.e. the beam extension δ_{nc} and rotation θ_{nc}, see Figure 3A.1. These terms are expressed as:

$$\begin{bmatrix} \delta_{nc} \\ \theta_{nc} \end{bmatrix} = \begin{bmatrix} \frac{L}{EA} & 0 \\ 0 & \frac{L}{EI} \end{bmatrix} \begin{bmatrix} N \\ M \end{bmatrix} , \qquad \text{(A3.3)}$$

Here I is the moment of inertia and A the section area. For SEN specimen with L being the gauge length, W the width and B the thickness, the equation can be written as:

$$\begin{bmatrix} \delta_{nc} \\ \theta_{nc} \end{bmatrix} = \begin{bmatrix} L/EBW & 0 \\ 0 & 12L/EBW^3 \end{bmatrix} \begin{bmatrix} N \\ M \end{bmatrix}, \qquad \text{(A3.4)}$$

Considering the SEN specimen (gauge section) "attached" to its threaded-ends with non uniform cross sections. The specimen can now be seen as a combination of small sections, which have different lengths (L_i) and different cross section A_i, as shown in Figure A3.2. The total extension and rotation are expressed as

$$\begin{bmatrix} \delta^t_{nc} \\ \theta^t_{nc} \end{bmatrix} = \begin{bmatrix} \delta_{nc} \\ \theta_{nc} \end{bmatrix} + \sum_{i=1}^{n} \begin{bmatrix} \frac{\Delta L_i}{EA_i} & 0 \\ 0 & \frac{\Delta L_i}{EI_i} \end{bmatrix} \begin{bmatrix} N \\ M \end{bmatrix} . \qquad \text{(A3.5)}$$

From the definition of L_b, we have

$$\begin{bmatrix} \delta_{nc}^{t} \\ \theta_{nc}^{t} \end{bmatrix} = \begin{bmatrix} \frac{L_b}{EBW} & 0 \\ 0 & \frac{12L_b}{EBW^3} \end{bmatrix} \begin{bmatrix} N \\ M \end{bmatrix} \quad . \tag{A3.6}$$

When comparing Eq.(A3.6) with Eq.(A3.5), it is easy to figure out that

$$L_b = L + \sum_{i=1}^{n} \Delta L_i \frac{BW}{A_i} \, . \tag{A3.7}$$

The physical zero-rotation length (L_b^{real}) which can be taken as the distance between the first thread of the grips, can be calculated as

$$L_b^{real} = L + \sum_{i=1}^{n} \Delta L_i \quad . \tag{A3.8}$$

For the particular SEN specimen considered, we always have

$$L_b < L_b^{real} \quad . \tag{A3.9}$$

which is in agreement with the intuitive engineering guess.

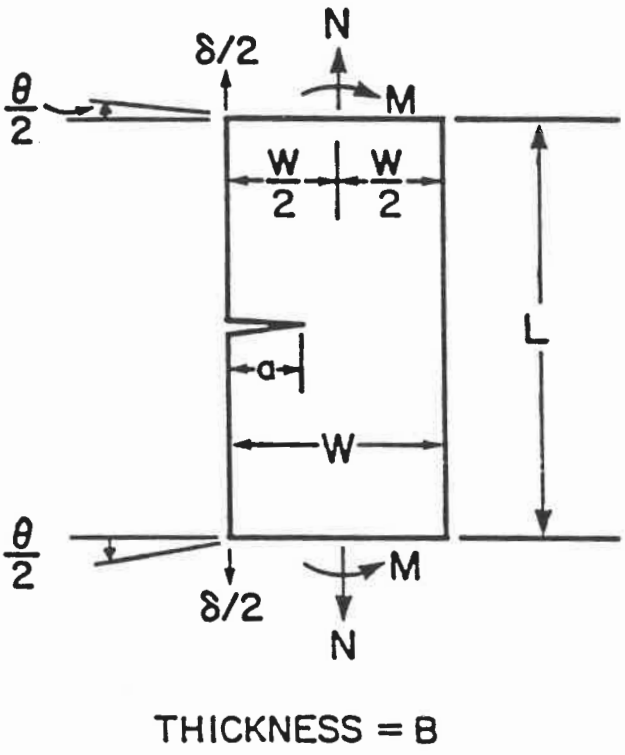

A3.1 The model used for compliance analysis in the KI calculation.

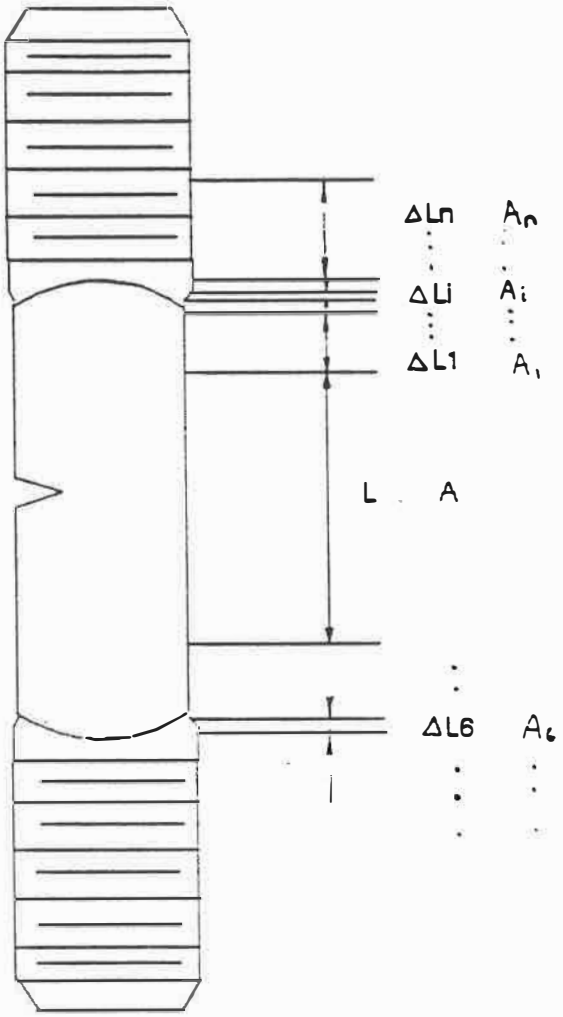

A3.2 A model used for estimating the actural zero rotation section length Lb

APPENDIX IV

THE FLOW CHART OF TMF-1 SOFTWARE

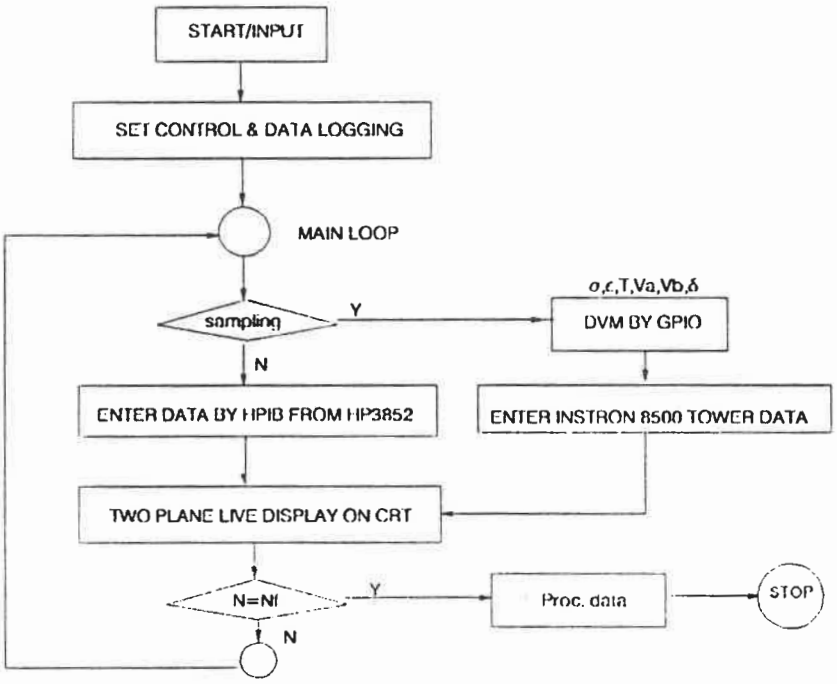

A4.1 The main program chart for TMF-1 software